CISM International Centre for Mechanical Sciences 573
Courses and Lectures

Stéphane Avril
Sam Evans *Editors*

Material Parameter Identification and Inverse Problems in Soft Tissue Biomechanics

International Centre
for Mechanical Sciences

Springer

CISM International Centre for Mechanical Sciences

Courses and Lectures

Volume 573

The series presents lecture notes, monographs, edited works and proceedings in the field of Mechanics, Engineering, Computer Science and Applied Mathematics. Purpose of the series is to make known in the international scientific and technical community results obtained in some of the activities organized by CISM, the International Centre for Mechanical Sciences.

More information about this series at http://www.springer.com/series/76

Stéphane Avril · Sam Evans
Editors

Material Parameter Identification and Inverse Problems in Soft Tissue Biomechanics

Springer

Editors
Stéphane Avril
Center for Biomedical and Healthcare Engineering
MINES Saint-Étienne
Saint-Étienne
France

Sam Evans
School of Engineering
Cardiff University
Cardiff
UK

ISSN 0254-1971 ISSN 2309-3706 (electronic)
CISM International Centre for Mechanical Sciences
ISBN 978-3-319-45070-4 ISBN 978-3-319-45071-1 (eBook)
DOI 10.1007/978-3-319-45071-1

Library of Congress Control Number: 2016949095

Printed on acid-free paper

This Springer imprint is published by Springer Nature
The registered company is Springer International Publishing AG
The registered company address is: Gewerbestrasse 11, 6330 Cham, Switzerland

Contents

List of Figures

List of Tables

Introduction

The current book follows the very successful and popular course C1511 that took place at the International Center for Mechanical Sciences (CISM), Udine (Italy) during 12–16 October 2015.

Although many fields in medicine have always needed accurate measurements of local tissue properties, the need for training on hybrid experimental—computational methods for soft tissues appeared clearly after the successful Euromech colloquium that took place at Saint-Etienne (France) in May 2012. Other meetings about this topic were further organized in different international conferences, including a one-day symposium during the World Congress of Biomechanics at Boston in 2014. Several special issues were also published by important journals (Journal of the Mechanical Behaviour of Biomedical Materials, Computer Methods in Biomechanics and Biomedical Engineering journal, Strain) on related topics.

All these series of events, and especially the popular CISM C1511 course, highlight the increasing number of researchers involved in characterizing soft tissues biomechanics and this has been the main motivation for writing this textbook.

Indeed, it has become a common practice to combine video based full-field displacement measurements experienced by tissue samples in vitro, with custom inverse methods to infer (using nonlinear regression) the best-fit material parameters and the rupture stresses and strains. Similar approaches also exist for characterizing the material parameters of soft tissues in vivo, where advanced medical imaging can provide precise measurements of tissue deformation under different modes of action, and inverse methodologies are used to derive material properties from those data.

Nowadays, these approaches offer important possibilities for fundamental mechanobiology which aims at gaining better insight in the growth, remodelling and ageing effects in biological tissues. It is well known that biological soft tissues appear to develop, grow, remodel, and adapt so as to maintain particular mechanical metrics (e.g. stress) near target values. To accomplish this, tissues often develop regionally varying stiffness, strength and anisotropy. Important challenges in soft tissue mechanics are now to develop and implement hybrid experimental–computational method to quantify regional variations in properties in situ. For this, some kind of inverse approach is needed, where an experiment has to be simulated and the material parameters are adjusted until the model matches the experiment.

Several important questions are raised by inverse approaches in soft tissue biomechanics:

1. Experimental measurements on biological tissues present many practical and theoretical difficulties. Experimental and numerical errors also increase the uncertainty, as do inadequate constitutive models.
2. An inverse problem requires a computational model that can be solved repeatedly with different material parameters. This requires a model that can be solved quickly and reliably; these are not attributes one usually associates with computational models of biological tissues.
3. Biological tissue mechanical behaviour exhibits special characteristics that may affect the mechanical response and disturb material identification, such as viscoelasticity, multi-scale properties, variability of properties and remodelling.
4. Once the necessary experimental data and computational models are in place, it is essential to implement an appropriate optimisation strategy to adjust the material parameters to give the best match with the experimental results, and to consider issues of uniqueness of the identified parameters. Where only a single parameter is optimised, for example the stiffness of the material, it is relatively easy to ensure that a global optimum has been found, but for complex models with many parameters there are often many different parameter sets that will produce equally good results.
5. The question of uniqueness can be tackled by increasing the quantity of experimental data. To this purpose, tracking the full-field deformation of tissues using optical measurements or medical imaging techniques becomes quite commonplace but these novel measurement approaches have only been recently applied to material identification of biological tissues and they still have to be well calibrated and validated for them.
6. It has also been identified that in certain situations useful patient-specific results can be obtained without precise knowledge of patient-specific properties of tissues. This situation arises when computational biomechanical models can be loaded kinematically or when structures under consideration are approximately statically determinate. Problems that meet these requirements frequently arise in image-guided surgery and modelling and analysis of thin-walled biological organs.

The current textbook tentatively provides some background to address these important questions.

In Chap. 1, the basics of tissue biology are presented, which permits understanding where mechanical properties of soft tissues come from. The link between the microstructure and the macroscale properties of soft tissues are detailed and illustrated on several types of tissues: tendons, heart valves. Finally, the different experimental techniques available for characterizing these material properties are presented.

In Chap. 2, constitutive models for soft tissues biomechanics are introduced, first by presenting the basics of continuum mechanics and hyperelasticity. After summarizing other types of constitutive equations for soft tissues, we present recent developments of experimental biomechanics and inverse methods aimed at quantifying constitutive parameters of soft tissues. A focus is given to in vitro characterization of hyperelastic parameters based on full-field data that can be collected with digital image correlation (DIC) systems during the experimental tests.

In Chap. 3, we present in more details the DIC technique and its application to the measurement of strain fields in soft tissues. Then the basics about the finite-element (FE) method and the specificities of its use on soft tissues are presented. Finally, the combination of FE analyses and DIC measurements through inverse problems to derive constitutive material properties is discussed in terms of efficiency and uncertainty quantification.

In Chap. 4, we review vessel wall histology and summarize relevant continuum mechanical concepts to study mechanics-induced tissue damage. Indeed, damage and failure in soft tissues are important questions for which the use of hybrid experimental–computational methods is still in its infancy. Specifically, modelling vascular failure by a fracture process zone is discussed, such that initialization and coalescence of micro-defects is mechanically represented by a phenomenological cohesive traction separation law. Failure of ventricular tissue due to deep penetration illustrates the applicability of the approach. Besides appropriate continuum mechanical approaches, it is also shown that laboratory experiments that are sensitive to constitutive model parameters and ensure controlled failure propagation are crucial for a robust parameter identification of failure models.

In Chap. 5, we describe the main features of standard tests for a mechanical characterisation of biological materials, like uniaxial, biaxial and shear tests. After that, the inverse, mixed experimental/numerical methods are introduced as a tool to create more freedom in the design of experiments and to make the transition from ex vivo testing to in vivo testing possible. A short introduction to the algorithms that can be used to minimise the difference between the experimental results and the numerical results is discussed, followed by two practical examples related to skin. The chapter finishes with a comparison between the advantages and disadvantages of in vivo and ex vivo testing.

In Chap. 6, we show how patient-specific FE models of human soft tissues and organs can be made compatible with the clinical constraints. We discuss more specifically the question of calibrating the material properties in this context, with choices that should be done between calibrations based on ex vivo or in vivo tissue loadings. Computer-assisted maxillofacial surgery is used as an example.

Chapter 1
Structural Building Blocks of Soft Tissues: Tendons and Heart Valves

Himadri S. Gupta and Hazel R. C. Screen

Abstract Modelling the mechanical behaviour of soft tissues like tendon, ligament, skin and cartilage requires a knowledge of the structural and mechanical properties of the constitutive elements. These tissues have a hierarchical architecture from the molecular to the macroscopic scale, and are composites of different molecular building blocks. Here we first review the structure of the proteins and polysaccharides comprising such tissues. We then consider the structure and mechanical properties of two prototypical soft tissues: tendons and heart valves. An overview of their structure is followed by a description of the known mechanical behaviour of these tissues. Consideration is given to the role of different constituent components in mechanical response, structural anisotropy and testing methods which can probe mechanical deformation at multiple levels.

1.1 Structural Components of Soft Tissues

Connective soft tissues like tendon, cartilage, skin, ligament and arteries are required to resist a range of mechanical loads as part of their normal physiological function. These mechanical requirements exhibit considerable variation: for instance, tendon is built to resist uniaxial loading, skin to provide a structural barrier against the environment and against multidirectional loads, while cartilage provides frictionless sliding and compressive resistance at the ends of bones [1]. These properties are critically enabled by the structure and architecture of the extracellular matrix (ECM) which is secreted by cells such as tenocytes and chondrocytes.

By themselves, the mechanical properties of cells (∼kPa) are far too low to enable effective resistance to the typical loads of a few MPa that are experienced *in vivo*. Cells must therefore secrete a range of biological macromolecules—both proteins and polysaccharides—which self-assemble into fibrils, lamellae and fibre bundles to form

---

H.S. Gupta (✉) · H.R.C. Screen
School of Engineering and Materials Science, Queen Mary University of London,
Mile End Road, London E1 4NS, UK
e-mail: h.gupta@qmul.ac.uk

S. Avril and S. Evans (eds.), *Material Parameter Identification and Inverse Problems in Soft Tissue Biomechanics*, CISM International Centre
for Mechanical Sciences 573, DOI 10.1007/978-3-319-45071-1_1

the ECM. The structural diversity of the motifs formed [2] are the key which enable such tissues—made out of mechanically relatively unimpressive components—to achieve impressive adaptation and optimization to their *in vivo* loading regimes [3].

In this chapter, we first review the structure and properties of common molecular building blocks of soft tissues. We then identify some common structural and mechanical motifs that appear repeatedly, with different constituents, across biological materials. Finally, we describe the specific properties of two prototypical soft tissues: tendons and heart valves, and relate how structure enables mechanical behaviour, to the extent currently known.

1.1.1 Hierarchical Structure of Proteins

The most common proteins in soft tissues, by decreasing frequency of occurence, are collagen, elastin and fibrillin. The proportions of these components can vary considerably between the tissues of origin: skin, tendon, arteries, lungs and heart valves. The primary structure of collagen-like and elastin-like proteins are distinct. While collagens are characterized by a predominance of the repeating amino acid triplet glycine-X-Y (where X and Y are either proline or hydroxyproline) elastin contains 30 % glycine with the majority of other amino acids being valine, alanine or proline [4, 5]. The secondary structure of collagens is a triple helix, while elastin-like proteins consist of alpha-helices and beta-turns. In both, the covalent cross-linking is through lysine residues.

Collagen: Collagens consist of triplets of polypeptide chains (known as α-chains), with each chain characterized, at the level of primary structure, by a repeating of the triplet (Gly-X-Y), where Gly stands for glycine and X- and Y- are most commonly either proline or hydroxyproline. This characteristic repeat, together with the small size of the glycine residue, results the chains forming a tight right-handed triple helical conformation, with the glycine residue on the interior of the helix [6]. Over 29 different types of collagens are known, which can be divided (from a bioengineering viewpoint) into fibril-forming and non-fibrillar collagens. The fibrillar collagens—mainly Type I–III as well as smaller proportions of type V and IX—are structurally the most significant contributors to the mechanics of soft tissues acting as stiff fibrous units within tissues. Collagens may be classified as homotrimeric (where the three α-chains are identical, as in Type II and III) or heterotrimeric (where not all the α-chains are identical, as in Type I). These are denoted via the shorthand notation $[\alpha 1(I)]_2\alpha 2(I)$ (for Type I) and $[\alpha 1(II)]_3$ (for Type II). These fibrillar collagens comprise a triple helical central region, typically around 1000 residues long (or 330–340 (Gly-X-Y) triplets), with non-helical ends at the C- and N-termini. Collagen I is the most commonly found variant in tendon and heart valves, the focus of this chapter.

At the nanometre length scale the individual tropocollagen molecules assemble into insoluble fibrils, which are (for Type I collagen) typically in the 50–200 nm diameter range. Fibril-associated collagens (FACITs) are found typically on the surface of the fibrils. Collagen molecules typically aggregate in a highly regular manner both axially (along the length of the tropocollagen helix) as well as laterally (side-by-side packing of the helices). This results in a characteristic banding pattern with a $\mathrm{D} = 65$–67 nm pattern visible in electron or scanning probe microscopy as well as in small-angle X-ray diffraction, which arises from the repeated staggered arrangement of molecules. Adjacent tropocollagen molecules are laterally shifted by D, to maximize contact between hydrophobic regions. Since the length of a tropocollagen molecule is 300 nm, which is not an integral multiple of D, the lateral stagger leads to regions of high and low electron density inside the array of tropocollagen molecules comprising the fibril. The D-period is sensitive to hydration, with dry collagen having a D-period of 65 nm and wet collagen 67 nm. There are about 234 amino acids per D-period repeat [7]. In vertebrates, collagen fibrils are synthesized with relatively short lengths (1–3 μm) initially, and form much longer fibrils of unknown length by the process of axial fusion. In certain tissues like skin, branched networks of fibrils are also formed [8].

The fibril is often classed as the fundamental building block of tissues, and in different tissue types, it further aggregates into fibres or bundles. At the scale above individual fibrils, aggregation into fibre bundles, lamellae or fibres occurs depending largely on the tissue type. In tendons, characteristic fibres of diameter of the order of tens of microns are present [9], while in mineralized collagenous tissues lamellae of fibrils in a plywood arrangement are characteristic [10]. Considerable inter-tissue variation is present.

Elastin: Elastin is a stable, insoluble and rubbery protein [2, 4] which comprises the bulk ($>90\,\%$) of elastic fibres in tissues like skin, ligament, arteries and lung. The insolubility of elastin arises from extensive lysine cross-linking between adjacent elastin molecules. The mechanics of elastin networks is driven primarily by entropic elasticity [11], as they are far more rubber-like in conformation compared to collagen fibrils. Analogues of elastin are found in a range of phyla: lamprey cartilage and mussels have proteins which have similarities to elastin [4]. Tropoelastin is the soluble precursor of elastin and contains two types of domains: hydrophobic domains with nonpolar amino acids (glycine, valine, proline and alanine) [4] and hydrophilic domains contain lysine and alanine. Hydrophilic domains are involved in cross-linking of adjacent elastin molecules. Similar to the process of fibril formation, microfibrils of elastin are formed in the extracellular compartments adjacent to the secreting cells and are rapidly cross-linked. Fibre diameters show some variability: intervertebral disc and cartilage have thin fibres <1 μm, while in the ligamentum nuchae fibres of ~ 1 μm are comprised of subfibrils of 200 nm diameter [11]. These fibres are arranged into larger scale lamellae, as seen in aortic media. Figure 1.1 from [12] shows the differences in structure between the elastic fibrils in arteries and in ligament.

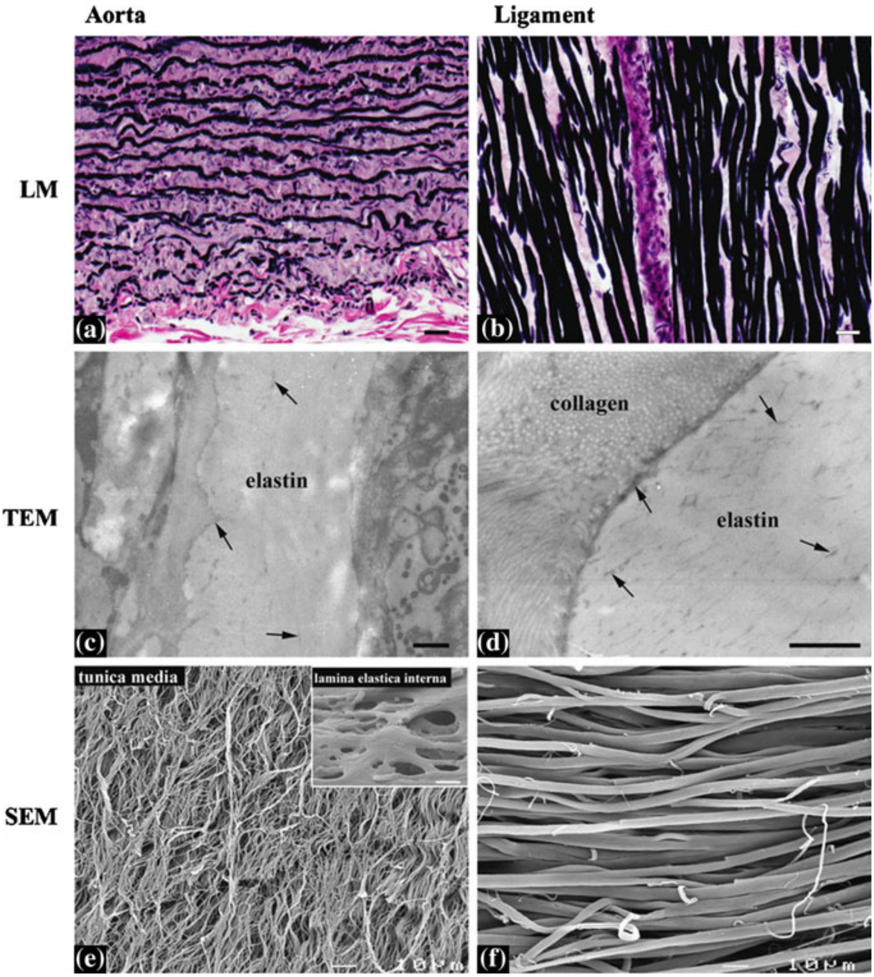

Fig. 1.1 Images of elastin fibres in aorta **a** and ligament **b**, taken with permission from [12]. The *top row* **a**–**b** shows light microscopic images of stained (Verhoeff-Van Gieson) tissue; elastic fibres are black while collagenous tissue is pink. *Middle row* **c**–**d** report transmission electron microscopy images from the same tissues and the *lowest row* **e**–**f** shows scanning electron microscopy (SEM) images. A thinner fibre diameter, and less ordered fibrous arrangement, is evident in the aorta

1.1.2 Hierarchical Structure of Polysaccharides

Polysaccharides consist of aldoses and ketoses, and are characterized by the general formulae $C_n(H_2O)_n$. They include mono-, oligo- and polysaccharides. Monosaccharides are the basic building blocks, an example of which is glucose ($C_6(H_2O)_6$). They can form disaccharides (with two monosaccharides) or oligosaccharides (between three and ten), which are monosaccharides combined via a glycosidic linkage.

Monosaccharide chains with more than ten monosaccharide units are denoted as polysaccharides, and include widespread materials like starch, chitin or cellulose.

Polysaccharides can form fibres (as in chitin) but in soft tissues are more commonly found in gel-like phases coexisting with the stiffer protein-based fibrous networks of collagen and elastin. These will now be briefly described.

Chitin: Like proteins, polysaccharides can also display a hierarchical structure: the chitin within the cuticle in arthropod skeletons, for instance, is comprised of α-chitin fibrils in a protein matrix, aggregated into fibres and lamellae [2, 13]. Indeed, at least five levels of hierarchy have been identified in chitinous tissues [14] which serves as an example of a structural biomaterial with polysaccharide (chitin) fibres as a principal building block. At the macroscopic scale, there are three layers to the cuticle: a thin outer epicuticle, a calcified exocuticle, and a less dense endocuticle, which have thicknesses of the order of a few hundred microns. The exo- and endocuticle are comprised of lamellae of chitin fibres, which undergo a 180° rotation around the axis perpendicular to the cuticle surface within each lamella. At this scale, a second phase of fibres running perpendicular to the lamellae have been identified. These fibres are found in pore canals which form a honeycomb-like structure together with the lamellae [2, 13]. The fibres have diameters between 50 and 250 nm, and are in turn comprised of 2–5 nm diameter chitin fibrils together with a mixture of crystalline and amorphous calcium carbonate and an amorphous protein phase. The fibrils comprise of several chitin molecules aggregated in an antiparallel manner and wrapped by protein. The multiple hierarchical levels are shown in Fig. 1.2.

Glycosaminoglycans and proteoglycans: Glycosaminoglycans (GAGs) like hyaluronic acid are large, unbranched polysaccharides which form a gel-like phase coexisting with the fibrous proteins in soft tissues like tendon, cartilage and ligament. They are typically highly hydrophilic with a negative charge density, and as a result attract cations like Ca^{+2} or Na^{+}. Hyaluronic acid (often abbreviated HA) is a polysaccharide with molecular weight between 10^5 and 10^7 Daltons, containing about 10^4 disaccharides. The building blocks of HA are N-acetyl-D-glucosamine and D-glucoronic acid.

GAGs are most typically found in the form of proteoglycans, which consist of a core protein chain with GAG chains branching off from the core. Proteoglycans play an especially important mechanical role in resisting compression and shear in tissues such as cartilage and the annulus fibrosus of the intervertebral disc, due to their negative fixed charge density and consequent swelling pressure. In addition, their hydrophilic nature increases the water content of the tissue, thus also increasing osmotic pressure. Examples of PGs are aggrecan and decorin. Aggrecan is typically about 400 nm in length, with chondroitin sulphate GAG chains branching off from the core protein with a length of 40 nm and globular domains at the end (*CITE*). It has a molecular weight of $\sim$225–250 kDa. Decorin is a much smaller PG, and a member of the SLRP family. It has one GAG chain (either dermatan sulphate or chondroitin sulphate).

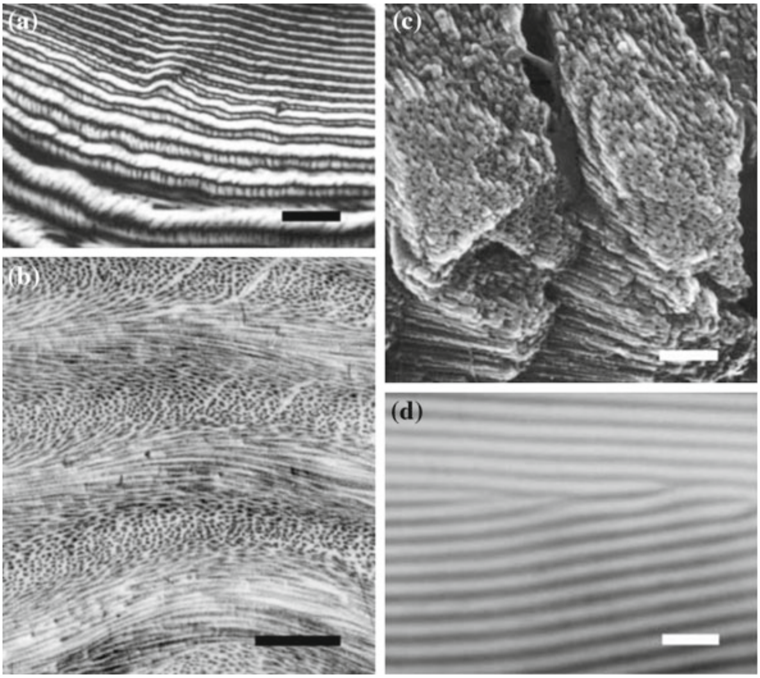

Fig. 1.2 Chitin fibre networks from crab cuticle and synthetic chitinous materials, image taken with permission from [15]. Image **a** reports polarized light microscopic imaging (scale bar is 20 μm). **b** The cholesteric liquid crystal arrangement within a single lamellae, seen from electron microscopic imaging of sections of cuticle, where fibres at different angles to the sectioning plane appear as oblique or perpendicular to the plane (scale bar is 1 μm). **c** Shows an image of (undecalcified) cuticle, where a calcium carbonate phase is present along with the fibrils (scale bar is 0.2 μm). **d** An example of synthetic colloidal suspensions of colloidal chitin, imaged with polarized light microscopy, with the banding characteristic of the lamellar structure shown (scale bar is 100 μm)

1.1.3 Design Principles of Biological Materials

Structural organization of the fibre–matrix in different patterns The relatively restricted set of biopolymers described in Sects. 1.1.1 and 1.1.2 of this chapter are used by cells in soft tissues to build ECM with a wide range of mechanical properties and structural motifs [2]: from the compressive and sliding resistance of cartilage, to the fatigue resistance of tendon and heart valves or (considering biomineralized tissues) the toughness of bone and related calcified tissues. Biologists may concern themselves with questions relating to rates of cell secretion of ECM matrix, rates of removal and turnover and whether these can be manipulated in synthetic or *in vitro* conditions to build tissues in a biomimetic manner (the domain of tissue engineering). However, the bioengineer may have equal if not greater interest in understanding how these building blocks self-assemble to optimize certain mechanical properties.

Broadly speaking, the types of ECM molecules described above are usually found in fibre composite arrangements, implying fibrouse and gel/matrix phases, usually in close spatial association (at multiple levels). Fibres are used to provide high stiffness and strength, whilst matrix phases can both transfer forces between fibrils as well as provide stability to the fibres and bind or stabilize the water phase. We will now consider, from a structural perspective, fibre composite designs as found in several soft tissues, and discuss which particular mechanical property will be optimized for a given arrangement.

In Fig. 1.3a, the same fibre–matrix arrangement is shown in three different orientations with respect to the loading direction. In the first, the fibres are parallel to the loading direction, and as a result the material is expected to be stiff and exhibit high elastic recovery. Conversely, if the load is applied perpendicular to the fibre long axis, the soft and viscous matrix phase (which corresponds to the PG/GAG rich interfibrillar material) will dominate the strain response, leading to less elastic recovery and a more compliant material. Finally, when the fibres are at an angle to the loading direction, the fibres will bear (approximately) the projection of the force

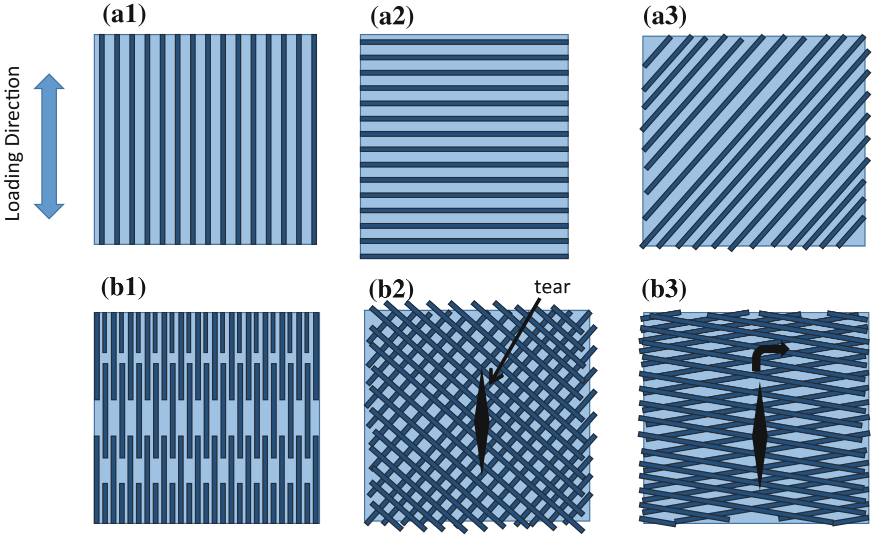

Fig. 1.3 **a** Fibres (*dark blue*) inside a ductile matrix (*light blue*) mimicking the fibre composite structure found in numerous soft tissues. If the loading direction is as indicated by the *arrow*, the fibres will bear the tensile load in the left image (Voigt loading as in [16]), while very little load in the centre image (Reuss loading as in [16]). In the middle image, depending on the degree of viscosity and stiffness of the matrix, fibres will reorient toward the loading direction. **b** *Left* Finite length of the fibres implies interfibrillar shear transfer through the matrix. *Middle* By having multiple fibre orientations (as in skin or arteries), crack propagation can be hindered, as there will always be a proportion of fibres which need to be fractured (with high breaking stress) for the crack to propagate. *Right* A schematic of the fibre geometry as found in arteries, where resistance to circumferential loading is most important. Cracks will be diverted from the initial direction to run in the "weak" direction between fibres rather than across them

onto the fibre axis, but may also be induced to rotate in the matrix toward the loading direction. When the length of fibres is reduced (Fig. 1.3b1) the contribution of the matrix to material mechanics is increased, as in this case the force is not borne end to end (in the tissue) by the fibre, but is transferred (via shearing mechanisms [16]) through the viscous matrix. By controlling the degree of overlap of the fibres, as well as the interfibrillar matrix spacing, the effectiveness of the shear transfer can be controlled.

Whilst aligned fibres are beneficial in some tissues such as tendon, in many tissues, loading is multidirectional, lending itself to fibre arrangements, such as Fig. 1.3b2. Matted or plywood-like structures will achieve stiffness in multiple directions (as there are always a proportion of fibres along the loading direction), and can limit the extent of fibre reorientation. However, such an arrangement provides the additional benefit that cracks cannot propagate easily through the material (incidentally, this is true in both loading directions), because such a propagation will require reaching the high tensile strength of an individual fibre, thus making the material tough.

These idealized structures are surprisingly close to the fibre–matrix architectures found in soft tissues. Figure 1.3b1, for example, is a close match (at both the fibre and fibril level [9]) for the structure of tendon. Similarly, Fig. 1.3b2 can be found in both skin and arteries. In skin, the planar structure of the tissue and the requirements for resistance to multidirectional loading mean that an isotropic fibre distribution maximizes both strength and toughness. Fibre arrangement is a tradeoff—the toughness brought about by multidirectional fibres against the need for tensile strength in a certain loading direction—and hence in arteries, where high strength is required (Fig. 1.3b3) an orientation of fibres in the circumferential direction provides increased strength, but at the risk of damage propagation in that direction.

Fibre composite theory The shear transfer between fibres and matrix is a problem that materials engineers have considered since at least the 1950s, initially in relation to the paper-making industry through the work of Cox [16, 17]. The simplest model which is presented in textbooks is the "shear-lag" model [16, 17]. This model attempts to describe how effective a fibre is in increasing the stiffness of a (compliant) matrix in which it is placed. It gives quantitative estimates of the minimum length needed for the stress on the fibre to reach its maximum value (limited by the tensile strength of the fibre); fibres which are shorter than this are clearly not as effective as they could be in maximizing the stiffness of the ECM composite they are part of. This concept is captured by the idea of the critical fibre length, which is the minimum length necessary for all the force applied through the matrix to be transferred to the fibre, and is given by $l_c = \sigma r/\tau$ where r is the radius of the fibre, σ is the maximum tensile stress, and τ is the shear in the matrix.

In the shear-lag model, the ends of each fibre are free of normal stress, which builds up progressively toward the centre of the fibre (Fig. 1.4b, c). As a result, the contribution of the fibres to the maximum force is reduced. While in the case of infinitely long fibres with a volume fraction V_f, the elastic modulus is given by the serial or Voigt expression

$$E_c = E_f V_f + E_m(1 - V_f) \tag{1.1}$$

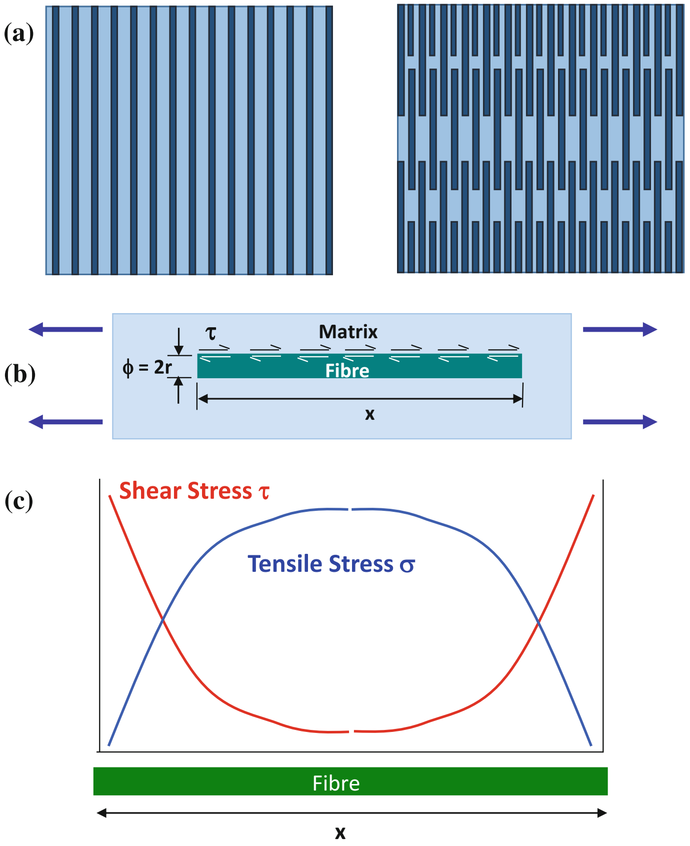

Fig. 1.4 Shear-lag model of fibre load transfer: *Top row* shows that when the fibre length no longer extends across the entire specimen, some degree of interfibrillar load transfer through the interfibrillar matrix is necessary. *Middle* Schematic of a single fibre (*dark blue*) in a matrix (*light blue*), showing the shear τ acting across the length x of the fibre. In response to a far-field load (*arrows* on the left and right of the schematic), a progressive build up of axial fibre stress (*blue line*) occurs, with the ends of the fibre being free from axial stress. The shear stress (*red line*) is maximum at the ends and (by symmetry) is zero at the centre of the fibre. If the fibre is long enough, the maximum axial strength of the fibre can be reached in the middle region of the fibre

where f is for fibre, m is for matrix, and c is for composite.

In a composite with fibres of finite length a correction factor $V_f(z) < V_f$ is necessary [1]. Specifically, the modulus of the composite is

$$E_c = E_f V_f(z) + E_m(1 - V_f) \tag{1.2}$$

where z is a correction factor dependent on the shear modulus of the matrix G, the elastic modulus E and the radius and length of the fibre. The correction factor accounts for the imperfect bonding and progressive shear transfer across the length of the fibre.

Hierarchical organization and toughness As the soft tissues discussed here can be considered fibre composites at different hierarchical levels, it is worth considering how the fibre–matrix interaction changes across the hierarchy and the effect this may have on toughness. In general, for soft tissues, it appears that at the lowest length scale (fibrils in tendon, for example) the bonds between fibril and matrix is quite strong, leading to homogeneous strain fields in low stress deformation. However, at higher stress levels, when cracks or damage may appear in the material, weak interfaces at higher length scales (such as between the fibres or fascicles in tendon) play an important role in making the tissue notch-insensitive and as a result tough.

Another strategy to increase toughness [1] is the use of holes at different length scales. Such an approach is more common in tissues such as wood and plant cells or in bone, and will only be briefly discussed here. The idea is that holes can act to blunt or deflect oncoming cracks, and create extensive tortuous crack paths. The reduction of stress-concentrations caused by crack blunting will prevent further cracks from occurring and is known as the Cook-Gordon crack stopping mechanism [1]. Naturally, too many holes would weaken the material, so a balance has to be maintained. It is worth noting that such “holes” (like the pore canals in cuticle or the vessels in plant xylem) usually have a transport function (of water and nutrients) of their own.

Prestress and pre-strain: While the protein (and polysaccharide)-based fibres described above are excellent in resisting tension, the presence of water in most soft tissues is utilized to increase resistance to compression. First, the GAG/PG-rich gel described in previous sections is hydrophilic and has a high negative fixed charge density, as a result of which the water is stabilized within a gel-like phase interpenetrated by a web of fibres in tension. The tissues may be considered as fibre-linked containers, where the collagen (and other) fibrils restrain the swelling pressure of the gel. As a result, the fibrils are in constant tension or a state of pre-strain. The role of prestress and pre-strain has been well-established for arteries [18], and is a critical component of fibril reinforced models for cartilage [19]. Alterations in swelling pressure in the ECM due to reduction in fixed charge density are also implicated in the reduction of the load bearing capacity of the nucleus pulposus of the intervertebral disc [1].

1.2 Structure and Function of Tendons

1.2.1 Function of Tendons

Tendons are designed to transmit forces between muscles and bone [20]. Long tendons remove the need to have muscles placed close to the joints. As a result of these requirements, they need to be relatively inextensible (failure strains of around 10–20 %), as well as absorb impact forces encountered during gait. Some tendons are additionally elastic to enable storage of energy during locomotory gait. Ligaments, in contrast to tendon, connect two bones, rather than bone to muscle, preventing large torsion or twisting between joints.

Fig. 1.5 Pie chart showing composition of tendon with approximate percentages of different molecular constituents

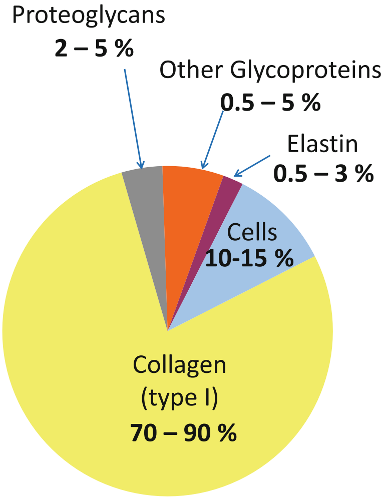

The main components of tendon and ligament are shown in Fig. 1.5. Collagen (at 70–90 %) is by far the most plentiful constituent, while the next most abundant components (proteoglycans and other glycoproteins) account for less than 10 % of the tissue. A small proportion of elastin is also present. The range of glycoproteins present can be quite diverse, including decorin, aggrecan, versican, fibromodulin, lumican, tenascin-C [21], COMP (Cartilage Oligomeric Matrix Protein) and lubricin [22, 23]. However, decorin usually dominates in most tendons. Cells account for the remaining 10–15 %, highlighting that tendon like many connective tissues is a largely acellular tissue [20, 24, 25].

The structure of tendon is in many ways a prototype of the hierarchical structures of other more complex soft tissues like arteries and heart valves. A schematic of the structure is shown in Fig. 1.6, adapted from [26]. It is observed that tendon can be considered an aligned fibre composite at multiple levels, and that a characteristic motif of "stiff-fibres/ductile matrix" is observed at multiple levels from the

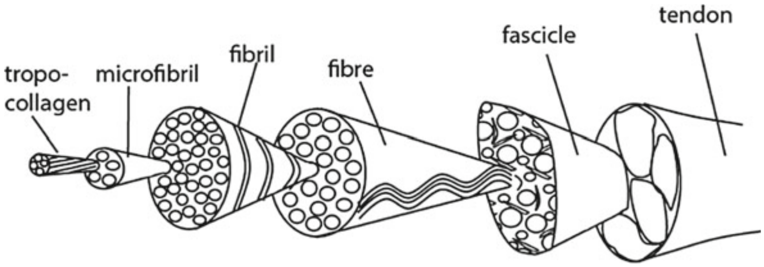

Fig. 1.6 Hierarchical architecture of tendon, adapted from [34]. Collagen aggregates, from the molecular level of the tropocollagen molecule, up through the nanometre scale fibril, microscale fibres to the mesoscale fascicle and entire tendon tissue

nanoscale to macroscale. Interspersed inside the ECM composite are the tenocytes (or ligamentocytes) [26, 27].

At the smallest scale, we have the tropocollagen molecules with diameter 1.5 and 300 nm length [28]. These are tightly cross-linked into microfibrils [29]; diameter ($\sim$3–4 nm) and fibrils (diameters between 20 and 200 nm depending on species, maturity and tissue location), with increased collagen fibril area also a predictor for age in tendons [30]. In between the fibrils is a proteoglycan-rich matrix, with decorin among the PGs which bind to adjacent fibrils [31]. This fibril/matrix motif repeats itself at the next higher level of fibres (10–50 µm diameter) and fascicles (50–400 µm) where tendon cells (tenocytes) are interspersed in rows between fibres and fascicles along the tendon [9]. At the tissue level, fascicles (visible to the eye) are surrounded by interfascicular matrix or endotendon, and bound together to make tendon [26].

Certain features of the fibre–matrix arrangement occur at multiple length scales: for instance, crimped structures are visible both at the fibrillar level and the fibre level. It is noted that tendon is poorly vascularized, and the blood vessels that are present are between fascicles. The matrix between fascicles, which is termed the interfascicular matrix (IFM), contains loose connective tissue matrix, with a higher amount of collagen type III, elastin and proteoglycans such as lubricin [32]. Whilst a generic tissue structure and composition has been presented, ligaments and tendons differ somewhat in composition. In general ligaments have somewhat lower collagen content, greater fraction of elastin and have a more weave-like structure [33]. However, it is notable that tendons vary widely in composition in order to adapt their mechanical behaviour to meet their functional need, emphasizing the exquisite capacity for our tissues to utilize their complex hierarchical arrangements to adapt to mechanical needs. Certain features of the fibre–matrix arrangement occur at multiple length scales: for instance, crimped structures are visible both at the fibrillar level and the fibre level. It is noted that tendon is poorly vascularized, and the blood vessels that are present are between fascicles. The IFM contains loose connective tissue matrix, with a higher amount of collagen type III, elastin and proteoglycans such as lubricin [32]. Whilst a generic tissue structure and composition has been presented, ligaments and tendons differ somewhat in composition. In general, ligaments have somewhat lower collagen content, greater fraction of elastin and have a more weave-like structure [33]. However, it is notable that tendons vary widely in composition in order to adapt their mechanical behaviour to meet their functional need, emphasizing the exquisite capacity for our tissues to utilize their complex hierarchical arrangements to adapt to mechanical needs.

1.2.2 Specialized Regions of Tendon–Ligament

The osseotendinous junction is a mechanically crucial interface between tendon and bone [35]. Owing to the very different mechanical properties of bone ($\sim$20 GPa Young's modulus) and tendon ($\sim$1–2 GPa), a functionally graded transition is needed between the two organs. It is clinically relevant as it is a potential weak point in structure, and prone to injury. It is characterized by a linear increase in mineral concentration across the junction, a transition zone with type II collagen and a loss of the predominant collagen orientation in tendon. Analogous structures include the interface between muscle and tendon (where mechanical differences are less pronounced), known as the myotendinous junction, characterized by an interdigitation of muscle and collagen fibres.

1.2.3 Mechanical Properties of Tendon and Ligament

The mechanical properties of tendons and ligaments in tension (the most relevant loading mode) can be considered in comparison with standard man-made materials like metals or rubbers. Typical stress–strain curves for metals and rubbers are shown

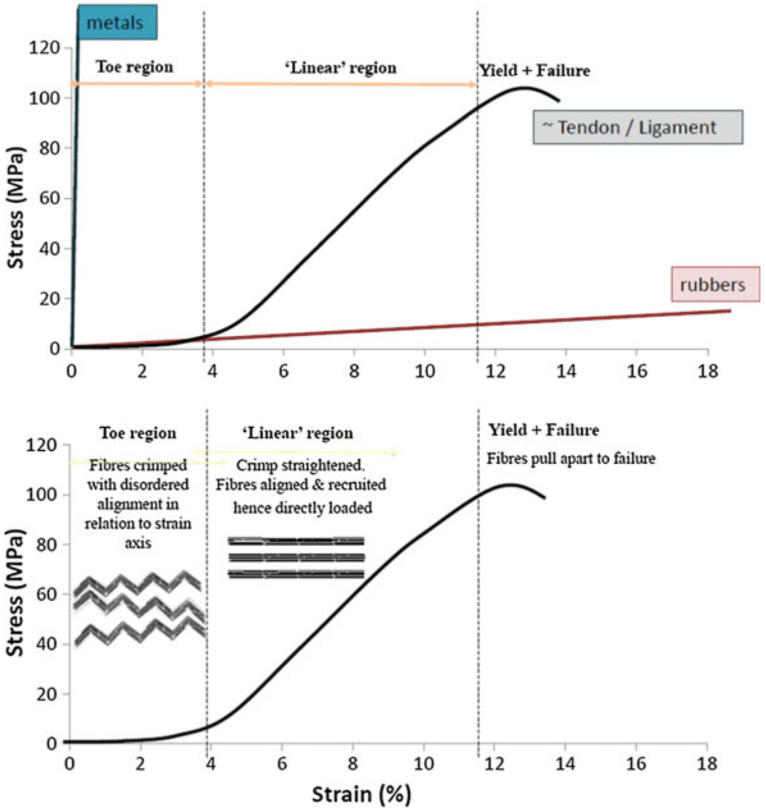

Fig. 1.7 Comparison of the stress–strain curve of tendon, in tension, with that of metal (*left*) and rubbers (*right*). In the lower graph, the three different strain regimes: toe, linear and yield are indicated together with a brief description of the structural changes

in Fig. 1.7a, with—in comparison—a typical stress–strain curve for tendon. It is observed that the maximal deformation of tendons (∼10–20 %) is much larger than the yield strain of metals (∼1 %) and much smaller than the ∼500 % failure strain in rubbers. Characteristic features of the stress–strain curve in tendon are an initial *toe* and *heel* region up to ∼4 %, a nearly linear increase of stress with strain from ∼4–12 % and a short yield and failure region thereafter. The tangent modulus in the linear region is ∼1–2 GPa, much lower than ∼100 GPa range for metals, but larger than the <1 GPa moduli in rubbers.

Considerable attention has been paid to understanding how the hierarchical structure described in the previous sections can lead to the aforementioned mechanical behaviour, and a fairly complete understanding of at least the main mechanisms are now known (reviewed in [36]). In the toe region, the tendon starts out in a macroscopically crimped configuration (these crimps are visible under the light microscope). The removal of these crimps plus alignment of collagen in loading axis occurs over the toe region with nearly no increase in tissue stress. However, the initial nonlinear increase of the stress just after the toe region (the heel region) involves smaller structural units in the hierarchy. Misof et al. [37] proposed the involvement of molecular level vibrations, lateral to the force direction, by analyzing the changes in the X-ray diffraction intensity arising from the lateral packing of the collagen molecules. In their model, an lateral vibration in the gap regions of the tropocollagen molecules is reduced in amplitude on deformation, explaining the alterations in X-ray scattering intensity; this "rubber-like" contribution to the internal free energy thus influences the stress–strain curve in the heel region.

In the linear region, the crimps (and smaller scale structural features) are straightened and fully aligned with the loading direction so the fibres now are fully recruited to bear the load [38]. In this region at the ultrastructural level, the consensus is that some degree of inter- as well as intrafibrillar sliding, coupled with elongation of the tropocollagen molecules, occurs [39, 40]. These mechanisms can be quantified by analyzing peak shifts in X-ray diffraction patterns arising from meridional packing of collagen molecules in the fibrils. The deformation remains regular, i.e. a similar intra- and interfibrillar structural rearrangement occurs across the tissue over the fibrils. Recent data demonstrates that sliding also occurs between fibres and fascicles, and the relative contributions of sliding through the different hierarchical levels of the tissue can be modulated by altering the matrix composition and subsequently its mechanical properties at different levels in the hierarchy. Finally, fibres pull apart and fracture in the nonlinear and fracture region [34].

Given that tendon (and ligaments) are subjected to time-dependent loading over most of their lifetime, it is of equal importance to understand the viscoelastic mechanical behaviour. The simplest types of tests for understanding viscoelasticity are stress relaxation (holding the tissue at a constant strain and monitoring the reduction in stress) and creep (holding the tissue at constant load and measuring elongation). Creep in tendon can be categorized into the initial rapid (primary) creep, followed by a slower (secondary) creep and eventually by a very rapid tertiary creep which leads to failure [41]. It is observed that creep behaviour changes with age; in particular, the duration of secondary creep and extent of sample elongation is much longer

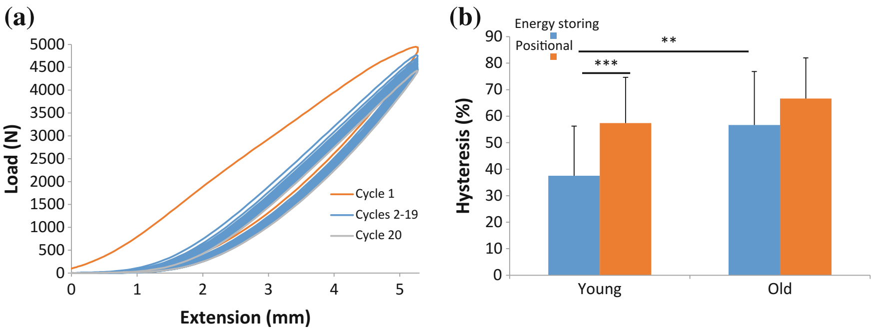

Fig. 1.8 **a** Cyclic loading of tendon leads to viscoelastic energy loss, measured by the hysteresis (% of area between loading and unloading cycles). **b** The degree of hysteresis is lower in energy storing versus positional tendons

in older tendons, likely due to an increase in intra- and interfibrillar cross-linking. Another important parameter for viscoelastic behaviour is the energy loss during cyclic loading (Fig. 1.8, left). The degree of hysteresis (area between the loading and unloading curves) is a parameter characterizing the extent of energy loss. The degree of hysteresis in cyclic tensile loading of tendon is dependent both on the age of the tendon as well as the type of tendon. For example, energy storing tendons show a smaller hysteresis than positional tendons (Fig. 1.8, right).

1.2.4 Hierarchical Analysis Techniques

The hierarchical structural elements (from fibrils at the nanoscale to fascicles at the macroscale) affect the mechanics of tendon and related tissues in distinct ways. Different experimental techniques—both mechanical as well as imaging-based, and some combining the two—need therefore to be applied or developed to understand the micro- and nanoscale mechanics. At the molecular and the nanoscale, methods to probe mechanical deformation include X-ray diffraction (to measure helical pitch in tropocollagen molecules) [43], Raman spectroscopy (to identify different functional groups like amides in the protein and to observe stress-induced shifts) [44], small-angle X-ray diffraction to measure the fibril D-period [39, 40, 42, 45, 46]. These are generally employed to visualize sample strain response, whilst the tendon is strained within an appropriately designed loading rig. Techniques like atomic force microscopy and microelectromechanical-sensors (MEMS) have also been utilized to deform individual collagen molecules and fibrils [47]. In addition, the use of *ab-initio* molecular dynamics simulations for studying deformation of individual collagen molecules as well as small aggregates of molecules (proto-fibrils) should also be mentioned [48], with the proviso that the short timescales (of the order of nanoseconds) in molecular dynamics necessarily make the mechanical testing timescales in such computational studies quite far from those used in most laboratory tests as well as in *in vivo* testing.

These sub-micron scale mechanical test methods are complemented by high-resolution imaging methods like electron microscopy in order to help correlate local mechanics with tissue structure. Between the microscale and the macroscopic scale, however, there are a lesser number of well-established methods for mechanical testing linking structure to mechanics. Examples of techniques which have been applied at this scale are confocal microscopy, digital light microscopy and photography, usually in combination with mechanical testing methods. These are complemented by standard biological imaging methods like histology and histochemistry combined with light microscopy. At the macroscale, real-time mechanical testing methods include image correlation techniques, photography and polarized light microscopy: it is observed that there is some overlap of methods with the sub-mm scale mentioned above, but the analysis is usually at a lower level of resolution and presents fewer problems with interpretation.

We consider first the deformation at the macro- and microscale. Examples of use of photography to image different stages of the tensile deformation of tendon are shown in Fig. 1.9 from [9]. The change in the crimp structure (left) can be seen, as well as the straightening of fibres in the linear region. The fractured, rough surface of the tendon at rupture likewise indicates a sliding of fibres as they shear past one another as the

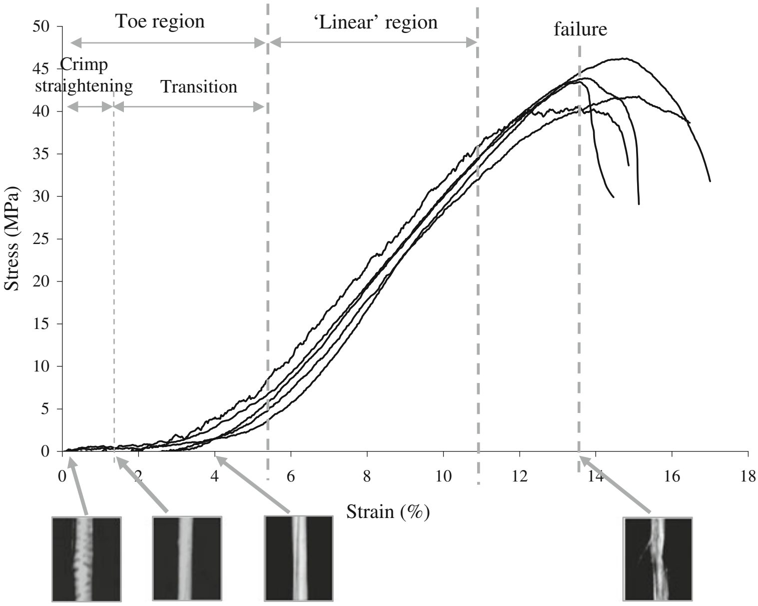

Fig. 1.9 Five prototypical stress–strain curves of rat-tail tendon, strained to failure at 1 mm/min. *Lower* frames show video capture photos at progressively increasing strain levels. Data and figure from [9]

tendon fails. At one scale below this, confocal microscopy combined with *in situ* testing of tendon samples can image the deformation of fibres and fascicles [9, 49] within tendon as the samples are strained. By tracking cell displacement within the tissue, or directly staining and visualizing collagen within samples, the fibre extension and interfibre sliding can both be measured. It has been found that the fibre extension is considerably less than interfibre sliding, indicating considerable shear between the fibres [9]. Interestingly, some degree of hysteresis is observable at both the inter- and intrafibre level [50]. We note that recently, a variant of notch-tensile testing used on tendons to obtain the interfibrillar shear stresses has been developed. This is a novel application of a macroscale test methodology to obtain fibrillar level mechanical parameters [51], and confirms shear transfer between collagen units through the tendon hierarchy.

At the fibrillar level, using small-angle X-ray diffraction (SAXD), the D-periodic variation of the electron density along the axis of the fibril generates a set of Bragg peaks along the orientation of the fibril. Use of high brilliance synchrotron radiation enables rapid acquisition of SAXD frames, within a few seconds [39, 40, 42, 45, 46]. When a microtensile tester containing tissue in a fluid chamber is mounted in a synchrotron SAXD beamline, concurrent application of mechanical test protocols like uniaxial stretch to failure, stress relaxation or creep can lead to the simultaneous measurement of fibril strain with macroscopic stress and strain. Sasaki and colleagues showed [40] that the majority of the changes in the X-ray diffraction spectrum could be explained by elongation of tropocollagen molecules, rather than intrafibrillar slippage of adjacent molecules or by increase of the gap (separation) region between axially separated fibrils. However, both earlier [45] and later [39] studies using similar methods have indicated that alterations in the gap/overlap ratio (indicative of intrafibrillar sliding) is playing a role in tendon deformation, as seen from changes in the relative intensities of different Bragg peaks in the SAXD spectrum. High strain rate deformation of tendon [52] found that intrafibrillar sliding and damage preceded macroscopic failure, as well as identifying a maximum D-period (for tendon collagen) of 68.4 nm below which all changes in fibrillar D-period were reversible.

The viscoelastic nature of the extrafibrillar matrix was demonstrated by [53], who showed that deformation in tendon could be modelled via assumptions of largely elastic fibrils and largely viscous interfibrillar matrices. When the collagen cross-linking was reduced, the situation reversed, with collagen fibrils now being much more viscous than the matrix. A combination of synchrotron and confocal testing of tendon during stress relaxation [42] was able to quantify the degree of fibrillar and fibre relaxation at different levels of macroscopically applied relaxation strains (Fig. 1.10). A two-level viscoelastic model, exhibiting the multiscale decay observed in tendon, was used to explain the data (Fig. 1.11). Intriguingly, however, the *magnitude* of the fibrillar and fibre relaxation argue against the prior theory of significant interfibrillar sliding. It is observed that the amount of fibrillar and fibre relaxation are nearly the same, and are both much smaller the interfibre shear. Such a finding

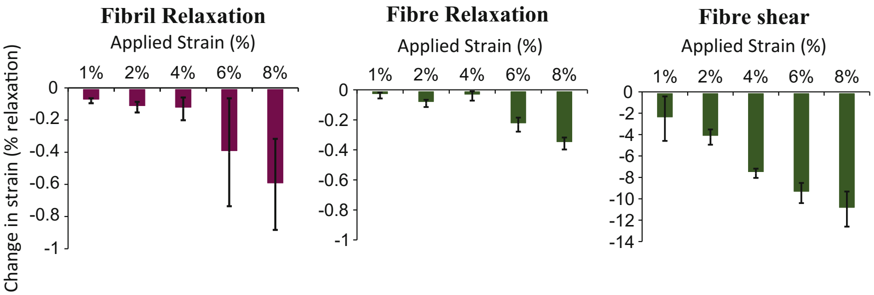

Fig. 1.10 Comparison of fibrillar and fibre strains and fibre shear during tensile deformation of tendon, measured via SAXD and confocal microscopy. Data from experiments reported in [42]

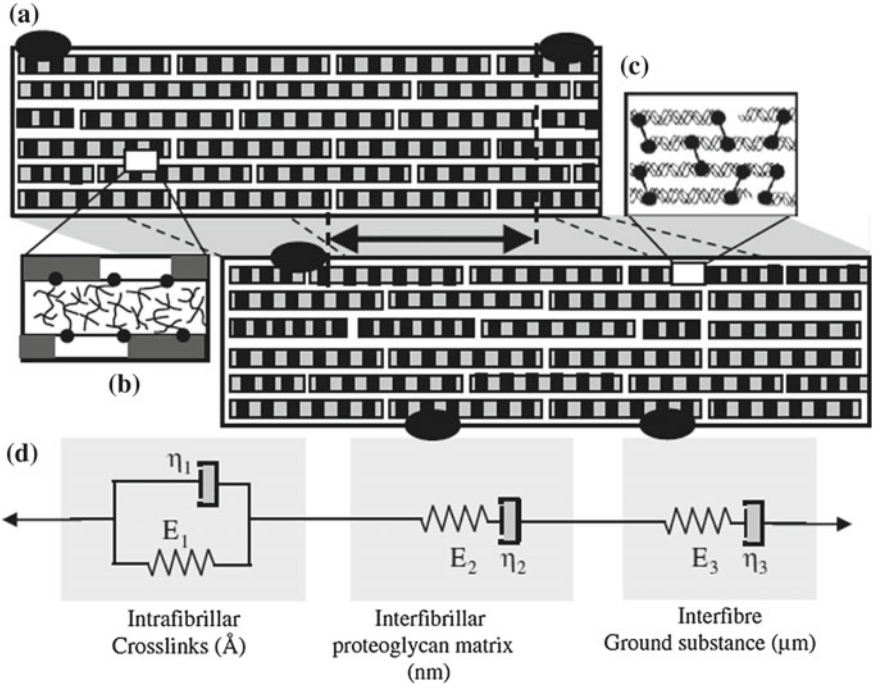

Fig. 1.11 A model of interfibrillar sliding during stress relaxation in tendons, based on *in situ* X-ray diffraction and confocal microscopy. Image taken with permission from [42]

would suggest that the fibrils within a fibre are deforming largely as one group, with little sliding between fibrils, and that a major contributor to sliding is the non-fibrous matrix at larger structural levels. Such results have stimulated renewed investigation into the viscoelastic properties of the IFM [54].

1.2.5 *Effects of Matrix Composition and Tendon Type*

Whilst general data describing tendon composition and mechanics have been covered thus far, recent data highlights the effect of matrix composition and tendon type. Tendon structure–function relationships can be investigated utilizing enzymatic digestion or knockout models, to establish how altered matrix composition influences tendon mechanics. Structurally, treatment of tendons in phosphate buffered saline (PBS) led to 20 % increase in water content and 11 % loss of GAG, while chondroitinase treatment led to 16 % increase in water content and 99 % loss of GAGs [56]. Interestingly, the swelling of samples or removal of GAGs had little discernible effect on gross tendon mechanics. However, the PBS swollen tendon samples showed significantly increased levels of fibril sliding, an effect which was negated by the removal of the GAG chains [55] (Fig. 1.12). More recently, biglycan and decorin knockout models of mice have also been adopted to investigate the role of GAGs in tendon mechanics. These have shown altered mechanical properties near the insertion site [57]. Whilst tendon quasi-static mechanics are little affected by changes to protoeglycans, viscoelastic properties show a number of changes. Fatigue resistance is lowered after GAG digestion, with more rapid stress relaxation as seen in Fig. 1.13a [58]. Whilst no significant viscoelastic phase shift was observed in patellar tendons from decorin knockout mice, it was noted that there was a tendency to increased stress relaxation levels with a reduction in the decorin level, as seen in Fig. 1.13b [59]. Studies into the effects of elastin have focused primarily on ligament, showing that removal of the small elastin component in ligament increases the length of the initial toe region of the stress–strain curve, suggesting that elastin primarily contributes to ligament function within the low load region, whilst failure properties are governed by collagen fibre failure [60]. Prior work on tendons and palmar aponeuroses showed a considerable reduction in modulus and increased hysteresis in elastase treated samples, whilst chondrotinase treatment appeared to reduce sample hysteresis [61].

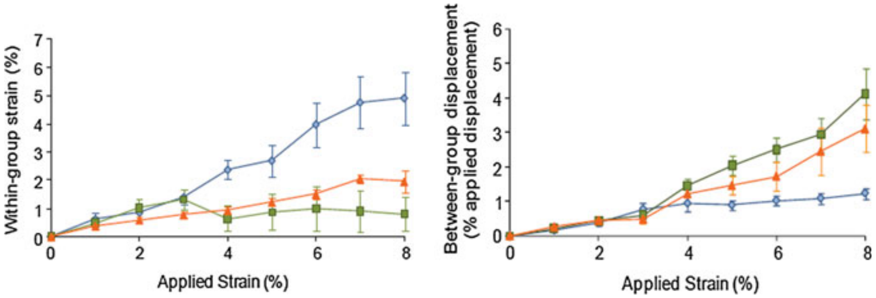

Fig. 1.12 Increased inter- and intrafibre sliding on removal of proteoglycans (digestion with chondroitinase ABC) in tendons. Data from [55]

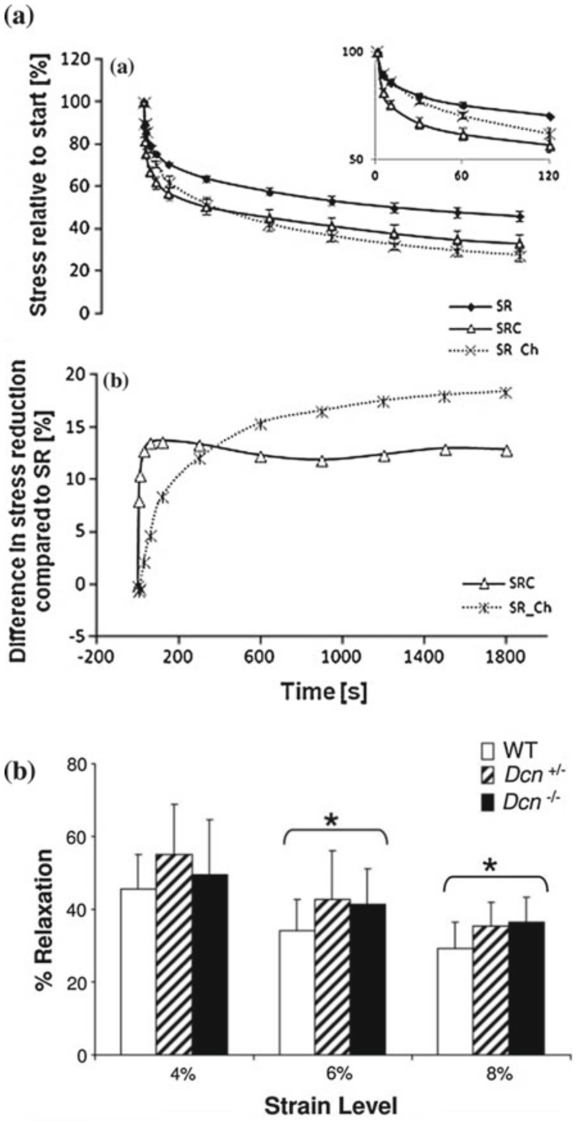

Fig. 1.13 **a** Greater stress relaxation in chondroitinase-digested tendon (main graph) versus controls (*inset*). Image reproduced with permission from [58]. **b** Increased percentage relaxation of tendon with both strain level and decorin removal (Dcn −/− is decorin knockout). Image reproduced with permission from [59]

In recent years, structure-function studies in tendon have focused on the clear functional differences between different tendons, looking to establish how structural variations are adopted to meet functional need. All tendons function to transfer muscle force to the skeleton and position limbs (positional tendons) but some have an additional role in locomotion, stretching to store energy which they can release back into the system to improve the efficiency of movement (energy storing tendons). Energy storing tendons, such as the Achilles tendon, or equine equivalent (the

Fig. 1.14 Differences between stress–strain curves for energy storing and positional tendons; lower tangent modulus and maximum failure strain are observed in energy storing tendons

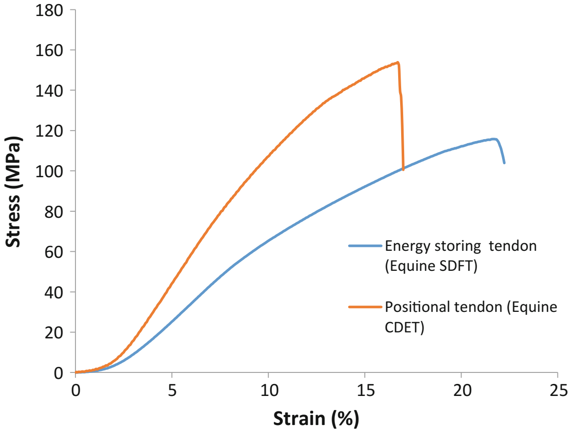

superficial digital flexor tendon—SDFT) [62, 63] are subjected to high strains and elastic recoil in use, and show high incidences of tendinopathy, whilst the low strains experienced by positional tendons make them less injury prone.

Energy storing tendons are less stiff and more extensible than positional tendons, facilitating energy storage and protecting the tendon from damage when subjected to large forces (Fig. 1.14) [64]. Furthermore, studies have additionally highlighted how energy storing tendons are significantly more fatigue resistant than positional tendons, enabling them to resist a greater degree of cyclic loading without damage (Fig. 1.15) [32]. Adopting hierarchical analysis techniques, it is possible to investigate the structural adaptations of energy storing tendons that facilitate these altered mechanics.

Data have highlighted that fibril and fibre sliding is less apparent in energy storing tendons, and that extension in these tendons adopts fascicle level sliding, mediated by the IFM [64]. The IFM is rich in elastin and lubricin to facilitate sliding and recoil behaviour (Fig. 1.16) [65], and levels of both of these proteins are higher in the IFM of energy storing tendons, resulting in significantly more fatigue resistant IFM in these samples [32, 54] (Fig. 1.17).

Fascicles within energy storing tendons are also helically arranged, providing additional resistance to fascicle damage as energy storing tendons are subjected to greater cyclical loads [66]. Interestingly, studies in ageing energy storing tendons have highlighted how these functional specialisms are lost with ageing. The helical organization of fascicles is reduced, whilst the IFM becomes stiffer, perhaps providing insight into the increased injury-risk seen in aged energy storing tendons [67].

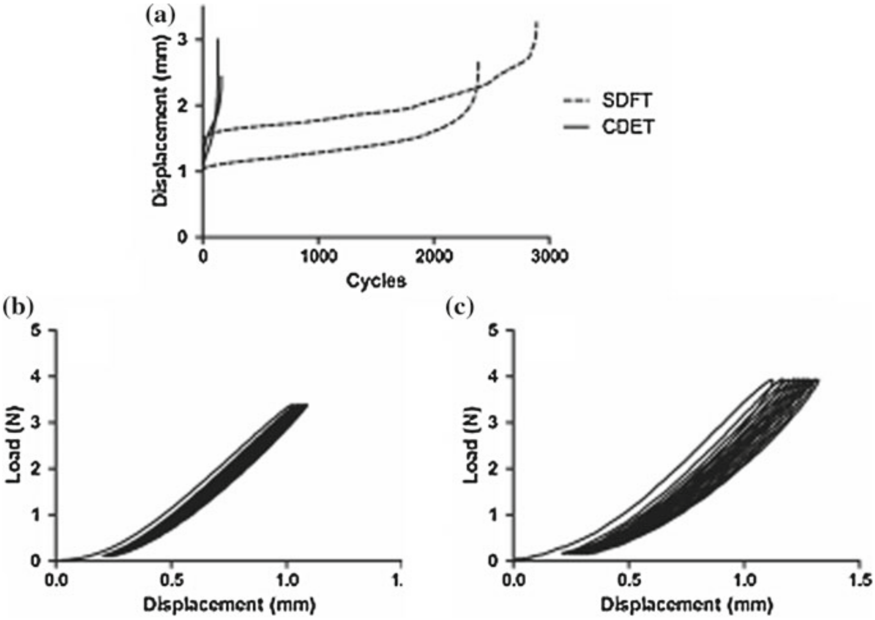

Fig. 1.15 **a** Creep curves for fascicles from superficial digital flexor and common digital extensor tendons (respectively SDFT and CDET) **b** and **c** Loading and unloading curves for the first 10 cycles for SDFT and CDET respectively. Data from [32]

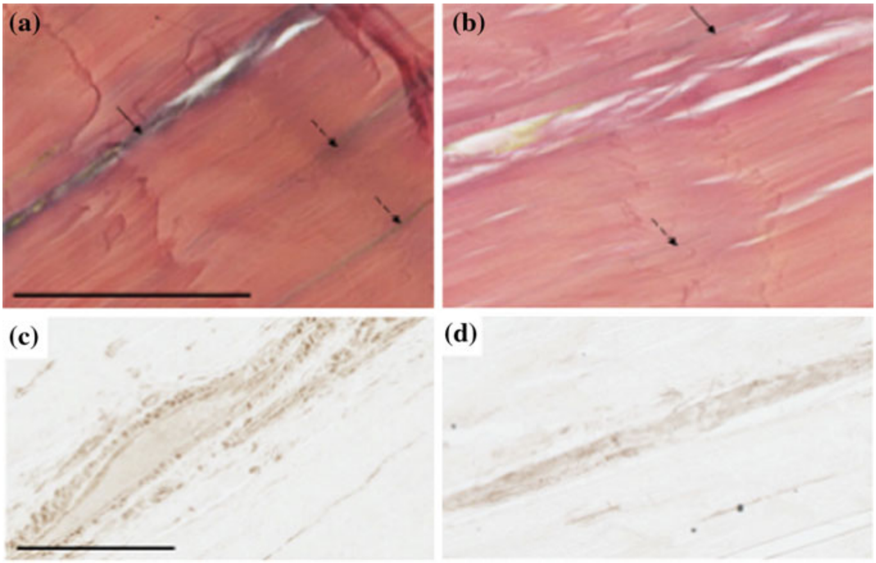

Fig. 1.16 Elastic von Giesons stained SDFT and CDET tissue (**a** and **b** respectively), with elastic fibres viewed as *blue/black lines*. SDFT exhibits elastin staining in the IFM (*solid arrow*) and a little inside the fascicles (dashed arrows). Lower numbers of elastic fibres are evident in CDET. **c** and **d** Immunohistochemical staining of lubricin in the IFM and within the fascicles of SDFT and CDET, showing considerable lubricin staining in the IFM of SDFT

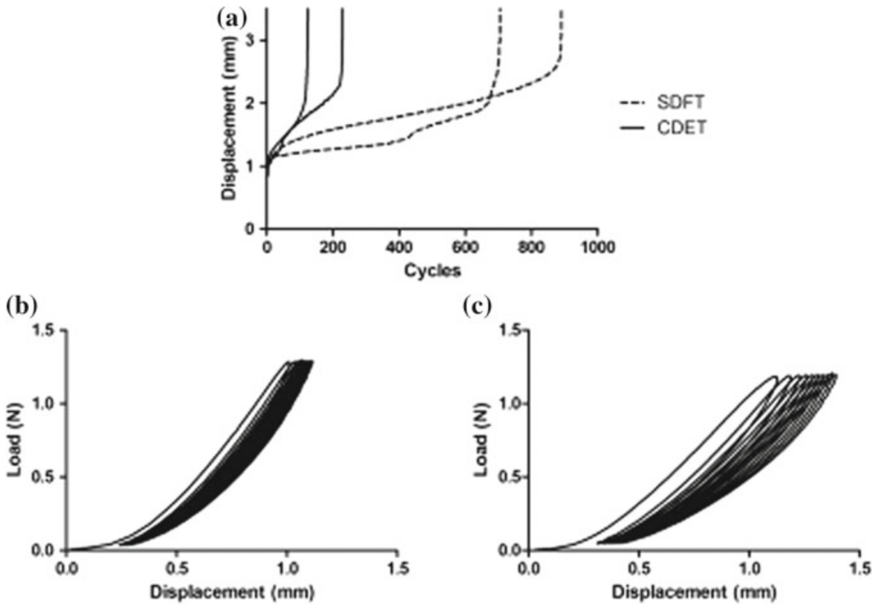

Fig. 1.17 **a** Creep curves for the interfascicular matrix (IFM) from SDFT and CDET tendons **b** and **c** Loading and unloading curves for the first 10 cycles for SDFT and CDET respectively [32, 54]

1.3 Heart Valves and Their Mechanical Properties

1.3.1 Types of Heart Valves

Heart valves enable the unidirectional flow of blood through the heart. There are four valves: the mitral, aortic, pulmonary and tricuspid. The tricuspid valve is between right atrium and right artery, the pulmonary valve between the right ventricle and pulmonary artery, the aortic valve between the left ventricle and the aorta and the mital valve between left atrium and left ventricle. Heart valves are passive structures, which open and close in response to the surrounding haemodynamic environment. The valve mechanics are reflective of the differences in pressures on the left and right hand side of the heart, with an overall × eightfold higher baseline pressure on the left side of the heart leading to more fatigue resistance in the aortic and mitral valves.

An alternate series of valves opening and closing occurs over a cardiac cycle. During the diastolic phase, the pressure in the ventricles is below atrial pressure. As a result, the mitral and tricuspid valves open, allowing blood flow from atria to ventricles. Concurrently, the aortic and pulmonary valves close to prevent a reverse flow of blood into either the aorta or pulmonary artery. In the systole, the atrium first contracts to push any remaining blood to ventricles. This is followed by ven-

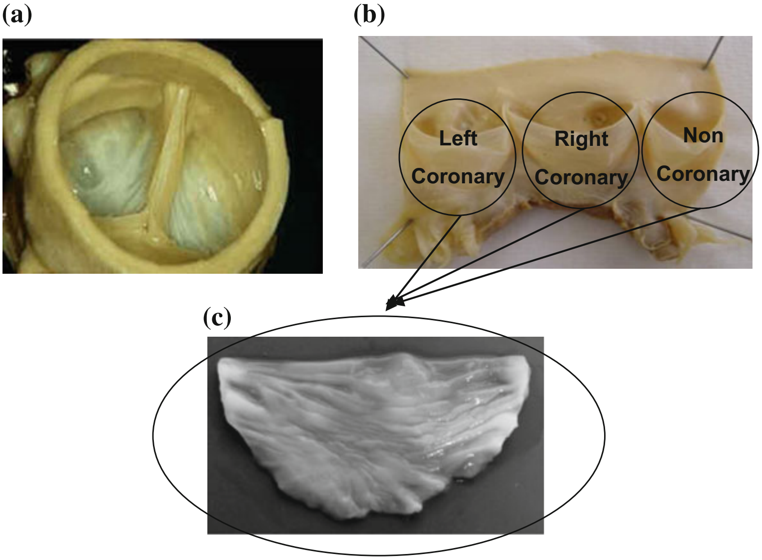

Fig. 1.18 **a** Photograph of an aortic valve **b** an unfolded valve opened to show the three coronary leaflets. **c** An unfolded leaflet showing the curved shape and anisotropic structure

tricular contraction, pushing blood into circulation, at which point the mitral and tricuspid valves close to prevent blood flowing back into the atria while the aortic and pulmonary valves open.

The aortic valve, also known as the semilunar valve, is shown in Fig. 1.18. In the aortic and pulmonary valve, three semicircular coronary leaflets are present, which flex against the walls of the aorta as blood flows out of the heart, but coapt perfectly as the valve closes to prevent backflow. By contrast, the mitral and tricuspid valves are called the atrio-ventricular valves, owing to their location between the atria and ventricle of both sides of the heart. The mitral valve has two primary leaflets, known as anterior and posterior leaflets, whilst the tricuspid valve has three. In both valves, the leaflets are corrugated, with the corrugations called scallops. The attachment of the valve leaflets to the papillary ventricular muscles are via a special type of tendinous structures known as chordae tendinae. The chordae tendinae are required to prevent the valve leaflets from inverting under applied pressure (prolapse). The mitral and aortic valves, being located on the high pressure side of the heart, are more prone to damage and hence have been subjected to more attention from a bioengineering standpoint. In contrast the tricuspid and pulmonary valves are on the low pressure side of the heart and have a lower incidence of damage.

1.3.2 Heart Valve Disorders

There are two main diseases or disorders which affect heart valve function: stenosis and regurgitation. Stenosis is the narrowing of the valve opening, limiting the flow of blood, and is usually a result of valve stiffening. The etiology may involve rheumatic fever or congenital defects. Regurgitation is when the valve does not close properly, and can be caused by failure of chordae tendinae, enlargement of surrounding heart structures, infections or Ehlers–Danlos syndrome. In general, these disorders affect the highly loaded aortic and mitral valves, with the mitral valve commonly regurgitating and the aortic valve often undergoing stenosis.

A stenotic aortic valve cannot flex out of the way as easily when blood is pushed out of the heart, meaning the left ventricle must generate higher pressure with each contraction, leading to muscular thickening of left ventricle walls and eventual dilation of the left ventricle and deterioration of systolic function. Congenital bicuspid aortic valve formation occurs during pregnancy when two aortic leaflets fuse together. It affects about 1–2 % of the general population and the altered valve mechanics increases valve calcification rates. Mitral valve regurgitation is the most common valve disorder. It usually occurs as a result of the chordae tendinae stretching over time to the point at which they can no longer hold the mitral valve leaflets in place, but allow them to invert or prolapse during systole.

1.3.3 Structure Function Relations in Aortic Valves

In aortic valves there is a consistent high pressure environment on both sides of the valve. The valve undergoes high, multidirectional strains and must rapidly open and close, necessitating flexion. Structurally, the valve is a corrugated trilayer structure, as shown schematically in (Fig. 1.19). At the top, a collagen rich layer (*fibrosa*)

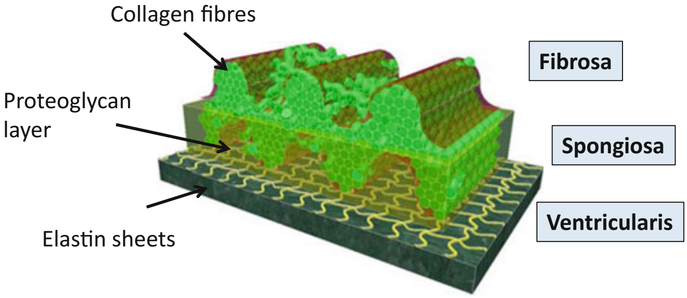

Fig. 1.19 Schematic model of the layered structure of the aortic valve leaflet. The collagen fibrils are shown as *green* rods, in a ridged/corrugated structure. The elastin fibres form a cross-linked network at the base of the valve layer in the ventricularis

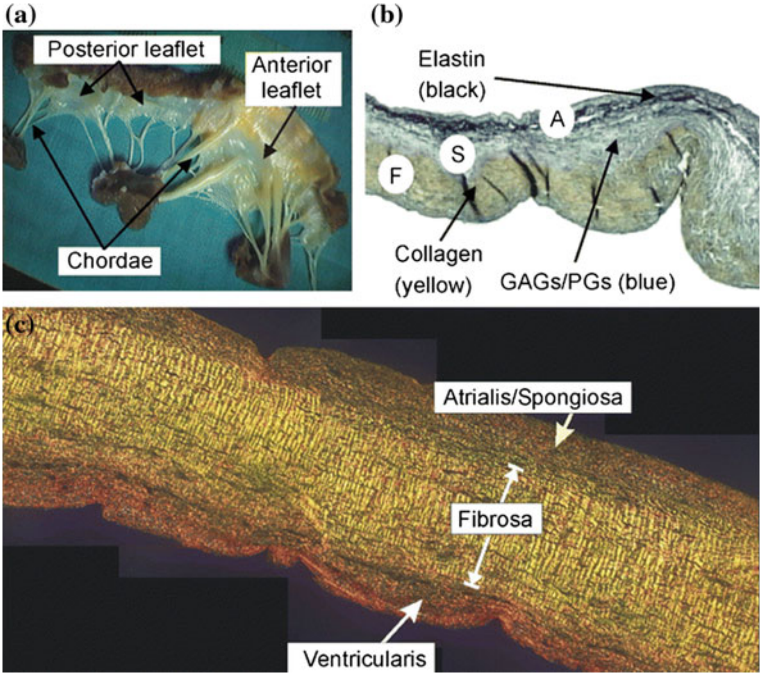

Fig. 1.20 **a** An image of a sectioned mitral valve, where the chordae tendinae and leaflets are clearly visible **b** Pentachrome stained cross-sections of mitral valves showing the different tissue layers. The elastic fibres are shown in *black*, the collagen in *yellow* and the PG/GAG phase in *blue* **c** Polarized light microscopy showing the different fibre texture and density in the ventricularis, fibrosa and spongiosa. (Image reproduced with permission from [68]

contains a multidirectional set of collagen fibres providing tensile strength. In the middle layer (*spongiosa*) a high proportion of proteoglycans allow other layers to shear, enabling large flexion. In the bottom layer (*ventricularis*), the elastin-rich layer provides considerable extension and recoil. The collagen fibres in the fibrosa form coarse bundles which run across the width of the valve, providing the corrugations that are characteristic of valve leaflets. Typically, the fibrosa is the thickest layer, as shown in Fig. 1.20. Confocal microscopy of the different layers of the aortic valve shows clearly the orientation differences as well as the degree of crimping (Fig. 1.21).

1.3.4 Structure Function Relations in Mitral Valves

The mitral valve structure is clinically important as it is more often repaired than replaced, hence the need to design a correct annulus. During the cardiac cycle, there is a significant pressure difference between the atrial and ventricular side of the valve, and the mitral valve must open and close with little resistance, but not pro-

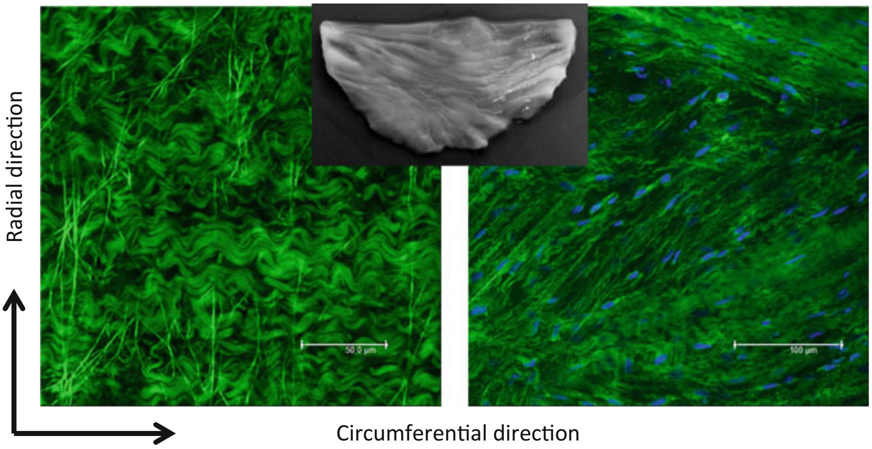

Fig. 1.21 Confocal microscopy of aortic valve leaflet layers showing the corrugated fibrosa region on the *left* and the underlying elastin-rich ventricularis on the *right* (Screen et al. unpublished work)

lapse against high pressure in the ventricle. During the heart beat, the annulus of the mitral valve can change shape significantly, going from circular at ventricular diastole to kidney shaped at peak systole. Structurally, the mitral valve is (in cross-section) a four-layered structure, with looser, elastin-rich layers at either external surface (ventricularis and atrialis) while the interior of the valve contains the collagen rich fibrosa and proteoglycan-rich spongiosa. Smooth muscle cells, nerve fibres and vascular channels are also present.

As seen in histological and microscopic images [69], mitral valves with deteriorated structure exhibit leaflet thickening and elongation of tendinous chords. In cross-section, it is seen that floppy mitral valves show very few collagen fibres in the central fibrosa region, significantly reducing the tensile resistance of the valve and making it more prone to collapse.

1.3.5 Anisotropic Structure and Mechanical Implications

The shape and structure of heart valves, with multiple leaflets, each composed of microscopically distinct layers, means that in order to understand the structure–function relations in this complex tissue, a range of mechanical test methods must be utilized. These can include uniaxial, biaxial and multiaxial tensile testing, with either point loading or pressurized loading in addition to testing with flexion. These will be briefly described in the following text:

Uniaxial mechanical properties In carrying out a uniaxial tensile test on a valve, one must first define a principal axis of loading. Despite the complex curved shape of each valve leaflet, two main directions can be defined, with respect to the position of the valve in its native state (Fig. 1.22a). The first, along the direction perpendicular to

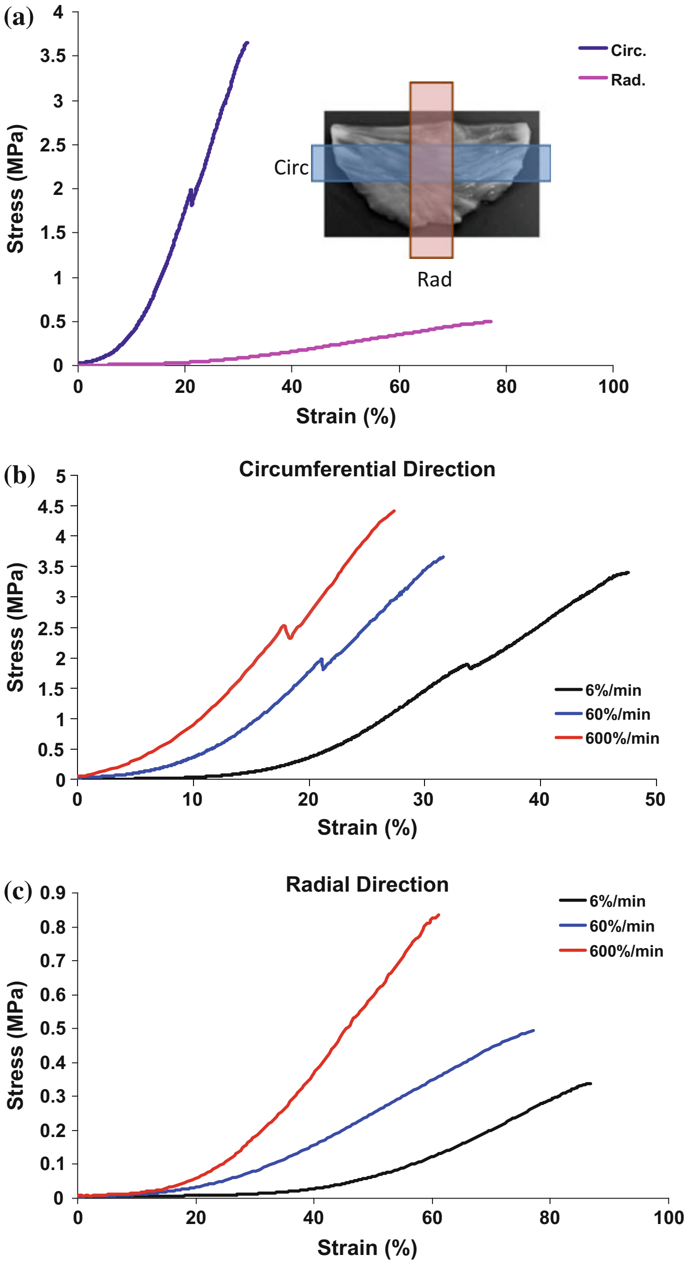

Fig. 1.22 **a** Uniaxial mechanical test of aortic heart valve leaflet tissue in the circumferential direction (*blue*) shows much higher stiffness, lower maximum strain and higher maximum stress compared to radial direction (*pink*). **b** and **c** Increasing strain rate significantly increases stiffness, reduces maximum strain and increases maximum stress. Inset: photograph of aortic valve, with sample sections along the circumferential and radial direction indicated

Fig. 1.23 **a** Schematic of tensile deformation of heart valves, showing three distinct zones of deformation with different tangent moduli. **b** The proposed collagen–elastin linkage model of [71]. Figure after [71]

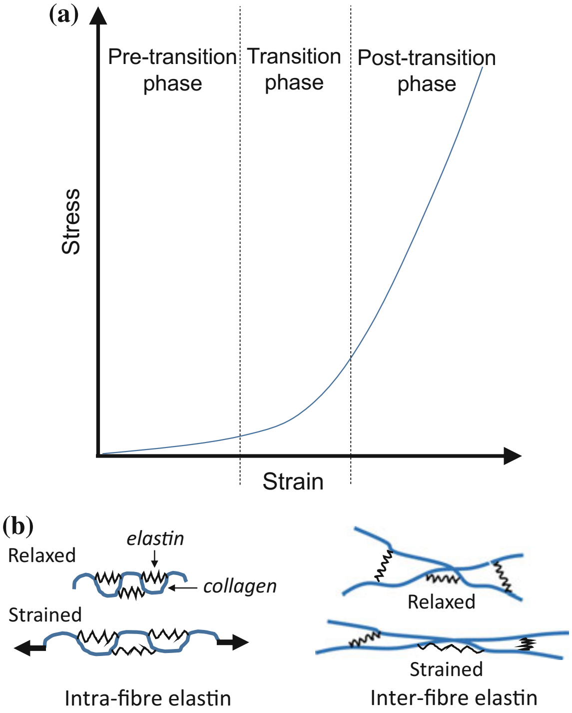

the blood flow, is called the circumferential direction, while the second, which follows the main blood flow direction is called the radial direction. Tensile test curves from the longitudinal and radial directions are shown in Fig. 1.22a. It is observed that the maximum tangent modulus of the circumferential (C) sample is much larger than the radial (R) sample. This difference is mainly because there is a greater proportion of the collagen fibres along the loading direction in the C- than in the R-direction.

Both directions show strong strain rate sensitivity, with an increasing tangent modulus with strain rate observed in each case (Fig. 1.22b, c). Tests are normally carried out on strips running through the centre of the leaflet, but it is possible to cut circumferential or radial strips across a leaflet, with data showing the middle strip is stiffest in both cases [70].

To relate these mechanical data to the prior discussion on tendons, it is useful to divide the stress–strain curve schematically into three regions as shown in Fig. 1.23a. In the pre-transition phase, there is straightening of macro-crimp with elastin providing the main resistance to extension. In the middle (transition or heel region) the collagen fibres are progressively recruited to bear load and oriented in the loading direction. In the post-transition region (which is also closer to a linear stress–strain curve than the previous two) there is elastic extension.

Scott and Vesely [71] have proposed a linkage between the elastin and collagen fibres to enable recoil or return of the connective tissues in the heart valve. As per

Fig. 1.24 Anisotropy of stress–strain response to biaxial deformation of aortic heart valves leaflet (Screen et al. unpublished work)

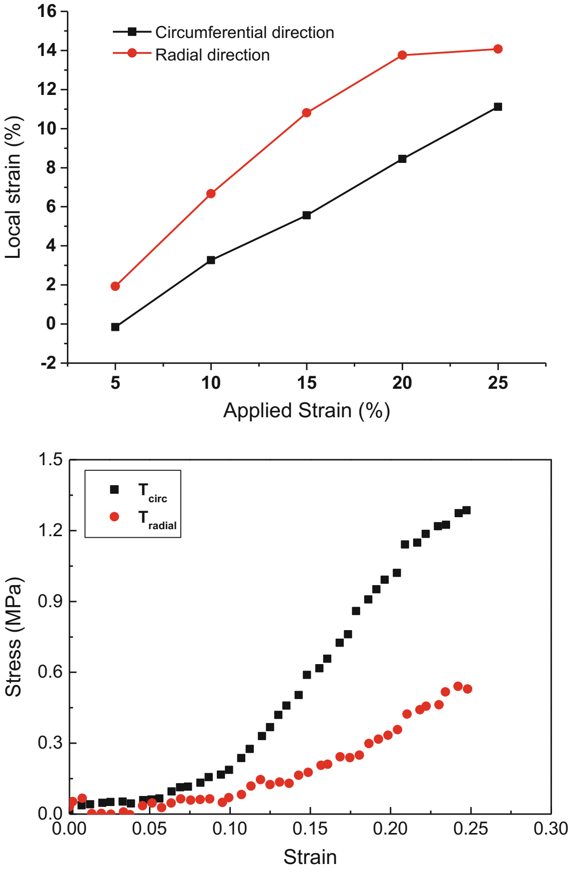

the mechanisms sketched in Fig. 1.23b, the interfibre connections via rubbery elastin linkages may enable the collagen bundles to return to their crimped state when relaxed.

Biaxial mechanical properties Biaxial mechanical testing protocols of heart valves, incorporating in-plane shear, have been described in [72]. Gripping is achieved via sutures so as not to constrain deformation in either direction. To ensure noncontact measurement of strain, marks are placed in a grid on the sample surface, and the attachment to the valve is via hooks which insert into the side of the tissue. Using a similar protocol, Screen et al. (unpublished) show that the local strain is larger in the radial direction compared to the circumferential direction (Fig. 1.24). Such a result is expected based on the predominant fibre orientation in the circumferential direction increasing the stress and stiffness along this axis. Likewise, an increased stress is observed in the circumferential direction.

Flexural mechanical properties Flexural mechanical tests on heart valves can measure the flexural stiffness either by bending with the curvature direction or against it. Bending against curvature leads to larger stresses (0.70 ± 0.13 MPa) than bending with curvature (0.50 ± 0.13 MPa) [73]. Bending with curvature is dominated by tension in the ventricularis layer with little support from the fibrosa. This is because the fibrous layer is on the concave inner surface of the valve, as a result of which it is placed under compression when bending with curvature. Conversely, when the valve is bent against curvature the fibrosa is placed under tensile loading, which it can resist more effectively. Owing to the predominance of collagen in the fibrosa the modulus is higher in this case.

Enzymatic digestion tests Analogous to the enzymatic digestion testing described earlier for tendon, the removal of different ECM components of heart valves have a significant effect on the mechanics [74]. Elastin digestion of heart valves results in lowered modulus, increased extensibility in both circumferential and radial directions, and in each separate layer: fibrosa, spongiosa and ventricularis.

1.4 Conclusion

The hierarchical nature of connective tissues, together with the widely differing mechanical properties of the constituent elements, make the assignment of material parameters a challenging and scale-dependent problem. Methodologies to address these will be discussed in companion chapters of this volume. Here we note that on the experimental side, the use of multiscale analysis techniques (including microscopy and spectroscopy) may provide quantitative information on the stiffness and strain at different length scales, to be used together with modelling methodologies.

References

1. Vincent, J. F. V. (2012). *Structural biomaterials*. Princeton University Press.
2. Meyers, M. A., Chen, P.-Y., Lin, A. Y.-M., & Seki, Y. (2008). Biological materials: Structure and mechanical properties. *Progress in Materials Science*, *53*, 1–206.
3. Wainwright, S. A. (1982). *Mechanical design in organisms*. Princeton University Press.
4. Vrhovski, B., & Weiss, A. S. (1998). Biochemistry of tropoelastin. *European Journal of Biochemistry*, *258*(1), 1–18.
5. Yigit, S., Dinjaski, N., & Kaplan, D. L. (2015). Fibrous proteins: At the crossroads of genetic engineering and biotechnological applications. *Biotechnology and Bioengineering*.
6. Hulmes, D. J. S. (2008). Collagen diversity, synthesis and assembly. In P. Fratzl (Ed.), *Collagen: Structure and mechanics* (pp. 15–47). New York: Springer Science+Business Media.
7. Meek, K. M., Chapman, J. A., & Hardcastle, R. A. (1979). The staining pattern of collagen fibrils. Improved correlation with sequence data. *Journal of Biological Chemistry*, *254*(21), 10710–10714.
8. Kadler, K. E., Holmes, D. F., Graham, H., & Starborg, T. (2000). Tip-mediated fusion involving unipolar collagen fibrils accounts for rapid fibril elongation, the occurrence of fibrillar branched networks in skin and the paucity of collagen fibril ends in vertebrates. *Matrix Biology*, *19*(4), 359–365.

9. Screen, H. R. C., Lee, D. A., Bader, D. L., & Shelton, J. C. (2004). An investigation into the effects of the hierarchical structure of tendon fascicles on micromechanical properties. *Proceedings of the Institution of Mechanical Engineers, Part H: Journal of Engineering in Medicine*, *218*(2), 109–119.
10. Weiner, S., Traub, W., & Wagner, H. D. (1999). Lamellar bone: Structure-function relations. *Journal of Structural Biology*, *126*(3), 241–255.
11. Green, E. M., Mansfield, J. C., Bell, J. S., & Winlove, C. P. (2014). The structure and micromechanics of elastic tissue. *Interface Focus*, *4*(2), 20130058.
12. Daamen, W. F., Veerkamp, J. H., Van Hest, J. C. M., & Van Kuppevelt, T. H. (2007). Elastin as a biomaterial for tissue engineering. *Biomaterials*, *28*(30), 4378–4398.
13. Raabe, D., Sachs, C., & Romano, P. (2005). The crustacean exoskeleton as an example of a structurally and mechanically graded biological nanocomposite material. *Acta Materialia*, *53*(15), 4281–4292.
14. Fabritius, H.-O., Sachs, C., Triguero, P. R., & Raabe, D. (2009). Influence of structural principles on the mechanics of a biological fiber-based composite material with hierarchical organization: The exoskeleton of the lobster homarus americanus. *Advanced Materials*, *21*(4), 391–400.
15. Sanchez, C., Arribart, H., & Guille, M. M. G. (2005). Biomimetism and bioinspiration as tools for the design of innovative materials and systems. *Nature Materials*, *4*(4), 277–288.
16. Hull, D., Clyne, T. W. (1996). An introduction to composite materials. Cambridge university press.
17. Cox, H. L. (1952). The elasticity and strength of paper and other fibrous materials. *British Journal of Applied Physics*, *3*(3), 72.
18. Chuong, C. J., & Fung, Y. C. (1986). Residual stress in arteries. In *Frontiers in biomechanics* (pp. 117–129). Springer.
19. Korhonen, R. K., Laasanen, M. S., Töyräs, J., Lappalainen, R., Helminen, H. J., & Jurvelin, J. S. (2003). Fibril reinforced poroelastic model predicts specifically mechanical behavior of normal, proteoglycan depleted and collagen degraded articular cartilage. *Journal of Biomechanics*, *36*(9), 1373–1379.
20. Blevins, F. T. (1996). Structure, function, and adaptation of tendon. *Current Opinion in Orthopaedics*, *7*(6), 57–61.
21. Riley, G. P., Harrall, R. L., Cawston, T. E., Hazleman, B. L., & Mackie, E. J. (1996). Tenascin-C and human tendon degeneration. *The American Journal of Pathology*, *149*(3), 933.
22. Benjamin, M., & Ralphs, J. R. (1997). Tendons and ligaments—an overview. *Histology and Histopathology*, *12*(4), 1135–1144.
23. Smith, R. K. W., Zunino, L., Webbon, P. M., & Heinegård, D. (1997). The distribution of cartilage oligomeric matrix protein (COMP) in tendon and its variation with tendon site, age and load. *Matrix Biology*, *16*(5), 255–271.
24. Yoon, H. J., & Halper, J. (2005). Tendon proteoglycans: Biochemistry and function. *J Musculoskelet Neuronal Interact*, *5*(1), 22–34.
25. Thorpe, C. T., Birch, H. L., Clegg, P. D., & Screen, H. R. C. (2013). The role of the non-collagenous matrix in tendon function. *International Journal of Experimental Pathology*, *94*(4), 248–259.
26. Kastelic, J., Galeski, A., & Baer, E. (1978). The multicomposite structure of tendon. *Connective Tissue Research*, *6*(1), 11–23.
27. Dyer, R. F., & Enna, C. D. (1976). Ultrastructural features of adult human tendon. *Cell and Tissue Research*, *168*(2), 247–259.
28. Ramachandran, G. N. (1988). Stereochemistry of collagen. *International Journal of Peptide and Protein Research*, *31*(1), 1–16.
29. Orgel, J. P. R. O., Irving, T. C., Miller, A., & Wess, T. J. (2006). Microfibrillar structure of type I collagen in situ. *Proceedings of the National Academy of Sciences*, *103*(24), 9001–9005.
30. Goh, K. L., Holmes, D. F., Lu, H.-Y., Richardson, S., Kadler, K. E., Purslow, P. P., et al. (2008). Ageing changes in the tensile properties of tendons: Influence of collagen fibril volume fraction. *Journal of Biomechanical Engineering*, *130*(2), 021011.

31. Scott, J. E. (2003). Elasticity in extracellular matrix “shape modules” of tendon, cartilage, etc. A sliding proteoglycan-filament model. *The Journal of Physiology*, *553*(2), 335–343.
32. Thorpe, C. T., Riley, G. P., Birch, H. L., Clegg, P. D., & Screen, H. R. C. (2016). Fascicles and the interfascicular matrix show adaptation for fatigue resistance in energy storing tendons. *Acta Biomaterialia*.
33. Buckwalter, J. A., Einhorn T. A., & Simon, S. R. (2000). *Orthopaedic basic science: Biology and biomechanics of the musculoskeletal system* (vol. 1). Amer Academy of Orthopaedic.
34. Kastelic, J., Palley, I., & Baer, E. (1980). A structural mechanical model for tendon crimping. *Journal of Biomechanics*, *13*(10), 887–893.
35. Smith, L., Xia, Y., Galatz, L. M., Genin, G. M., & Thomopoulos, S. (2012). Tissue-engineering strategies for the tendon/ligament-to-bone insertion. *Connective Tissue Research*, *53*(2), 95–105.
36. Gupta, H. S. (2008). Nanoscale deformation mechanisms in collagen. In P. Fratzl (Ed.), *Collagen: Structure and mechanics* (pp. 155–173). New York: Springer Science+Business Media.
37. Misof, K., Rapp, G., & Fratzl, P. (1997). A new molecular model for collagen elasticity based on synchrotron x-ray scattering evidence. *Biophysical Journal*, *72*(3), 1376.
38. Atkinson, T. S., Ewers, B. J., & Haut, R. C. (1999). The tensile and stress relaxation responses of human patellar tendon varies with specimen cross-sectional area. *Journal of Biomechanics*, *32*(9), 907–914.
39. Fratzl, P., Misof, K., Zizak, I., Rapp, G., Amenitsch, H., & Bernstorff, S. (1998). Fibrillar structure and mechanical properties of collagen. *Journal of Structural Biology*, *122*(1), 119–122.
40. Sasaki, N., & Odajima, S. (1996). Elongation mechanism of collagen fibrils and force-strain relations of tendon at each level of structural hierarchy. *Journal of Biomechanics*, *29*(9), 1131–1136.
41. Wang, X. T., & Ker, R. F. (1995). Creep rupture of wallaby tail tendons. *Journal of Experimental Biology*, *198*(3), 831–845.
42. Gupta, H. S., Seto, J., Krauss, S., Boesecke, P., & Screen, H. R. C. (2010). In situ multi-level analysis of viscoelastic deformation mechanisms in tendon collagen. *Journal of Structural Biology*, *169*(2), 183–191.
43. Sasaki, N., & Odajima, S. (1996). Stress-strain curve and Young’s modulus of a collagen molecule as determined by the X-ray diffraction technique. *Journal of Biomechanics*, *29*(5), 655–658.
44. Masic, A., Bertinetti, L., Schuetz, R., Chang, S.-W., Metzger, T. H., Buehler, M. J., et al. (2015). Osmotic pressure induced tensile forces in tendon collagen. *Nature Communications*, *6*.
45. Mosler, E., Folkhard, W., Knörzer, E., Nemetschek-Gansler, H., Nemetschek, T., & Koch, M. H. J. (1985). Stress-induced molecular rearrangement in tendon collagen. *Journal of Molecular Biology*, *182*(4), 589–596.
46. Sasaki, N., Shukunami, N., Matsushima, N., & Izumi, Y. (1999). Time-resolved X-ray diffraction from tendon collagen during creep using synchrotron radiation. *Journal of Biomechanics*, *32*(3), 285–292.
47. Eppell, S. J., Smith, B. N., Kahn, H., & Ballarini, R. (2006). Nano measurements with micro-devices: Mechanical properties of hydrated collagen fibrils. *Journal of the Royal Society Interface*, *3*(6), 117–121.
48. Buehler, M. J. (2006). Nature designs tough collagen: Explaining the nanostructure of collagen fibrils. *Proceedings of the National Academy of Sciences*, *103*(33), 12285–12290.
49. Scree, H. R. C., Lee, D. A., Bader, D. L., & Shelton, J. C. (2003). Development of a technique to determine strains in tendons using the cell nuclei. *Biorheology*, *40*, 361–368.
50. Screen, H. R. C., Bader, D. L., Lee, D. A., & Shelton, J. C. (2004). Local strain measurement within tendon. *Strain*, *40*(4), 157–163.
51. Szczesny, S. E., Caplan, J. L., Pedersen, P., & Elliott, D. M. (2015). Quantification of interfibrillar shear stress in aligned soft collagenous tissues via notch tension testing. *Scientific Reports*, *5*.

52. Knörzer, E., Folkhard, W., Geercken, W., Boschert, C., Koch, M. H. J., Hilbert, B., et al. (1986). New aspects of the etiology of tendon rupture. *Archives of Orthopaedic and Traumatic Surgery*, *105*(2), 113–120.
53. Puxkandl, R., Zizak, I., Paris, O., Keckes, J., Tesch, W., Bernstorff, S., et al. (2002). Viscoelastic properties of collagen: Synchrotron radiation investigations and structural model. *Philosophical Transactions of the Royal Society of London B: Biological Sciences*, *357*(1418), 191–197.
54. Thorpe, C. T., Godinho, M. S. C., Riley, G. P., Birch, H. L., Clegg, P. D., & Screen, H. R. C. (2015). The interfascicular matrix enables fascicle sliding and recovery in tendon, and behaves more elastically in energy storing tendons. *Journal of the Mechanical Behavior of Biomedical Materials*, *52*, 85–94.
55. Screen, H. R. C., Shelton, J. C., Chhaya, V. H., Kayser, M. V., Bader, D. L., & Lee, D. A. (2005). The influence of noncollagenous matrix components on the micromechanical environment of tendon fascicles. *Annals of Biomedical Engineering*, *33*(8), 1090–1099.
56. Screen, H. R. C., Chhaya, V. H., Greenwald, S. E., Bader, D. L., Lee, D. A., & Shelton, J. C. (2006). The influence of swelling and matrix degradation on the microstructural integrity of tendon. *Acta Biomaterialia*, *2*(5), 505–513.
57. Connizzo, B. K., Sarver, J. J., Lozzo, R. V., Birk, D. E., & Soslowsky, L. J. (2013). Effect of age and proteoglycan deficiency on collagen fiber re-alignment and mechanical properties in mouse supraspinatus tendon. *Journal of Biomechanical Engineering*, *135*(2), 021019.
58. Legerlotz, K., Riley, G. P., & Screen, H. R. C. (2013). GAG depletion increases the stress-relaxation response of tendon fascicles, but does not influence recovery. *Acta Biomaterialia*, *9*(6), 6860–6866.
59. Dourte, L. A. M., Pathmanathan, L., Jawad, A. F., Lozzo, R. V., Mienaltowski, M. J., Birk, D. E., et al. (2012). Influence of decorin on the mechanical, compositional, and structural properties of the mouse patellar tendon. *Journal of Biomechanical Engineering*, *134*(3), 031005.
60. Henninger, H. B., Underwood, C. J., Romney, S. J., Davis, G. L., & Weiss, J. A. (2013). Effect of elastin digestion on the quasi-static tensile response of medial collateral ligament. *Journal of Orthopaedic Research*, *31*(8), 1226–1233.
61. Millesi, H., Reihsner, R., Hamilton, G., Mallinger, R., & Menzel, E. J. (1995). Biomechanical properties of normal tendons, normal palmar aponeuroses, and tissues from patients with dupuytren's disease subjected to elastase and chondroitinase treatment. *Clinical Biomechanics*, *10*(1), 29–35.
62. Birch, H. L. (2007). Tendon matrix composition and turnover in relation to functional requirements. *International Journal of Experimental Pathology*, *88*(4), 241–248.
63. Ker, R. F., Wang, X. T., & Pike, A. V. (2000). Fatigue quality of mammalian tendons. *Journal of Experimental Biology*, *203*(8), 1317–1327.
64. Thorpe, C. T., Udeze, C. P., Birch, H. L., Clegg, P. D., & Screen, H. R. C. (2012) Specialization of tendon mechanical properties results from interfascicular differences. *Journal of the Royal Society Interface*, p. rsif20120362.
65. Thorpe, C. T., Karunaseelan, K. J., Ng Chieng Hin, J., Riley, G. P., Birch, H. L., Clegg, P. D., et al. (2016). Distribution of proteins within different compartments of tendon varies according to tendon type. *Journal of Anatomy*.
66. Thorpe, C. T., Klemt, C., Riley, G. P., Birch, H. L., Clegg, P. D., & Screen, H. R. C. (2013). Helical sub-structures in energy-storing tendons provide a possible mechanism for efficient energy storage and return. *Acta Biomaterialia*, *9*(8), 7948–7956.
67. Thorpe, C. T., Riley, G. P., Birch, H. L., Clegg, P. D., & Screen, H. R. C. (2014). Fascicles from energy-storing tendons show an age-specific response to cyclic fatigue loading. *Journal of the Royal Society Interface*, *11*(92), 20131058.
68. Grande-Allen, J. K., & Liao, J. (2011). The heterogeneous biomechanics and mechanobiology of the mitral valve: Implications for tissue engineering. *Current Cardiology Reports*, *13*(2), 113–120.
69. McCarthy, K. P., Ring, L., & Rana, B. S. (2010). Anatomy of the mitral valve: Understanding the mitral valve complex in mitral regurgitation. *European Heart Journal-Cardiovascular Imaging*, *11*(10), i3–i9.

70. Missirlis, Y. F., & Chong, M. (1978). Aortic valve mechanics-part I: Material properties of natural porcine aortic valves. *Journal of Bioengineering*, *2*(3–4), 287–300.
71. Scott, M., & Vesely, I. (1995). Aortic valve cusp microstructure: The role of elastin. *The Annals of Thoracic Surgery*, *60*, S391–S394.
72. Sacks, M. S. (1999). A method for planar biaxial mechanical testing that includes in-plane shear. *Journal of Biomechanical Engineering*, *121*(5), 551–555.
73. Merryman, D. W., Huang, H.-Y. S., Schoen, F. J., & Sacks, M. S. (2006). The effects of cellular contraction on aortic valve leaflet flexural stiffness. *Journal of Biomechanics*, *39*(1), 88–96.
74. Vesely, I. (1997). The role of elastin in aortic valve mechanics. *Journal of Biomechanics*, *31*(2), 115–123.

Chapter 2
Hyperelasticity of Soft Tissues and Related Inverse Problems

Stéphane Avril

Abstract In this chapter, we are interested in the constitutive equations used to model macroscopically the mechanical function of soft tissues. After reviewing some basics about nonlinear finite strain constitutive relations, we present recent developments of experimental biomechanics and inverse methods aimed at quantifying constitutive parameters of soft tissues. A focus is given to in vitro characterization of hyperelastic parameters based on full-field data that can be collected with digital image correlation systems during the experimental tests. The specific use of these data for membrane-like tissues is first illustrated through the example of bulge inflation tests carried out onto pieces of aortic aneurysms. Then an inverse method, based on the principle of virtual power, is introduced to estimate regional variations of material parameters for more general applications.

2.1 Introduction

A better understanding of many issues of human health, disease, injury, and their treatment thereof necessitates a detailed quantification of how biological cells, tissues, and organs respond to applied loads. Thus, experimental and computational mechanics can, and must, play a fundamental role in cell biology, physiology, pathophysiology, and clinical intervention. The goal of this chapter is to discuss some of the recent developments of experimental biomechanics based on the use of digital image correlation and inverse methods for quantifying the finite strain behavior of biological soft tissues in terms of nonlinear constitutive relations. After a brief review of these constitutive relations, two recent developments of the author's experience are presented to illustrate the potential of digital image correlation and inverse methods in experimental biomechanics of soft tissues.

S. Avril (✉)
Inserm U1059, Mines Saint–Étienne, University of Lyon, Saint–Étienne, France
e-mail: avril@emse.fr

S. Avril and S. Evans (eds.), *Material Parameter Identification and Inverse Problems in Soft Tissue Biomechanics*, CISM International Centre for Mechanical Sciences 573, DOI 10.1007/978-3-319-45071-1_2

2.2 Basic Constitutive Equations of Soft Tissues

This section presents the theoretical background for understanding the foundations of constitutive models in soft tissues. This background is essential for the following sections and for the other chapters of this book. The presentation of this background follows the approach of a seminal paper from Millard [1].

2.2.1 Kinematics of Finite Deformation

Since the early 1940s there has been enormous progress in the development of a theory of elastic materials subjected to large deformations. Significant theoretical results, many confirmed by experiments, have projected considerable light on the physical behavior of rubberlike materials such as synthetic elastomers, polymers and biological tissue, in addition to natural rubber. The mathematical theory of elasticity of materials subjected to large deformations is inherently nonlinear. The theory of elasticity of materials for which there exists an elastic potential energy function is known as *hyperelasticity*. Before presenting the constitutive equations for a hyperelastic solid, we begin with a sketch of the principal kinematical relations used to describe the finite deformation of a continuum and with the Cauchy stress principle and equations of kinetics. A body $B = \{P_k\}$ is a set of material points P_k called particles. A reference frame is a set $\Upsilon = \{O, \mathbf{e}\}$ consisting of an origin point O and an orthonormal vector basis $\mathbf{e}$. The motion of a particle P relative to Υ is described by the time locus of its position vector $\mathbf{x}(P, t)$ relative to Υ. This locus is the trajectory or path of P in Υ. A typical particle P may be identified by its position vector $\mathbf{X}(P)$ in Υ at some reference time t_0. The domain κ_0 of $\mathbf{X}$, the region in Euclidian space occupied by B at time t_0 is called a reference configuration of B. Then, relative to Υ the motion of a particle P from κ_0 is described by the vector function

$$\mathbf{x} = \chi(\mathbf{X}, t) \tag{2.1}$$

The domain κ of $\mathbf{x}$, the region in Euclidian space occupied by B at time t_0 is called a current configuration of B. Hence, $\mathbf{x}$ denotes the place at time t in the current configuration κ which is occupied by the particle P whose place was X in the reference configuration of B. The velocity and acceleration of a particle P relative to Υ are defined by

$$\mathbf{v}(\mathbf{X}, t) = \dot{\mathbf{x}}(\mathbf{X}, t) \tag{2.2}$$

$$\gamma(\mathbf{X}, t) = \dot{\mathbf{v}}(\mathbf{X}, t) = \ddot{\mathbf{x}}(\mathbf{X}, t) \tag{2.3}$$

We shall assume henceforward that the body is a contiguous collection of particles, we call this body a continuum. It is assumed that χ is a smooth one-to-one map of every material point of $\kappa_0 \to \kappa$ with

$$J = \det \mathbf{F} > 0, \tag{2.4}$$

in which

$$\mathbf{F} = \partial \mathbf{x} / \partial \mathbf{X} = \mathbf{Grad}\, \mathbf{x} \tag{2.5}$$

is called the deformation gradient. This tensor transforms the tangent element d$\mathbf{X}$ of a material line $\mathfrak{L}_0$ in κ_0 into the tangent element d$\mathbf{x}$ of its deformed image line $\mathfrak{L}$ in κ. Hence,

$$\mathrm{d}\mathbf{x} = \mathbf{F}\mathrm{d}\mathbf{X} \tag{2.6}$$

Let $\|\mathrm{d}\mathbf{x}\| = \mathrm{d}l$ and $\|\mathrm{d}\mathbf{X}\| = \mathrm{d}L$, where l and L are the arc length parameters for $\mathfrak{L}$ and $\mathfrak{L}_0$ respectively. Then Eq. 2.6 may be written:

$$\lambda \mathbf{e} = \mathbf{F}\mathbf{E} \tag{2.7}$$

in which $\mathbf{e} = \mathrm{d}\mathbf{x}/\mathrm{d}l$ and $\mathbf{E} = \mathrm{d}\mathbf{X}/\mathrm{d}L$ are unit vectors tangent to $\mathfrak{L}$ and $\mathfrak{L}_0$ at $\mathbf{x}$ and $\mathbf{X}$ and

$$\lambda = \mathrm{d}l/\mathrm{d}L \tag{2.8}$$

is named the stretch, the ratio of the current length ds to the reference length dS of the material element. These lengths are commonly called the deformed and undeformed lengths, respectively. However it is not essential that the reference configuration be an undistorted reference configuration, nor one that the body actually needs to occupy at any time during its motion. It is seen that Eq. 2.7 expresses the physical result that $\mathbf{F}$ rotates $\mathbf{E}$ into the direction $\mathbf{e}$ and stretches it by an amount $0 < \lambda < \infty$. This is essentially the substance of the more general and physically useful polar decomposition theorem of linear algebra applied pointwise to the nonsingular tensor $\mathbf{F}$

$$\mathbf{F} = \mathbf{R}\mathbf{U} = \mathbf{V}\mathbf{R} \tag{2.9}$$

The proper orthogonal tensor $\mathbf{R}$ characterizes the local rigid body rotation of a material element. The positive symmetric tensors $\mathbf{U}$ and $\mathbf{V}$ describe the local deformation of the element. They are called the right and the left stretch tensors, respectively. The decomposition of the deformation gradient $\mathbf{F}$ into a pure stretch $\mathbf{U}$ at $\mathbf{X}$ followed by a rigid body rotation $\mathbf{R}$, or by the same rigid body rotation followed by a pure stretch $\mathbf{V}$ at $\mathbf{x}$ is unique. Because $\mathbf{U}$ and $\mathbf{V}$ usually are tedious to compute, it is customary to use their squares

$$\mathbf{C} = \mathbf{F}^T\mathbf{F} = \mathbf{U}^2 \text{ and } \mathbf{B} = \mathbf{F}\mathbf{F}^T = \mathbf{V}^2 \tag{2.10}$$

The corresponding positive symmetric tensors are respectively known as the right and the left Cauchy–Green deformation tensors. It follows that $\mathbf{U}$ and $\mathbf{V}$ ($\mathbf{C}$ and $\mathbf{B}$)

have the same principal values λ_k (λ_k^2) and respective principal directions $\boldsymbol{\mu}$ and $\boldsymbol{\nu}$ are related by the rotation $\mathbf{R}$

$$\boldsymbol{\nu} = \mathbf{R}.\boldsymbol{\mu} \tag{2.11}$$

The λ_k are the stretches of the three principal material lines, they are called the principal stretches.

Formulae relating the respective material surface area and volume elements $\mathrm{d}a$ and $\mathrm{d}v$ in κ to their respective reference images $\mathrm{d}A$ and $\mathrm{d}V$ in κ_0 may be easily derived by application of

$$\mathbf{n}\mathrm{d}a = J\,\mathbf{F}^{-T}.\mathbf{N}\mathrm{d}A \quad \text{and} \quad \mathrm{d}v = J\mathrm{d}V \tag{2.12}$$

where $\mathbf{n}$ is the exterior unit normal vector to $\partial\mathscr{P}$ in κ and $\mathbf{N}$ is the exterior unit normal vector to $\partial\mathscr{P}$ in κ_R.

The previous relation shows that det $\mathbf{F}$ is the ratio of the current (deformed) volume to the reference (undeformed) volume of a material element. Therefore the deformation is isochoric if $J = 1$. It is evident on physical grounds that $0 < \det \mathbf{F} < \infty$. The material time rate of the deformation of a continuum is described by the velocity gradient tensor $\mathbf{L}$

$$\mathbf{L} = \mathbf{Grad}\,\dot{\mathbf{x}} = \dot{\mathbf{F}}\mathbf{F}^{-1} \tag{2.13}$$

The symmetric part $\mathbf{D}$ and antisymmetric part $\mathbf{W}$ of $\mathbf{L}$ are the stretching and spin tensors, respectively.

2.2.2 *The Cauchy Stress Principle and the Equations of Motion*

The forces that act on any part $\mathscr{P} \subset \mathscr{B}$ of a continuum $\mathscr{B}$ are of two kinds: a distribution of contact force $\mathbf{t_n}$ per unit area of the boundary $\partial\mathscr{P}$ of $\mathscr{P}$ in κ, and a distribution of body force $\mathbf{b}$ per unit volume of $\mathscr{P}$ in κ. The total force $\mathscr{F}(\mathscr{P}, t)$ and the total torque $\mathscr{T}(\mathscr{P}, t)$ acting on the part $\mathscr{P}$ are related to the momentum and the moment of momentum of the material points of $\mathscr{B}$ in an inertial frame Φ in accordance with Euler's laws of motion

$$\mathscr{F}(\mathscr{P}, t) = \int_{\partial\mathscr{P}} \mathbf{t_n}\,\mathrm{d}a + \int_{\mathscr{P}} \mathbf{b}\,\mathrm{d}v = \frac{\mathrm{d}}{\mathrm{d}t}\int_{\mathscr{P}} \mathbf{v}\,\mathrm{d}m \tag{2.14}$$

$$\mathscr{T}(\mathscr{P}, t) = \int_{\partial\mathscr{P}} \mathbf{x} \times \mathbf{t_n}\,\mathrm{d}a + \int_{\mathscr{P}} \mathbf{x} \times \mathbf{b}\,\mathrm{d}v = \frac{\mathrm{d}}{\mathrm{d}t}\int_{\mathscr{P}} \mathbf{x} \times \mathbf{v}\,\mathrm{d}m \tag{2.15}$$

The moments in Eq. 2.15 are to be computed with respect to the origin in Φ. Note that $\mathrm{d}m = \rho\,\mathrm{d}v$ is the material element of mass with density ρ per unit volume in κ.

The principle of balance of mass requires also that $\mathrm{d}m = \rho_R \,\mathrm{d}V$ where ρ_R is the density of mass per unit volume V in κ_R. Therefore one finds that the respective mass densities are related by the local equation of continuity

$$\rho_R = J\rho \tag{2.16}$$

Application of the first law of Euler to an arbitrary tetrahedral element leads to Cauchy's stress principle

$$\mathbf{t_n} = \boldsymbol{\sigma}.\mathbf{n} \tag{2.17}$$

Hence the traction or stress vector $\mathbf{t_n}$ is a linear transformation of the unit normal $\mathbf{n}$ by the Cauchy stress tensor $\boldsymbol{\sigma}$. Use of previous equations and the divergence theorem yields Cauchy first law of motion

$$\operatorname{div} \boldsymbol{\sigma} + \mathbf{b} = \rho\gamma \tag{2.18}$$

The second law of Eq. 2.15 together with Eqs. 2.17 and 2.18 yields the equivalent local moment balance condition restricting the Cauchy stress $\boldsymbol{\sigma}$ to the space of symmetric tensors

$$\boldsymbol{\sigma} = \boldsymbol{\sigma}^T \tag{2.19}$$

The Cauchy stress characterizes the contact force distribution $\mathbf{t_n}$ in κ per unit current area in κ. But this is often inconvenient in solid mechanics because the deformed configuration generally is not known a priori. Therefore, the engineering stress tensor $\mathbf{T}_R$, also known as the first Piola-Kirchhoff stress tensor, is introduced to define the contact force distribution $\mathbf{t_n} \equiv \mathbf{T}_R.\mathbf{N}$ in κ per unit reference area in κ_R. Then for the same contact force $\mathrm{d}\mathscr{F}(\mathscr{P}, t)$, we must have

$$\mathrm{d}\mathscr{F}(\mathscr{P}, t) \equiv \mathbf{t_n}\,\mathrm{d}a = \boldsymbol{\sigma}.\mathbf{n}\,\mathrm{d}a = \mathbf{T}_R.\mathbf{N}\,\mathrm{d}A = \mathbf{t_N}\,\mathrm{d}A \tag{2.20}$$

The vector $\mathbf{t_N}$ is named the engineering stress tensor. We thus obtain the rule

$$\mathbf{T}_R = J\,\boldsymbol{\sigma}\mathbf{F}^{-T} \tag{2.21}$$

relating the engineering and Cauchy stress tensors.

The corresponding stress principle and balance laws become

$$\mathbf{t_N} = \mathbf{T}_R.\mathbf{N} \tag{2.22}$$

$$\operatorname{Div} \mathbf{T}_R + \mathbf{b}_R = \rho_R\,\gamma_R \tag{2.23}$$

$$\mathbf{T}_R\mathbf{F}^T = \mathbf{F}\mathbf{T}_R^T \tag{2.24}$$

Hence the engineering stress $\mathbf{T}_R$ generally is not symmetric. Equation $\mathbf{b}_R \equiv J\mathbf{b}$ identifies the body force per unit volume in κ_R, and Div denotes the divergence operator with respect to $\mathbf{X}$ in κ_R, whereas div is with respect to $\mathbf{x}$ in κ.

Another stress tensor that will be useful is the second Piola-Kirchhoff stress defined as

$$\boldsymbol{\pi} = \mathbf{F}^{-1}\mathbf{T}_R = J\,\mathbf{F}^{-1}\boldsymbol{\sigma}\mathbf{F}^{-T} \tag{2.25}$$

Thus far, the deformation of a continuum and the actions that produces it have been treated separately without the mention of any special material characteristics that the body may possess. Of course the inherent constitutive nature of the material dictates its deformation response to action by forces and torques. For a specific class of materials, the specific relationship between the deformation gradient $\mathbf{F}$, the rate of deformation $\dot{\mathbf{F}}$, and the stress $\boldsymbol{\sigma}$, $\mathbf{T}_R$ or $\boldsymbol{\pi}$ is described by an equation known as a constitutive equation. In the next section, the principle of balance of mechanical energy will be applied to derive the constitutive equation for a special class of perfectly elastic materials called hyperelastic solids.

2.2.3 Hyperelasticity

Thermodynamics foundation The first law of thermodynamics tells that the time rate of change of the internal energy $E(\mathscr{P}, t)$ for any part $\mathscr{P} \subset \mathscr{B}$ of a body $\mathscr{B}$ is balanced by the total mechanical power $W(\mathscr{P}, t)$ and the total heat flux $Q(\mathscr{P}, t)$.

$$\dot{E}(\mathscr{P}, t) = W(\mathscr{P}, t) + Q(\mathscr{P}, t) \tag{2.26}$$

The second law of thermodynamics tells that the time rate of change of entropy $\dot{S}(\mathscr{P}, t)$ for any part $\mathscr{P} \subset \mathscr{B}$ of a body $\mathscr{B}$ can be decomposed into exchanges of entropy and production of entropy and that the latter can only be positive, or zero if the transformation is reversible (no dissipation). If Θ denotes temperature, exchanges of entropy at constant temperature (isotherm transformations will be assumed further) may be written such as: Q/Θ. Finally, the second law of thermodynamics tells

$$\dot{S}(\mathscr{P}, t) \geq \frac{Q(\mathscr{P}, t)}{\Theta} \tag{2.27}$$

$$\dot{E}(\mathscr{P}, t) - \Theta\dot{S}(\mathscr{P}, t) \leq W(\mathscr{P}, t) \tag{2.28}$$

$\mathscr{P}$ being an arbitrary tetrahedral element, and $\boldsymbol{\sigma} : \mathbf{D}$ being the mechanical power per unit volume, it may be written at any time t

$$\rho(\dot{e} - \Theta\dot{s}) \leq \boldsymbol{\sigma} : \mathbf{D} \tag{2.29}$$

where e denotes the local specific internal energy and s denotes the local specific entropy. This equation points out that the work done by the stress would induce either an increase of the specific internal energy or a decrease of the specific entropy. In the case of elasticity, the transformation is reversible and it may be written

$$\rho(\dot{e} - \Theta\dot{s}) = \boldsymbol{\sigma} : \mathbf{D} \tag{2.30}$$

When the work done by the stress induces mostly an increase of the specific internal energy ($|\Theta\dot{s}| << \dot{e}$), we speak of enthalpic elasticity (in an isotherm transformation, $\dot{e} = \dot{\text{h}}$ where h would be the specific enthalpy). Enthalpic elasticity is the elasticity of crystals where the deformation comes mostly from a change of distances between atoms. Elastic response of the crystalline solids is due to the change of the equilibrium interatomic distances under stress and therefore, the change in the internal energy of the crystal.

When the work done by the stress induces mostly a decrease of entropy ($\dot{e} << |\Theta\dot{s}|$), we speak of entropic elasticity. Elasticity of soft biological tissues is composed from the elastic responses of the chains crosslinked in the network sample. External stress changes the equilibrium end-to-end distance of a chain, and it thus adopts a less probable conformation, its entropy therefore decreases. Therefore, the elasticity of soft biological tissues is of purely entropic nature.

Introducing the specific free energy $\phi = e + \Theta s$, and still assuming isotherm transformations ($\dot{\Theta} = 0$), it may be written

$$\rho\dot{\phi} = \boldsymbol{\sigma} : \mathbf{D} \tag{2.31}$$

It is now the time to define what a *hyperelastic solid* is. A hyperelastic solid is a material whose specific free energy depends only on the strain. It may be written

$$\phi(\mathbf{X}, t) = \phi(\mathbf{F}(\mathbf{X}, t), \mathbf{X}) \tag{2.32}$$

The $\psi = \rho\phi$ function is a strain energy density function. Then the constitutive equation for a hyperelastic solid can be written

$$\boldsymbol{\pi} = \frac{\partial\psi}{\partial\mathbf{E}} = 2\frac{\partial\psi}{\partial\mathbf{C}} \tag{2.33}$$

$$\mathbf{T}_R = \frac{\partial\psi}{\partial\mathbf{F}} = \mathbf{F}\frac{\partial\psi}{\partial\mathbf{E}} = 2\mathbf{F}\frac{\partial\psi}{\partial\mathbf{C}} \tag{2.34}$$

$$\boldsymbol{\sigma} = J^{-1}\frac{\partial\psi}{\partial\mathbf{F}}\mathbf{F}^T = J^{-1}\mathbf{F}\frac{\partial\psi}{\partial\mathbf{E}}\mathbf{F}^T = 2J^{-1}\mathbf{F}\frac{\partial\psi}{\partial\mathbf{C}}\mathbf{F}^T \tag{2.35}$$

Isotropic compressible hyperelastic solids For an isotropic solid, the strain energy function must be an isotropic scalar valued function of the principal invariants alone

$$\psi = \psi(\mathbf{C}) = \psi(\mathbf{B}) = \psi(I_1, I_2, I_3) \tag{2.36}$$

wherein, specifically,

$$I_1 = \mathrm{tr}(\mathbf{B}) \tag{2.37}$$

$$I_2 = \frac{1}{2}\left[I_1^2 - \mathrm{tr}(\mathbf{B}^2)\right] \tag{2.38}$$

$$I_3 = \det(\mathbf{B}) \tag{2.39}$$

Note that Eq. 2.35 may be rewritten such as

$$\boldsymbol{\sigma} = 2J^{-1}\frac{\partial\psi}{\partial\mathbf{B}}\mathbf{B} \tag{2.40}$$

Then, introducing the principal invariants

$$\boldsymbol{\sigma} = \left(\frac{\partial\psi}{\partial J} + 2J^{-1}\frac{\partial\psi}{\partial I_2}I_2\right)\mathbf{1} + 2J^{-1}\frac{\partial\psi}{\partial I_1}\mathbf{B} - 2J^{-1}\frac{\partial\psi}{\partial I_{-1}}\mathbf{B}^{-1} \tag{2.41}$$

where $I_{-1} = I_2/I_3 = \mathrm{tr}(\mathbf{B}^{-1})$.

Isotropic hyperelastic incompressible solids The Cauchy stress on an incompressible, hyperelastic material, is determined by **F** only to within an arbitrary stress which is proportional to the identity tensor. Then the constitutive equation for an incompressible, isotropic, hyperelastic material is given by

$$\boldsymbol{\sigma} = -p\mathbf{1} + 2\frac{\partial\psi}{\partial I_1}\mathbf{B} - 2\frac{\partial\psi}{\partial I_2}\mathbf{B}^{-1} \tag{2.42}$$

where p is an undetermined scalar of $\mathbf{x}$. Note that $I_2 = I_{-1}$ for an incompressible solid.

A particular type of strain energy functions may be written such as polynomials

$$\psi = \sum_{j=0}^{N_j}\sum_{i=0}^{N_i} C_{ij}(I_1 - 3)^i (I_2 - 3)^j \tag{2.43}$$

when $N_i = 3$ and $N_j = 0$ it is referred to as Yeoh strain energy function, when $N_i = 1$ and $N_j = 1$ but $C_{11} = 0$, we have the Mooney–Rivlin material. The special case when $N_i = 1$ and $N_j = 0$ is the neo-Hookean material.

Another particular type which is meaningful for biological tissues may be written

$$\psi = \frac{\mu_0}{2\gamma}\left[e^{\gamma(I_1-3)} - 1\right] \tag{2.44}$$

Isotropic hyperelastic nearly incompressible solids It is common for nearly incompressible hyperelastic solids to assume a perfect decoupling between purely volumetric and purely isochoric effects, and then to decompose the strain energy density function additively in two components: one depending only on volume changes and the second one independent of volume changes

$$\psi = U(J) + \bar{\psi}(\bar{I}_1, \bar{I}_2) \tag{2.45}$$

$$\begin{aligned}\boldsymbol{\sigma} = &\left(\frac{\partial\psi}{\partial J} + 2J^{-1}\frac{\partial\psi}{\partial I_2}I_2\right)\mathbf{1} \\ &+ 2J^{-1}\frac{1}{J^{2/3}}\frac{\partial\bar{\psi}}{\partial\bar{I}_1}\mathbf{B} - 2J^{-1}\frac{1}{J^{4/3}/J^2}\frac{\partial\bar{\psi}}{\partial\bar{I}_2}\mathbf{B}^{-1}\end{aligned} \tag{2.46}$$

where $\bar{I}_1 = \mathrm{tr}(\bar{\mathbf{B}})$, $\bar{I}_2 = \frac{1}{2}\left[\bar{I}_1^2 - \mathrm{tr}(\bar{\mathbf{B}}^2)\right] = \mathrm{tr}(\bar{\mathbf{B}}^{-1})$, $\bar{\mathbf{B}} = \bar{\mathbf{F}}\bar{\mathbf{F}}^T$ and $\bar{\mathbf{F}} = J^{-1/3}\mathbf{F}$.

$$\begin{aligned}\boldsymbol{\sigma} = &\left[\left(\frac{\partial\psi}{\partial J} + 2J^{-1}\frac{\partial\psi}{\partial I_2}I_2\right) + \frac{\partial\bar{\psi}}{\partial\bar{I}_1}\frac{\partial\bar{I}_1}{\partial J} + \frac{\partial\bar{\psi}}{\partial\bar{I}_2}\frac{\partial\bar{I}_2}{\partial J}\right]\mathbf{1} \\ &+ 2J^{-1}\frac{\partial\bar{\psi}}{\partial\bar{I}_1}\bar{\mathbf{B}} - 2J^{-1}\frac{\partial\bar{\psi}}{\partial\bar{I}_2}\bar{\mathbf{B}}^{-1}\end{aligned} \tag{2.47}$$

$$\begin{aligned}\boldsymbol{\sigma} = &\left[\left(\frac{\partial\psi}{\partial J} + 2J^{-1}\frac{\partial\psi}{\partial I_2}I_2\right) - \frac{2}{3}J^{-1}\frac{\partial\bar{\psi}}{\partial\bar{I}_1}\bar{I}_1 - \frac{4}{3}J^{-1}\frac{\partial\bar{\psi}}{\partial\bar{I}_2}\bar{I}_2\right]\mathbf{1} \\ &+ 2J^{-1}\frac{\partial\bar{\psi}}{\partial\bar{I}_1}\bar{\mathbf{B}} - 2J^{-1}\frac{\partial\bar{\psi}}{\partial\bar{I}_2}\bar{\mathbf{B}}^{-1}\end{aligned} \tag{2.48}$$

$$\begin{aligned}\boldsymbol{\sigma} = &\left[\left(\frac{\partial\psi}{\partial J} + 2J^{-1}\frac{\partial\psi}{\partial I_2}I_2\right) - 2J^{-1}\frac{\partial\bar{\psi}}{\partial\bar{I}_2}\bar{I}_2 - \frac{2}{3}J^{-1}\frac{\partial\bar{\psi}}{\partial\bar{I}_1}\bar{I}_1 + \frac{2}{3}J^{-1}\frac{\partial\bar{\psi}}{\partial\bar{I}_2}\bar{I}_2\right]\mathbf{1} \\ &+ 2J^{-1}\frac{\partial\bar{\psi}}{\partial\bar{I}_1}\bar{\mathbf{B}} - 2J^{-1}\frac{\partial\bar{\psi}}{\partial\bar{I}_2}\bar{\mathbf{B}}^{-1}\end{aligned} \tag{2.49}$$

Finally,

$$\boldsymbol{\sigma} = \left[\frac{\partial \psi}{\partial J} - \frac{2}{3}J^{-1}\frac{\partial \bar{\psi}}{\partial \bar{I}_1}\bar{I}_1 + \frac{2}{3}J^{-1}\frac{\partial \bar{\psi}}{\partial \bar{I}_2}\bar{I}_2\right]\mathbf{1} + 2J^{-1}\frac{\partial \bar{\psi}}{\partial \bar{I}_1}\bar{\mathbf{B}} - 2J^{-1}\frac{\partial \bar{\psi}}{\partial \bar{I}_2}\bar{\mathbf{B}}^{-1}$$
$$= \frac{\partial \psi}{\partial J}\mathbf{1} + 2J^{-1}\mathrm{Dev}\left(\frac{\partial \bar{\psi}}{\partial \bar{I}_1}\bar{\mathbf{B}} - \frac{\partial \bar{\psi}}{\partial \bar{I}_2}\bar{\mathbf{B}}^{-1}\right) \tag{2.50}$$

where Dev denotes the deviatoric tensor.

The Cauchy stress is then decomposed additively into a hydrostatic component related to J and into a deviatoric component related to $\bar{I}_1$ and $\bar{I}_2$.

$$\boldsymbol{\sigma} = -p\mathbf{1} + \mathbf{s} \tag{2.51}$$

where $p = -\partial U / \partial J$ and

$$\mathbf{s} = 2J^{-1}\mathrm{Dev}\left(\frac{\partial \bar{\psi}}{\partial \bar{I}_1}\bar{\mathbf{B}} - \frac{\partial \bar{\psi}}{\partial \bar{I}_2}\bar{\mathbf{B}}^{-1}\right) \tag{2.52}$$

Common models of isotropic hyperelastic nearly incompressible solids The compressible version of a neo-Hookean material may be written

$$\psi = C_{10}(\bar{I}_1 - 3) + \frac{1}{D}(J-1)^2 \tag{2.53}$$

The compressible version of a Yeoh material may be written

$$\psi = \sum_{i=0}^{3} C_{i0}(\bar{I}_1 - 3)^i + \sum_{i=0}^{3} \frac{1}{D_i}(J-1)^{2i} \tag{2.54}$$

Another common model in compressible hyperelasticity is the Arruda Boyce model. Although its formulation is based on a thermodynamical background, it is not often used for biological tissues. The strain energy density may be written

$$\psi = \mu \sum_{i=0}^{5} \frac{C_i}{\lambda_m^{2i-2}}(\bar{I}_1^i - 3^i) + \frac{1}{D}\left[\frac{(J^2-1)}{2} - \ln(J)\right] \tag{2.55}$$

where: $C_1 = \frac{1}{2}$, $C_2 = \frac{1}{20}$, $C_3 = \frac{11}{1050}$, $C_4 = \frac{19}{7050}$, $C_5 = \frac{51}{673750}$.

A more common model is the Ogden model, which may be written

$$\psi = \frac{2\mu}{\alpha^2}(\lambda_1^{2\alpha} + \lambda_2^{2\alpha} + \lambda_3^{2\alpha}) + \frac{1}{D}(J^2 - 1) \tag{2.56}$$

where λ_1, λ_2 and λ_3 are the principal stretches.

2.2.4 More Sophisticated Constitutive Models

The aim of this section is to introduce the basics for the following sections of this chapter but also for the following chapters of this book. It is not rare that soft tissues are modeled with constitutive equations including other features than the ones of isotropic hyperelasticity. The main ones are summarized hereafter.

Anisotropic hyperelastic models Soft tissues may often present anisotropic effects. The most common effect is a different stress–stretch curve when they are subjected to uniaxial tension in two different directions. Very common models permitting to represent these effects may describe the material such as a composite made of a neo-Hookean matrix in which fiber families are embedded

$$\psi = C_{10}(\bar{I}_1 - 3) + \sum_{i=1}^{N} \frac{k_{1i}}{2k_{2i}} \left[e^{k_{2i}(\bar{\lambda}_i^2 - 1)} - 1 \right] + \frac{1}{D}(J^2 - 1) \tag{2.57}$$

where $\bar{\lambda}_i^2 = \bar{\mathbf{C}} : (\mathbf{M_i} \otimes \mathbf{M_i}) = \bar{\mathbf{C}}\mathbf{M_i}.\mathbf{M_i}$.

$\mathbf{M_i}$ are vectors defining orientations of a fiber family in the reference configuration. Although motivated by microstructural information, this type of models was developed primarily to capture phenomenologically the anisotropic response of soft tissues subjected to multidirectional tensile tests, which ultimately depends on constituent fractions, fiber orientations, cross-linking, physical entanglements, and so forth.

Irreversible effects When subjected to cycled uniaxial tensile tests (or other types of testing), the loading unloading profile of biological tissues often presents an hysteresis on the first cycle. With repeated loading cycles the load-deformation curves shift to the right in a load-elongation diagram and the hysteretic effects diminish. In a load-time diagram the load-time curves shift upwards with increasing repetition number. By repeated cycling, eventually a steady state is reached at which no further change will occur unless the cycling routine is changed. In this state the tissue is said to be preconditioned. Any change of the lower or upper limits of the cycling process requires new preconditioning of the tissue. Preconditioning occurs due to internal changes in the structure of the tissue. Hysteresis, nonlinearity, relaxation and preconditioning are common properties of all soft tissues, although their observed degrees vary.

The difference between the loading and unloading response can be simulated using an isotropic damage formulation. It consists in writing the strain energy in the form of

$$\psi = (1-d)\bar{\psi} + \frac{1}{D}(J^2 - 1) \tag{2.58}$$

where $1-d$ is a reduction factor and d is a scalar damage variable defined in $0 \leq d \leq 1$. When $d = 0$ the material is undamaged. The value $d = 1$ is an upper limit in which the material is completely damaged and failure occurs. The evolution of damage may be described by a function of a maximum equivalent strain defined such as $\zeta^m = \max_{t\in[-\infty,t]}\sqrt{2\bar{\psi}(\mathbf{E}(t)}$ where $\mathbf{E}(t)$ is the Green–Lagrange strain tensor for the pseudotime t of the deformation process. The evolution of damage can be described with an exponential form

$$1 - d(\zeta^m) = \beta + (1-\beta)\frac{1 - e^{-\zeta^m/\alpha}}{\zeta^m/\alpha} \tag{2.59}$$

where α and β are material parameters.

Damage can also be modeled with the concept of softening hyperelasticity. In this concept, instead of having a strain energy tending to infinity when the norm of the stretch tensor tends to infinity, the stored energy is bounded [2].

More details about damage models are given in Chap. 4 of this book.

Time dependent effects The hysteresis in the stress–strain relationship may also show the viscoelastic behavior of soft biological tissue. The simplest model of viscoelasticity is the Kelvin model combining a linear spring and a dashpot. In analogy to linear viscoelasticity in small strain, we can assume an additive free energy potential with the form $\psi = \psi_0 + \psi_v$ where ψ_0 measures the energy stored in the elastic branch (equilibrium) and ψ_v measured the energy stored in the viscous branch, which progressively disappears during relaxation.

In a viscoelastic material the history of strain affects the actually observed stress. As well, loading and unloading occur on different stress–strain paths. The hysteresis of most biological tissues is assumed to show only little dependence on the strain rate within several decades of strain rate variation. This insensitivity to strain rate over several decades is not compatible with simple viscoelastic models consisting for instance of a single spring and dashpot element. With such a simple viscoelasticity approach the material model will show a maximum hysteresis loop at a certain strain rate whereas all other strain rates will show a smaller hysteresis loop. A model consisting of a discrete number of spring-dashpot elements therefore produces a discrete hysteresis spectrum with maximum dissipation at discrete strain rates. It may be written as

$$\bar{\psi} = \int_0^t \left[\left(1 - \sum_{k=1}^{N} g_k(1 - e^{-\frac{t-\tau}{\tau_k}})\right) \times \frac{d\psi_0}{d\tau}\right] d\tau \tag{2.60}$$

where τ_k are the relaxation times and g_k are the relaxation coefficients.

It is widely accepted that soft connective tissues are multiphasic materials. They are sometimes modeled as a mixture of two immiscible constituents: an solid hyperelastic matrix and an interstitial incompressible fluid. This type of models, sometimes called poroelastic models, can particularly describe both the stress distribution and interstitial fluid motion within the cartilage tissue under various loading conditions. Moreover the interaction between the solid and the fluid phases has been identified to be responsible for the apparent viscoelastic properties in the compression of hydrated soft tissues.

Active models It is often assumed that in the presence of an actin-myosin complex in the soft tissue, the total Cauchy stress can be split into two parts: $\boldsymbol{\sigma} = \boldsymbol{\sigma}_p + \boldsymbol{\sigma}_a$, where $\boldsymbol{\sigma}_p$ and $\boldsymbol{\sigma}_a$ denote passive and active stress respectively. The passive stress results from the elastic deformation of the tissue and can be derived from the theory of hyperelasticity. The active stress is generated in myofibrils or in smooth muscle cells by activation and is directed parallel to the fiber orientation. Hence: $\boldsymbol{\sigma}_a = \sigma_a \boldsymbol{\epsilon} \otimes \boldsymbol{\epsilon}$ where $\boldsymbol{\epsilon}$ is the unit vector identifying the orientation. The mechanism for generating σ_a involves internal variables.

2.2.5 Growth and Remodelling Models

Many experiments have shown that the stress field dictates, at least in part, the way in which the microstructure of soft tissues is organized. This observation leads to the concept of functional adaptation wherein it is thought that soft tissues functionally adapt so as to maintain particular mechanical metrics (e.g., stress) near target values. To accomplish this, tissues often develop regionally varying stiffness, strength, and anisotropy.

Models of growth and remodelling necessarily involve equations of reaction diffusion. There has been a trend to embed the reaction diffusion framework within tissue mechanics [3, 4]. The primary assumption is that one models volumetric growth through a growth tensor $\mathbf{F}_g$, which describes changes between two fictitious stress-free configurations: the original body is imagined to be fictitiously cut into small stress-free pieces, each of which is allowed to grow separately via $\mathbf{F}_g$, with $\det(\mathbf{F}_g) \neq 1$. Because these growths need not be compatible, internal forces are often needed to assemble the grown pieces, via $\mathbf{F}_a$, into a continuous configuration. This, in general, produces residual stresses, which are now known to exist in many soft tissues. The formulation is completed by considering elastic deformations, via $\mathbf{F}_a$, from the intact but residually stressed traction-free configuration to a current configuration that is induced by external mechanical loads. The initial boundary value problem is solved by introducing a constitutive relation for the stress response to the deformation $\mathbf{F}_e\mathbf{F}_a$, which is often assumed to be incompressible hyperelastic, plus a relation for the evolution of the stress-free configuration via $\mathbf{F}_g$. Thus, growth is assumed to occur in stress-free configurations and typically not to affect material properties.

Although the previous theory called the theory of kinematic growth yields many reasonable predictions, Humphrey and coworkers have suggested that it models consequences of growth and remodelling, not the processes by which they occur. Growth and remodelling necessarily occur in stressed, not fictitious stress-free, configurations, and they occur via the production, removal, and organization of different constituents; moreover, growth and remodelling need not restore stresses exactly to homeostatic values. Hence, Humphrey and coworkers introduced a conceptually different approach to model growth and remodelling, one that is based on tracking the turnover of individual constituents in stressed configurations (the constrained mixture model [5, 6]).

2.3 Characterization of Hyperelastic Properties Using a Bulge Inflation Test

After the introduction of basics about nonlinear finite–strain constitutive relations, we now introduce approaches of experimental biomechanics and inverse methods aimed at quantifying constitutive parameters of soft tissues.

2.3.1 Introduction

Traditional characterization of material constants in hyperelastic solids The hyperelastic constants in the strain energy density function of a material determine its mechanical response. For identifying these hyperelastic materials, simple deformation tests (consisting of six deformation models—see Fig. 2.1) can be used. It is always recommended to take the data from several modes of deformation over a wide range of strain values.

Even though the superposition of tensile or compressive hydrostatic stresses on a loaded incompressible body results in different stresses, it does not alter deformation of a material. Upon the addition of hydrostatic stresses, the following modes of deformation are found to be identical: uniaxial tension and equibiaxial compression, uniaxial compression and equiaxial tension, and planar tension and planar compression. It reduces to three independent deformation states for which we can obtain experimental data.

For each of the three independent tests, the resultant force F can be expressed analytically with respect to the applied stretch λ using the following formulas of incompresssible hyperelasticity which are derived from the equations introduced above:

1. in uniaxial tension:

$$F = 2S_0(\lambda - \lambda^{-3})\left(\frac{\partial\psi}{\partial I_1} + \frac{\partial\psi}{\partial I_2}\right) \tag{2.61}$$

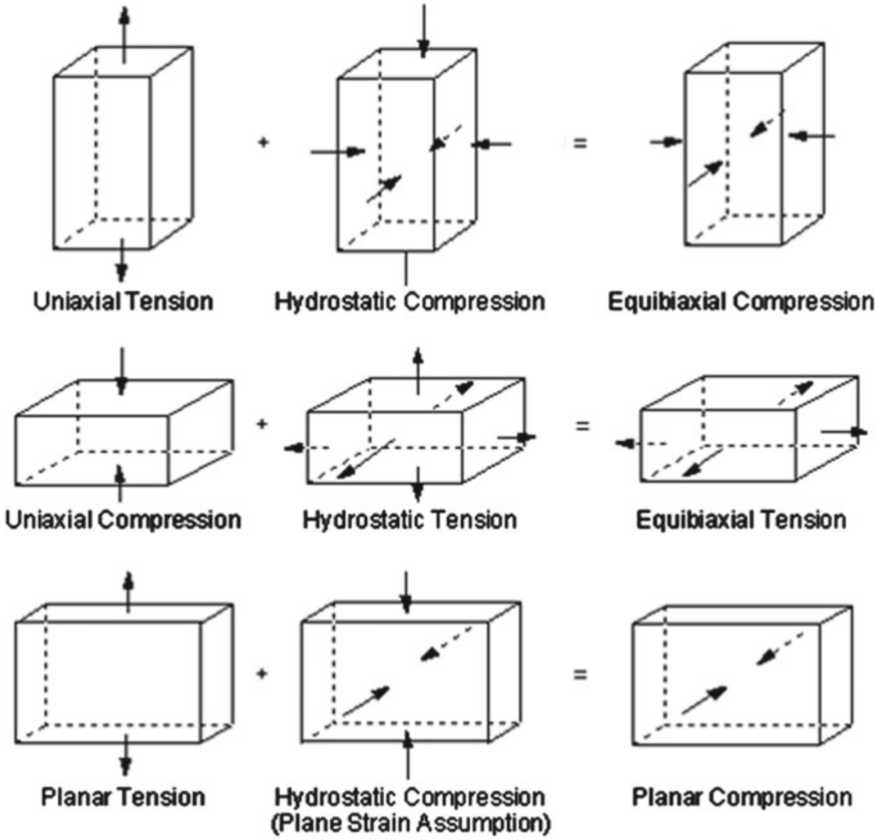

Fig. 2.1 Schematic representation of independent testing modes for hyperelastic materials

2. in planar tension:

$$F = 2S_0(\lambda - \lambda^{-3})\left(\lambda\frac{\partial\psi}{\partial I_1} + \frac{\partial\psi}{\partial I_2}\right) \tag{2.62}$$

3. in equibiaxial tension:

$$F = 2S_0(\lambda - \lambda^{-5})\left(\frac{\partial\psi}{\partial I_1} + \lambda^2\frac{\partial\psi}{\partial I_2}\right) \tag{2.63}$$

where S_0 is the initial cross-sectional area of the sample.

The identification of the material constants is achieved by a least-squares fit analysis which consists in minimizing the sum of squared discrepancies between the experimental values (if any) of F and the values predicted by the models. This yields a set of simultaneous equations which are solved for the material constants.

The identification of material constants is seldom achieved on cylindrical specimens where analytical formulas can also be derived to perform again least-squares fit analysis [7].

The bulge inflation test combined with digital image correlation As introduced previously, traditional characterization of material constants in hyperelastic solids is based on a least-squares fit analysis of F versus λ curves. In the tests, λ is usually measured using traditional extensometry techniques being either based on tracking the motion of the grips in the machine used to apply the deformation on the tissue, sometimes based on tracking the motion of markers or dots drawn on the tissue itself.

Recently, it has become a common practice to combine video based full-field displacement measurements experienced by tissue samples in vitro, with custom inverse methods to infer (using nonlinear regression) the best-fit material parameters and the rupture stresses and strains. These approaches offer important possibilities for fundamental mechanobiology research as they permit to quantify regional variations in properties in situ.

Here we present an illustrative example of the author's experience where bulge inflation tests are carried out on aneurysm samples for characterizing the regional variations of hyperelastic constants across them.

2.3.2 Materials and Methods

Experimental arrangements The study deals with the characterization of aortic tissues collected on patients having an ascending thoracic aortic aneurysm (ATAA). In this reported example, an unruptured ATAA section was collected from a patient undergoing elective surgery to replace his ATAA with a graft in accordance with a protocol approved by the Institutional Review Board of the University Hospital Center of Saint–Etienne. After retrieval, the specimen was placed in saline solution and stored at 4 °C until testing, which occurred within 48 h of the surgery. Immediately prior to testing, the ATAA was cut into a square specimen approximately 45 × 45 mm. Any fatty deposits were removed from the surface of the tissue to ensure that during mechanical testing the tissue did not slip in the clamps. An average thickness was found for the sample by measuring the thickness of the tissue at a minimum of five locations.

The specimen was clamped in the bulge inflation device, Fig. 2.2, so that the luminal side of the tissue faced outward. Then a speckle pattern was applied to the luminal surface using black spray paint. The sample was inflated using a piston driven at 15 mm/min to infuse water into the cavity behind the sample. During the test, the pressure was measured using a digital manometer (WIKA, DG-10). Images of the inflating specimen were collected using a commercial DIC system (GOM, 5M LT) composed of two 8-bit CCD cameras equipped with 50 mm lenses (resolution: 1624 × 1236 px). The cameras were positioned 50 cm apart at an angle of 30° with an aperture of $f/11$. This produced a depth of field of 15.4 mm which was sufficient to

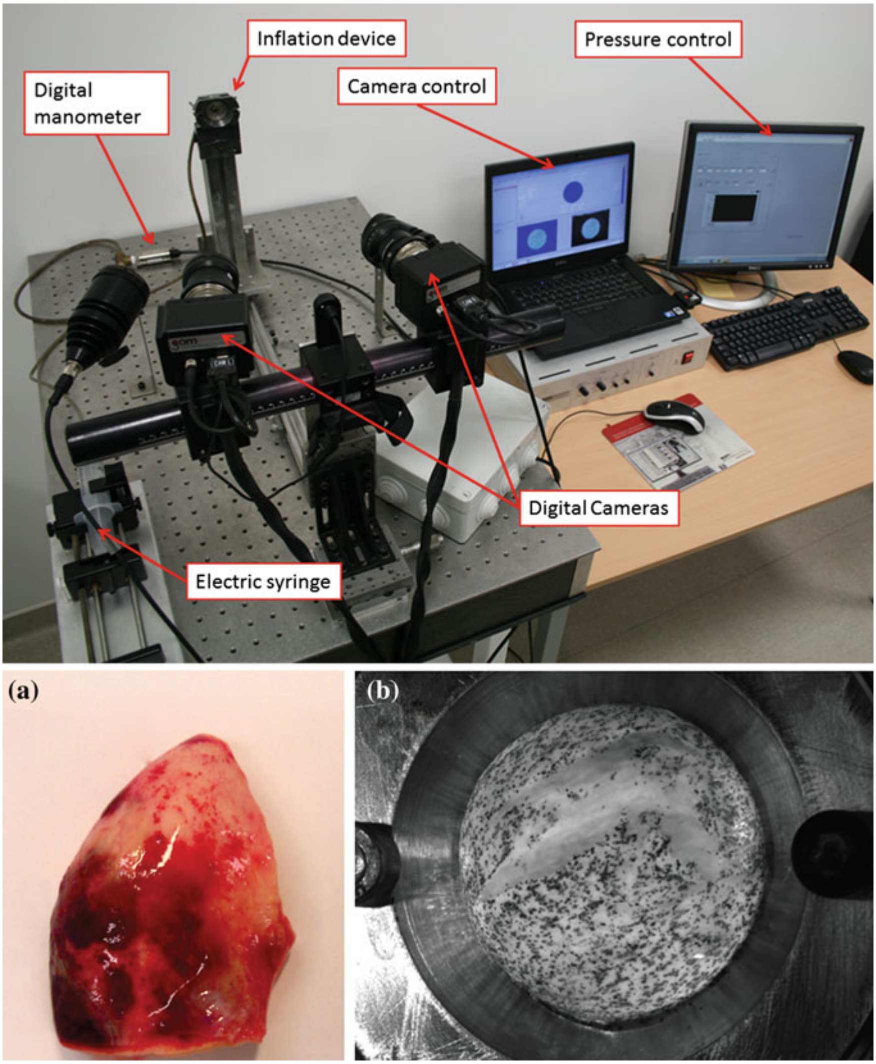

Fig. 2.2 Experimental setup and test sample **a** before testing and **b** after rupture

capture the deformation of the tissue up to failure. Images of the deforming sample were collected every 3 kPa until the sample ruptured.

After rupture, the collected images were analyzed using the commercial correlation software ARAMIS (GOM, v. 6.2.0) to determine the three-dimensional displacement of the tissue surface. For the image analysis, a facet size of 21 px and a facet step of 5 px were chosen based on the speckle pattern dot size, distribution, and contrast. The selected parameters produced a cloud of approximately 15,000 points where the three displacement values were calculated. Details about the error quantification of the method may be found in the original paper [8].

Geometric reconstruction A deforming NURBS mesh was extracted by morphing a NURBS template to the DIC point clouds. The template was a circular domain with a diameter slightly less than that of the point cloud in the first pressure state. The NURBS surface was parameterized as a single patch containing clamped knots of 20 divisions in each parametric direction, with 22 × 22 control points. Since NURBS control points, in general, do not fall on the surface they describe, they cannot be directly derived from the DIC clouds. Instead, the positions of the Gauss points were obtained first using the moving least square method [9]. For each Gauss point, a set of nearest image points in the DIC point cloud were identified based on their distance to the Gauss point in the first pressure state. The radius of the neighboring region was automatically adjusted to that it contained at least six image points. The position of each Gauss point, $\mathbf{y}_g$, was computed using an affine interpolation

$$\mathbf{y}_g = \frac{\sum_{\mathbf{y}\in\Omega_g} w_j \mathbf{y}_j}{\sum_{\mathbf{y}\in\Omega_g} w_j} \tag{2.64}$$

where $\mathbf{y}_j$ is the position vector for each image point in the neighborhood, Ω_g, and w_i is the weighting function taken to be the inverse of the distance from $\mathbf{y}_j$ to the Gauss point. Using the same weights calculated in the first stage, the Gauss points in every pressure stage were identified.

A global least squares problem was then formulated to compute the best-fit positions of the control points. The NURBS surface was represented as

$$\mathbf{x} = \sum_i N_i(u_1, u_2)\mathbf{Q}_i \tag{2.65}$$

where N_i are the NURBS basis functions, $\mathbf{Q}_i$ are the control points, and the pair of knot variables, (u_1, u_2), represent a material point. The position of a modeled Gauss point is then given by $\mathbf{x}_g = \sum_i N_i(u_{1g}, u_{2g})\mathbf{Q}_i$. The position of the control points were obtained by minimizing a weighted sum of $\|\mathbf{x}_g - \mathbf{y}_g\|^2$ over all Gauss points. This procedure was applied to each pressure state.

The accuracy of this reconstruction method was previously assessed and showed by [10].

Strain reconstruction Surface strains were computed in the local NURBS curvilinear coordinate system. The surface coordinates, u_α, $(\alpha, \beta = 1, 2)$ induce a set of convected basis vectors $(\mathbf{a}_1, \mathbf{a}_2)$ where $\mathbf{a}_\alpha = \frac{\partial \mathbf{x}}{\partial \mathbf{u}_\alpha}$ and $\mathbf{x}(u_1, u_2)$ is the NURBS representation given in Eq. 2.65. The reciprocal basis $\left(\mathbf{a}^1, \mathbf{a}^2\right)$ are computed such that $\mathbf{a}_\alpha \cdot \mathbf{a}_\beta = \delta_{\alpha\beta}$. In the reference configuration, the basis vectors are denoted by $(\mathbf{A}_1, \mathbf{A}_2)$ and $\left(\mathbf{A}^1, \mathbf{A}^2\right)$.

The surface deformation gradient tensor is

$$\mathbf{F} = \mathbf{a}_\alpha \otimes \mathbf{A}^\alpha \,. \tag{2.66}$$

It then follows that the surface Cauchy–Green deformation tensor, **C**, and the Green–Lagrangian strain tensor, **E**, are given by

$$\mathbf{C} = \left(\mathbf{a}_\alpha \cdot \mathbf{a}_\beta\right) \mathbf{A}^\alpha \otimes \mathbf{A}^\beta \tag{2.67}$$

$$\mathbf{E} = \frac{1}{2} \left(\mathbf{a}_\alpha \cdot \mathbf{a}_\beta - \delta_{\alpha\beta}\right) \mathbf{A}^\alpha \otimes \mathbf{A}^\beta \,. \tag{2.68}$$

The physical components of **C** and **E** are computed by identifying a local orthonormal basis $(\mathbf{G}_1, \mathbf{G}_2)$ that is constructed in the tangent plane spanned by $(\mathbf{A}_1, \mathbf{A}_2)$. The physical components of the Cauchy–Green deformation tensor, $C_{\alpha\beta}$, and Green–Lagrangian strain tensor, $E_{\alpha\beta}$, are $C_{\alpha\beta} = \mathbf{G} \cdot \mathbf{C}\,\mathbf{G}$ and $E_{\alpha\beta} = \mathbf{G} \cdot \; \mathbf{E}\,\mathbf{G}$, respectively.

Wall stress reconstruction For an inverse membrane boundary value problem the deformed configurations and boundary conditions are given as inputs to the FE model and the wall stress is calculated. The balance equation that governs static equilibrium is [11, 12]

$$\frac{1}{\sqrt{\mathrm{a}}} \left(\sqrt{\mathrm{a}} t^{\alpha\beta} \mathbf{a}_\alpha\right)_{,\beta} + p\mathbf{n} = 0 \tag{2.69}$$

where a is det $\left(\mathbf{a}_\alpha \, \mathbf{a}_\beta\right)$, **t** is the Cauchy wall tension, p is the applied internal pressure, **n** is an outward facing unit normal, and $(\,)_{,\beta}$ indicates $\frac{\partial}{\partial u^\beta}$. Note that the Cauchy wall tension **t** is directly related to the Cauchy stress, $\boldsymbol{\sigma}$, through the current thickness of the membrane, h, via $t^{\alpha\beta} = h\sigma^{\alpha\beta} = t^{\beta\alpha}$.

The weak form of the boundary value problem reads

$$\int_\Omega t^{\alpha\beta} \mathbf{a}_\alpha . \delta \mathbf{x}_{,\beta} \, \mathrm{d}a - \int_\Omega p\mathbf{n} . \delta \mathbf{x} \, \mathrm{d}a = 0, \tag{2.70}$$

where $\delta\mathbf{x}$ is any admissible variation to the current configuration Ω. The details of the FE procedure for solving Eq. 2.70 were presented in [13]. Briefly, the Cauchy wall tension is regarded as a function of the inverse deformation gradient. The weak form subsequently yields a set of nonlinear algebraic equations for the positions of control points in the reference configuration. At the same time, the tension field in the current state is determined. An auxiliary material model is needed to perform the inverse analysis. The material model influences the predicted undeformed configuration; however, due to the static determinacy of Eq. 2.69, the influence is weak [13–16]. As in a previous study [17], a neo-Hookean model was implemented. For computational efficiency, the stiffness parameter of the model was set to unrealistically high values to ensure a robust convergence.

To simulate the experimental boundary conditions the outermost edge of the specimen was fixed. This boundary condition was applied directly to the control points on the outer boundary of the mesh. Applying any displacement-based constraint in the inverse membrane analysis creates a boundary region in the solution where the stresses are inaccurate [13]. To minimize the influence of boundary effect, the outer ring of elements was excluded from further analyses. Since the influence region of each control point spans three elements in each of the two parametric directions, the outer three rings of elements were deemed to be the boundary region. By a retrospective comparison with the forward analysis reported the size of the boundary region was confirmed [18].

Material property identification Using inverse membrane analysis, the stress was calculated at every Gauss point. Combining the stress data with the local surface strains calculated from Eqs. 2.66–2.68, the stress–strain response at every Gauss point in the mesh is known. The local material properties at each Gauss point were then identified by fitting the local stress–strain response to a hyperelastic surface energy density. An anisotropic strain energy function was used, this anisotropy being implemented on the principle of Eq. 2.57. More specifically here, we used a modified form of the strain energy density proposed by Gasser, Ogden, and Holzapfel (GOH) [19] which may be written such as

$$w = \frac{\mu_1}{2}\left(\mathfrak{I}_1 - \ln\left(\mathfrak{I}_2\right) - 2\right) + \frac{\mu_2}{4\gamma}\left(\mathrm{e}^{\gamma(\mathfrak{I}_k - 1)^2} - 1\right) \tag{2.71}$$

where $\mathfrak{I}_1 = \operatorname{tr}\mathbf{C}$ and $\mathfrak{I}_2 = \det\mathbf{C}$ are the principal invariants of the Cauchy–Green deformation tensor and $\mathfrak{I}_\kappa = \mathbf{C}:(\kappa\mathbf{1} + (1-2\kappa)\,\mathbf{M}\otimes\mathbf{M})$ is a compound invariant consisting of isotropic and anisotropic contributions.

Litteraly, Eq. 2.71 models a composite material made a matrix reinforced with fibers. In the compound invariant $\mathfrak{I}_\kappa$, the unit vector $\mathbf{M} = \cos\theta\,\mathbf{G}_1 + \sin\theta\,\mathbf{G}_2$ defines the orientation along which the tissue is stiffest while κ characterizes the degree of anisotropy, varying from 0 to 1. When $\kappa = 0$ it would model a composite with all the fibers perfectly aligned in the direction $\mathbf{M}$ and at $\kappa = 1$ the fibers would be perfectly aligned in the perpendicular direction, $\mathbf{M}^\perp$. Finally, $\kappa = \frac{1}{2}$ models the case where fibers would have no preferential direction (isotropic). The parameters μ_1 and μ_2 are the effective stiffnesses of the matrix and fiber phases, respectively, both having dimensions of force per unit length. The parameter γ is a nondimensional parameter that governs the tissue's strain stiffening response.

The second Piola–Kirchhoff wall tension, $\mathbf{S}$, is written as

$$\mathbf{S} = 2\frac{\partial w}{\partial \mathfrak{I}_1}\mathbf{1} + 2\frac{\partial w}{\partial \mathfrak{I}_2}\mathfrak{I}_2\mathbf{C}^{-1} + 2\frac{\partial w}{\partial \mathfrak{I}_\kappa}\left(\kappa\mathbf{1} + (1-2\kappa)\,\mathbf{M}\otimes\mathbf{M}\right) . \tag{2.72}$$

Substituting Eq. 2.71 into Eq. 2.72 one finds

$$\mathbf{S} = \mu_1\left(\mathbf{1} - \mathbf{C}^{-1}\right) + \mu_2\,\mathrm{e}^{\gamma(\mathfrak{I}_\kappa - 1)^2}\left(\mathfrak{I}_\kappa - 1\right)\left(\kappa\mathbf{1} + (1-2\kappa)\,\mathbf{M}\otimes\mathbf{M}\right) \tag{2.73}$$

noting that the second Piola-Kirchoff wall tension is related to the Cauchy wall tension via $\mathbf{t} = \frac{1}{\sqrt{\mathfrak{I}_2}}\,\mathbf{F}\,\mathbf{S}\,\mathbf{F}^{\mathrm{T}}$.

The values of the model parameters μ_1, μ_2, γ, κ, and θ were determined by minimizing the sum of the squared difference between the stress computed from the inverse membrane analysis and those computed using Eq. 2.73. The nonlinear minimization was solved in Matlab (MathWorks, v. 7.14) where the model parameters were constrained such that: $\mu_1, \mu_2, \gamma > 0$, $0 \leq \theta \leq \frac{\pi}{2}$, and $0 \leq \kappa \leq 1$. Due to the boundary effect in the stress analysis the perimeter ring of elements were excluded from the material parameter identification.

2.3.3 Results

Geometric reconstruction A bulge inflation test to failure was performed on a ATAA collected from a male patient who was 55 years old. The diameter of the aneurysm as determined by pre-surgical CT scan was 55 mm. The mean thickness of the sample was 2.35 mm. The pressure and DIC data during the bulge inflation tests were used to generate a deforming NURBS mesh and identify the local stress–strain response during the bulge inflation test. Using the pointwise stress–strain data, the spatial distribution of the mechanical properties was identified.

Using the experimental DIC point cloud a deforming NURBS mesh was generated of the ATAA sample.

Local stress and strain response Fig. 2.3 shows the distributions of the magnitude of the Cauchy wall tension, $\bar{t}$, and Green–Lagrangian strain, $\overline{E}$, at an applied pressure of 117 kPa for a given ATAA sample. The distribution of wall tension and strain remained similar throughout the inflation of the specimen. In general, at each Gauss point both the normal strains and the planar shear strains were nonzero. To facilitate plotting of the local stress–strain response, the axes of principal strain were identified and the local stresses and strains were rotated into the principal strain axes. In [8], the three components of the wall tension in the principal strain axes, $\tilde{t}_{11}$, $\tilde{t}_{12}$, and $\tilde{t}_{22}$ were

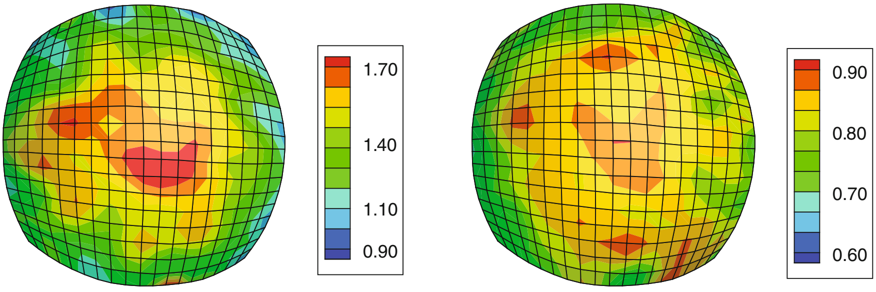

(a) Wall Tension (b) Green-Lagrange strain

Fig. 2.3 Contours of the magnitude of the **a** wall tension (N/m) and **b** Green–Lagrange strain at a pressure of 117 kPa. Adapted from [8] plotted against the principal stretches λ_1 and λ_2. As expected, the local stress–strain response showed the nonlinear stiffening behavior that is common in arteries. The shear stresses, $\tilde{t}_{12}$, were much smaller than the normal stresses, $\tilde{t}_{11}$ and $\tilde{t}_{22}$. In a small region where rupture eventually occurred, the ATAA appeared to yield. The locations of this localized yielding correspond to strain concentrations in zones where rupture initiates (Fig. 2.3b).

Material property identification The proposed model for the elastic behavior of the ATAA was able to fit the bulge inflation data well ($0.81 < R^2 < 0.99$). Lower values of the correlation coefficient were located in the small zone where rupture eventually occurred. Excluding this region the minimum value of R^2 was 0.96. The experimental data (points) and model fits (lines) for three Gauss points were shown in [8].

The distributions of the material parameters are plotted in Fig. 2.4. Clearly the material parameters display a heterogeneous distribution. The parameter μ_1 displayed the sharpest changes in value while the parameters μ_2, κ, and γ changed more gradually. Not surprisingly, the values of μ_2 are an order of magnitude larger than μ_1 reflecting the difference in stiffness between the collagen fibers and matrix. The values of κ are approximately 0.5 in the center suggesting an isotropic organization of the collagen fibers. Towards the edges of the specimen the collagen fibers become more aligned signaling that the sample is regionally anisotropic. In Fig. 2.4e, the angle θ that defines the stiffest direction is plotted. Note that θ is defined locally relative to the horizontal meshlines. Keep in mind that when the value of κ is approximately 0.5, there is no stiffest direction.

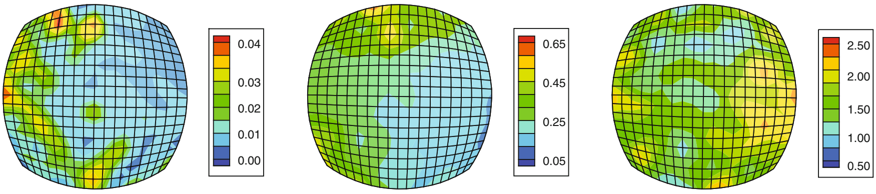

(a) μ_1 (N/mm) (b) μ_2 (N/mm) (c) γ

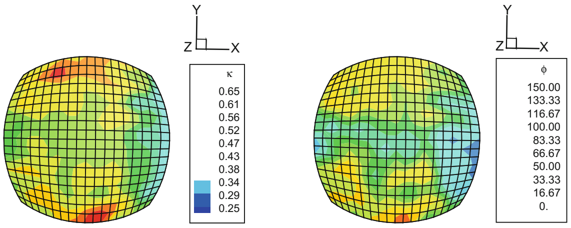

(d) κ (e) θ (rad)

Fig. 2.4 **a** μ_1 (N/mm). **b** μ_2 (N/mm). **c** γ. **d** κ. **e** θ (rad). Distribution of the identified material parameters over the ATAA. Adapted from [8]

This pointwise method was used to identify the distribution of material properties of 10 human ATAA samples [18]. Our method was able to capture the varying levels of heterogeneity in the ATAA from regional to local. The distributions of the material properties for each patient were examined to study the inter- and intra-patient variability. Future studies on the heterogeneous properties of the ATAA would benefit from some form of local structural analysis such as histology or multi-photon microscopy. The structural data and knowledge of the spatial trends should provide the information necessary to move from merely measuring the local material properties to uncovering the links that exist between the underlying microstructure and local properties.

2.4 Characterization of Hyperelastic Material Properties Using a Tension-Inflation Test and the Virtual Fields Method

In the previous section, it was shown that in some cases which are referred to as isostatic, it may be possible to derive the stress distribution independently of the material properties of the tissues. When strain distributions are also available, stress–strain curves can be derived locally and the inverse problem turns into a semi-forward problem [20], where the material parameters can be identified directly by fitting the curves with a model.

In case of hyperstatic situations, it is not possible to derive the stress distribution independently of the material properties of the tissues. A possible solution for the identification of local material properties may still be found using the Virtual Fields Method (VFM). The VFM is one of the techniques developed to identify the parameters governing constitutive equations, the experimental data processed for this purpose being displacement or strain fields. It will be shown in this chapter that one of its main advantages is the fact that, in several cases, the sought parameters can be directly found from the measurements, without resorting to a FE software.

The VFM relies on the Principle of Virtual Power (PVP) which is written with particular virtual fields.

2.4.1 General Principle

The PVP represents in fact the weak form the local equations of equilibrium which are classically introduced in mechanics of deformable media. Assuming a quasi-static transformation (the absence of acceleration forces) and assuming the absence of body forces, the PVP can be written as follows for any domain defined by its volume $\omega(t)$ in the current configuration and by its external boundary $\partial\omega(t)$:

$$\underbrace{-\int_{\omega(t)} \boldsymbol{\sigma} : (\mathbf{Grad}\,\mathbf{v}^{*}) d\omega}_{P^{*}_{int}} + \underbrace{\int_{\partial\omega(t)} \mathbf{t_n}.\mathbf{v}^{*} ds}_{P^{*}_{ext}} = 0 \tag{2.74}$$

where $\boldsymbol{\sigma}$ is the Cauchy stress tensor, $\mathbf{v}^{*}$ is a virtual velocity field defined across the volume of the solid, $\mathbf{Grad}\,\mathbf{v}^{*}$ is the gradient of $\mathbf{v}^{*}$, $\mathbf{t_n}$ are the tractions across the boundary (surface denoted $\partial\omega(t)$), P^{*}_{int} is the virtual power of internal forces and P^{*}_{ext} is the virtual power of external forces.

A very important property is in fact that the equation above is satisfied for any kinematically admissible (KA) virtual field $\mathbf{v}^{\star}$. By definition, a KA virtual field must satisfy the boundary conditions of the actual velocity field in order to cancel the contribution of the resulting forces on the portion of the boundary along which actual displacement are prescribed. It must be pointed out that this requirement is not really necessary in all cases, but this point is not discussed here for the sake of simplicity. KA virtual fields are also assumed to be $\mathcal{C}_0$ functions [21].

2.4.2 Example of Application of the Principle of Virtual Power for Membranes

The PVP may be a powerful tool to derive global or semi-local equilibrium equations which eventually appear useful for the identification of material parameters. Here we illustrate this for deriving a useful equation for a hyperelastic membrane. This is purely for the sake of giving an example, but an infinity of other equations could be derived.

Let us consider a membrane-like structure made of a hyperelastic prestressed tissue. The membrane is defined by a three-dimensional surface, namely defined by a set of points $\mathbf{M}(\xi_1, \xi_2)$, where (ξ_1, ξ_2) are the surface parametric coordinates associated with the local basis $(\mathbf{g}^1, \mathbf{g}^2)$. Vector $\mathbf{g}^1$ points the direction of the maximum principal curvature and vector $\mathbf{g}^2$ points the direction of the minimum principal curvature. The thickness of the membrane is named $h(\xi_1, \xi_2)$ and we denote $\kappa^1(\xi_1, \xi_2)$ and $\kappa^2(\xi_1, \xi_2)$ respectively the maximum and minimum principal curvatures at (ξ_1, ξ_2).

There is no particular assumption related to the thickness of the membrane but it is assumed that through-thickness shear is negligible. A third coordinate ξ_3 is introduced along the direction normal to the surface (through-thickness coordinate), with $\xi_3 = 0$ at the inner surface and $\xi_3 = 1$ at the outer surface.

Let us consider a quadrilateral patch across the membrane surface. This patch is denoted n and we will apply the PVP on its volume. For that, the following virtual field u^* is defined across the given patch n:

$$\mathbf{u}^*(\xi_3) = \frac{(1/\kappa_n^1 - h)(1/\kappa_n^2 - h)(1/\kappa_n^1 + 1/\kappa_n^2 - 2h)}{(1/\kappa_n^1 - (1-\xi)h)(1/\kappa_n^2 - (1-\xi)h)}\,\mathbf{n}_n \tag{2.75}$$

where $1/\kappa_n^1$ is the average radius of curvature on the outer surface along the direction of the maximum principal curvature and $1/\kappa_n^2$ is the average radius of curvature on the outer surface along the direction of the minimum principal curvature. The radii of curvature at any position ξ_3 between the inner ($\xi_3 = 0$) and outer ($\xi_3 = 1$) surfaces are then $(1/\kappa_n^1 - (1-\xi_3)h)$ and $(1/\kappa_n^2 - (1-\xi_3)h)$. Vector $\mathbf{n}_n$ points the direction normal to the surface.

The gradient of $\mathbf{u}^*$ may be written as follows:

$$\begin{aligned}
\mathbf{Grad}\,\mathbf{u}^*(\xi_3) = {} & \left[\frac{(1/\kappa_n^1 - h)(1/\kappa_n^2 - h)(1/\kappa_n^1 + 1/\kappa_n^2 - 2h)}{(1/\kappa_n^1 - (1-\xi_3)h)^2(1/\kappa_n^2 - (1-\xi_3)h)}\right]\mathbf{g}_n^1 \otimes \mathbf{g}_n^1 \\
& + \left[\frac{(1/\kappa_n^1 - h)(1/\kappa_n^2 - h)(1/\kappa_n^1 + 1/\kappa_n^2 - 2h)}{(1/\kappa_n^1 - (1-\xi_3)h)(1/\kappa_n^2 - (1-\xi_3)h)^2}\right]\mathbf{g}_n^2 \otimes \mathbf{g}_n^2 \\
& - \left[\frac{(1/\kappa_n^1 - h)(1/\kappa_n^2 - h)(1/\kappa_n^1 + 1/\kappa_n^2 - 2h)}{(1/\kappa_n^1 - (1-\xi_3)h)^2(1/\kappa_n^2 - (1-\xi_3)h)}\right. \\
& \left. + \frac{(1/\kappa_n^1 - h)(1/\kappa_n^2 - h)(1/\kappa_n^1 + 1/\kappa_n^2 - 2h)}{(1/\kappa_n^1 - (1-\xi_3)h)(1/\kappa_n^2 - (1-\xi_3)h)^2}\right]\mathbf{n}_n \otimes \mathbf{n}_n
\end{aligned} \tag{2.76}$$

Plugging in and evaluating the integral expression for P^*_{int} (cf. Eq. 2.74)

$$\begin{aligned}
P^*_{int}(t) = {} & -h(t)(1/\kappa_n^1(t) - h(t))(1/\kappa_n^2(t) - h(t))(1/\kappa_n^1(t) + 1/\kappa_n^2(t) - 2h(t)) \\
& \int_0^1 \left[\frac{\sigma^w_{11,n}(t,\xi_3) - \sigma^w_{33,n}(t,\xi_3)}{(1/\kappa_n^1 - (1-\xi_3)h)^2(1/\kappa_n^2 - (1-\xi_3)h)}\right. \\
& \left. + \frac{\sigma^w_{22,n}(t,\xi_3) - \sigma^w_{33,n}(t,\xi_3)}{(1/\kappa_n^1 - (1-\xi_3)h)(1/\kappa_n^2 - (1-\xi_3)h)^2}\right] A_n(t,\xi_3)\,\mathrm{d}\xi_3
\end{aligned} \tag{2.77}$$

where $A_n(t, \xi_3)$ is the area of patch n at radial position ξ_3 and may be written

$$A_n(t,\xi_3) = (1/\kappa_n^1(t) - (1-\xi_3)h(t))(1/\kappa_n^2(t) - (1-\xi_3)h(t))\Theta_n^1(t)\Theta_n^2(t) \tag{2.78}$$

where Θ_n^1 and Θ_n^2 are two angles defining the angular sector of patch n along the directions of the maximum and minimum principal curvatures, respectively. Introducing the expression of $A_n(t, \xi_3)$ into Eq. 2.77, we obtain

$$P^*_{int}(t) = -h(t)(1/\kappa^1_n(t) - h(t))(1/\kappa^2_n(t) - h(t))(1/\kappa^1_n(t) + 1/\kappa^2_n(t) - 2h(t))$$
$$\Theta^1_n(t)\Theta^2_n(t) \int_0^1 \left[\frac{\sigma^w_{11,n}(t,\xi_3) - \sigma^w_{33,n}(t,\xi_3)}{(1/\kappa^1_n - (1-\xi_3)h)} + \frac{\sigma^w_{22,n}(t,\xi_3) - \sigma^w_{33,n}(t,\xi_3)}{(1/\kappa^2_n - (1-\xi_3)h)} \right] \mathrm{d}\xi_3 \tag{2.79}$$

Regarding the virtual work on the boundaries, shear stresses are null so only the virtual work of the internal pressure needs to be considered

$$P^*_{ext}(t) = P(t)(1/\kappa^1_n(t) - h(t))(1/\kappa^2_n(t) - h(t))\Theta^1_n(t)\Theta^2_n(t)$$
$$(1/\kappa^1_n(t) + 1/\kappa^2_n(t) - 2h(t)) \tag{2.80}$$

so combining all the equations we have

$$P(t) = h(t) \int_0^1 \left[\frac{\sigma^w_{11,n}(t,\xi_3) - \sigma^w_{33,n}(t,\xi_3)}{(1/\kappa^1_n - (1-\xi_3)h)} + \frac{\sigma^w_{22,n}(t,\xi_3) - \sigma^w_{33,n}(t,\xi_3)}{(1/\kappa^2_n - (1-\xi_3)h)} \right] \mathrm{d}\xi_3 \tag{2.81}$$

Finally the obtained equation is a generalized expression of the traditional Laplace law commonly used in biomechanics of soft tissues [22].

2.4.3 Identification of Hyperelastic Parameters Using the VFM

The principle of virtual power (PVP) has been used for the identification of material properties since 1990 through the virtual fields method (VFM), which is an inverse method based on the use of full-field deformation data [21, 23, 24]. The VFM was recently applied to the identification of uniform material properties in arterial walls [23].

The first step of the VFM consists in introducing the constitutive equations. In the case of hyperelasticity, Eq. 2.74 becomes

$$-\int_{\omega(t)} \left(J^{-1}\mathbf{F}\frac{\partial\psi}{\partial\mathbf{E}}\mathbf{F}^T \right) : (\mathbf{Grad}\,\mathbf{v}^*)d\omega + \int_{\partial\omega(t)} \mathbf{t_n}.\mathbf{v}^* ds = 0 \tag{2.82}$$

This equation being satisfied for any KA virtual field, any new KA virtual field provides a new equation. The VFM relies on this property by writing Eq. 2.82 above with a set of KA virtual fields chosen a priori [25]. The number of virtual fields and their type depend on the nature of the strain energy function. Two different cases can be distinguished.

- **Case #1**: the strain energy density function depends linearly on the sought parameters. Writing Eq. 2.82 with as many virtual fields as unknowns leads to a system of linear equations which provides the sought parameters after inversion.
- **Case #2**: the strain energy density function involve nonlinear relations with respect to the constitutive parameters. In this case, identification must be performed by minimizing a cost function derived from Eq. 2.82.

Let us illustrate this with the strain energy function of Eq. 2.71. It provides a membrane constitutive equation, *i.e.* it yields the tension and not the Cauchy stress so the integrals will be written across a given surface $\nu(t)$ figuring a portion of the membrane

$$\begin{aligned}
&-\mu_1 \int_{\nu(t)} \frac{1}{\sqrt{\Im_2}} \left(\mathbf{B} - \sqrt{\Im_2}\mathbf{1}\right) : (\mathbf{Grad}\,\mathbf{v}^*) d\nu \\
&\quad - \mu_2 \kappa \int_{\nu(t)} \frac{1}{\sqrt{\Im_2}} \mathrm{e}^{\gamma(\Im_\kappa - 1)^2} (\Im_\kappa - 1)\, \mathbf{B} : (\mathbf{Grad}\,\mathbf{v}^*) d\nu \\
&- \mu_2 (1 - 2\kappa) \int_{\nu(t)} \frac{1}{\sqrt{\Im_2}} \mathrm{e}^{\gamma(\Im_\kappa - 1)^2} (\Im_\kappa - 1) \left(\mathbf{FM} \otimes \mathbf{MF}^T\right) : (\mathbf{Grad}\,\mathbf{v}^*) d\nu \\
&\qquad + \int_{\nu(t)} \mathbf{t_n}.\mathbf{v}^* dl = 0 \qquad (2.83)
\end{aligned}$$

The equation may be rewritten such as

$$\mu_1 A_{ij} + \mu_2 \kappa B_{ij}(\gamma) + \mu_2 (1 - 2\kappa) C_{ij}(\gamma, \theta) = L_{ij} \qquad (2.84)$$

where A_{ij}, B_{ij}, C_{ij} and L_{ij} can be evaluated directly from the experimental measurements. Index i is for different possible choices of virtual fields and index j is for different possible stages of the experiment for which deformations and loads are measured.

Equation 2.84 is an equation of the unknown material parameters for each choice of virtual field i and at every stage j of the test. The equation is linear in μ_1, $\mu_2\kappa$ and $\mu_2(1 - 2\kappa)$ but it is nonlinear in γ and θ. The solution is found by minimizing a cost function defined such as

$$\sum_i \sum_j \left(\mu_1 A_{ij} + \mu_2 \kappa B_{ij}(\gamma) + \mu_2 (1 - 2\kappa) C_{ij}(\gamma, \theta) - L_{ij}\right)^2 \qquad (2.85)$$

This cost function can be minimized by the simplex method or using a genetic algorithm in case of multiple minima. The chosen virtual fields and other details about the experiments can be found in [23, 26] for applications to blood vessels.

A recent extension of the method was proposed for the inverse characterization of regional, nonlinear, anisotropic properties of the murine aorta [27]. Full-field biaxial data were collected using a panoramic-digital image correlation system and the VFM was used to estimate values of material parameters regionally for a microstructurally motivated constitutive relation. The experimental-computational approach was validated by comparing results to those from standard biaxial testing. Results for the non-diseased suprarenal abdominal aorta from apolipoprotein-E null mice revealed material heterogeneities, with significant differences between dorsal and ventral as well as between proximal and distal locations, which may arise in part due to differential perivascular support and localized branches. Overall results were validated for both a membrane and a thick-wall model that delineated medial and adventitial properties.

Whereas full-field characterization can be useful in the study of normal arteries, we submit that it will be particularly useful for studying complex lesions such as aneurysms. Indeed, many vascular disorders, including aortic aneurysms and dissections, are characterized by localized changes in wall composition and structure. Notwithstanding the importance of histopathologic changes that occur at the microstructural level, macroscopic manifestations ultimately dictate the mechanical functionality and structural integrity of the aortic wall. Understanding structure–function relationships locally is thus critical for gaining increased insight into conditions that render a tissue susceptible to disease or failure.

2.5 Conclusion

In this chapter, after a brief review of the constitutive relations commonly used for soft tissues, two recent developments of the author's experience were presented to illustrate the potential of digital image correlation and inverse methods in experimental biomechanics of soft tissues.

The inverse problems, including the semi-forward problems [20], posed by the identification of material properties in soft biological tissues are not the simplest due to the complex microstructure of soft biological tissues, their finite range of deformation, their inter-individual variability, their anisotropy, their point-dependent nonlinear behavior, and their permanent functional adaptation to the environment. Determining the mechanical properties of such tissues has nevertheless become a field of intense research since stress analysis in the tissues has been shown to be meaningful for medical diagnosis in a number of medical applications as for instance in the context of vascular medicine, indicating the risk of rupture of an aneurysm [28] or the risk of stroke [29].

The current chapter has focused on in vitro characterization. The in vivo identification of soft tissues present other important issues. They suppose both the existence of reliable experimental facilities for inducing a mechanical stimulus (natural blood pressure variations, local external compression, shear waves [30]) and the existence of imaging devices for measuring the response of tissues (Ultrasound Imaging [31], Magnetic Resonance Imaging [32] or Optical Coherence Tomography [33]). In all these situations where some elements of the response of soft tissues subjected to mechanical stimuli are measured, the access to the mechanical parameters is never direct and inverse problems have to be posed and solved. The inverse problems posed by the in vivo identification of soft tissues will be discussed more specifically in Chaps. 5 and 6 of this book.

Acknowledgments The author of this chapter would like to thank all the students and colleagues who participated to cited studies: Aaron Romo, Pierre Badel, Frances Davies, Ambroise Duprey, Jean-Pierre Favre, Olfa Trabelsi, Yuanming Luo, Jia Lu, Matt Bersi, Chiara Bellini, Katia Genovese, Jay Humphrey.

References

1. Millard, F. B. (1987). Topics in finite elasticity: Hyperelasticity of rubber, elastomers, and biological tissues with examples. *Applied Mechanics Reviews*, *40*(12), 1699–1734.
2. Volokh, K. Y. (2011). Modeling failure of soft anisotropic materials with application to arteries. *Journal of the Mechanical Behaviour of Biomedical Materials*, *4*(8), 1582–1594.
3. Barocas, V. H., & Tranquillo, R. T. (1997). An anisotropic biphasic theory of tissue-equivalent mechanics: The interplay among cell traction, fibrillar network deformation, fibril alignment, and cell contact guidance. *Journal of Biomechanical Engineering*, *119*(2), 137–145.
4. Tözeren, A., & Skalak, R. (1988). Interaction of stress and growth in a fibrous tissue. *Journal of Theoretical Biology*, *130*(3), 337–350.
5. Humphrey, J. D., & Rajagopal, K. R. (2002). A constrained mixture model for growth and remodeling of soft tissues. *Mathematical Models and Methods in Applied Sciences*, *12*(03), 407–430.
6. Baek, S., Rajagopal, K. R., & Humphrey, J. D. (2006). A theoretical model of enlarging intracranial fusiform aneurysms. *Journal of Biomechanical Engineering*, *128*(1), 142–149.
7. Humphrey, J. D. (2013). *Cardiovascular solid mechanics: Cells, tissues, and organs*. Springer Science & Business Media.
8. Davis, F. M., Luo, Y., Avril, S., Duprey, A., & Lu, J. (2015). Pointwise characterization of the elastic properties of planar soft tissues: Application to ascending thoracic aneurysms. *Biomechanics and Modeling in Mechanobiology*, *14*(5), 967–978.
9. Belytschko, T., Liu, W. K., Organ, D., Fleming, M., & Krysl, P. (1996). Meshless methods: An overview and recent developments. *Computer Methods in Applied Mechanics and Engineering*, *139*, 3–47.
10. Lu, J. (2011). Isogeometric contact analysis: Geometric basis and formulation for frictionless contact. *Computer Methods in Applied Mechanics and Engineering*, *200*(5–8), 726–741.
11. Green, A. E., & Adkins, J. E. (1970). *Large elastic deformations*. Oxford: Clarendon Press.
12. Lu, J., Zhou, X. L., & Raghavan, M. L. (2007). Computational method for inverse elastostatics for anisotropic hyperelastic solids. *International Journal for Numerical Methods in Engineering*, *69*, 1239–1261.
13. Lu, J., Zhou, X., & Raghavan, M. L. (2008). Inverse method of stress analysis for cerebral aneurysms. *Biomechanics and modeling in mechanobiology*, *7*(6), 477–486.
14. Zhao, X., Raghavan, M. L., & Lu, J. (2011). Identifying heterogeneous anisotropic properties in cerebral aneurysms: A pointwise approach. *Biomechanics and Modeling in Mechanobiology*, *10*(2), 177–189.
15. Miller, K., & Lu, J. (2013). On the prospect of patient-specific biomechanics without patient-specific properties of tissues. *Journal of the Mechanical Behavior of Biomedical Materials*, *27*, 154–166.
16. Lu, J., Hu, S., & Raghavan, M. L. (2013). A shell-based inverse approach of stress analysis in intracranial aneurysms. *Annals of biomedical engineering*, *41*(7), 1505–1515.

17. Genovese, K., Casaletto, L., Humphrey, J. D., & Lu, J. (2014). Digital image correlation-based point-wise inverse characterization of heterogeneous material properties of gallbladder in vitro. *Proceedings of Royal Society A*, *470*(2167).
18. Davis, F. M., Luo, Y., Avril, S., Duprey, A., & Lu, J. (2016). Local mechanical properties of human ascending thoracic aneurysms. *Journal of the Mechanical Behaviour of Biomedical Materials* (Accepted).
19. Christian, T. C., Ogden, R. W., & Holzapfel, G. A. (2006). Hyperelastic modelling of arterial layers with distributed collagen fibre orientations. *Journal of the Royal Society Interface*, *3*(6), 15–35.
20. Morin, C.. & Avril, S. (2015). Inverse problems in the mechanical characterization of elastic arteries. In *MRS Bulletin* (vol. 40). Materials Research Society.
21. Pierron, F., & Grédiac, M. (2012). *The virtual fields method: extracting constitutive mechanical parameters from full-field deformation measurements*. Springer Science & Business Media.
22. Fung, Y. -C. (2013). *Biomechanics: mechanical properties of living tissues*. Springer Science & Business Media.
23. Avril, S., Badel, P., & Duprey, A. (2010). Anisotropic and hyperelastic identification of in vitro human arteries from full-field optical measurements. *Journal of Biomechanics*, *43*(15), 2978–2985.
24. Avril, S., Bonnet, M., Bretelle, A.-S., Grediac, M., Hild, F., Ienny, P., et al. (2008). Overview of identification methods of mechanical parameters based on full-field measurements. *Experimental Mechanics*, *48*(4), 381–402.
25. Grédiac, M. (1989). Principe des travaux virtuels et identification. *Comptes Rendus de l Académie des Sciences*, 1–5 (In French with abridged English version).
26. Kim, J.-H., Avril, S., Duprey, A., & Favre, J.-P. (2012). Experimental characterization of rupture in human aortic aneurysms using full-field measurement technique. *Biomechanics and Modeling in Mechanobiology*, *11*(6), 841–854.
27. Bersi, M. R., Bellini, C., Achille, P. D., Humphrey, J. D., Genovese, K., & Avril, S. (2016). Novel methodology for characterizing regional variations in material properties of murine aortas. *Journal of Biomechanical Engineering* (In press).
28. Fillinger, M. F., Marra, S. P., Raghavan, M. L., & Kennedy, F. E. (2003). Prediction of rupture risk in abdominal aortic aneurysm during observation: Wall stress versus diameter. *Journal of Vascular Surgery*, *37*(4), 724–732.
29. Li, Z.-Y., Howarth, S. P. S., Tang, T., & Gillard, J. H. (2006). How critical is fibrous cap thickness to carotid plaque stability? A flow-plaque interaction model. *Stroke*, *37*(5), 1195–1199.
30. Frauziols, F., Molimard, J., Navarro, L., Badel, P., Viallon, M., Testa, R., et al. (2015). Prediction of the biomechanical effects of compression therapy by finite element modeling and ultrasound elastography. *IEEE Transactions on Biomedical Engineering*, *62*(4), 1011–1019.
31. Bercoff, J., Tanter, M., & Fink, M. (2004). Supersonic shear imaging: A new technique for soft tissue elasticity mapping. *IEEE Transactions on Ultrasonics, Ferroelectrics and Frequency Control*, *51*(4), 396–409.
32. Bensamoun, S. F., Ringleb, S. I., Littrell, L., Chen, Q., Brennan, M., Ehman, R. L., et al. (2006). Determination of thigh muscle stiffness using magnetic resonance elastography. *Journal of Magnetic Resonance Imaging*, *23*(2), 242–247.
33. Yabushita, H., Bouma, B. E., Houser, S. L., Aretz, H. T., Jang, I.-K., Schlendorf, K. H., et al. (2002). Characterization of human atherosclerosis by optical coherence tomography. *Circulation*, *106*(13), 1640–1645.

Chapter 3
How Can We Measure the Mechanical Properties of Soft Tissues?

Sam Evans

Abstract Measuring the mechanical properties of soft tissues presents three interlinked problems. First, we must carry out experimental measurements to quantify the actual behaviour of the tissue. Second, we need to represent this by some kind of mathematical model, which typically has to be solved using numerical techniques such as the finite element (FE) method. Third, we need to find the parameter values in the model that best match the experiment and to quantify the uncertainty in the resulting material properties. Experimental measurements present numerous difficulties in comparison with conventional engineering materials and care is needed in the choice of test method, sample selection and preparation, calibration and interpretation of the results. Typically an optical technique may be needed to measure the deformation, such as digital image correlation (DIC). FE models of soft tissues are inherently difficult to solve because of their extreme nonlinearity and the typical stiffening behaviour with increasing deformation which leads to numerical instabilities. Possible ways to reduce convergence problems and increase the reliability of these models are discussed. The most common method to find the parameter values that match an experiment is to use an optimisation algorithm to try to find the parameters that best match the experimental results. However this is slow and there is no way of knowing whether the best parameters have been found or what range of other values could also be compatible with the experiment. A better approach is to generate a statistical emulator that predicts the result of the model and then to evaluate a wide range of parameter values in order to find the range of values that could be compatible with the experiment. This gives revealing insights into the uncertainty of the procedure and the validity of the final results.

S. Evans (✉)
School of Engineering, Cardiff University, Cardiff, Wales, UK
e-mail: EvansSL6@cardiff.ac.uk

S. Avril and S. Evans (eds.), *Material Parameter Identification and Inverse Problems in Soft Tissue Biomechanics*, CISM International Centre for Mechanical Sciences 573, DOI 10.1007/978-3-319-45071-1_3

3.1 Introduction

Measuring the mechanical properties of soft tissues is a complex problem. A fundamental difficulty is to decide what the properties are that we want to measure. Material properties in a quantitative sense are parameters in a mathematical constitutive model (for example, Young's modulus is a parameter in Hooke's Law), and in general we do not have good constitutive models that fully describe the behaviour of soft tissues. Indeed it is possible that we will never have such models, since the structure and behaviour of soft tissues is so complex; a model that fully describes a tissue's behaviour might have so many unknown parameters that it would be impossible to measure them all. We therefore need to make an intelligent choice of a model that will describe the behaviour of the material sufficiently well for the purpose we have in mind, while having a minimum of parameters to measure, and then to bear in mind that it will never be a precisely accurate representation of the behaviour of the actual material. We will need to be aware of its limitations in using it and to be careful to validate it as far as possible through experimental observations.

Having chosen an appropriate constitutive model, we then need to do three things. First, we will need to carry out some experimental measurements, and this raises a number of theoretical and practical challenges. Second, we need some kind of mathematical model of the experiment, and for all but the simplest experimental designs and constitutive models this is likely to require a numerical solution, typically using FE techniques. Third, we need a way to extract the material parameters from the combination of the experiment and the mathematical model, and if possible to quantify the uncertainty in the results. This chapter will discuss each of these three aspects and present some examples of possible techniques.

3.2 Experimental Measurements

There are several particular problems that must be considered when testing soft tissues that do not arise when carrying out conventional tests on engineering materials. For engineering materials the conventional test methods have evolved over many years in order to address these problems, but the same approaches and solutions do not typically apply when testing different materials and there are many things that are taken for granted in testing conventional engineering materials but which must be considered properly when testing soft tissues.

A fundamental problem in testing any biological material is that they are much more variable than engineering materials (where a great deal of effort goes into making them as consistent as possible) and so much more care is needed in selecting samples to make sure they are representative and carrying out multiple measurements and statistical analysis to assess their variability and its implications for the conclusions that can be drawn. This is of course true for all biological measurements and biologists have evolved methods to address these problems. It is highly informative for any engineer to spend time with biologists and see their approach to experimental work. They take great care in selecting their subjects, often in terms of parameters such as age, sex, body mass, activity levels, diet, and other factors that might be expected to influence the results, and they will document these parameters for future comparison as well as trying to make sure that groups to be compared are similar or even matched between groups. It would not be expected that the same material would have the same properties at different anatomical sites. Multiple samples are always needed and it would be usual also to repeat the entire experiment at least once and make sure that the results are consistent. Standards for testing metals typically require a minimum of five samples and this is about the smallest number that can give a reasonable sense of the variability of the material and hence the uncertainty in the results. To obtain meaningful comparisons between biological samples much larger numbers are needed, often tens or even hundreds of measurements to detect small differences in variable populations, and an appropriate statistical analysis is absolutely essential. Every factor that could conceivably have an influence is kept constant between experiments, and the accuracy and repeatability of measurements is checked thoroughly and regularly. This is also a useful exercise when using engineering testing equipment, as even apparently accurate devices such as load cells can frequently produce significant errors and other measurements such as the displacement of a testing machine are often not calibrated and may be quite different from the actual relative displacement of the grips or the ends of the sample.

Preparing samples of biological materials presents significant difficulties as it is not easy to cut them accurately to a particular shape. Cutting forces cause significant distortion and it is often unclear what is the unloaded free shape of the material anyway. Methods such as indentation tests which do not require such preparation can have significant advantages in this respect. Cutting materials which have large scale structures such as fibres often significantly alters their properties and this also is an argument for testing materials intact rather than cutting specimens from them. A further issue to consider in preparing specimens is that the material is often inhomogenous and anisotropic and so the position and orientation of the specimen within the sample must be carefully considered and defined.

A very important question to consider is the environment, both during the transport, preparation, and storage of the specimens and during the actual testing. Soft tissues are likely to be sensitive to temperature and hydration and also to factors such as the concentration of electrolytes which may cause swelling or dehydration. Preservation of samples is difficult as freezing or chemical fixation are likely to cause significant changes in mechanical properties. For these reasons it is advantageous to test tissues *in situ* in living subjects although this introduces other complications.

The choice of test configuration is also important. In metals, a tensile test will effectively predict behaviour in compression, shear or other situations, since the mathematical models that are used correctly describe what happens under different types of loading. For soft tissues this is generally not the case; data from tensile tests will not necessarily correctly predict behaviour in compression or vice versa. Similarly the models that are currently used may not correctly describe what will happen under multiaxial loading. It is therefore a good idea wherever possible to test in a similar loading configuration to the actual application (this is also the case for some engineering materials such as polymers).

For some simple tests such as uniaxial tensile tests, it may be possible to calculate the material properties directly from the load-displacement data, though this comes at the cost of greater difficulties in preparing accurate, parallel specimens. For more complicated geometries it will probably be necessary to use a computational model to derive the material properties from the experimental data. Note though that even for such apparently simple tests there may be complications. For example, Legerlotz et al. [1] showed that in tensile tests on tendons the interior of the specimen slides relative to the outside where it is gripped and it is difficult to obtain uniform tension except in very long, thin specimens.

Tensile tests are widely used for engineering materials but have some limitations for soft tissues. Gripping the specimens is difficult and many researchers resort to measures such as freezing the specimens to the grips or using adhesives. The fundamental problem is that the specimens are not only slippery but have a high Poisson's ratio and undergo large strains, so that as they are stretched they become much thinner and slip out of the grips. Using wedge or pneumatic grips that will tighten as the specimen contracts is much more effective than using screw clamps. Clamping the specimen for a time before testing to squeeze out water can also be helpful. Whichever of these measures is used, the grips will have an effect on the properties and may cause a stress concentration and premature failure. This can be alleviated by making specimens with wider ends but this may not be effective where the material is very anisotropic.

Compression tests are challenging because the specimens must be short to avoid buckling, but this leads to significant effects of friction between the specimen and the platens. This constrains the ends of the specimen so they do not expand as much as they would in pure compression, causing barrelling and inaccurate results. It is possible to compensate for this by modelling the test but this requires assumptions about the friction. Another type of compression test, often used for cartilage, confines the specimen in a cylinder with porous platens that allow fluid to flow through them. Theoretically this leads to 1D deformation and fluid flow and an analytical solution is possible, although in practice there are again issues with unknown friction between the specimen and the cylinder.

A more satisfactory alternative may be to use an indentation test, which is much less sensitive to friction. For homogenous materials analytical solutions are available [2]; for more complex materials it may be possible to estimate the properties at different depths using different sizes or shapes of indenters [3]. Fundamentally only a limited amount of information is available from the load-displacement curve and this limits what can be learned from the test; using additional strain measurements may allow more information to be extracted [4]. The test is sensitive to the stiffness (for example the Young's modulus) but insensitive to the Poisson's ratio, which is useful for measuring the stiffness but unhelpful if the Poisson's ratio is also needed, and it clearly has serious limitations for anisotropic materials. A major advantage of indentation tests is that they require minimal specimen preparation and so they are often used for *in situ* tests on living tissue. A suction test where the tissue is drawn into an aperture is similar to an inverted indentation test and shares many of the same advantages and disadvantages [5].

An interesting method for testing tissues that are commonly under biaxial tension, for example aneurysms, is to clamp a circular specimen around its edges and inflate it with a fluid pressure applied to one side [6]. In its most sophisticated form, the curvature and strain distribution can be measured using optical methods and the curvature can be used to calculate the stress, allowing the full stress strain curve to be mapped out locally across the tissue.

3.3 Strain Measurement

When testing materials, it is often necessary to use some kind of additional strain measurement if accurate stiffness measurements are to be obtained. Accurate results cannot be obtained from the machine displacement alone as this will include extra deflections due to the load cell stretching, the frame of the machine itself deforming, and the grips and the ends of the specimens deforming as well as the actual gauge length to be tested. Often this can add several millimetres of extra deformation with the result that the stiffness of the specimen may be severely underestimated. When testing metals, this is usually done by attaching an extensometer to the specimen, but these cannot normally be attached to soft tissue specimens and in any case would be much too heavy. An optical method is best to avoid applying additional loads to the specimen. Alternatives include simple camera systems, dedicated video extensometers, motion analysis systems, and DIC. In all cases careful preparation and calibration is essential as is careful camera setup. All these techniques rely on good quality images.

An example of a camera-based system was presented by Screen and Evans [7]. A tendon sample was loaded in tension and held at a constant displacement while monitoring stress relaxation. The cells were stained and the tendon was observed using a confocal microscope. This produced a series of images (Fig. 3.1) which were then thresholded to identify the cells which were tracked using a Matlab-based tracking programme. The cells were thus used as markers to track the deformation of the tissue. In order to calculate the strain, the cell centroids were meshed with a triangular Delaunay mesh and the strain was calculated using the usual FE mathematical approach. This approach produced accurate displacement measurements of a modest number of points and therefore a coarse strain measurement, which was sufficient to demonstrate the very large inhomogeneities that were present but not enough to show the full strain field in detail.

Another method that has some advantages is to use a commercial motion capture system, with different lenses if necessary to work at a shorter distance with a higher magnification. An example was presented by Mahmud et al. [8], where deformation of the skin on the arm was measured using a Qualisys motion capture system. Markers were punched from self -adhesive retroreflective tape and attached to the skin. It is

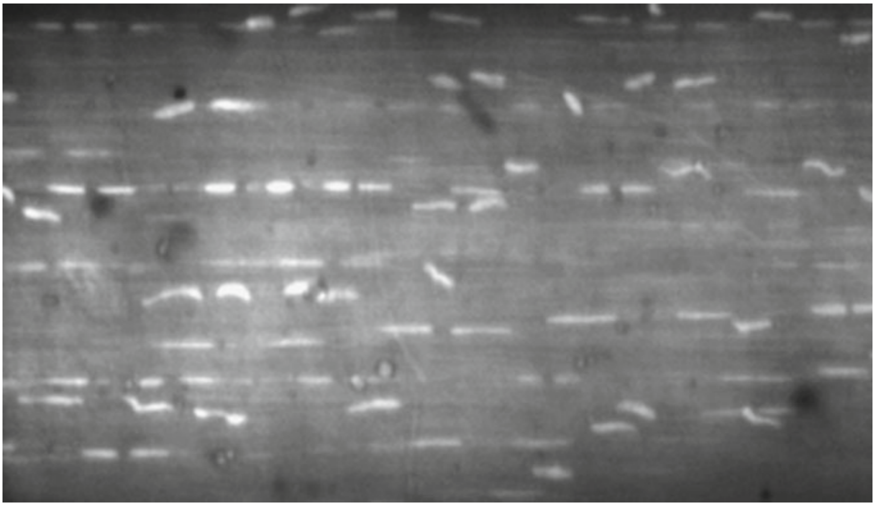

Fig. 3.1 Typical confocal image of tendon under load, showing fibres and tenocytes [7]

possible to use quite a large number of markers to obtain more detailed displacement measurements but this requires at least three cameras to avoid tracking problems. The advantage of this approach is that it can measure movements at a relatively high sampling rate with minimal postprocessing, using equipment that is commonly available in biomechanics labs. The resolution is much better than the pixel resolution of the camera, typically around 1/60,000 of the field of view.

If detailed strain measurements are needed, the best approach may be to use DIC. Here a speckle pattern is applied to the surface (using face paint, for example) and this provides distinctive patterns in subsets of pixels which can be matched in consecutive images or between different cameras in order to track the movement of the surface and calculate its location in three dimensions. Using commercial systems this is a relatively quick and straightforward process which also gives subpixel resolution and tracks the movement of a much larger number of points, typically many thousands, allowing detailed strain calculations. While the technique can be very accurate, the results depend on the quality of the speckle pattern, the calibration and the stability, and focus of the cameras, and these aspects are critical if good results are to be obtained.

It is possible to develop more complex optical measurement systems using DIC or other techniques. For example, Genovese et al. [4] demonstrated a system for indentation tests that combines panoramic DIC using a single camera and a conical mirror with fringe projection to measure surface deflection. A limitation of all these methods is that they only measure strain at the surface and not inside the material, and other techniques such as 3D DIC using ultrasound, tagged MRI [9] or elastography may be valuable in the future although they are in their infancy at present.

3.4 Nonlinear FE Modelling of Soft Materials

Having made some experimental measurements of deformation in a material, we next need a mathematical model to describe the experiment which we can use to identify the values of the material parameters. In some simple cases it may be possible to solve this model using an analytical solution, but in most cases a numerical solution is required, generally using FE methods. This process is difficult, unreliable and frustrating, and it is very helpful to understand in simple terms how the solution algorithm works and how and why it goes wrong.

The basic concept of the FE method is that the unknown, continuous displacement field is approximated by a piecewise continuous field, defined by a number of discrete variables. The region to be modelled is divided into a set of subregions (or elements) in which the displacement is approximated by a simple function of the position, typically a linear or quadratic function although higher order approximations are sometimes used. If we imagine for example that we wish to represent the continuous displacement field shown in Fig. 3.2, we can approximate it by a series of linear functions which are defined by the displacement at some known points (called nodes), in this case at the ends of each linear section (or element). This greatly simplifies the problem because now we only have to find the displacements of the nodes and not the whole continuously varying displacement field. However it is obvious that the quality of the results will depend very strongly on the quality of the approximation and the assumptions that are made about how the displacement will vary. If the number of elements is insufficient, then it will be impossible for the approximated displacement field to properly match the true, varying displacement and the results will be inaccurate. Since we are constraining the displacement within each element to vary in a particular way, using a coarser mesh with fewer elements always increases the stiffness and tends to underestimate the displacement. Where there are localised variations in displacement or strain, we need to have a sufficiently fine mesh to describe the true displacement field, otherwise the solution will be inaccurate. On the other hand, increasing the number of elements greatly increases the computational cost, so there is always a compromise between accuracy and solution time. Fortunately St. Venant's principle dictates that although a coarse mesh may

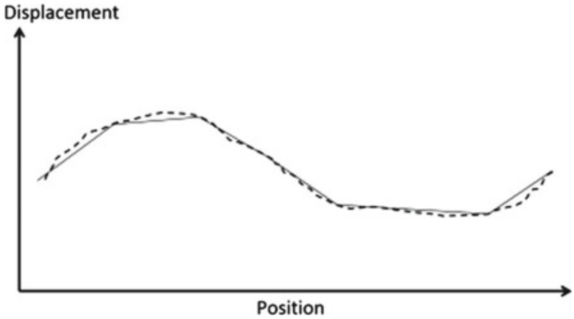

Fig. 3.2 A continuously varying displacement field is approximated by a series of linear segments

result in local inaccuracies, it should not greatly affect accuracy in regions further away, and this means that an experienced modeller can refine the mesh in areas of interest while using a coarser mesh elsewhere.

Having defined the mesh of elements and nodes that will be used to approximate the displacement field, the next step is to calculate the actual displacements at the nodes. This is defined by differential equations that describe the mechanics of deformation, constitutive models that provide a mathematical description of the behaviour of the material and boundary conditions that describe the loads and constraints acting on it. Combining these produces a set of equations that must be solved in order to approximate the solution. There are two fundamentally different approaches that may be used to do this, explicit solution algorithms and implicit solution algorithms, and it is valuable to understand the difference between them and the strengths and weaknesses of the two approaches.

Having defined the mesh, the problem is to find the displacements of all the nodes which will result in all the internal forces in the elements (due to the stress generated by deformation of the material) being in equilibrium with each other and with the external forces. Alternatively, for a dynamic problem it is necessary to find the out of equilibrium forces and the resultant accelerations, velocities, and displacements. An explicit solution uses the latter approach to find a quasi-static solution, by applying the loads and simulating the motion of the material until it eventually reaches equilibrium. An implicit approach can be used for dynamic problems, but can also be used to find a static solution directly.

The explicit solution algorithm is very simple. Starting with the initial displacements of the nodes, we find the strain in each element, then use the constitutive model to find the corresponding stress, then integrate the stress to find the force in the element. The forces at each node are then summed, with the external forces, to find the total residual force. The mass of the elements is assumed to be lumped at the nodes (for example, for a square element a quarter of its mass might be assumed to be lumped at each corner) and so the acceleration of each node can be found using Newton's Second Law. Multiplying the acceleration by a small time step we find the change in velocity, which is then added to the velocity of the node, and multiplying the velocity by a short time step we find the change in displacement. The process is then repeated for a large number of time steps.

This approach has several advantages. It is easy to programme and requires only a modest amount of memory to store the displacement, residual, acceleration, and velocity vectors. It is also easily parallelised as most of the computational effort is in calculating the stresses and forces in the elements, and this can be shared between processors. It is often also more reliable than an implicit method in terms of producing a solution, although there is no inherent way of knowing if the solution is correct.

A major disadvantage of the explicit approach is that it requires very small time steps, otherwise it becomes unstable. Roughly speaking the time step must be shorter than the time taken for a sound wave to travel across the smallest element, commonly a fraction of a microsecond, and so a very large number of time steps are needed to model even a short test. This means that explicit solutions are better suited for high speed dynamic events such as impacts and can be very slow for quasi-static problems.

To reach static equilibrium some damping is also needed; this is normally applied through simplified and unrealistic models and the parameters are approximated by trial and error. To obtain a fast quasi-static solution it is possible to increase the mass, in order to increase the timesteps, and increase the damping to reduce the duration of oscillation.

A further disadvantage of the explicit approach is that there is no inbuilt check on the accuracy of the solution, and so although it often produces results there is no easy way of knowing if they are correct. For nonlinear materials and contacts it is possible to have localised oscillations and instabilities which may not be correct, even if there is no large scale instability.

Implicit solution algorithms take other approaches to find a set of displacements where there is static equilibrium. The general concept is illustrated in Fig. 3.3, which shows the simplest possible FE model consisting of a single spring element with only one degree of freedom. There is an internal force F_i in the spring and an external force F_{ext} is applied to it. The total force on the end of the spring is therefore $R = F_{ext} - F_i$. The problem is then to find the displacement x at which $R = 0$, or at least is close to zero within an appropriate tolerance. The internal force could be linearly proportional to the displacement, following Hooke's Law, but it could equally be nonlinear and not necessarily elastic; the graph shows a typical tensile curve for a metal as an example.

If the spring is linearly elastic, the problem is simple: we calculate the initial residual R and then find the appropriate displacement using Hookes Law as $x = k^{-1}R$. If we have more elements and more degrees of freedom we can replace R with a vector of residual components at each node and x with a corresponding vector of displacements; then k is replaced with a stiffness matrix $\mathbf{K}$ which we can assemble from the known stiffness of each element. Then the solution can be found as $\mathbf{x} = \mathbf{K}^{-1}\mathbf{R}$ (in practice the stiffness matrix is not actually inverted but various ingenious algorithms are used to solve the system of equations directly and more efficiently). This is the basis of the standard FE method and offers a fast and efficient solution which has been very highly optimised.

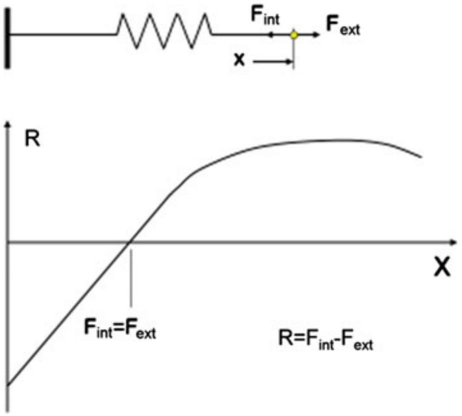

Fig. 3.3 A simple FE model consisting of a single element. The *graph* shows the residual force R as a function of the displacement x of the node

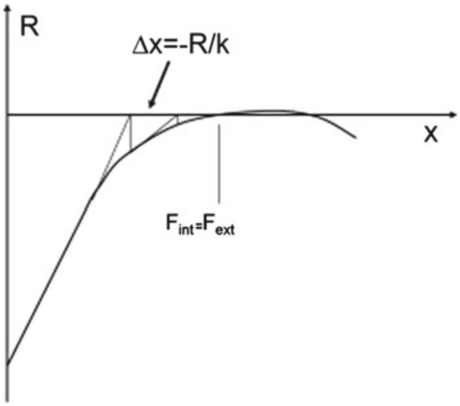

Fig. 3.4 Newton–Raphson method for solution of a nonlinear FE problem. Convergence is good where the stiffness of the material reduces

Although this method is fast and effective, it does not necessarily scale so well for large problems as the explicit algorithm. The size of the stiffness matrix is proportional to the square of the number of degrees of freedom (although it is symmetric, so only half of it needs to be stored, and sparse with many zeroes which also allows efficiencies of storage) and so for large problems with many elements it is slow to assemble and requires a very large amount of memory. Solving the resulting system of equations can also be time consuming for large problems.

For nonlinear problems, the usual approach is to use a Newton–Raphson method as illustrated in Fig. 3.4. The initial residual is calculated, then the tangent stiffness is used to find a better estimate of the solution and the process is repeated until it converges on an adequately good solution (various convergence criteria can be used but it is important to check that they are set appropriately to ensure an accurate solution). This approach works well for materials that soften or in other words where the stress decreases below the linear elastic value, for example metals that plastically deform as shown. As long as the stress does not go above the maximum of the curve (the ultimate tensile strength) then it should converge smoothly to a stable solution as shown.

There are two situations where this approach will not work so well. The first, which is not illustrated, is where the load-displacement curve is not smooth and continuous but has sudden steps or changes of gradient. This occurs for example with contact problems and it should be obvious that in this case it will be more difficult to get reliable convergence. It is common to end up with a situation where the algorithm oscillates in and out of contact and does not converge to a solution, or, worse, diverges and fails.

The other situation which is fundamentally difficult is shown in Fig. 3.5, which shows what happens with a material which becomes stiffer with increasing strain. In this case the initial linear estimate of the stiffness will overestimate the displacement, and then the force on the next iteration will be much too high. This in turn may result in a huge underestimate on the subsequent iteration, an even larger overestimate on the following one, the elements become excessively distorted and convergence fails. Typically the excessive distortion of the elements results in parts of them turning

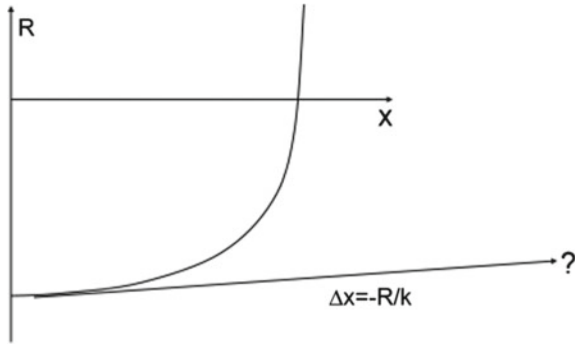

Fig. 3.5 Where the stiffness increases, the initial tangent modulus results in an overestimate of the displacement and convergence is very difficult

inside out, resulting in the negative Jacobian message which is familiar to anyone who uses FE to model soft materials.

The way to work around this frustrating problem is to increase the load in a series of very small increments, iterating until convergence on each increment before going on to the next one. Hopefully the tangent stiffness does not increase too much on each increment and excessive displacements and distortion do not occur. This is often effective, especially when combined with algorithms that automatically reduce the load increment and try again when convergence fails. However, it makes the process extremely slow and frustratingly unreliable.

A useful way to reduce this problem, which is widely used, is to include a line search, in which the displacement that is applied on each iteration is reduced to a suitable fraction of that predicted by the Newton–Raphson algorithm. The fraction of the displacement that is applied must be determined by trial and error, which slows down each iteration, but hopefully greatly reduces the number of iterations and increments that are needed. For any given iteration there is an optimum step length which will give the biggest step towards the solution, but finding this by trial and error is time consuming and usually we look only for a step length which improves the solution and not for the exact optimum.

Another approach to the problem is to consider the solution as an optimisation problem in which we seek to minimise the total strain and potential energy in the structure. For the simple example we considered first, moving the node to the left of the optimum will increase the potential energy, while moving it to the right will increase the strain energy. The sum of the two is a minimum at the equilibrium point. In general if we disturb a structure that is in equilibrium we will have to do work on it by applying a force that moves it through some finite distance and so we will increase the potential energy. The equilibrium position is therefore the position of lowest energy.

Another way to look at this is to remember that the behaviour of a hyperelastic (or elastic) material is defined by a strain energy function, which we then differentiate with respect to the strain to find the stress and again to find the stiffness. If we consider a structure made of such a material, we can differentiate the total energy to find the residual force; to find the minimum energy we look for the point where the differential is zero and hence the residual is zero.

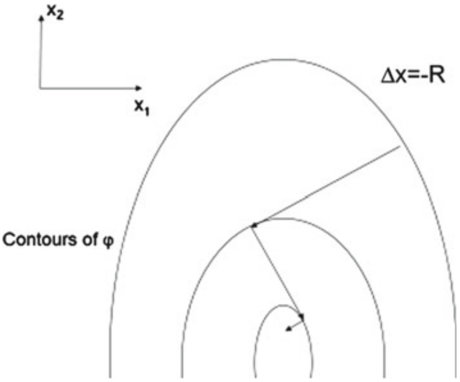

Fig. 3.6 Solution as optimisation. The node now has two degrees of freedom and can move in two directions. The contours show the potential energy at different positions of the node. Moving the node downhill in the direction of the potential energy gradient (which is the direction of the residual force) moves it towards the solution, but there is a tendency to zigzag in ever smaller steps

Looking at the problem in this way opens up a whole range of solution algorithms developed for optimisation problems. In fact the conventional Newton–Raphson technique is well known in optimisation but there are many other methods that can be used. An unusual aspect of the problem is that it is difficult to calculate the total energy with sufficient accuracy to use it effectively in optimisation near the minimum due to rounding errors and approximations in a numerical model. We therefore work with the first differential (the residual vector) and possibly the second differential (the stiffness matrix). Although the stiffness matrix can be useful it is very cumbersome to calculate and store and it can be advantageous not to use it, especially for large models.

A simple approach is to move the nodes in the direction of the residual force on each iteration. This is called a steepest descent method as the nodes move in the direction where the potential energy drops most steeply. A line search is needed to work out how far to move in the chosen direction. The problem with this method can be seen in Fig. 3.6: the node moves in a zigzag in decreasing steps that become smaller and smaller as it approaches the solution, and so the solution is very slow. This can easily be overcome using some combination of the current direction and the direction on the previous step, which smooths out the zigzags, and this is called the conjugate gradient method. Various formulae are possible to determine the new step direction and some, such as the Hager–Zhang method [10] are proven to converge for smooth, continuous functions even if they are nonlinear. Such methods offer the possibility of much faster solution than an explicit solver for quasi-static problems while having the same advantages of reduced memory requirements, efficient parallelisation, and good scalability for large models.

Another very efficient method is to estimate the tangent stiffness matrix from the actual changes in force and displacement on each iteration rather than recalculating it every time. This is the Broyden–Fletcher–Goldfarb–Shanno (BFGS) method [11] which is used in software such as FEBio and can be very fast and effective when combined with an efficient linear solver.

It is obvious that current solution methods for nonlinear FE models are far from optimal and there is still considerable scope for further development before we have a fast, reliable method that allows rapid analysis of soft tissue deformation. In the meantime it is very helpful to have some understanding of how the algorithms work if we are to persuade them to converge and give us reliable results. We have seen that all these methods provide only an approximate solution to a specified tolerance and it is very important to check this tolerance and make sure that it is tight enough to give an accurate answer but not excessively tight resulting in overly long solution times.

The following suggestions may be useful when struggling to get a nonlinear FE model to converge:

- *Reduce the load increments*. Using smaller load increments (sometimes presented as timesteps) is generally helpful. If there is automatic adjustment of the increments, understand how it works and use it to ensure that you have really small increments for parts of the solution where convergence is difficult.
- *Avoid excessive deformation*. This is not particularly helpful if you are trying to model a very large deformation, but in general the larger the deformation the greater the convergence problems. If you do not know the exact load or material properties then look at your model and make sure that the deformations you predict are not unrealistically large. A model cannot be expected to converge if the deformation is beyond what would be feasible in reality.
- *A finer mesh can help*. Often increasing the number of elements can help to reduce the distortion of individual elements and therefore help convergence. This is particularly true for contact problems where having a large number of elements in the contact region is usually helpful. Sometime the opposite occurs and a coarser mesh converges better.
- *Some material models work better than others*. Simple models such as the neo-Hookean and Ogden models often work well while more complex ones such as the Gasser-Ogden-Holzapfel model are often more difficult. Some, such as the Arruda-Boyce model, often seem to cause convergence problems. Changing the material model, even to a special case of another model which produces mathematically identical results, can often help convergence.
- *Adjust the bulk modulus*. For most hyperelastic models the bulk modulus is a separate parameter and is often extremely sensitive. Realistic values often lead to convergence problems as the volumetric stiffness is so much higher than the shear stiffness. Reducing the bulk modulus somewhat can often give better convergence without sacrificing significant accuracy in most cases. A value of the order or 1000 times greater than the shear modulus often works well. Experimenting with changing the bulk modulus is often very useful when trying to solve convergence problems.

- *Adjust contact parameters*. Contact problems introduce discontinuities in the load displacement curve and therefore cause problems with all solution algorithms. The contact penalty parameter is generally very sensitive and values that are too small will cause interpenetration of the contact surfaces while values that are too large cause convergence failure. Experimenting with different penalty parameters and contact formulations is often a fruitful way to solve convergence problems.

3.5 Parameter Identification and Uncertainty Quantification

Having carried out an experiment and successfully created a numerical model, the next challenge is to find the parameter values in the model that match the experiment. This is often done by varying the model parameters (typically the material parameters) using some sort of optimisation algorithm to try to find the best match with the experiment. This method is often known as inverse FE or FE model updating. As an approach it suffers from two major problems: it is often necessary to run the model a very large number of times, typically serially one after another, making the process very slow, and there is no way of knowing whether the final parameter set is the true optimum or what range of other values might be consistent with the experiment. It is often found that a very wide range of values of some parameters may be consistent with the experiment—for example, in an indentation test the stiffness is very insensitive to the Poisson's ratio of the material and so a very wide range of values may produce nearly identical apparent stiffness. There are also uncertainties and inaccuracies in the experiment, for example in the calibration of the equipment, and ideally we would like to be able to define the range of possible parameter values that could be compatible with the experiment so that we really know the accuracy of our measurement/modelling/parameter identification process.

A third question which affects any measurement of soft tissue properties is that we do not have well developed and reliable constitutive models that we know will correctly describe their behaviour in any circumstances. We must therefore always think about validation and testing that the chosen model and parameters will correctly predict behaviour under different types of loading.

A typical example of the inverse FE process was presented by Evans and Holt [12], who used DIC to measure the deformation of skin under in plane traction and modelled the experiment using a simple 2D FE model. The measured displacements around the edges of the region of interest were used as boundary conditions together with the measured load. A stochastic optimisation approach was then used to identify the material parameters that resulted in the closest match to the measured displacement field. This required several thousand iterations using a specially developed solver. It was possible to identify parameter values that fitted the measured behaviour very well, but there was considerable uncertainty and a wide range of parameters that generated quite small errors. There was a strong interaction between the para-

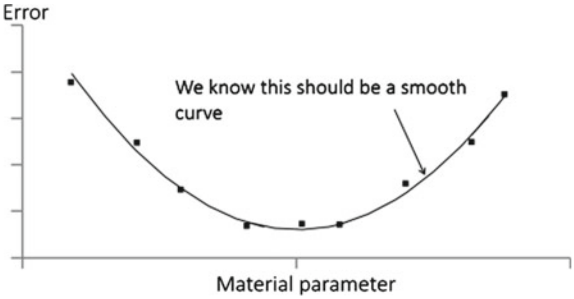

Fig. 3.7 Typical response curve when matching a model to an experiment. As the material parameter is varied, the error increases or decreases to a minimum when the best match is obtained. The *points* show the results of individual simulations, which could be assumed to follow a Gaussian distribution around an underlying smooth curve due to numerical error

meters, such that if one changed then the optimum value of the others also changed, and there was a large range of parameter values that produced similar results with a fairly small error and could potentially be compatible with the experiment. There is thus a large uncertainty in the measured material properties, and this is typical of this type of approach. We need to remember this when using material properties generated by such methods.

The combination of numerical inaccuracies such as rounding errors, a finite convergence tolerance and other computational factors also means that there is some error in the results. Of course there may also be systematic errors such as increased stiffness of the model due to an excessively coarse mesh. This noise makes it difficult to identify the global optimum accurately when looking only at local results. Figure 3.7 shows a generic response curve that we might expect from such an experiment. The error is plotted as a function of a single parameter and the numerical results follow a smooth curve with some random noise superimposed. It is clear that if we just look at the data points, especially locally around the optimum, it would not be easy to identify exactly where the true optimum is. The point with the lowest error is not in fact the minimum of the underlying curve. We can obtain a far better understanding of the data if we take advantage of our prior knowledge that the response should be a smooth curve. If we fit such a curve to the data we can easily identify the global optimum. Better still, we can then predict the result for any other parameter value without having to solve the model again and this could allow us to evaluate many more combinations of parameters very quickly to see if they could be compatible with the experimental results. We can also predict and evaluate the effect of numerical inaccuracies.

This approach has been well developed in the field of climate modelling, among others, using a Bayesian statistical framework to develop a mathematical model of the response on the assumption that actual model results are normally distributed about an underlying smooth curve [13]. The model or emulator can be developed from a few hundred model runs with parameters chosen to give a good spread over the expected space, and these runs can be carried out in parallel as the parameters used do not depend on previous results as would be the case when using optimisation algorithms. Having made an emulator that predicts the results of the model, it is then possible to evaluate many thousands of parameter combinations and see which ones are compatible with the experimental results, including the uncertainty in the experimental measurement, numerical uncertainty in the computational results and experimental variables or unknowns such as precise alignment of the test fixtures and coefficients of friction. This gives a full understanding of the parameter space, the range of combinations of parameter values that could be correct, and the sensitivity of the results to each parameter. This shows where additional measurements are needed, or changes to the experimental method, in order to properly assess the effects of certain parameters.

3.6 Summary

We have seen that there are many potential errors and uncertainties in developing models of the behaviour of soft tissues. Variation between specimens, measurement errors in experiments, experimental tolerances such as specimen and fixture dimensions and alignment, and experimental unknowns such as friction coefficients all play their part. A major uncertainty arises from the use of constitutive models that we know are simplistic and inaccurate; this means that if we fit the model to match the way the material behaved in a particular experiment, we cannot reliably generalise to predict the behaviour in different circumstances. The material parameters themselves are difficult to measure accurately and published data is often subject to large and unknown uncertainties. Finally there is often significant numerical and computational error in using FE methods, as well as a frustrating lack of speed or reliability. However, if these factors are known and appreciated, it is possible to use these methods to start to gain real insights into the behaviour of soft tissues and to produce useful practical predictions. Experimental methods, modelling algorithms, and parameter identification techniques are all promising areas of research with many opportunities for fruitful development and we can expect great advances in the future.

References

1. Legerlotz, K., Riley, G. P., & Screen, H. R. C. (2010). Specimen dimensions influence the measurement of material properties in tendon fascicles. *Journal of Biomechanics*, *43*(12), 2274–2280.
2. Hayes, W. C., Keer, L. M., Herrmann, G., & Mockros, L. F. (1972). A mathematical analysis for indentation tests of articular cartilage. *Journal of Biomechanics*, *5*(5), 541–551.
3. Groves, R. B., Coulman, S. A., Birchall, J. C., & Evans, S. L. (2012). Quantifying the mechanical properties of human skin to optimise future microneedle device design. *Computer Methods in Biomechanics and Biomedical Engineering*, *15*(1), 73–82.

4. Genovese, K., Montes, A., Martínez, A., & Evans, S. L. (2009). Full-surface deformation measurement of anisotropic tissues under indentation. *Medical Engineering and Physics*, *37*(5), 484–493.
5. Hendriks, F. M., Brokken, D. V., Van Eemeren, J. T. W. M., Oomens, C. W. J., Baaijens, F. P. T., & Horsten, J. B. A. M. (2003). A numerical-experimental method to characterize the non-linear mechanical behaviour of human skin. *Skin Research and Technology*, *9*(3), 274–283.
6. Romo, A., Badel, P., Duprey, A., Favre, J.-P., & Avril, S. (2014). In vitro analysis of localized aneurysm rupture. *Journal of Biomechanics*, *47*(3), 607–616.
7. Screen, H. R. C., & Evans, S. L. (2015). Measuring strain distributions in the tendon using confocal microscopy and finite elements. *The Journal of Strain Analysis for Engineering Design*, *44*(5), 327–335.
8. Mahmud, J., Holt, C. A., & Evans, S. L. (2010). An innovative application of a small-scale motion analysis technique to quantify human skin deformation in vivo. *Journal of Biomechanics*, *43*(5), 1002–1006.
9. Moerman, K. M., Sprengers, A. M. J., Simms, C. K., Lamerichs, R. M., Stoker, J., & Nederveen, A. J. (2011). Validation of SPAMM tagged MRI based measurement of 3D soft tissue deformation. *Medical Physics*, *38*(3), 1248–1260.
10. Hager, W. W., & Zhang, H. (2005). A new conjugate gradient method with guaranteed descent and an efficient line search. *SIAM Journal on Optimization*, *16*(1), 170–192.
11. Broyden, C. J. (1970). The convergence of a class of double-rank minimization algorithms 1. general considerations. *IMA Journal of Applied Mathematics*, *6*(1), 76–90.
12. Evans, S. L., & Holt, C. A. (2009). Measuring the mechanical properties of human skin in vivo using digital image correlation and finite element modelling. *The Journal of Strain Analysis for Engineering Design*, *44*(5), 337–345.
13. Kennedy, M. C., & O'Hagan, A. (2001). Bayesian calibration of computer models. *Journal of the Royal Statistical Society: Series B (Statistical Methodology)*, *63*(3), 425–464.

Chapter 4
Damage in Vascular Tissues and Its Modeling

T. Christian Gasser

Abstract The present chapter reviews vessel wall histology and summarizes relevant continuum mechanical concepts to study mechanics-induced tissue damage. As long as the accumulated damage does not trigger strain localizations, the standard nonpolar continuum mechanical framework is applicable. As an example, a damage model for collagenous tissue is discussed and used to predict collagen damage in the aneurysm wall at supra-physiologic loading. The physical meaning of model parameters allow their straight forward identification from independent mechanical and histological experimental data. In contrast, if damage accumulates until the material's stiffness looses its strong ellipticity, more advanced continuum mechanical approaches are required. Specifically, modeling vascular failure by a fracture process zone is discussed, such that initialization and coalescence of micro-defects is mechanically represented by a phenomenological cohesive traction separation law. Failure of ventricular tissue due to deep penetration illustrates the applicability of the model. Besides appropriate continuum mechanical approaches, laboratory experiments that are sensitive to constitutive model parameters and ensure controlled failure propagation are crucial for a robust parameter identification of failure models.

4.1 Introduction

Understanding damage mechanisms of soft biological tissue is critical to the sensitive and specific characterization of tissue injury tolerance. Such knowledge may help improving clinical treatment planning by accurately assessing the rupture risk of Abdominal Aortic Aneurysms (AAAs) or the vulnerability of carotid plaques, for example. In addition, design optimization of medical devices critically depends on the proper understanding of short-term and long-term damage effects on the interaction

---

T.C. Gasser (✉)
KTH Solid Mechanics, School of Engineering Sciences,
KTH Royal Institute of Technology, Stockholm, Sweden
e-mail: tg@hallf.kth.se

S. Avril and S. Evans (eds.), *Material Parameter Identification and Inverse Problems in Soft Tissue Biomechanics*, CISM International Centre for Mechanical Sciences 573, DOI 10.1007/978-3-319-45071-1_4

of such devices with the biological tissue. Relating tissue chemical morphology to engineering concepts like constitutive models, i.e., histomechanical modeling is one promising way to better understanding tissue damage.

Mechanical force is transmitted from the macroscopic (tissue) length scale down to the atomistic length scale, and different microstructural constituents are loaded differently. Consequently, raising the macroscopic load leads to local stress concentrations in the tissue, and, if high enough, starts damaging it at specific spots. For example, micro-defects like breakage and/or pull-out of collagen fibrils gradually develop, which in turn weakens/softens the tissue. In healthy tissues at physiological stress levels, healing continuously repairs such defects in order to maintain the tissue's structural integrity. For example in bones, osteoclasts remove damaged tissue which is then newly formed by osteoblasts. However, at supra-physiological stress level or for diseased tissues, healing cannot fully repair such micro-defects and the tissue continues to accumulate weak links, which in turn irreversibly diminish its strength. If the damage level, i.e., the numbers of defects per tissue volume exceeds a certain threshold, micro-defects join each other, and form macro-defects. Finally, a single macro-defect may propagate and finally rupture the tissue.

Despite increasing experimental and analytical efforts to investigate failure-related irreversible effects of soft biological tissue, the underlying mechanisms are still poorly understood. There is still no clear definition of what damage is, and conventional indicators of mechanical injury (such as visible failure and loss of stiffness) may not identify the tissue's tolerance to injury appropriately. Micro-defects locally weaken the material and a Kachanov-like [1] damage parameter can only represent damage of inert material, but neglects all biological aspects of tissue damage. Consequently, a more complete definition of damage in a biological tissue is needed, and "*a description of the mechanical and physiological changes that result in anatomical and functional damage*" [2] defines more broadly damage of soft biological tissues. Clearly, damage mechanisms and specific injury tolerance is closely related to the individual tissue type.

This chapter adresses only the passive mechanical aspects of vascular tissue. Its first section outlines general consequences of damage and failure on the solution of (initial) boundary value problems. The second section reviews tissue histology with focus on the collagen in vessel walls. Then, a histologically motivated constitutive model for collagenous soft biological tissue for supra-physiological stress states is introduced. Finally, a continuum mechanics concept for strain localization problems is reviewed, and representative examples demonstrate the proposed modeling approaches.

4.2 Continuum Mechanical Consequences of Damage—The Basics

Local damage diminishes local tissue stiffness, and, if massively enough, defines a strain softening material. For a strain softening material the stress decreases with increasing strain, such that the tissue's stiffness matrix is no longer positive definite. This changes the fundamental physics of the underlying mechanical problem, which is demonstrated by a simple rod under tension shown in Fig. 4.1. The rod of cross-section A is made of a material with a strain-dependent Young's modulus $E(\varepsilon)$. Here, the strain $\varepsilon = u' = \partial u/\partial x$ depends on the displacement u, and the notations $\ddot{u} = \partial^2 u/\partial t^2$ and $u'' = \partial^2 u/\partial x^2$ are used. Equilibrium along the axial direction, i.e., $-\rho A \mathrm{d}x \ddot{u} - A[\sigma]_x + A[\sigma]_{x+\mathrm{d}x} = 0$, leads, with the Taylor series expansion $[\sigma]_{x+\mathrm{d}x} = [\sigma]_x + [E(\varepsilon)\mathrm{d}^2u/\mathrm{d}x^2]_x \mathrm{d}x + \mathcal{O}(2)$, to the governing equation

$$\ddot{u} - cu'' = 0 \quad \text{with } c = \frac{E(\varepsilon)}{\rho} , \tag{4.1}$$

with $\mathcal{O}(2)$ denoting second-order terms. Most important, the parameter c renders the physics of the problem, i.e., for $c < 0$ the problem is hyperbolic, while for $c > 0$ it is elliptic. Consequently, for $E(\varepsilon) > 0$ waves can propagate along the rod, while this is prohibited for $E(\varepsilon) < 0$, i.e., at strain softening conditions. For the multidimensional small strain case the 1D condition $E(\varepsilon) > 0$ relates to the strong ellipticity condition. This condition states that $\Delta\boldsymbol{\varepsilon} : \mathbb{C} : \Delta\boldsymbol{\varepsilon} > 0$ for all possible strain increments $\Delta\boldsymbol{\varepsilon}$, where $\mathbb{C}$ denotes the (nonconstant) elasticity tensor [3]. For finite strain problems a similar condition holds [4, 5].

4.2.1 *Strain Localization*

Following [6], strain localization is considered in a rod of length L that is discretized by n finite elements of equal lengths. The rod's material follows the bilinear stress

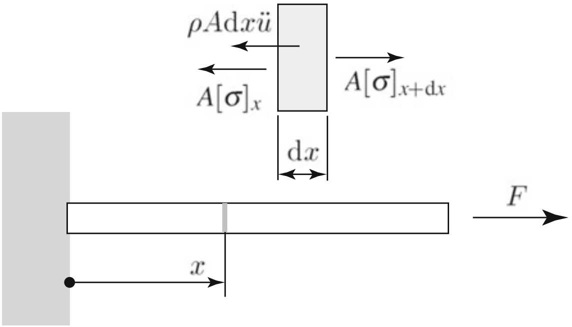

Fig. 4.1 Forces acting on the material point of a rod under tension

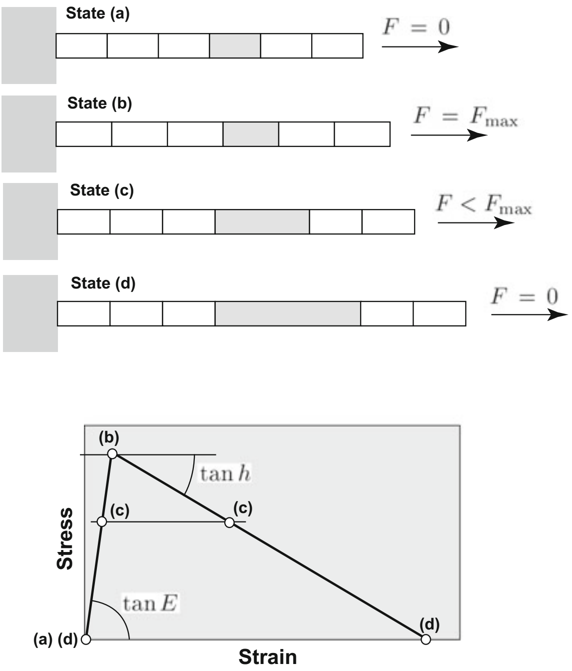

Fig. 4.2 Development of a strain localization in a rod of material with bilinear stress–strain properties and discretized by n finite elements. In the *upper part* of the figure different loading states are sketched and related to labeled points in the stress strain curve

versus strain law as shown in Fig. 4.2. First, the stress increases linearly (at the stiffness E) until it reaches the elastic limit stress Y, and then it decreases linearly (at the softening h) until it is stress-free.

The rod's right end is pulled to the right, at the gradually increasing displacement Δ_0. In response to that, the load F in the rod gradually increases to the maximum load $F = F_{\max}$ (state (b) in Fig. 4.2), where all finite elements are strained equally $\varepsilon = \Delta/L$. Further increase in Δ causes a reduction of the load F and the solution bifurcates. Specifically, a single element (the one with the (numerically) smallest cross-section; in Fig. 4.2 this element is filled grey) follows the strain softening path, while all the other finite elements elastically unload (state (c) in Fig. 4.2) until the rod is completely stress-free (state (d) in Fig. 4.2). Consequently, the grey finite element in Fig. 4.2 accumulates the total strain, i.e., it developed a strain localization.

Next we introduce the averaged (smeared) strain

$$\bar{\varepsilon} = \Delta/L = \frac{h}{L}[(n-1)\varepsilon + \varepsilon^*] = \frac{1}{n}\left[\frac{(n-1)\sigma + Y}{k} + \frac{Y - \sigma}{h}\right], \tag{4.2}$$

all over the rod. Here, $\varepsilon = \sigma/k$ and $\varepsilon^* = Y/k + (Y - \sigma)/h$ denote the strain in the $n - 1$ non-localized and in the one localized finite elements, respectively. In order to derive this relation, the equilibrium, i.e., equal stress σ in all finite elements, was used. Relation (4.2) is linear and can be inverted to express the stress versus averaged strain response

$$\sigma = \frac{\bar{\varepsilon} hkn - Y(h+k)}{h(n-1) - k}. \tag{4.3}$$

Most importantly, Eq. (4.2) depends on the number n of finite elements, i.e., on the used discretization. Figure 4.3 illustrates this dependence.

4.2.2 Dissipation

The dissipation for complete failure relates to the energy per reference volume that is dissipated until the force diminishes and reads

$$\mathcal{D} = \int_0^{\bar{\varepsilon}_1} \sigma \mathrm{d}\bar{\varepsilon} = \frac{Y^2}{2k} + \int_{\bar{\varepsilon}_0}^{\bar{\varepsilon}_1} \sigma \mathrm{d}\bar{\varepsilon} = \frac{Y^2}{2n}\left(\frac{1}{h} + \frac{1}{k}\right). \tag{4.4}$$

Here, $\bar{\varepsilon}_0 = Y/k$ and $\bar{\varepsilon}_1 = Y(h+k)/(hkn)$ denote the strains at the elastic limit and at zero stress (complete failure), respectively. This relation can also be derived by taking the dissipation of the localized element $Y^2(1/k + 1/h)/2$ and weighting it according to the volume ratio, i.e., by $1/n$.

Again, the total dissipation depends on the number n of finite elements used to discretize the rod. Most surprisingly, the dissipation vanishes for $n \to \infty$, i.e., the continuum solution of the problem. This was already indicated in Fig. 4.3a (case $n = 10\,000$), where loading and unloading pathes were practically identical. This is an obviously nonphysical result (*How can an inherently dissipative process like damage have no dissipation?*) and direct consequence of localization. Specifically, for this (non-regularized) case the material volume that is affected by the localization tends to zero, such that also the dissipation vanishes. It is emphasized that this is not

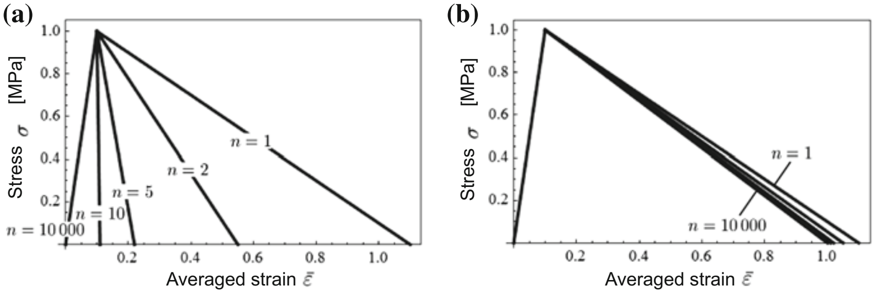

Fig. 4.3 Stress–strain response of a rod discretized by n number of elements and using non-regularized (**a**) and regularized (**b**) approaches. The case uses an initial elastic stiffness $E = 10$ MPa and a elastic limit $Y = 1$ MPa. Localization is induced by linear softening $h = 1$ MPa (**a**), and the regularized linear softening $h = 1/n$ MPa (**b**), respectively

a problem of the finite element model but the hypothetical entity of a nonpolar continuum yields vanishing localization volume [7]. In contrast to the volume, the localization defines a surface, which area remains finite, i.e., for the above discussed rod problem, the localization area is equal to the rod's cross-sectional area A.

4.2.3 Regularization

For every material, the material's microstructure prevents from a vanishing localization volume. For example in collagenous tissues at tensile failure, the length of the pulled-out collagen fibers introduces an internal length scale, which in turn leads to a finite localization volume. Such an internal length scale can also be introduced in the model to prevent from a vanishing localization volume. The simplest solution is to relate the softening modulus h to the finite element size according to $h_{\mathrm{reg}} = h/n$. Consequently, the regularized averaged strain and the regularized dissipation (i.e., regularized versions of Eqs. (4.2) and (4.4)) read:

$$\bar{\varepsilon}_{\mathrm{reg}} = \frac{1}{n}\left[\frac{(n-1)\sigma + Y}{k} + \frac{Y-\sigma}{h/n}\right] \; ; \; \mathcal{D}_{\mathrm{reg}} = \frac{Y^2}{2n}\left(\frac{1}{h/n} + \frac{1}{k}\right). \tag{4.5}$$

The stress versus regularized strain is shown in Fig. 4.3b, and it is noted that the regularized dissipation of the continuum problem $\mathcal{D}_{\mathrm{reg}\,n\to\infty} = Y^2/(2h)$ yields the physically correct result. Despite such a regularization fully resolves the 1D problem, it leads to stress locking for general 3D problems that is discretized by an unstructured FE mesh. More advanced approaches will be discussed in Sect. 4.5 of this chapter.

4.2.4 Experimental Consequences

Experimental tensile testing into the strain softening region forms at least one localization (failure) zone, which is schematically illustrated in Fig. 4.4. Consequently, the data, that is recorded in the softening region (i.e., post the localization) is dependent on the marker positions, which were used to calculate the averaged strain $\bar{\varepsilon} = (l - L)/L$. Here, l and L denote the spatial and referential distances between two markers, see Fig. 4.4. Markers that are close to the localization zone (case (a) in Fig. 4.4) yield a rather ductile response, while markers that are far away from the localization zone (case (c) in Fig. 4.4) show much more brittle test results. Case (c) shows even snap-back, i.e., average strain and force decrease with failure progression. In such a case neither force-control nor clamp displacement-control can ensure stable failure progression, and other control mechanism are needed.

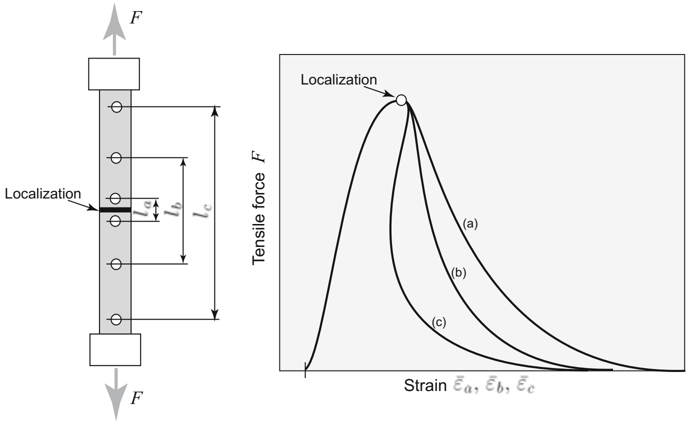

Fig. 4.4 Tensile experiment to complete tissue failure. Averaged strains $\bar{\varepsilon}$ are computed from three different sets of markers, i.e., $\bar{\varepsilon}_i = (l_i - L_i)/L_i$ $i = 1, 2, 3$ with l and L denoting deformed and undeformed distances between markers, respectively. To the right the schematic averaged strain versus stress curves that are associated with the three different sets of marker positions are shown

Summary Mechanical damage triggers micro-defects, which diminishes tissue stiffness. Continuous accumulation of damage may lead to coalescence of micro-defects and the formation of strain localization. A strain localization is triggered as soon as the strong ellipticity condition is violated, and requires regularized computational models paired with properly controlled experimental designs.

4.3 Histology of the Vessel Wall

A sound histological understanding is imperative for the mechanical characterization of vascular tissue. The vessel wall is composed of intima, media, and adventitia (see Fig. 4.5), layers that adapt to their functional needs within certain physiologic limits.

The intima is the innermost layer of the artery. It comprises primarily a single layer of endothelial cells lining the arterial wall, resting on a thin basal membrane, and a subendothelial layer of varying thickness (depending on topography, age, and disease).

The media is the middle layer of the artery and consists of a complex three-dimensional network of Smooth Muscle Cells (SMCs), elastin and bundles of collagen fibrils, structures that are arranged in repeating Medial Lamellar Units (MLU) [8]. The thickness of MLUs is independent of the radial location in the wall and the number of units increases with increasing vessel diameter. The tension carried by a single MLU in the normal wall remains constant at about 2 + 0.4 N/m [8]. The layered structure is lost towards the periphery and clear MLUs are hardly seen in muscular arteries.

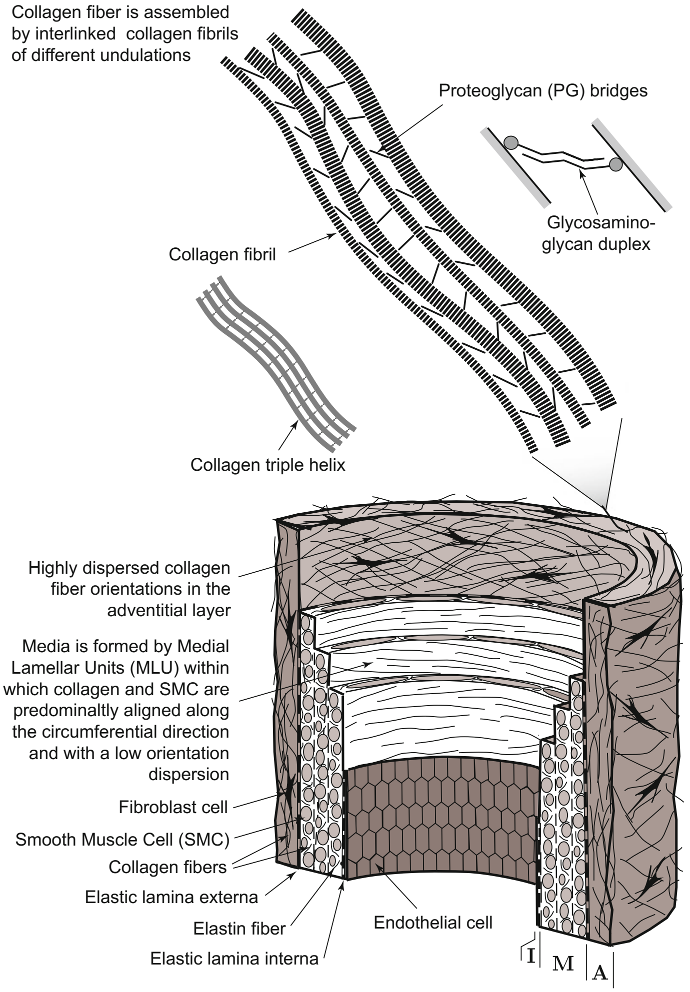

Fig. 4.5 Histomechanical idealization of a young and normal elastic artery. It is composed of three layers: intima (I), media (M), adventitia (A). The intima is the innermost layer consisting of a single layer of endothelial cells, a thin basal membrane and a subendothelial layer. Smooth Muscle Cells (SMCs), elastin, and collagen are key mechanical constituents in the media arranged in a number of Medial Lamellar Units (MLUs). In the adventitia the primary constituents are collagen fibers and fibroblasts. Collagen fibers are assembled by collagen fibrils of different undulations that are interlinked by ProteoGlycan (PG) bridges

The adventitia is the outermost layer of the artery and consists mainly of fibroblasts and ExtraCellular Matrix (ECM) that contains thick bundles of collagen fibrils. The adventitia is surrounded by loose connective tissue that anchors the vessel in the body. The thickness of the adventitia depends strongly on the physiological function of the blood vessel and its topographical site.

4.3.1 The Extracellular Matrix

The ECM provides an essential supporting scaffold for the structural and functional properties of vessel walls. The ECM mainly contains elastin, collagen, and proteoglycans (PGs) [9] and their three-dimensional organization is vital to accomplish proper physiological functions. The ECM, therefore, rather than being merely a system of scaffolding for the surrounding cells, is an active mechanical structure that controls the micro-mechanical and macro-mechanical environments to which vascular tissue is exposed.

While elastin in the ECM is a stable protein having half-life times of tens of years [10], collagen is normally in a continuous state of deposition and degradation [11] at a normal half-life time of 60–70 days [12]. Physiological maintenance of the collagen structure relies on a delicate (coupled) balance between degradation and synthesis. Fibroblasts, myofibroblasts, SMCs, and other cells perceive changes in the mechanical strains/stresses and adjust their expression and synthesis of collagen molecules in order to account for the changes in their micro-mechanical environment. In parallel, collagen is continuously degraded by matrix metalloproteinases (MMPs).

4.3.2 Collagen and Its Organization

Collagen determines the mechanics of the vessel wall at high loads, i.e., loading states that are of primary interest when studying mechanics-induced accumulation of damage. Collagen fibrils, with diameters ranging from fifty to a few hundreds of nanometers are the basic building blocks of fibrous collagenous tissues [13]. Clearly, the way how fibrils are organized into suprafibrilar structures has a large impact on the tissue's macroscopic mechanical properties. Already 60 years ago *Roach and Burton* [14] reported that collagen mainly determines the mechanical properties of arterial tissue at high strain levels. Since that time a direct correlation between the collagen content and the tissue's stiffness and strength has become generally accepted. Earlier observations indicated that the collagen-rich abdominal aorta was stiffer than the collagen-poor thoracic aorta [15, 16] and later regional variations of aortic properties were specifically documented, see [17] for example. Numerous further references were provided by the seminal works of *Fung* [18] and *Humphrey* [19]. Besides the amount of collagen fibers in the wall, also their spatial orientation [13] (and their spread in orientations [20]) are critical microstructural parameters with significant implications on the tissue's macroscopic mechanical properties.

Collagen is intrinsically birefringent and Polarized Light Microscopy (PLM) provides an ideal method for its detection and analysis [21–23]. Combined with a Universal Rotary Stage (URS), PLM allows a quantitative analysis of collagen organization in the vessel wall [24–26]. Figure 4.6 shows a histological image of the AAA wall and illustrates a large mix bag of azimuthal alignment. Extinctions within the larger collagen fibers (see Fig. 4.6b) arose from the planar zigzag structure of collagen fib-

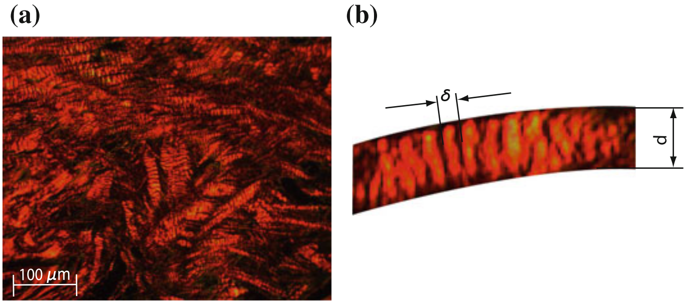

Fig. 4.6 Polarized Light Microscopy (PLM) image taken from the Abdominal Aortic Aneurysm (AAA) wall. **a** Typically observed collagen organizations in the AAA wall, showing a large mix bag of azimuthal alignment. The *horizontal sides* of the images denote the circumferential direction. The collagen that is oriented perpendicular to the linear polarized light defines the extinctions seen in the image. Picrosirius *red* was used as a birefringent enhancement stain and the images were taken at crossed polars on the microscope. **b** Segmented portion of a single collagen fiber of diameter d that is formed by a bundle of collagen fibrils. Extinctions at distances of δ denote the wavelength of the collagen fibrils that form the collagen fiber

rils [27, 28]. The quantitative analysis of such images provides the 3D collagen fiber orientation density function $\rho_{\text{exp}}(\theta, \phi)$, where θ and ϕ denote azimuthal and elevation angles, respectively. Specifically, these angels are defined by (in-plane) rotation and (out-of-plane) tilting of the URS until an individual collagen fiber lies perpendicular to the light ray of the PLM [24]. Finally, the experimentally identified collagen fiber orientations may be fitted to a statistical distribution, like the Bingham distribution [29]

$$\rho(\theta, \phi) = c^{-1} \exp[\kappa_1(\cos\theta\cos\phi)^2 + \kappa_2(\cos\phi\sin\theta)^2], \tag{4.6}$$

where κ_1 and κ_2 denote distribution parameters to be identified from experimental data. In addition c serves a as normalization parameter, such that $\int_{\phi=0}^{\pi/2}\int_{\theta=0}^{2\pi}\rho\cos\phi \mathrm{d}\phi\mathrm{d}\theta = 1$ holds, i.e., the total amount of collagen fibers remains constant. Further details are given elsewhere [26] and Fig. 4.7 illustrates the collagen fiber distribution in the AAA wall, for example.

4.3.3 *Proteoglycans*

Proteoglycan (PG) bridges may provide interfibrillar load transition [30, 31], a necessity for a load-carrying collagen fiber. Specifically, small proteoglycans such as decorin bind noncovalently but specifically to collagen fibrils and cross-link adjacent collagen fibrils at about 60 nm intervals [30]. Reversible deformability of the PG bridges is crucial to serve as shape-maintaining modules [30] and fast and slow deformation mechanisms have been identified. The fast (elastic) deformation is supported by the sudden extension of about 10 % of the L-iduronate (an elastic sugar)

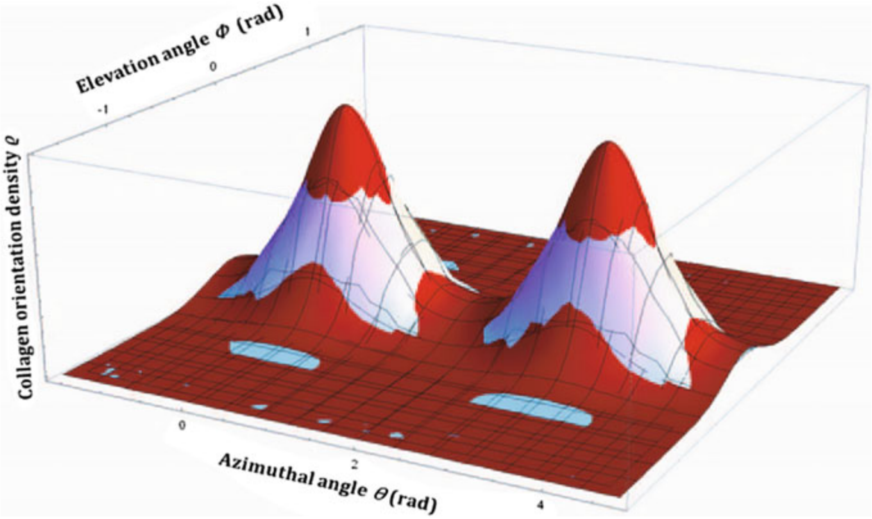

Fig. 4.7 Bingham distribution function (*red*) fitted to the experimentally measured fiber orientation distribution (*light-blue*) in the Abdominal Aortic Aneurysm (AAA) wall. Least-square optimization of Eq. (4.6) with experimental measurements taken from Polarized Light Microscopy (PLM) defined Bingham parameters of $\kappa_1 = 11.6$ and $\kappa_2 = 9.7$

at a critical load of about 200 pN [32]. The slow (viscous) deformation is based on a sliding filament mechanism of the twofold helix of the glycan [30], and explains the large portion of macroscopic viscoelasticity seen when experimentally testing collagen.

PG-based cross-linking is supported by numerous experimental studies showing that PGs play a direct role in inter-fibril load sharing [30, 33–35]. This has also been verified through theoretical investigations [36–38]. However, it should also be noted that the biomechanical role of PGs is somewhat controversial, and some data indicates minimal, if any, PG contribution to the tensile properties of the tissue [36, 39, 40].

Summary At higher strains collagen fibers, and their interaction with the ECM, are the dominant load-carrying structures in the vascular wall. Specifically, the amount and organization of these structures dominate vessel wall's stiffness, strength, and toughness. Consequently, mechanical failure of soft biological tissues is often closely related to rupture, pull-out or plastic stretching of collagen fibers.

4.4 Irreversible Constitutive Modeling of Vascular Tissue

Constitutive modeling of vascular tissue is an active field of research and numerous descriptions have been reported. A phenomenological approach [41–45] may successfully fit experimental data, but it cannot allocate stress or strain to the different histological constituents in the vascular wall. Structural constitutive descriptions [20, 46–52] overcome this limitation and integrate histological and mechanical information of the arterial wall.

Specifically, one class of models, histomechanical constitutive models say, aims at integrating collagen fiber stress σ and orientation density ρ according to *Lanir's* pioneering work [46]. This powerful approach assumes that the macroscopic Cauchy stress $\boldsymbol{\sigma}$ is defined by a superposition of individual collagen fiber contributions, i.e.,

$$\boldsymbol{\sigma} = \frac{2}{\pi} \int_{\phi=0}^{\pi/2} \int_{\theta=0}^{\pi/2} \rho(\phi, \theta)\sigma(\lambda)\mathrm{d}ev(\mathbf{m} \otimes \mathbf{m}) \cos\phi \mathrm{d}\phi \mathrm{d}\theta + p\mathbf{I}, \tag{4.7}$$

where $\mathbf{m} = \mathbf{FM}/|\mathbf{FM}|$ denotes the spatial orientation vector of the collagen fiber. In Eq. (4.7) the collagen fiber's Cauchy stress $\sigma(\lambda)$ is related to its stretch λ. In addition, the term $p\mathbf{I}$ denotes the hydrostatic stress with p being a Lagrange parameter that is independent from the tissue's constitution but is defined by the problem's boundary conditions.

Equation (4.7) is numerically integrated by spherical t-designs, i.e., $\int_\omega (\bullet)\mathrm{d}\omega \approx (4\pi/l_{\mathrm{int}}) \sum_{l=1}^{l_{\mathrm{int}}} (\bullet)_l$, where l_{int} denotes the total number of integration points. A spherical t-design integrates a polynomial expression $(\bullet)$ of degree $\leq t$ exactly [53], and further details regarding the numerical integration are given elsewhere [54].

4.4.1 An Elastoplastic Damage Model for Collagenous Tissue

Exposing biological soft tissue to supra-physiological mechanical stresses rearranges the tissue's microstructure by irreversible deformations. Damage-related effects (such as, for tendon and ligament [55, 56] and for vascular tissue [57–59]) and plasticity-related effects (such as, for skin [60], tendon and ligament [55, 61, 62] and vascular tissues [59, 63]) have been documented. These observations triggered the development of models that account for damage [64–66], plasticity [67, 68], and fracture [69–73]. Most commonly a macroscopic (single scale) view of tissues is followed, which cannot account for the (experimentally observed) localized structural rearrangement of collagen fibrils at supra-physiological mechanical stress. For example, in tendon tissue spatial micro-failure (most likely collagen fibril rupture) is seen already at 51 ± 12 % of the ultimate tissue strength [74], which might even have been preceded by damage from intra-fibrillar sliding [75]. In contrast to a macroscopic metric, histomechanical modeling according to Eq. (4.7) naturally integrates localized damage of individual collagen fibers.

Modeling assumptions Vascular tissue is regarded as a solid mixture at finite deformations, where collagen fibers are embedded in an isotropic matrix material. An orientation density function $\rho(\mathbf{M}) = \rho(-\mathbf{M})$ defines the spatial alignment of collagen

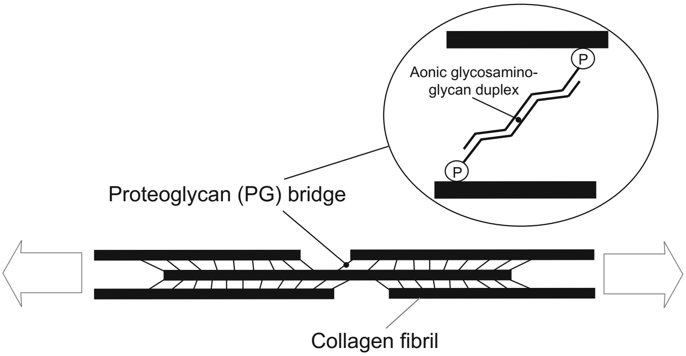

Fig. 4.8 Schematic load-carrying mechanisms of a collagen fiber assembled by a number of collagen fibrils. Load transition across collagen fibrils is provided by Proteglycan (PG) bridges. Antiparallel anionic glycosaminoglycan duplex binds non-covalently to the collagen fibrils at the proteglycan protein (P)

fibers with respect to the reference volume, see Sect. 4.3.2. Specifically, $\rho(\mathbf{M})$ defines the amount of collagen that is aligned along the direction $\mathbf{M}$ with $|\mathbf{M}| = 1$, see [20, 46].

A particular collagen fiber is assembled by a bundle of collagen fibrils, and the model assumes that all such collagen fibrils engage simultaneously at the straightening stretch λ_{st}, i.e., no continuous engagement (as it has been suggested elsewhere [47, 49, 52]), has been regarded. Beyond λ_{st}, collagen fibrils are stretched and interfibrilar material is sheared, see Fig. 4.8. Specifically, the mechanical properties of the PG bridges determine sliding of collagen fibrils relatively to each other.

Sliding of the PG bridge becomes irreversible as soon as the overlap of the glycan chains decreases below a critical level (see [30] and references therein), which in turn causes irreversible (plastic) deformations that are observed in macroscopic experimental testing of vascular tissues, for example. At increasing stretch, PG bridges slide apart (rupture), and the loss of cross-links weakens (damages) the collagen fiber. PG filament sliding represents a slow (viscous) deformation mechanism [31], and the loss of PG bridges is regarded as a gradual and time-dependent process.

The above-discussed deformation mechanism of a collagen fiber motivates the introduction of a ‘stretch-based’ constitutive concept, where irreversible (plastic) sliding of the collagen fibrils not only defines the fiber’s irreversible elongation but also its state of damage. Consequently, plastic deformation of the collagen fiber is directly linked to fiber damage.

Kinematics The assumed affine deformation between matrix and collagen fibers directly relates the total fiber stretch $\lambda = \sqrt{\mathbf{M} \cdot \mathbf{C}\mathbf{M}} = |\mathbf{F}\mathbf{M}|$ to the matrix deformation. Following multiplicative decomposition, the total stretch $\lambda = \lambda_{\text{el}}\lambda_{\text{st}}$ is decomposed into λ_{st}, a stretch that removes fiber undulation, and λ_{el} that elastically stretches the fiber.

Constitutive model of the collagen fiber The model assumes that collagen fibers (and fibrils) have no bending stiffness, and at stretches below λ_{st} the fiber stress is zero. Exceeding λ_{st}, a linear relation between the effective second Piola-Kirchhoff stress $\widetilde{S}_{\mathrm{c}}$ and the elastic stretch λ_{el} holds, i.e., $\widetilde{S}_{\mathrm{c}} = c_{\mathrm{f}}\langle\lambda_{\mathrm{el}} - 1\rangle = c_{\mathrm{f}}\langle\lambda/\lambda_{\mathrm{st}} - 1\rangle$, where c_{f} and λ denote the stiffness of the collagen fiber and its total stretch, respectively. The Macauley-brackets $\langle\bullet\rangle$ have been introduced to explicitly emphasize that a collagen fiber can only carry tensile load.

Considering incompressible elastic fiber deformation, the effective first Piola-Kirchhoff stress reads $\widetilde{P}_{\mathrm{c}} = c_{\mathrm{f}}\langle\lambda_{el}^2 - \lambda_{el}\rangle$, which reveals the constitutive relation using work-conjugate variables. Within reasonable deformations, this relation shows an almost linear first Piola-Kirchhoff stress versus engineering strain $\varepsilon_{el} = \lambda_{\mathrm{el}} - 1$ response, which is also experimentally observed [76, 77].

The state of damage of the collagen fiber is defined by an internal state (damage) variable d, such that the second Piola-Kirchhoff stress of the collagen fiber reads

$$S_{\mathrm{c}} = (1-d)\widetilde{S}_{\mathrm{c}} = (1-d)c_{\mathrm{f}}\langle\lambda/\lambda_{\mathrm{st}} - 1\rangle. \tag{4.8}$$

The damage variable d reflects the loss of stiffness according to slid apart (broken) PG bridges.

Plastic Deformation. Plastic deformation develops at large sliding of PG bridges, i.e., as soon as the overlap between the glycan chains of a PG bridge decrease below a critical level [30]. The proposed model records plastic deformation by a monotonic increase of the straightening stretch $\lambda_{\mathrm{st}\,0} \le \lambda_{\mathrm{st}} < \infty$, where $\lambda_{\mathrm{st}\,0}$ denotes the straightening stretch of the initial (not yet plastically deformed) tissue. The initial straightening stretch $\lambda_{\mathrm{st}\,0}$ is thought to be a structural property defined by the continuous turn-over of collagen and determined by the biomechanical and biochemical environment that the tissue experiences in vivo. Following the theory of plasticity [78, 79], we introduce an elastic threshold Y that classifies the following load cases,

$$\left.\begin{array}{l} \widetilde{S}_{\mathrm{c}} < Y \text{ elastic deformation,} \\ \widetilde{S}_{\mathrm{c}} = Y \text{ plastic deformation,} \\ \widetilde{S}_{\mathrm{c}} > Y \text{ to be ruled out.} \end{array}\right\} \tag{4.9}$$

At quasi-static loading conditions an ideal plastic response is considered with $Y = Y_0$ reflecting the elastic limit (in an effective second Piola Kirchhoff setting) of the collagen fiber. In contrast, time-dependent plastic loading is thought to induce a hardening effect, i.e., $Y = Y_0 + H$, where H reflects the increase of resistance against collagen fibril sliding due to the slow (viscous) sliding mechanism of the PG bridges. Consequently, a viscoplastic behavior of the collagen fibers is considered, and (for simplicity) the first-order rate equation

$$H = \eta\dot{\lambda}_{\mathrm{st}} \tag{4.10}$$

defines the viscous hardening, with η denoting a material parameter.

Table 4.1 Material and structural parameters used for computing a tensile test of tissue from the Abdominal Aortic Aneurysm (AAA) wall

Collagen fiber orientation	
Bingham parameters	$\kappa_1 = 11.6\ ;\ \kappa_2 = 9.7$
Matrix material properties	
neoHookean parameter	$c = 0.02$ MPa
Collagen fiber properties	
Straightening stretch	$\lambda_{\text{st}\,0} = 1.08$
Collagen fiber stiffness	$c_{\text{f}} = 0.23$ MPa
Elastic limit	$Y_0 = 0.063$ MPa
Hardening viscosity	$\eta = 0.2$ MPa s
Damage property	$a = 50.0$

Damage accumulation. As detailed above, larger irreversible (plastic) deformation of the collagen fiber causes failure of PG bridges, which in turn weakens the collagen fiber. The mechanical effect from ruptured PG bridges, i.e. the loss of stiffness of the collagen fiber is recorded by the damage parameter d, where an exponential relation

$$d = 1 - \exp[-a(\lambda_{\text{st}}/\lambda_{\text{st}\,0} - 1)^2] \tag{4.11}$$

with respect to the plastic deformation (reflected by $\lambda_{\text{st}}/\lambda_{\text{st}\,0}$) is considered. Equation (4.11) has the properties $d(\lambda_{\text{st}}/\lambda_{\text{st}\,0} = 1.0) = 0.0$ and $d(\lambda_{\text{st}}/\lambda_{\text{st}\,0} \to \infty) = 1.0$, and a denotes a material parameter. Specifically, small and large values of a define ductile and brittle-like failure of the collagen fiber, respectively.

Details regarding the numerical implementation of this model are given elsewhere [50].

Basic model characteristics A single finite element was used to investigate basic characteristics of the constitutive model. To this end constitutive parameters (listed in Table 4.1) were manually estimated from in vitro tensile test data of the AAA wall, and the histologically measured collagen orientation distribution was prescribed, see Sect. 4.3.2.

The model captures the strongly nonlinear stiffening at lower stresses (toe region up to 50 kPa), where the initial straightening stretch $\lambda_{\text{st}\,0}$ allows to control the transition point from a matrix-dominated to a collagen-dominated tissue response, see Fig. 4.9.

By increasing the load beyond the toe region, a slightly nonlinear relation between the first Piola-Kirchhoff stress and stretch is observed, before collagen fibers gradually exceed their elastic limit, which in turn defines a concave stress–stretch response, see Fig. 4.9. Again, gradually exceeding the collagen fibers' elastic limit defines a smooth transition from a convex to a concave curve, a response typically observed in experimental testing of vascular tissue.

Significant plastic deformation is required before the ultimate first Piola-Kirchhoff strength of about 0.18 MPa is reached. A further increase in stretch causes material instability, i.e., loss of ellipticity, and the deformation localizes. As outlined in

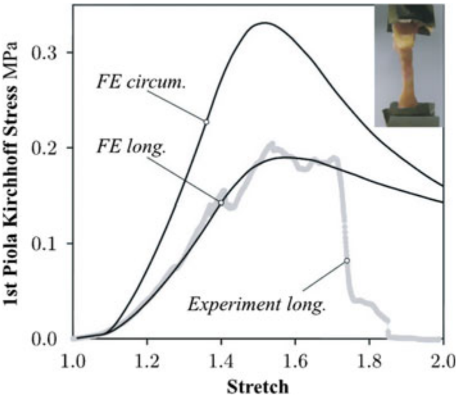

Fig. 4.9 Macroscopic constitutive response of Abdominal Aortic Aneurysm (AAA) wall tissue under uniaxial tension. *Solid black curves* denote tension responses along the circumferential and longitudinal directions, respectively. The *grey curve* illustrates the response from in vitro experimental stretching of a single AAA wall specimen along the longitudinal direction. The test specimen used for experimental characterization of AAA wall tissue is shown at the *top right*

Sect. 4.2, in the strain softening region the results strongly depend on the test specimen's length. Here, neither the computational model used an internal length scale nor the experimental setup allowed controlled failure progression, such that these curves contain no constitutive information in the strain softening region. Influence of the strain rate and model response to cyclic loading are detailed in [50].

Summary Damage of vascular tissue can involve several interacting irreversible mechanisms. The presented model considered a coupling between plastic elongation and weakening of collagen fibers, irreversible mechanisms that can be explained by the deformation of PG bridges. The mechanical complexity of vascular tissue leads to descriptions that require many material parameters, which naturally complicates inverse parameter estimation—especially if parameters are mathematically not independent. A constitutive descriptions with model parameters of physical interpretation are particularly helpful for a robust model parameter identification.

4.5 Failure Represented by Interface Models

As shown in Sect. 4.2.1 of this chapter, stretching a rod until the strong ellipticity condition is violated, causes strains to localize within a small (infinitesimal) volume. For such a case the nonpolar continuum yields nonphysical post localization results. However, the cross-sectional area, within which strain localizes, remains finite. Consequently, introducing a failure surface, within which all inelastic processes take place, successfully resolves this issue. Such defined failure surface is then equipped with constitutive information, i.e., a cohesive traction separation law defines the traction that acts at the discontinuity as a function of its opening, i.e., the opening of the fracture. Such an approach goes back to the pioneering works for elastoplastic fracture in metals [80, 81], and for quasi-brittle failure of concrete materials [82].

4.5.1 Continuum Mechanical Basis

Discontinous kinematics As illustrated in Fig. 4.10, $\partial\Omega_{0\,\mathrm{d}}$ denotes a strong discontinuity embedded in the reference configuration Ω_0 of a body. The discontinuity separates the body into two sub-bodies occupying the referential sub-domains Ω_{0+} and Ω_{0-}. The orientation of the discontinuity at an arbitrary point $\mathbf{X}_\mathrm{d}$ is defined by its normal vector $\mathbf{N}(\mathbf{X}_\mathrm{d})$, where $\mathbf{N}$ is assumed to point into Ω_{0+}, see Fig. 4.10.

The discontinuous displacement field $\mathbf{u}(\mathbf{X}) = \mathbf{u}_\mathrm{c}(\mathbf{X}) + \mathcal{H}(\mathbf{X})\mathbf{u}_\mathrm{e}(\mathbf{X})$ at a referential position $\mathbf{X}$ is based on an additive decomposition of $\mathbf{u}(\mathbf{X})$ into compatible $\mathbf{u}_\mathrm{c}$ and enhanced $\mathcal{H}\mathbf{u}_\mathrm{e}$ parts, respectively [83, 84]. Here, $\mathcal{H}(\mathbf{X})$ denotes the Heaviside function, with the values 0 and 1 for $\mathbf{X} \in \Omega_{0-}$ and $\mathbf{X} \in \Omega_{0+}$, respectively. Note that both introduced displacement fields, i.e., $\mathbf{u}_\mathrm{c}$ and $\mathbf{u}_\mathrm{e}$ are continuous and the embedded discontinuity is represented by the Heaviside function $\mathcal{H}$.

Following [85–87], we define a *fictitious* discontinuity $\partial\Omega_\mathrm{d}$ as a bijective map of $\partial\Omega_{0\,\mathrm{d}}$ to the current configuration. Specifically, $\partial\Omega_\mathrm{d}$ is placed in between the two (physical) surfaces defining the crack, see Fig. 4.10. Therefore, we introduce an average deformation gradient $\mathbf{F}_\mathrm{d}$ at $\mathbf{X}_\mathrm{d}$ according to

$$\mathbf{F}_\mathrm{d}(\mathbf{X}_\mathrm{d}) = \mathbf{I} + \mathbf{Grad}\left(\mathbf{u}_\mathrm{c} + \frac{1}{2}\mathbf{u}_\mathrm{e}\right) = \mathbf{I} + \mathbf{Grad}\,\mathbf{u}_\mathrm{c} + \frac{1}{2}\mathbf{u}_\mathrm{e} \otimes \mathbf{N}, \tag{4.12}$$

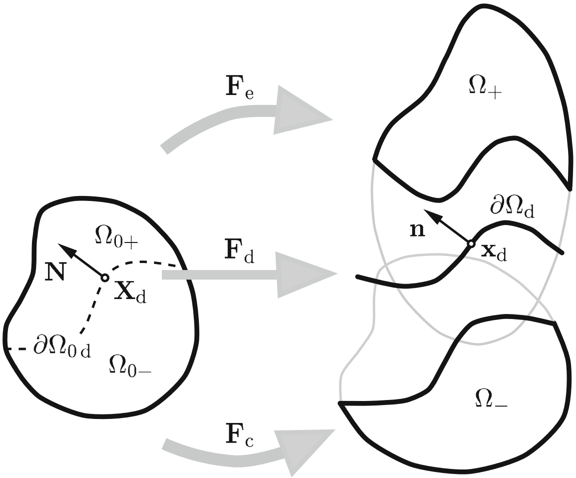

Fig. 4.10 Discontinuous kinematics representing the reference configuration $\Omega_0 = \Omega_{0+} \cup \Omega_{0-} \cup \partial\Omega_{0\,\mathrm{d}}$ and the current configuration $\Omega = \Omega_+ \cup \Omega_- \cup \partial\Omega_\mathrm{d}$ of a body separated by a strong discontinuity. The associated three deformation gradients: (i) $\mathbf{F}_\mathrm{e} = \mathbf{I} + \mathbf{Grad}\,\mathbf{u}_\mathrm{c} + \mathbf{Grad}\,\mathbf{u}_\mathrm{e}$, (ii) $\mathbf{F}_\mathrm{d} = \mathbf{I} + \mathbf{Grad}\,\mathbf{u}_\mathrm{c} + \mathbf{u}_\mathrm{e} \otimes \mathbf{N}/2$ and (iii) $\mathbf{F}_\mathrm{c} = \mathbf{I} + \mathbf{Grad}\,\mathbf{u}_\mathrm{c}$

where the factor $1/2$ enforces the fictitious discontinuity $\partial\Omega_{\mathrm{d}}$ to be placed in the middle between the two (physical) surfaces defining the crack. Based on the deformation (4.12), the unit normal vector $\mathbf{n}$ to the fictitious discontinuity is defined by

$$\mathbf{n} = \frac{\mathbf{N}\mathbf{F}_{\mathrm{d}}{}^{-1}}{|\mathbf{N}\mathbf{F}_{\mathrm{d}}{}^{-1}|}, \tag{4.13}$$

which can be interpreted as a weighted *push-forward* operation of the covariant vector $\mathbf{N}$.

Consequently, the introduced kinematical description of a strong discontinuity requires three deformations, as illustrated in Fig. 4.10, i.e., (i) the compatible deformation gradient $\mathbf{F}_{\mathrm{c}} = \mathbf{I} + \mathbf{Grad}\,\mathbf{u}_{\mathrm{c}}$ (with $\det \mathbf{F}_{\mathrm{c}} = J_{\mathrm{c}} > 0$), which maps Ω_{0-} into Ω_{-} as known from standard continuum mechanics; (ii) the enhanced deformation gradient $\mathbf{F}_{\mathrm{e}} = \mathbf{I} + \mathbf{Grad}\,\mathbf{u}_{\mathrm{c}} + \mathbf{Grad}\,\mathbf{u}_{\mathrm{e}}$ (with $\det \mathbf{F}_{\mathrm{e}} = J_{\mathrm{e}} > 0$), which maps Ω_{0+} into Ω_{+}, and finally, (iii) the average deformation gradient $\mathbf{F}_{\mathrm{d}} = \mathbf{I} + \mathbf{Grad}\,\mathbf{u}_{\mathrm{c}} + \mathbf{u}_{\mathrm{e}} \otimes \mathbf{N}/2$ (with $\det \mathbf{F}_{\mathrm{d}} = J_{\mathrm{d}} > 0$), which maps the referential discontinuity $\partial\Omega_{0\,\mathrm{d}}$ into the (fictitious) spatial discontinuity $\partial\Omega_{\mathrm{d}}$. Finally, any strain measure directly follows from the introduced deformation gradients, see elsewhere [86] for example.

Cohesive traction response We assume the existence of a transversely isotropic (note that these type of models are denoted as isotropic elsewhere [88]) cohesive potential $\psi(\mathbf{u}_{\mathrm{d}}, \mathbf{n}, \delta)$ per unit undeformed area over $\partial\Omega_{0\,\mathrm{d}}$, which governs the material dependent resistance against failure in a phenomenological sense [88]. The cohesive zone's properties are assumed to be dependent on the gap displacement $\mathbf{u}_{\mathrm{d}} = \mathbf{u}_{\mathrm{e}}(\mathbf{X}_{\mathrm{d}})$, the current normal $\mathbf{n}$ and a scalar internal variable δ. Finally, the cohesive potential is subjected to objectivity requirements, i.e., $\psi(\mathbf{u}_{\mathrm{d}}, \mathbf{n}, \delta) = \psi(\mathbf{Q}\mathbf{u}_{\mathrm{d}}, \mathbf{Q}^{\text{-T}}\mathbf{n}, \delta)$, where $\mathbf{Q}$ is an arbitrary proper orthogonal tensor, i.e., $\mathbf{Q}^{\mathrm{T}} = \mathbf{Q}$, $\det \mathbf{Q} = 1$.

The model is complemented by the introduction of a damage surface $\phi(\mathbf{u}_{\mathrm{d}}, \delta)$ in the gap displacement $\mathbf{u}_{\mathrm{d}}$ space and Karush–Kuhn–Tucker loading/unloading $\dot{\delta} \geq 0$, $\phi \leq 0$, $\dot{\delta}\phi = 0$ and consistency $\dot{\delta}\dot{\phi} = 0$ conditions are enforced.

Based on the procedure by Coleman and Noll [89] the cohesive traction $\mathbf{T}$ and the internal dissipation $\mathcal{D}_{\mathrm{int}}$ take the form

$$\mathbf{T} = \frac{\partial\psi}{\partial\mathbf{u}_{\mathrm{d}}}, \quad \mathcal{D}_{\mathrm{int}} = -\frac{\partial\psi}{\partial\delta}\dot{\delta} \geq 0. \tag{4.14}$$

An efficient application of a cohesive model within the FE method requires a consistent linearization of the cohesive traction $\mathbf{T}$ with respect to the opening displacement $\mathbf{u}_{\mathrm{d}}$. In order to provide this, we introduce $\mathbf{C}_{\mathbf{u}_d} = \partial\mathbf{T}/\partial\mathbf{u}_{\mathrm{d}}$, $\mathbf{C}_{\mathbf{n}} = \partial\mathbf{T}/\partial\mathbf{n}$, $\mathbf{C}_{\delta} = \partial\mathbf{T}/\partial\delta$, which describes the cohesive zone's stiffness with respect to gap displacement opening, rotation and growing damage.

Variational formulation In order to provide the variational basis for a quasi-static FE model, we start with a single-field variational principle [90], i.e., $\int_{\Omega_0} \mathbf{Grad}\,\delta\mathbf{u} : \mathbf{P}(\mathbf{F})\mathrm{d}V - \delta\Pi^{ext}(\delta\mathbf{u}) = 0$, where $\mathbf{P}(\mathbf{F})$ and $\delta\mathbf{u}$ denote the first Piola-Kirchhoff stress tensor and the admissible variation of the displacement field. The integration is taken over the reference configuration Ω_0, where $\mathrm{d}V$ denotes the referential volume element. In addition, the contributions from external loading, i.e., body force and prescribed traction on the von Neumann boundary, are summarized in the virtual external potential energy $\delta\Pi^{ext}(\delta\mathbf{u})$.

According to the introduced displacement field, its admissible variation reads $\delta\mathbf{u} = \delta\mathbf{u}_\mathrm{c} + \mathcal{H}\delta\mathbf{u}_\mathrm{e}$. Consequently, $\mathbf{Grad}\,\delta\mathbf{u} = \mathbf{Grad}\,\delta\mathbf{u}_\mathrm{c} + \mathcal{H}\mathbf{Grad}\,\delta\mathbf{u}_\mathrm{e} + \delta_\mathrm{d}(\delta\mathbf{u}_\mathrm{e} \otimes \mathbf{N})$, which defines the two variational statements

$$\left.\begin{aligned} \int_{\Omega_0} \mathbf{Grad}\,\delta\mathbf{u}_\mathrm{c} : \mathbf{P}(\mathbf{F})\mathrm{d}V - \delta\Pi^{ext}_\mathrm{c}(\delta\mathbf{u}_\mathrm{c}) &= 0, \\ \int_{\Omega_{0+}} \mathbf{Grad}\,\delta\mathbf{u}_\mathrm{e} : \mathbf{P}(\mathbf{F})\mathrm{d}V + \int_{\partial\Omega_{0\,\mathrm{d}}} \mathbf{T}\cdot\delta\mathbf{u}_\mathrm{e}\mathrm{d}S - \delta\Pi^{ext}_\mathrm{e}(\delta\mathbf{u}_\mathrm{e}) &= 0, \end{aligned}\right\} \tag{4.15}$$

where $\delta\Pi^{ext}_\mathrm{c}(\delta\mathbf{u}_\mathrm{c})$ and $\delta\Pi^{ext}_\mathrm{e}(\delta\mathbf{u}_\mathrm{e})$ are external contributions associated with the compatible and enhanced displacements, respectively.

After some manipulations and a push-forward of Eq. (4.15), we achieve its spatial version [91],

$$\left.\begin{aligned} \int_{\Omega_-} \mathrm{sym}(\mathbf{g}rad_{\,\mathrm{c}}\delta\mathbf{u}_\mathrm{c}) : \boldsymbol{\sigma}_\mathrm{c}\mathrm{d}v + \int_{\Omega_+} \mathrm{sym}(\mathbf{g}rad_{\,\mathrm{e}}\delta\mathbf{u}_\mathrm{c}) : \boldsymbol{\sigma}_\mathrm{e}\mathrm{d}v - \delta\Pi^{ext}_\mathrm{c}(\delta\mathbf{u}_\mathrm{c}) &= 0, \\ \int_{\Omega_+} \mathrm{sym}(\mathbf{g}rad_{\,\mathrm{e}}\delta\mathbf{u}_\mathrm{e}) : \boldsymbol{\sigma}_\mathrm{e}\mathrm{d}v + \int_{\partial\Omega_\mathrm{d}} \mathbf{t}\cdot\delta\mathbf{u}_\mathrm{e}\mathrm{d}s - \delta\Pi^{ext}_\mathrm{e}(\delta\mathbf{u}_\mathrm{e}) &= 0, \end{aligned}\right\} \tag{4.16}$$

where $\mathrm{d}v$ and $\mathrm{d}s$ are the spatial volume and surface elements, respectively. Moreover, $\boldsymbol{\sigma}_\mathrm{c} = J_\mathrm{c}^{-1}\mathbf{P}(\mathbf{F}_\mathrm{c})\mathbf{F}_\mathrm{c}^\mathrm{T}$ and $\boldsymbol{\sigma}_\mathrm{e} = J_\mathrm{e}^{-1}\mathbf{P}(\mathbf{F}_\mathrm{e})\mathbf{F}_\mathrm{e}^\mathrm{T}$ denote the Cauchy stress tensors and $\mathbf{t} = \mathbf{T}\mathrm{d}S/\mathrm{d}s$ is the Cauchy traction vector associated with a fictitious discontinuity $\partial\Omega_\mathrm{d}$. The spatial gradients in (4.16) are defined according to $\mathbf{g}rad_{\,\mathrm{c}}(\bullet) = \mathbf{Grad}\,(\bullet)\mathbf{F}_\mathrm{c}{}^{-1}$, $\mathbf{g}rad_{\,\mathrm{e}}(\bullet) = \mathbf{Grad}\,(\bullet)\mathbf{F}_\mathrm{e}{}^{-1}$ and $\mathrm{sym}(\bullet) = ((\bullet) + (\bullet)^\mathrm{T})/2$ furnishes the symmetric part of $(\bullet)$.

The consistent linearization of the variational statements can be found elsewhere [70, 86].

4.5.2 Formulation for the Cohesive Material Model

In order to particularize the transversely isotropic cohesive model introduced in Sect. 4.5.1, we restrict our considerations to the class of models $\psi = \psi(\mathbf{u}_\mathrm{e} \otimes \mathbf{u}_\mathrm{e}, \mathbf{n} \otimes \mathbf{n}, \delta)$ and apply the theory of invariants [92]. Hence, the cohesive potential can be expressed according to $\psi = \psi(i_1, i_2, i_3, i_4, i_5, \zeta)$, where $i_1, \dots, i_5$ are invariants, which depend on the symmetric tensors $\mathbf{u}_\mathrm{e} \otimes \mathbf{u}_\mathrm{e}$, and $\mathbf{n} \otimes \mathbf{n}$ [91].

As a special case the isotropic particularization

$$\psi(i_1, \zeta) = \frac{t_0}{2\zeta}\exp(-a\delta^b)i_1 \tag{4.17}$$

is used. Here, $i_1 = \mathbf{u}_\mathrm{e} \cdot \mathbf{u}_\mathrm{e}$ is the first invariant, t_0 denotes the cohesive tensile strength and the nonnegative parameters a and b aim to capture the softening response from failure progression.

In addition, we define a damage surface $\phi(\mathbf{u}_\mathrm{e}, \delta) = |\mathbf{u}_\mathrm{e}| - \zeta = 0$ in the three-dimensional gap displacement space and assume $\dot{\zeta} = \dot{\overline{|\mathbf{u}_\mathrm{e}|}}$ for the evolution of the internal (damage) variable $\zeta \in [0, \infty[$. A proof of nonnegativeness of the dissipation, i.e., $\mathcal{D}_\mathrm{int} \geq 0$, of the introduced cohesive model is given elsewhere [91], and the underlying cohesive traction and associated stiffness measures read,

$$\mathbf{T} = c\mathbf{u}_\mathrm{e}, \quad \mathbf{C}_{\mathbf{u}_e} = c\mathbf{I}, \quad \mathbf{C}_\mathbf{n} = \mathbf{0}, \quad \mathbf{C}_\delta = -\gamma \mathbf{u}_\mathrm{e}, \tag{4.18}$$

where the two scalars

$$c = \frac{t_0}{\zeta} \exp(-a\zeta^b), \quad \gamma = \frac{c}{\zeta}(1 + ab\zeta^b) \tag{4.19}$$

uniquely describe the cohesive law at a certain state of damage δ.

Initialization criterion. The proposed FE implementation of the model assumes that the cohesive zone increases dynamically during the computation. In particular, the cohesive zone model is activated within a finite element if the initialization criterion $\mathcal{C}_\mathrm{init} > 0$ is satisfied. Herein, we use a Rankine criterion

$$\mathcal{C}_\mathrm{init} = \mathbf{n} \cdot \boldsymbol{\sigma}\mathbf{n} - t_0 \frac{\mathrm{d}s}{\mathrm{d}S}, \tag{4.20}$$

where $\mathbf{n}$ denotes the perpendicular direction to the discontinuity in the spatial configuration. The formulation of the cohesive potential ψ with respect to reference area, see Sect. 4.5.1, motivated the introduction of the area ratio $\mathrm{d}s/\mathrm{d}S$ in criterion (4.20).

Summary The introduced model for tissue failure postulates the existence of a cohesive fracture process zone, a discrete surface (discontinuity) that represents initialization and coalescence of micro-cracks. A phenomenological traction separation law specifies the failure mechanics, i.e., how the traction across the discontinuity decreases with increasing crack opening. Such defined discontinuity has been embedded in the continuum, which effectively allows post-localization analyses.

4.6 Applications

4.6.1 Organ Level Simulation of Abdominal Aortic Aneurysm Rupture

The elastoplastic damage model for collagenous tissue detailed in Sect. 4.4 was deployed to simulate AAA inflation until structural collapse, i.e., until a quasi-static solution of the problem could no longer be computed. The observed structural collapse might also have caused material instability, i.e., loss of strong ellipticity [93, 94]. However, this was not further investigated.

Modeling assumptions The AAA has been segmented from Computed Tomography-Angiography (CT-A) images (A4clinics Research Edition, VASCOPS GmbH), where deformable (active) contour models [95] supported an artifact-insensitive and operator-independent 3D reconstruction. The aneurysm was segmented between the renal arteries and about two centimeters distal the aortic bifurcation. The geometry was meshed by hexahedral finite elements, and the structural analysis was carried out in FEAP (University of California at Berkeley). Blood pressure was applied as a follower load, and all nodal degrees of freedom were locked at the aneurysm's bottom and top slices. No contact with surrounding organs was considered, and further modeling details are given elsewhere [50].

Load case (a) increased the blood pressure at 10 mmHg/s until structural collapse was experienced. In contrast, load case (b) assumed a cyclic pulsatile blood pressure between 280 mmHg and 120 mmHg and at a frequency of one Hertz. Note that the investigated aneurysm was rather small, such that unrealistically high blood pressures were required to trigger AAA rupture.

Results *Load Case (a).* The development of the maximum principal Cauchy stress and the plastic deformation (in terms of the averaged straightening stretch $\overline{\lambda}_{\mathrm{st}} = (1/l_{\mathrm{int}}) \sum_{l=1}^{l_{\mathrm{int}}} \lambda_{\mathrm{st}\,l}$) during inflation is illustrated in Fig. 4.11. The low loading rate of 10 mmHg/s caused localized plastic deformation and led to a rather brittle failure

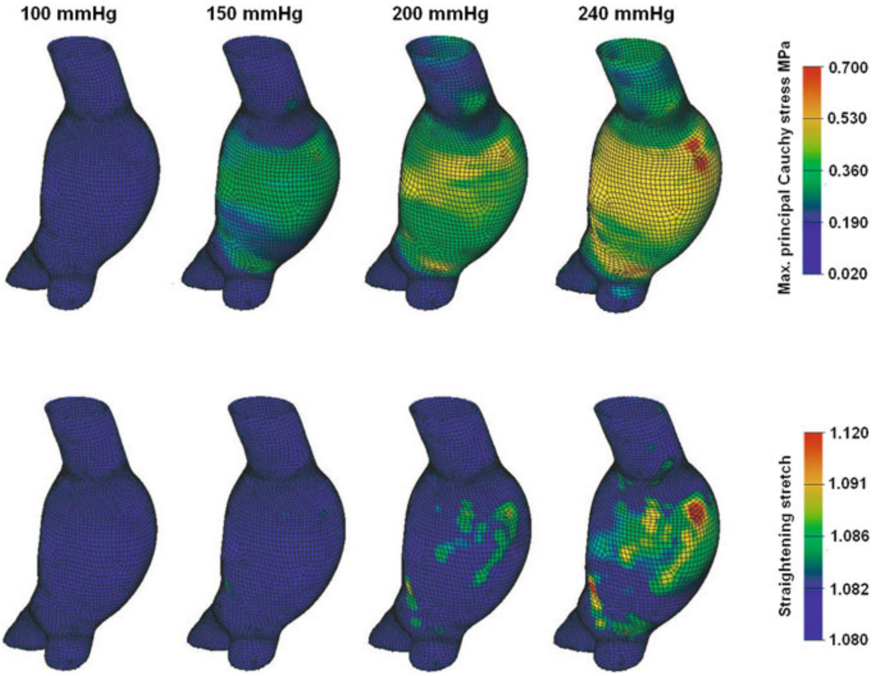

Fig. 4.11 Maximum principal Cauchy stress (*top row*) and plastic deformation (*bottom row*) of an Abdominal Aortic Aneurysm (AAA) at inflation according to Load Case (**a**). FE predictions were based on material properties given in Table 4.1

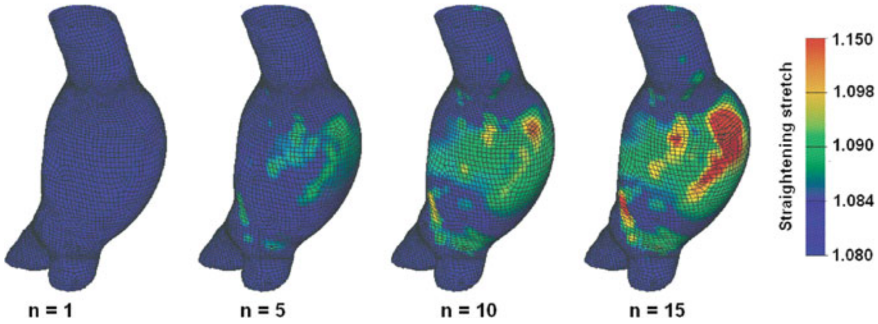

Fig. 4.12 Plastic deformation of an Abdominal Aortic Aneurysm (AAA) at cyclic inflation according to Load Case (**b**). AAA is shown at diastolic pressure, where n denotes the number of inflation cycles. FE predictions were based on material properties given in Table 4.1, and plastic deformation is expressed by the straightening stretch

response. Finally, a single region of concentrated plastic deformation (and tissue damage) developed prior the structure collapsed.

Load Case (b). The development of the plastic deformation (in terms of the averaged straightening stretch $\overline{\lambda}_{\mathrm{st}}$) during cyclic inflation is illustrated in Fig. 4.12, where n denotes the cycle number. The high loading rate of ±320 mmHg/s spread plastic deformations all over the aneurysmatic bulge. Above 15 load cycles the numerical convergence of the problem was poor and the computation was terminated. Plastically deformed wall segments that could have been buckled during deflation, or the highly distorted mesh could also have caused such poor numerical convergence.

4.6.2 Model Parameter Estimation from in Vitro Tensile Tests

Cohort and specimen preparation Tissue samples from the AAA wall (n=16; approximately 10 mm times 20 mm) and the Thoracic Aortic Aneurysm (TAA) wall (n=27; approximately 15 mm times 30 mm) were harvested during open surgical repair at Karolinska University Hospital, Stockholm, Sweden. Bone-shaped test specimens were punched-out from the dissected tissue patches using a custom-made pattern blade, see Fig. 4.13a. Test specimens from the AAA wall and from the TAA wall were aligned along the longitudinal and circumferential vessel directions, respectively. The length of the test specimens varied from 10 mm to 30 mm, and in order to improve specimen fixation in the testing machine, pieces of sand paper were glued to each end of the specimen (Super-adhesive glue, Loctite), see Fig. 4.13b. During specimen preparation the tissue was kept hydrated at any time. For the histological analysis, samples (taken from one part of each AAA test specimen and after the mechanical testing) were fixed, embedded in paraffin, sliced at a thickness of 7.0 μm and stained with picrosirius red to enhance the birefringent properties of

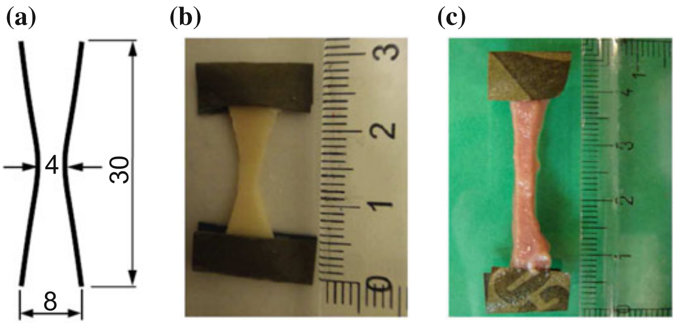

Fig. 4.13 Preparation of uniaxial test specimens. **a** Dimensions (in millimeters) of the pattern blade that was used to punch out test specimens from tissue patches. Typical specimens from the human Thoracic Aortic Aneurysm (TAA) wall (**b**) and from the porcine interventricular septum (**c**). Dimensions shown by the rulers are given in centimeters

collagen. The use of material from human subjects was approved by the local ethics committee and further detail regarding the cohorts is given in [96, 97].

Testing equipment and protocols Prior to failure testing, the test specimen's cross-section A at the neck, i.e., where the specimen was expected to rupture, was measured. Mechanical testing was performed with conventional testing systems (MTS for the AAA samples and Instron for the TAA samples). The load-displacement property of the test specimen was recorded during a displacement-controlled uniaxial tensile test at an elongation rate of 0.1 mm/s. During tensile testing, the test specimens remained entirely in Ringer solution at $37 \pm 0.5\,^\circ$C, and a load cell recorded the force that was applied to the specimen. Further details are given elsewhere [96, 97]. The ultimate first Piola-Kirchhoff strength $P_{\mathrm{ult}} = F_{\mathrm{ult}}/A$ was calculated, where F_{ult} denotes the measured ultimate tensile load.

Identification of collagen fiber orientation and thickness Collagen fiber orientations were identified from PicroSirius red stained histological slices. Measurements were taken with a BX50 polarized light microscope (Olympus) that was equipped with a URS (Carl Zeiss GmbH), as detailed in Sect. 4.3.2.

Numerical model, parameters estimation For each bone-shaped test specimen, a plane-stress FE model with 96 Q1P0 mixed elements [98] was generated. The model was equipped with the elastoplastic constitutive model for collagenous tissue (see Sect. 4.4), and the specimen-individual collagen orientation was considered. The FE models were used to estimate the set $\{c_{\mathrm{m}}, \lambda_{\mathrm{st}\,0}, c_{\mathrm{f}}, a\}$ of material parameters for each wall sample. (For the AAA wall samples, the parameter c_{m} that determines the matrix material was fixed to 0.012 MPa, i.e., a value reported in the literature [52].) The physical meaning of model parameters allowed their straight forward manual estimation. Specifically, parameters were alternated until FE model predictions matched the recorded stress–stretch curves in a least-square sense. Since the constitutive model is not suitable to predict strain localization, the strain softening region was disregarded. Finally, it is noted that a small amount of viscous hardening ($\eta = 0.0001\,\mathrm{MPa\,s}$, see

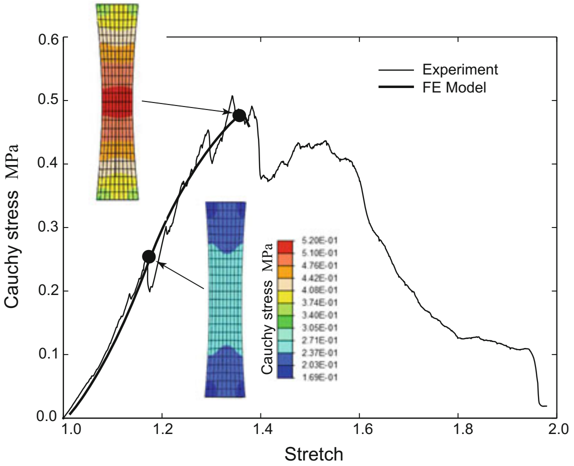

Fig. 4.14 Stress–stretch properties of a single Abdominal Aortic Aneurysm (AAA) wall specimen that is loaded along the axial vessel direction. Recordings from in vitro experiment is overlaid by FE predictions. *Colored-coded images* illustrate the Cauchy stress in tensile direction at two different stretch levels. Stretch is averaged over the length of the tensile specimen

Sect. 4.4) was required to stabilize the FE model, which virtually did not alter the quasi-static result.

Typical results For all cases the applied FE models provided good approximations to the recorded stress–stretch curves, see the representative plot in Fig. 4.14, for example. By increasing the load beyond the toe region, a slightly nonlinear relation between the first Piola-Kirchhoff stress and stretch was observed. Then the collagen fibers gradually exceeded their elastic limit, which led to a concave stress–stretch response. Gradually exceeding the collagen fibers' elastic limit defined a smooth transition from a convex to a concave curve, and significant plastic deformation accumulated before the ultimate strength P_{ult} was reached. A further increase in stretch caused material instability (see Sect. 4.2), which is not covered by the applied constitutive model.

The Cauchy stress in tensile direction at two different deformations is shown in Fig. 4.14a, b. The irreversible overstretching of the tissue homogenizes the stress in the neck of the specimen (not seen for the selected color coding in Fig. 4.14). For AAA wall samples the highest Cauchy stress σ_{ult}= 569(SD 411) kPa appeared in the neck of the specimen and was recorded at a stretch of 1.436(SD 0.118). For TAA samples a stress of σ_{ult}= 1062(SD 736) kPa was reached at a stretch of 1.514(SD 0.214). Identified model parameters are summarized in Table 4.2, and further details are given elsewhere [96, 97].

Table 4.2 Numerically estimated constitutive parameters of Abdominal Aortic Aneurysm (AAA) and Thoracic Aortic Aneurysm (TAA) wall specimens

Specimen	κ_1	κ_2	c_m MPa	λ_{st0}	c_f MPa	Y_0 MPa	a MPa
AAA 1	15.1	13	0.012	1.03	63	12.0	45
AAA 2	20.9	19.1	0.012	1.06	33	4.9	40
AAA 3	16.1	14.2	0.012	1.03	28	3.5	10
AAA 4	8	5.7	0.012	1.03	70	6.4	30
AAA 5	10.5	8.4	0.012	1.03	24	4.4	17
AAA 6a	10.4	7.7	0.012	1.10	25	1.8	10
AAA 6b	10.4	7.7	0.012	1.05	30	3.9	20
AAA 7	9	6.4	0.012	1.01	31	3.1	7
AAA 8	15.6	12.6	0.012	1.01	77	19.2	15
AAA 9	13.4	10.6	0.012	1.02	24	5.1	20
AAA 10	9.5	7.7	0.012	1.00	151	16.8	8
AAA 11a	8	6.3	0.012	1.01	73	9.8	17
AAA 11b	8	6.3	0.012	1.01	27	4.5	10
AAA 12	11.2	9.5	0.012	1.04	55	4.7	23
AAA 13	11.2	10.8	0.012	1.00	14	2.9	7
AAA 14	10.6	8.7	0.012	1.01	45	8.1	60
TAA BAV 1	27.6	25.1	0.05	1.23	7	1.4	20
TAA BAV 2	6.6	4.5	0.06	1.4	24	2.94	25
TAA BAV 3a	24.2	21.4	0.06	1.37	10	2.5	10
TAA BAV 3b	24.2	21.4	0.1	1.12	4.3	1.2	2
TAA BAV 4	27.3	23.5	0.04	1.22	3.2	1.27	10
TAA BAV 5	27.6	23	0.5	1.04	15	3	10
TAA BAV 6	27.1	24.3	0.12	1.11	4.8	1.1	3
TAA BAV 7	28.7	24.6	0.02	1.02	7.2	2.8	10
TAA BAV 8	28.1	22.7	0.17	1.24	7.7	3.5	4
TAA BAV 9	29	21.7	0.1	1.3	10	3.1	2
TAA BAV 10	28.7	23.7	0.13	1.32	13	4	4
TAA BAV 11a	28	23.8	0.06	1.3	10	3.6	7
TAA BAV 11b	28	23.8	0.1	1.17	9	2.2	7
TAA BAV 12	27	23.4	0.07	1.32	7	3.37	5
TAA BAV 13a	30.9	12.2	0.07	1.18	4.9	1.9	5
TAA BAV 13b	30.9	12.2	0.13	1.12	5	2.4	5
TAA TAV 1	12.7	10.6	0.05	1.2	5	0.47	20
TAA TAV 2	28	21.9	0.06	1.21	1.8	0.26	20
TAA TAV 3	23.7	20.1	0.03	1.15	3.6	0.75	5

(continued)

Table 4.2 (continued)

Specimen	κ_1	κ_2	c_{m} MPa	λ_{st0}	c_{f} MPa	Y_0 MPa	a MPa
TAA TAV 4a	26	22.9	0.07	1.28	3.4	0.85	4
TAA TAV 4b	26	22.9	0.1	1.2	1.6	0.7	17
TAA TAV 5	26.2	23.3	0.07	1.12	4.5	2	7
TAA TAV 6	26.9	23.4	0.04	1.1	2	0.65	0.4
TAA TAV 7	25.9	23.4	0.1	1.23	7	2.3	10
TAA TAV 9	26.5	24	0.04	1.17	9	2.9	10
TAA TAV 10	27.3	24.3	0.1	1.1	2.1	0.9	4
TAA TAV 11	29.2	23.9	0.1	1.17	3.1	0.99	4

Collagen orientation is given by the Bingham distribution parameters κ_1 and κ_2 (see Eq. 4.6), and the other parameters inform the irreversible constitutive model for vascular tissue detailed in Sect. 4.4. TAA wall data is separated into samples taken from patients with bicuspid (BAV) and tricuspid (TAV) aortic valves, respectively

4.6.3 Ventricular Tissue Penetration

Tensile testing Pig hearts (n=12) were taken from the butchery and bone-shaped specimens aligned in cross-fiber direction were prepared, see Fig. 4.13c. In total 64 specimens were prepared, using the preparation techniques detailed in Sect. 4.6.2.

Tensile testing was performed with a conventional MTS systems, where specimens were loaded at a prescribed elongation rate of 0.2 mm/s until they failed. Then the ultimate first Piola-Kirchhoff strength $P_{\mathrm{ult}} = F_{\mathrm{ult}}/A$ was calculated, where A denotes the initial cross-sectional area at the specimen neck. The studied myocardial tissue withstood a first Piola-Kirchhoff stress in cross-fiber direction of $P_{\mathrm{ult}} = 0.0326(SD\ 0.0159)$ MPa, and further details are given elsewhere [73].

Modeling the bulk material In addition to direct failure-related energy dissipation (like collagen fiber breakage) also viscoelastic energy dissipation at the crack tip could be an important factor of failure propagation in vascular tissue, i.e., similar to observations made in rubber-like materials [99]. Consequently, ventricular tissue has been modeled as a viscoelastic material.

We assume an additive decomposition of the free-energy function $\Psi = \Psi_{\mathrm{vol}}(J) + \Psi_{\mathrm{iso}}(\overline{\mathbf{F}}, t)$ into volumetric Ψ_{vol} and isochoric Ψ_{iso} contributions, where $\overline{\mathbf{F}} = J^{-1/3}\mathbf{F}$ denotes the unimodular part of the deformation gradient $\mathbf{F}$, with $J = \det\mathbf{F}$ and t being the time. In order to capture the non-linear mechanics of cardiac tissue, the polynomial free-energy

$$\Psi_{\mathrm{iso}}^{\infty} = c_1(I_1 - 3) + c_2(I_1 - 3)^2, \tag{4.21}$$

was used, where the invariant $I_1 = \mathrm{tr}\overline{\mathbf{C}}$ of the modified right Cauchy-Green strain $\overline{\mathbf{C}} = \overline{\mathbf{F}}^{\mathrm{T}}\overline{\mathbf{F}} = J^{-2/3}\mathbf{C}$ was introduced. This form of the constitutive relation has originally been proposed for rubber-like materials [100] and is frequently used in biomechanics

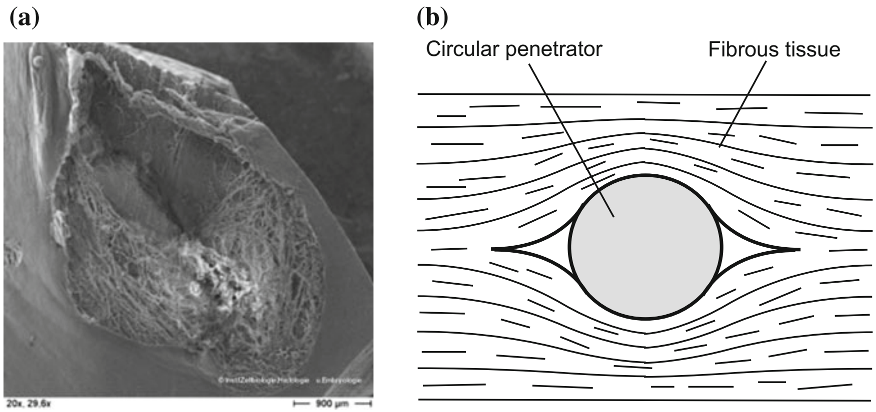

Fig. 4.15 **a** Electron microscopy image taken from ventricular tissue penetration experiments [104]. Image illustrates a splitting mode (mode-I) failure together with remaining deformations at the penetration site. **b** Idealized failure mode of ventricular tissue due to deep penetration. Crack faces are wedged open by the advancing circular punch defining a splitting mode (mode-I) failure (The punch advances perpendicular to the illustration plane.)

to describe the mechanics of the aneurysm wall, for example [101, 102]. For the present study, the parameters $c_1 = 10.0$ kPa and $c_2 = 7.5$ kPa were estimated form the myocardial tissue in cross-fiber direction [73].

In order to equip the formulation with rate-dependent properties, the constitutive model (4.21) was extended to viscoelasticity, and the isochoric free-energy

$$\Psi_{\text{iso}} = \left\{ 1 + \sum_{k=1}^{k} \beta_k [1 - \exp(-t/t_k)] \right\} \Psi_{\text{iso}}^{\infty} \tag{4.22}$$

was considered. Here, β_k and t_k are Prony series parameters defining the tissue's rate-dependency. The model can be regarded as a generalized standard viscoelastic solid with k linear viscoelastic Maxwell elements [3].

This study considered two sets $\{\beta_k, t_k\}$ of constitutive parameters. Set I represented properties of the medial layer of arteries used in the literature [103], and Set II doubled the rate-effects by doubling the β_k parameters of Set I.

Cohesive model of myocardial tissue splitting Experimental penetration of biaxially stretched myocardial tissue indicated that crack faces were wedged open by the advancing punch [104], see Fig. 4.15. Such a splitting failure was modeled by a fracture process zone and captured by a traction separation law. Specifically, a triangular traction separation law related the traction $\mathbf{t}$ and the displacement at the interface. The cohesive strength of the interface was set to $t_0 = 32.6$ kPa, i.e., the tissue strength identified from tensile testing in cross-fiber direction. Two different fracture energies $\mathcal{G}_0 = 6.32$ Jm^{-2} and $\mathcal{G}_0 = 12.64$ Jm^{-2} were used to investigate their influence on the punch force-displacement response.

FE model of deep penetration A single penetration of biaxially stretched myocardial tissue [104] was modeled, where a punch of 1.32 mm in diameter penetrated a 10.0 mm by 10.0 mm tissue patch (ABAQUS/Explicit (Dassault Systèmes)), see Fig. 4.16(left). A cohesive zone was introduced in the middle of the domain, i.e., where tissue splitting was expected, and symmetry conditions of the problem were considered.

The investigated domain was discretized by 8120 hexahedral finite elements (b-bar formulation [6]), where the mesh was refined at the site of penetration. A penalty contact formulation [105] (with automatic adaptation of the penalty parameter) was used to model the rigid and frictionless contact problem.

The numerically predicted Cauchy stress in cross-fiber direction at the crack tip is shown in Fig. 4.16 (right), while Fig. 4.17 presents the influence of model

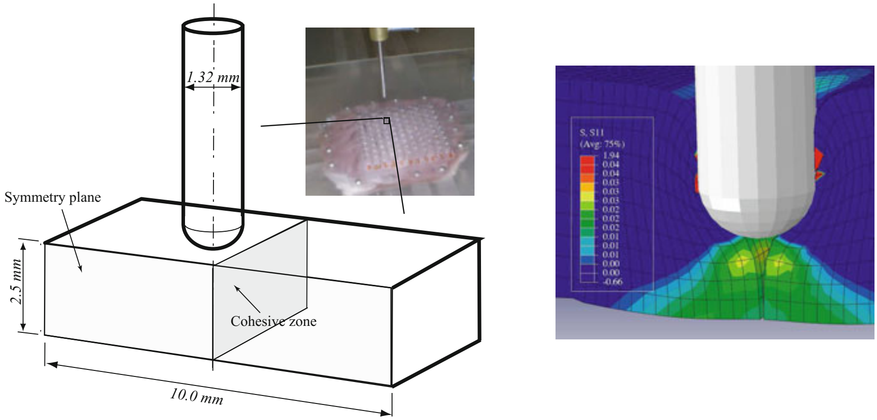

Fig. 4.16 *Left* FE model to investigate myocardial penetration by an advancing circular punch. Numerically predicted crack tip deformation and tissue stress during the crack faces are wedged open by the advancing circular punch

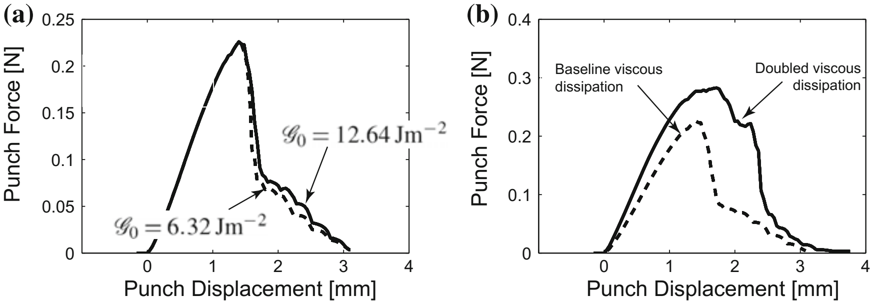

Fig. 4.17 Penetration force-displacement response of myocardium against deep penetration. **a** Impact of the fracture energy of the cohesive zone. **b** Impact of the viscoelasticity of the bulk material

parameters on the penetration force versus displacement properties. Specifically, Fig. 4.17a illustrates that the energy release in the fracture process zone has almost no impact, while rate-dependent effects of the bulk material massively influence the penetration force versus displacement properties, see Fig. 4.17b. Compared to the experimentally recorded data [104], the FE predictions were too soft with the peak penetration force being about 2–4 times lower.

4.7 Conclusions

Vascular biomechanics is critical in order to define new diagnostic and therapeutic methods that could have a significant influence on healthcare systems and even on the life style of human beings. Despite continued advances in computer technology and computational methods, such simulations critically depend on an accurate constitutive description of vascular tissue. For many vascular biomechanics problems, robust modeling of damage accumulation and even tissue failure is required.

The present chapter summarized relevant continuum mechanical concepts and discussed parameter identification for such models. As long as the accumulated tissue damage does not trigger strain localization, such problems can be studied within the standard nonpolar continuum mechanics. However, if damage accumulation results in strain localization, the nonpolar continuum fails and tailored continuum approaches are needed. In addition, parameters for such failure models need to be identified from appropriate experimental setups at controlled failure progression. Failure in conventional engineering materials like steel has successfully been studied within Linear Fracture Mechanics (LFM) and related concepts. However, such concepts assume a sharp crack tip, which is not seen in failure of vascular tissue. Here, the crack tip is bridged by collagen fibers and other tissue ligaments bridge and motivates the application of cohesive failure models.

Difficulties to identify model parameters from experimental data increase with increasing number of parameters. However, at the same time a large number of constitutive parameters is needed to account for the complex elastic and irreversible mechanics of vascular tissues. Consequently, the application of constitutive models with parameters of physical meaning is recommended, such that tailored experiments can be designed, from which a subset of parameters can estimated independently. In addition, the experimental design should support parameter identification [106], i.e., experimental readings should be (i) sensitive to the model parameters and (ii) provide enough experimental information for a robust identification.

The present chapter regarded vascular tissue as an inert and passive material, which is clearly not the case. Like other biological tissues, the vascular wall responds to its mechanical environment and predictions based on passive constitutive models, i.e., suppressing tissue remodeling and growth, can only cover a limited time period. Understanding the tissue's inherent properties to adapt to mechanical environments might improve vascular biomechanics predictions in the future.

Acknowledgments The author of this chapter would like to thank Andrii Grytsan, KTH Royal Institute of Technology, Stockholm for the valuable feed-back on the manuscript.

References

1. Kachanov, L. (2013). *Introduction to continuum damage mechanics* (vol. 10). Springer Science & Business Media.
2. Viano, D. C., King, A. I., Melvin, J. W., & Weber, K. (1989). Injury biomechanics research: An essential element in the prevention of trauma. *Journal of Biomechanics*, *22*(5), 403–417.
3. Malvern, L. E. (1969). *Introduction to the mechanics of a continuous medium.*
4. Bigoni, D., & Hueckel, T. (1991). Uniqueness and localization—I. Associative and non-associative elastoplasticity. *International Journal of Solids and Structures*, *28*(2), 197–213.
5. Fu, Y. B., & Ogden, R. W. (2001). *Nonlinear elasticity: Theory and applications* (vol. 283). Cambridge University Press.
6. Zienkiewicz, O. C., & Taylor, R. L. (2000). *The finite element method: Solid mechanics* (vol. 2). Butterworth-heinemann.
7. Bažant, Z. P. (2002). Concrete fracture models: Testing and practice. *Engineering Fracture Mechanics*, *69*(2), 165–205.
8. Clark, J. M., & Glagov, S. (1985). Transmural organization of the arterial media. The lamellar unit revisited. *Arteriosclerosis, Thrombosis, and Vascular Biology*, *5*(1), 19–34.
9. Carey, D. J. (1991). Control of growth and differentiation of vascular cells by extracellular matrix proteins. *Annual Review of Physiology*, *53*(1), 161–177.
10. Alberts, B., Bray, D., Lewis, J., Raff, M., Roberts, K., Watson, J. D., et al. (1995). Molecular biology of the cell. *Trends in Biochemical Sciences*, *20*(5), 210–210.
11. Humphrey, J. D. (1999). Remodeling of a collagenous tissue at fixed lengths. *Journal of Biomechanical Engineering*, *121*(6), 591–597.
12. Nissen, R., Cardinale, G. J., & Udenfriend, S. (1978). Increased turnover of arterial collagen in hypertensive rats. *Proceedings of the National Academy of Sciences*, *75*(1), 451–453.
13. Hulmes, D. J. S. (2008). Collagen diversity, synthesis and assembly. In P. Fratzl (Ed.), *Collagen: Structure and mechanics* (pp. 15–47). New York: Springer Science+Business Media.
14. Roach, M. R., & Burton, A. C. (1957). The reason for the shape of the distensibility curves of arteries. *Canadian Journal of Biochemistry and Physiology*, *35*(8), 681–690.
15. Bergel, D. H. (1961). The static elastic properties of the arterial wall. *The Journal of Physiology*, *156*(3), 445.
16. Langewouters, G. J., Wesseling, K. H., & Goedhard, W. J. A. (1984). The static elastic properties of 45 human thoracic and 20 abdominal aortas in vitro and the parameters of a new model. *Journal of Biomechanics*, *17*(6), 425–435.
17. Sokolis, D. P. (2007). Passive mechanical properties and structure of the aorta: Segmental analysis. *Acta Physiologica*, *190*(4), 277–289.
18. Fung, Y.-C. (2013). *Biomechanics: Mechanical properties of living tissues*. Springer Science & Business Media.
19. Humphrey, J. D. (2013). *Cardiovascular solid mechanics: Cells, tissues, and organs*. Springer Science & Business Media.
20. Gasser, T. C., Ogden, R. W., & Holzapfel, G. A. (2006). Hyperelastic modelling of arterial layers with distributed collagen fibre orientations. *Journal of the Royal Society Interface*, *3*(6), 15–35.
21. Vidal, B. D. C., Mello, M. L. S., & Pimentel, É. R. (1982). Polarization microscopy and microspectrophotometry of sirius red, picrosirius and chlorantine fast red aggregates and of their complexes with collagen. *The Histochemical Journal*, *14*(6), 857–878.
22. Lindeman, J. H. N., Ashcroft, B. A., Beenakker, J. W. M., Koekkoek, N. B. R., Prins, F. A., Tielemans, J. F., et al. (2010). Distinct defects in collagen microarchitecture underlie

vessel-wall failure in advanced abdominal aneurysms and aneurysms in marfan syndrome. *Proceedings of the National Academy of Sciences*, *107*(2), 862–865.

23. Weber, K. T., Pick, R., Silver, M. A., Moe, G. W., Janicki, J. S., Zucker, I. H., et al. (1990). Fibrillar collagen and remodeling of dilated canine left ventricle. *Circulation*, *82*(4), 1387–1401.
24. Canham, P. B., Finlay, H. M., Dixon, J. G., Boughner, D. R., & Chen, A. (1989). Measurements from light and polarised light microscopy of human coronary arteries fixed at distending pressure. *Cardiovascular Research*, *23*(11), 973–982.
25. Canham, P. B., & Finlay, H. M. (2004). Morphometry of medial gaps of human brain artery branches. *Stroke*, *35*(5), 1153–1157.
26. Gasser, T. C., Gallinetti, S., Xing, X., Forsell, C., Swedenborg, J., & Roy, J. (2012). Spatial orientation of collagen fibers in the abdominal aortic aneurysm's wall and its relation to wall mechanics. *Acta Biomaterialia*, *8*(8), 3091–3103.
27. Diamant, J., Keller, A., Baer, E., Litt, M., & Arridge, R. G. C. (1972). Collagen; ultrastructure and its relation to mechanical properties as a function of ageing. *Proceedings of the Royal Society of London B: Biological Sciences*, *180*(1060), 293–315.
28. Gathercole, L. J., Keller, A., & Shah, J. S. (1974). The periodic wave pattern in native tendon collagen: Correlation of polarizing with scanning electron microscopy. *Journal of Microscopy*, *102*(1), 95–105.
29. Bingham, C. (1974). An antipodally symmetric distribution on the sphere. *The Annals of Statistics*, 1201–1225.
30. Scott, J. E. (2003). Elasticity in extracellular matrix "shape modules" of tendon, cartilage, etc. a sliding proteoglycan-filament model. *The Journal of Physiology*, *553*(2), 335–343.
31. Scott, J. E. (2008). Cartilage is held together by elastic glycan strings. Physiological and pathological implications. *Biorheology*, *45*(3–4), 209–217.
32. Haverkamp, R. G., Williams, M. A. K., & Scott, J. E. (2005). Stretching single molecules of connective tissue glycans to characterize their shape-maintaining elasticity. *Biomacromolecules*, *6*(3), 1816–1818.
33. Liao, J., & Vesely, I. (2007). Skewness angle of interfibrillar proteoglycans increases with applied load on mitral valve chordae tendineae. *Journal of Biomechanics*, *40*(2), 390–398.
34. Robinson, P. S., Huang, T.-F., Kazam, E., Iozzo, R. V., Birk, D. E., & Soslowsky, L. J. (2005). Influence of decorin and biglycan on mechanical properties of multiple tendons in knockout mice. *Journal of Biomechanical Engineering*, *127*(1), 181–185.
35. Sasaki, N., & Odajima, S. (1996). Elongation mechanism of collagen fibrils and force-strain relations of tendon at each level of structural hierarchy. *Journal of Biomechanics*, *29*(9), 1131–1136.
36. Fessel, G., & Snedeker, J. G. (2011). Equivalent stiffness after glycosaminoglycan depletion in tendon—an ultra-structural finite element model and corresponding experiments. *Journal of Theoretical Biology*, *268*(1), 77–83.
37. Redaelli, A., Vesentini, S., Soncini, M., Vena, P., Mantero, S., & Montevecchi, F. M. (2003). Possible role of decorin glycosaminoglycans in fibril to fibril force transfer in relative mature tendons—a computational study from molecular to microstructural level. *Journal of Biomechanics*, *36*(10), 1555–1569.
38. Vesentini, S., Redaelli, A., & Montevecchi, F. M. (2005). Estimation of the binding force of the collagen molecule-decorin core protein complex in collagen fibril. *Journal of biomechanics*, *38*(3), 433–443.
39. Rigozzi, S., Müller, R., & Snedeker, J. G. (2009). Local strain measurement reveals a varied regional dependence of tensile tendon mechanics on glycosaminoglycan content. *Journal of Biomechanics*, *42*(10), 1547–1552.
40. Rigozzi, S., Müller, R., & Snedeker, J. G. (2010). Collagen fibril morphology and mechanical properties of the Achilles tendon in two inbred mouse strains. *Journal of Anatomy*, *216*(6), 724–731.
41. Vaishnav, R. N., Young, J. T., Janicki, J. S., & Patel, D. J. (1972). Nonlinear anisotropic elastic properties of the canine aorta. *Biophysical Journal*, *12*(8), 1008.

42. Fung, Y. C., Fronek, K., & Patitucci, P. (1979). Pseudoelasticity of arteries and the choice of its mathematical expression. *American Journal of Physiology-Heart and Circulatory Physiology*, *237*(5), H620–H631.
43. Chuong, C. J., & Fung, Y. C. (1983). Three-dimensional stress distribution in arteries. *Journal of Biomechanical Engineering*, *105*(3), 268–274.
44. Takamizawa, K., & Hayashi, K. (1987). Strain energy density function and uniform strain hypothesis for arterial mechanics. *Journal of Biomechanics*, *20*(1), 7–17.
45. Humphrey, J. D., Strumpf, R. K., & Yin, F. C. P. (1990). Determination of a constitutive relation for passive myocardium: I. A new functional form. *Journal of Biomechanical Engineering*, *112*(3), 333–339.
46. Lanir, Y. (1983). Constitutive equations for fibrous connective tissues. *Journal of Biomechanics*, *16*(1), 1–12.
47. Wuyts, F. L., Vanhuyse, V. J., Langewouters, G. J., Decraemer, W. F., Raman, E. R., & Buyle, S. (1995). Elastic properties of human aortas in relation to age and atherosclerosis: A structural model. *Physics in Medicine and Biology*, *40*(10), 1577.
48. Holzapfel, G. A., Gasser, T. C., & Ogden, R. W. (2000). A new constitutive framework for arterial wall mechanics and a comparative study of material models. *Journal of elasticity and the physical science of solids*, *61*(1-3), 1–48.
49. Zulliger, M. A., Fridez, P., Hayashi, K., & Stergiopulos, N. (2004). A strain energy function for arteries accounting for wall composition and structure. *Journal of Biomechanics*, *37*(7), 989–1000.
50. Christian, T. (2011). Gasser. An irreversible constitutive model for fibrous soft biological tissue: A 3-D microfiber approach with demonstrative application to abdominal aortic aneurysms. *Acta Biomaterialia*, *7*(6), 2457–2466.
51. Peña, J. A., Martínez, M. A., & Peña, E. (2011). A formulation to model the nonlinear viscoelastic properties of the vascular tissue. *Acta Mechanica*, *217*(1–2), 63–74.
52. Gasser, T. C. (2011). A constitutive model for vascular tissue that integrates fibril, fiber and continuum levels with application to the isotropic and passive properties of the infrarenal aorta. *Journal of Biomechanics*, *44*(14), 2544–2550.
53. Hardin, R. H., & Sloane, N. J. A. (1996). Mclaren's improved snub cube and other new spherical designs in three dimensions. *Discrete & Computational Geometry*, *15*(4), 429–441.
54. Gasser, T. C. (2010). Nonlinear elasticity of biological tissues with statistical fibre orientation. *Journal of the Royal Society Interface*, *7*(47), 955–966.
55. Parry, D. A. D., Barnes, G. R. G., & Craig, A. S. (1978). A comparison of the size distribution of collagen fibrils in connective tissues as a function of age and a possible relation between fibril size distribution and mechanical properties. *Proceedings of the Royal Society of London B: Biological Sciences*, *203*(1152), 305–321.
56. Liao, H., & Belkoff, S. M. (1999). A failure model for ligaments. *Journal of Biomechanics*, *32*(2), 183–188.
57. Emery, J. L., Omens, J. H., & McCulloch, A. D. (1997). Biaxial mechanics of the passively overstretched left ventricle. *American Journal of Physiology-Heart and Circulatory Physiology*, *272*(5), H2299–H2305.
58. Emery, J. L., Omens, J. H., & McCulloch, A. D. (1997). Strain softening in rat left ventricular myocardium. *Journal of Biomechanical Engineering*, *119*(1), 6–12.
59. Oktay, H. S., Kang, T., Humphrey, J. D., & Bishop, G. G. (1991). Changes in the mechanical behavior of arteries following balloon angioplasty. In *ASME Biomechanics Symposium AMD* (120).
60. Ridge, M. D., & Wright, V. (1966). Mechanical properties of skin: A bioengineering study of skin structure. *Journal of Applied Physiology*, *21*(5), 1602–1606.
61. Abrahams, M. (1967). Mechanical behaviour of tendon in vitro. A preliminary report. *Medical and Biological Engineering*, *5*, 433–443.
62. Lanir, Y., & Sverdlik, A. (2002). Time-dependent mechanical behavior of sheep digital tendons, including the effects of preconditioning. *Journal of Biomechanical Engineering*, *124*(1), 78–84.

63. Salunke, N. V., & Topoleski, L. D. (1996). Biomechanics of atherosclerotic plaque. *Critical Reviews in Biomedical Engineering*, *25*(3), 243–285.
64. Hokanson, J., & Yazdani, S. (1997). A constitutive model of the artery with damage. *Mechanics Research Communications*, *24*(2), 151–159.
65. Balzani, D., Schröder, J., & Gross, D. (2006). Simulation of discontinuous damage incorporating residual stresses in circumferentially overstretched atherosclerotic arteries. *Acta Biomaterialia*, *2*(6), 609–618.
66. Calvo, B., Pena, E., Martins, P., Mascarenhas, T., Doblare, M., Jorge, R. M. N., et al. (2009). On modelling damage process in vaginal tissue. *Journal of Biomechanics*, *42*(5), 642–651.
67. Tanaka, E., & Yamada, H. (1990). An inelastic constitutive model of blood vessels. *Acta Mechanica*, *82*(1–2), 21–30.
68. Gasser, T. C., & Holzapfel, G. A. (2002). A rate-independent elastoplastic constitutive model for biological fiber-reinforced composites at finite strains: Continuum basis, algorithmic formulation and finite element implementation. *Computational Mechanics*, *29*(4–5), 340–360.
69. Ionescu, I., Guilkey, J. E., Berzins, M., Kirby, R. M., & Weiss, J. A. (2006). Simulation of soft tissue failure using the material point method. *Journal of Biomechanical Engineering*, *128*(6), 917–924.
70. Gasser, T. C., & Holzapfel, G. A. (2006). Modeling dissection propagation in soft biological tissues. *The European Journal of Mechanics—A/Solids*, *25*, 617–633.
71. Gasser, T. C., & Holzapfel, G. A. (2007). Modeling plaque fissuring and dissection during balloon angioplasty intervention. *Annals of Biomedical Engineering*, *35*(5), 711–723.
72. Ferrara, A., & Pandolfi, A. (2008). Numerical modelling of fracture in human arteries. *Computer Methods in Biomechanics and Biomedical Engineering*, *11*(5), 553–567.
73. Gasser, T. C. (2011). Numerical simulation of the failure of ventricular tissue due to deep penetration: The impact of constitutive properties. *Journal of Biomechanics*, *44*(1), 45–51.
74. Quinn, K. P., & Winkelstein, B. A. (2008). Altered collagen fiber kinematics define the onset of localized ligament damage during loading. *Journal of Applied Physiology*, *105*(6), 1881–1888.
75. Knörzer, E., Folkhard, W., Geercken, W., Boschert, C., Koch, M. H. J., Hilbert, B., et al. (1986). New aspects of the etiology of tendon rupture. *Archives of Orthopaedic and Traumatic Surgery*, *105*(2), 113–120.
76. Gentleman, E., Lay, A. N., Dickerson, D. A., Nauman, E. A., Livesay, G. A., & Dee, K. C. (2003). Mechanical characterization of collagen fibers and scaffolds for tissue engineering. *Biomaterials*, *24*(21), 3805–3813.
77. Silver, F. H., Freeman, J. W., & Seehra, G. P. (2003). Collagen self-assembly and the development of tendon mechanical properties. *Journal of Biomechanics*, *36*(10), 1529–1553.
78. Lubliner, J. (2008). *Plasticity theory*. Courier Corporation.
79. Simo, J. C., & Hughes, T. J. R. (2006). *Computational inelasticity* (vol. 7). Springer Science & Business Media.
80. Dugdale, D. S. (1960). Yielding of steel sheets containing slits. *Journal of the Mechanics and Physics of Solids*, *8*(2), 100–104.
81. Barenblatt, G. I. (1962). The mathematical theory of equilibrium cracks in brittle fracture. *Advances in Applied Mechanics*, *7*, 55–129.
82. Hillerborg, A., Modéer, M., & Petersson, P.-E. (1976). Analysis of crack formation and crack growth in concrete by means of fracture mechanics and finite elements. *Cement and Concrete Research*, *6*(6), 773–781.
83. Oliver, J. (1996). Modelling strong discontinuities in solid mechanics via strain softening constitutive equations. part 1: Fundamentals. *International Journal for Numerical Methods in Engineering*, *39*(21), 3575–3600.
84. Armero, F., & Garikipati, K. (1996). An analysis of strong discontinuities in multiplicative finite strain plasticity and their relation with the numerical simulation of strain localization in solids. *International Journal of Solids and Structures*, *33*(20), 2863–2885.
85. Wells, G. N., & Sluys, L. J. (2001). Three-dimensional embedded discontinuity model for brittle fracture. *International Journal of Solids and Structures*, *38*(5), 897–913.

86. Gasser, T. C., & Holzapfel, G. A. (2003). Necking phenomena of a fiber-reinforced bar modeled by multisurface plasticity. In *IUTAM Symposium on Computational Mechanics of Solid Materials at Large Strains* (pp. 211–220). Springer.
87. Gasser, T. C., & Holzapfel, G. A. (2003). Geometrically non-linear and consistently linearized embedded strong discontinuity models for 3D problems with an application to the dissection analysis of soft biological tissues. *Computer Methods in Applied Mechanics and Engineering*, *192*(47), 5059–5098.
88. Ortiz, M., & Pandolfi, A. (1999). Finite-deformation irreversible cohesive elements for three-dimensional crack-propagation analysis. *International Journal for Numerical Methods in Engineering*, *44*(9), 1267–1282.
89. Coleman, B. D., & Noll, W. (1963). The thermodynamics of elastic materials with heat conduction and viscosity. *Archive for Rational Mechanics and Analysis*, *13*(1), 167–178.
90. Ogden, R. W. (1997). *Non-linear elastic deformations*. Courier Corporation.
91. Gasser, T. C., & Holzapfel, G. A. (2005). Modeling 3d crack propagation in unreinforced concrete using pufem. *Computer Methods in Applied Mechanics and Engineering*, *194*(25), 2859–2896.
92. Spencer, A. J. M. (1984). Constitutive theory for strongly anisotropic solids. In *Continuum theory of the mechanics of fibre-reinforced composites* (pp. 1–32). Springer.
93. Antman, S. S. (1995). *Nonlinear problems of elasticity*.
94. Ogden, R. W. (2003). Nonlinear elasticity, anisotropy, material stability and residual stresses in soft tissue. In *Biomechanics of soft tissue in cardiovascular systems* (pp. 65–108). Springer.
95. Auer, M., & Gasser, T. C. (2010). Reconstruction and finite element mesh generation of abdominal aortic aneurysms from computerized tomography angiography data with minimal user interactions. *IEEE Transactions on Medical Imaging*, *29*(4), 1022–1028.
96. Forsell, C., Swedenborg, J., Roy, J., & Gasser, T. C. (2013). The quasi-static failure properties of the abdominal aortic aneurysm wall estimated by a mixed experimental–numerical approach. *Annals of Biomedical Engineering*, *41*(7), 1554–1566.
97. Forsell, C., Björck, H. M., Eriksson, P., Franco-Cereceda, A., & Gasser, T. C. (2014). Biomechanical properties of the thoracic aneurysmal wall: Differences between bicuspid aortic valve and tricuspid aortic valve patients. *The Annals of Thoracic Surgery*, *98*(1), 65–71.
98. Simo, J. C., & Taylor, R. L. (1991). Quasi-incompressible finite elasticity in principal stretches. Continuum basis and numerical algorithms. *Computer Methods in Applied Mechanics and Engineering*, *85*(3), 273–310.
99. Persson, B. N. J., Albohr, O., Heinrich, G., & Ueba, H. (2005). Crack propagation in rubber-like materials. *Journal of Physics: Condensed Matter*, *17*(44), R1071.
100. Yeoh, O. H. (1993). Some forms of the strain energy function for rubber. *Rubber Chemistry and Technology*, *66*(5), 754–771.
101. Raghavan, M. L., & Vorp, D. A. (2000). Toward a biomechanical tool to evaluate rupture potential of abdominal aortic aneurysm: Identification of a finite strain constitutive model and evaluation of its applicability. *Journal of Biomechanics*, *33*(4), 475–482.
102. Gasser, T. C., Auer, M., Labruto, F., Swedenborg, J., & Roy, J. (2010). Biomechanical rupture risk assessment of abdominal aortic aneurysms: Model complexity versus predictability of finite element simulations. *European Journal of Vascular and Endovascular Surgery*, *40*(2), 176–185.
103. Holzapfel, G. A., Gasser, T. C., & Stadler, M. (2002). A structural model for the viscoelastic behavior of arterial walls: continuum formulation and finite element analysis. *European Journal of Mechanics-A/Solids*, *21*(3), 441–463.
104. Gasser, T. C., Gudmundson, P., & Dohr, G. (2009). Failure mechanisms of ventricular tissue due to deep penetration. *Journal of Biomechanics*, *42*(5), 626–633.
105. Wriggers, P. (2006). *Computational contact mechanics*. Springer Science & Business Media.
106. Lanir, Y., Lichtenstein, O., & Imanuel, O. (1996). Optimal design of biaxial tests for structural material characterization of flat tissues. *Journal of Biomechanical Engineering*, *118*(1), 41–47.

Chapter 5
Mechanical Behaviour of Skin: The Struggle for the Right Testing Method

Cees Oomens

Abstract This chapter describes the main features of standard tests for a mechanical characterisation of biological materials, like uniaxial, biaxial and shear tests. After that, the inverse, mixed experimental/numerical methods will be introduced as a tool to create more freedom in the design of experiments and to make the transition from ex vivo testing to in vivo testing possible. A short introduction to the algorithms that can be used to minimise the difference between the experimental results and the numerical results will be discussed, followed by two practical examples applied to skin. The chapter finishes with a comparison between the advantages and disadvantages of in vivo and ex vivo testing.

5.1 Introduction

The author's lectures at CISM in October 2015 had the same title as the present chapter. The subtitle: "the struggle for the right testing method" was meant to be a teaser for the students and defined a red line through the research at Eindhoven University of Technology in the last 30 years on testing methods for soft biological materials. Indeed is was a tortuous road to arrive where we are now and this road was presented chronologically during the CISM school. For this chapter, a different approach is chosen.

Skin is used as an example of soft biological tissues for which the proper mechanical tests had to be designed. All the difficulties associated with mechanical characterisation of soft biological materials, such as highly nonlinear, viscoelastic, anisotropic behaviour that may change over time (short term as well as long term through ageing), variation at different body locations and between individuals are encountered when working on skin. In addition skin is a heterogeneous material in the sense that it consists of different layers with varying dimensions and properties (ranging from a few μm's to the mm scale). It is difficult to make tissue samples with appropriate

---

C. Oomens (✉)
Eindhoven University of Technology, Eindhoven, The Netherlands
e-mail: C.W.J.Oomens@tue.nl

S. Avril and S. Evans (eds.), *Material Parameter Identification and Inverse Problems in Soft Tissue Biomechanics*, CISM International Centre for Mechanical Sciences 573, DOI 10.1007/978-3-319-45071-1_5

shapes for testing, to prepare and preserve the tissue and to fix it to grips of testing equipment. Last but not least in vivo skin is under pretension and it is difficult to account for this.

The good news is that human skin is accessible for noninvasive, in vivo measurements and a plethora of tests have been developed to measure in vivo skin properties. Unfortunately, many of these test are not really meant to measure parameters in constitutive equations, but are phenomenological and descriptive and only used in comparative studies (for example the effect of ageing or a certain pathology on skin properties). Data from these experiments are not suitable to be used as parameters in constitutive models. Or in other words: the outcome of the descriptive tests leads to a set of structural properties rather than material properties. However, material models are indispensable for simulations related to healthcare problems or for development of personal care devices. To be able to determine parameters in constitutive equations in an in vivo setting an inverse analysis has to be applied involving rather complicated (numerical) models to analyse the experiment.

The outline of the present chapter is as follows. In Sect. 5.2 the features of standard tests are described and a few examples are given where this technique is applied for ex vivo mechanical characterisation of skin. Section 5.3 explains how inverse methods work and this is illustrated with a few examples where this technique is applied for in vivo determination of the mechanical properties of skin. In Sect. 5.4 both methods will be compared and the pros and cons will be discussed.

5.2 Standard Tests for Ex Vivo Material Testing

Figure 5.1 shows some schematic drawings of standard tests to characterise materials. For a uniaxial test (Fig. 5.1a) a long slender dogbone shaped bar is clamped in a mechanical testing machine. The dogbone shape reduces clamping effects in the long slender part of the bar. If the material has homogeneous properties and the bar is indeed a long slender structure, with a length much higher than the cross-sectional dimensions, stretching of the bar will lead to a uniaxial stress state in the bar. The stress can be derived by dividing the measured force by the cross-sectional area. Usually the length change of the bar is measured with a contactless measurement system in the middle section of the bar (avoiding effects of slipping in the clamps) and sometimes the reduction of the cross-sectional area is measured, so the Poisson's ratio can also be derived from the test. This all works quite well for homogeneous, isotropic, stiff materials and for small deformations. In mechanical and civil engineering, for technical materials, this test is standardised and if performed well is a good way to determine material properties. The stress as well as the strain state can be derived directly from the measurements and the material properties: Young's modulus and Poisson's ratio can be determined easily.

The biaxial test in Fig. 5.1b is based on a similar idea. A square sample is clamped in a testing machine enabling to stretch the material in two directions independently. The clamping system is designed such that the square sample remains a square

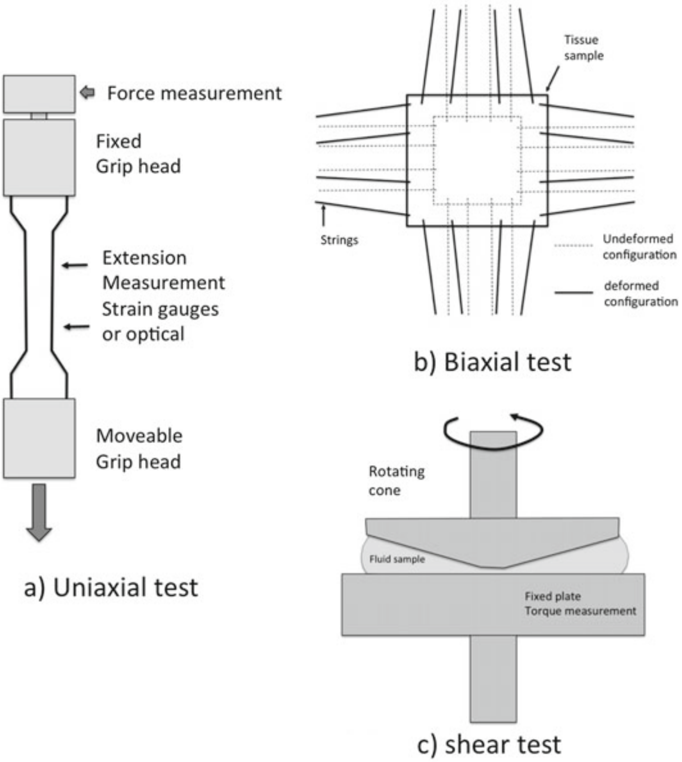

Fig. 5.1 Examples of standard tests **a** uniaxial extension **b** biaxial test **c** shear test

after it is being stretched. However, when the sample has anisotropic properties, the forces in the two directions will be different and anisotropic material properties can be derived. Like in the uniaxial test, for homogeneous material samples the stress and strain field is constant in a large part of the sample at a certain distance of the clamps, and can be measured directly, independent of the material properties of the used sample. From this stress and strain field the material parameters can be derived easily. One of the problems encountered in this type of test is the required uniformity in a part of the sample. The biaxial deformation is obtained using hooks that penetrate the skin. These hooks are usually attached to strings or slender bars that are stiff in tension, but can bend very easily to accommodate movement in the direction perpendicular to the pulling direction. The penetration locations lead to stress and strain concentrations around the hooks, which may lead to tearing of the tissue and a partly inhomogeneous strain field in the sample. This means that specimen design and attachment significantly affect the uniformity of the strain field produced in biaxial tests [1].

A final example is the shear test that is used for viscoelastic materials and fluids. The sample is placed between a plate and a cone or between two plates. The cone is rotated. This can either be with a constant rotation speed, a rotation to a certain degree and then held constant (relaxation test) or using a harmonic oscillation. For small deformations at each time point the shear strain rate is approximately the same in the entire sample and can be determined from the cone rotation. The torque on the lower plate is measured and the viscosity of the fluid can be derived. Usually the test is performed at a large range of strain amplitudes to find the linear region and for a very large range of frequencies. This frequency range can often be extended by performing the experiment at different temperatures and using time-temperature superposition to create a master curve over a very large range of frequencies. Typical outcomes are storage and loss modulus as a function of frequency [2].

These are just three examples of standard tests to characterise materials, but there are many more. For most of these tests standards are defined on how to perform the test properly. What is common in all the standard tests is the possibility to derive the stress as well as the strain directly from the experiment, independent of the type of material that is being tested.

For many technical materials it is relatively easy to make test samples according to the agreed standards, but for most biological materials this is much more difficult. Below a number of reasons are given why standard tests for biological materials are difficult

- To create a sample it has to be taken out of a body. If it concerns human tissue it is either left over material of surgery or post mortem material. An other option is to use tissue from animals. In all situations the material is taken out of the body, so it loses part of its integrity, the pretension found in the living system is (partly) gone or difficult to maintain, the tissue is no longer supplied with blood and will start to deteriorate quickly. However, when isolated and preserved in a proper way the negative effects of making samples of biological materials can be reduced considerably and the parameters may change, but the physical behaviour will be similar to the behaviour in vivo. Also during testing the physical and chemical environment of the material has to be controlled (humidity, temperature).
- It is extremely difficult to make samples according to the standards (e.g. a dogbone shape of a soft biological material). The amount of material available is usually small or very small. Clamping is a big issue.
- Often the material has inhomogeneous properties, so the assumption in standard tests that the stress strain field is homogeneous is not a valid assumption.
- Especially for soft biological materials the samples can be stretched to very high deformations, they behave highly nonlinear and viscoelastic so the strain and strain rate history play an important role.

Despite the difficulties given above, standard tests are done quite often because they are well defined and they constitute the only way to gain a good understanding of the physical behaviour of the material and to define constitutive equations. Some of the above problems can be circumvented or partly solved using mixed numerical/experimental or inverse methods. These inverse methods are the only way to determine in vivo material parameters of biological materials. This method will be discussed in the next section.

5.3 Inverse Methods for In Vivo Material Testing

The biggest difference between standard testing and what is referred to as inverse methods is the use of numerical (usually FE) models to describe or simulate the experiment. Material parameter estimation is then a process of performing a large number of FE simulations with different parameter sets to "fit" the simulation to the experimental data. The biggest advantage of this method is the enormous freedom that is created to design experiments alleviating some of the difficulties encountered in standard tests. The method is schematically summarized in Fig. 5.2.

Let us assume an experiment is designed to determine material parameters of some tissue. The input of the experiment comprises natural or essential boundary conditions and is represented by a column $\boldsymbol{u}$

$$\boldsymbol{u} = \begin{bmatrix} u_1 \\ u_2 \\ \vdots \\ u_N \end{bmatrix} \tag{5.1}$$

where N is a discrete, finite number of applied loads or displacements (these can be functions of time). The output of the experiment is represented by the column $\boldsymbol{m}$ with length M (typically $M \neq N$). The column $\boldsymbol{m}$ may contain displacements, forces, velocities or any relevant field information that is measured in the experiment. A numerical model, usually a FE model, is developed which gives a proper description of the experiment. Some constitutive model for the materials used in the FE model has to adopted a priori (this can be based on results of standard testing for example) and implemented in the FE code. The unknown parameters in this model are stored in a column $\boldsymbol{\theta} = [\theta_1, ..., \theta_P]^T$, where P is the number of parameters. Also an initial

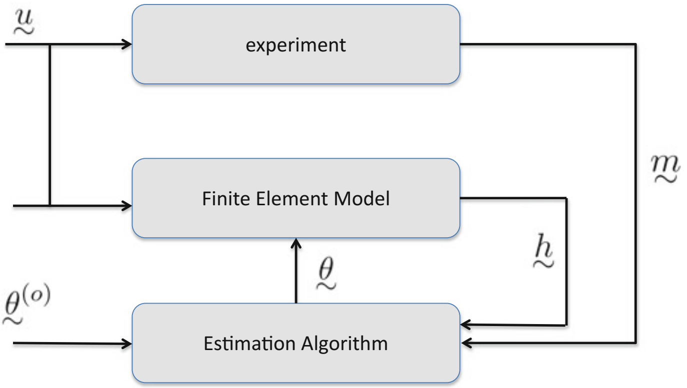

Fig. 5.2 Schematic drawing of a mixed numerical experimental or inverse method (adapted from [3])

estimate $\boldsymbol{\theta}^0$ of the material parameters has to be available. The input $\boldsymbol{u}$, boundary and initial conditions applied in the experiment, is also used as input for the FE simulation. The end result is a calculated output $\boldsymbol{h}$. The relation between the parameters $\boldsymbol{\theta}$ and the measurement $\boldsymbol{m}$ is written as

$$\boldsymbol{m} = \boldsymbol{h}(\boldsymbol{u}, \boldsymbol{\theta}) + \boldsymbol{\xi} \tag{5.2}$$

where $\boldsymbol{\xi}$ is an error column.

The contribution to the error column $\boldsymbol{\xi}$ can be categorised in two classes

- Measurement errors caused by the limited accuracy of the measurement system. As a consequence the measured response $\boldsymbol{m}$ is not exactly equal to the actual response.
- Modelling errors resulting from a constitutive model which is not correct or too simple or specimen geometry and/or boundary conditions that are not exact. Due to the presence of modelling errors it is not possible to find a parameter set for which the model predictions are exactly the same as the measured response, even in the absence of measurement errors.

Measurement errors can be taken into account in the parameter estimation process. For modelling errors this is much more difficult.

Minimization procedure

In this section, a short theory of the inverse method is given, largely based on [4]. This thesis was focussed on metals, but the theory has also been used a lot for biological materials. The aim of the inverse method is to find an estimation algorithm to determine the set of parameters $\boldsymbol{\theta}$ for which the model response $\boldsymbol{h}(\boldsymbol{\theta})$ is in closest agreement with the measurements $\boldsymbol{m}$. In many applications a quadratic objective function is defined of the following form:

$$J(\boldsymbol{\theta}) = [\boldsymbol{m} - \boldsymbol{h}(\boldsymbol{u}, \boldsymbol{\theta})]^T \boldsymbol{V} [\boldsymbol{m} - \boldsymbol{h}(\boldsymbol{u}, \boldsymbol{\theta})] + [\boldsymbol{\theta}^0 - \boldsymbol{\theta}]^T \boldsymbol{W} [\boldsymbol{\theta}^0 - \boldsymbol{\theta}] \tag{5.3}$$

In Eq. 5.3 the matrix $\boldsymbol{V}$ is a symmetric weighting matrix that accounts for the difference in accuracy of the entries of the column $\boldsymbol{m}$. The second term with the positive weighting matrix $\boldsymbol{W}$ accounts for the difference between current and initial parameters and expresses the confidence in the a priori estimates. The column $\boldsymbol{m}$ may contain properties with different dimensions (e.g. forces and displacements) and large differences in measurement accuracy. Using statistical properties of the measurement error, for example the mean and covariance given by

$$E\{\boldsymbol{\xi}\} = \boldsymbol{0} \quad ; \quad E\{\boldsymbol{\xi}\boldsymbol{\xi}^T\} = \boldsymbol{\Psi} \tag{5.4}$$

with $E\{.\}$ the expected value operator and $\boldsymbol{\Psi}$ the covariance matrix. An often used choice for $\boldsymbol{V} = \boldsymbol{\Psi}^{-1}$ and $\boldsymbol{W} = \boldsymbol{0}$ leading to a dimensionless J and an objective function where accurate measurements are weighted stronger than inaccurate measurements. This estimator is known as a Gauss–Markov estimator. If the error distribution of the measurement noise is available, the maximum likelihood estimator can be applied to use this extra information. This estimator chooses the parameter set which maximises the probability of obtaining the measurement set that was actually obtained. In case the noise has a normal distribution, the maximum likelihood estimator equals the Gauss–Markov estimator [5].

In some cases prior information about the parameter values is available. Then Bayesian estimators can be applied to include this extra information. In these estimators the parameters are considered to be random variables. In a technical application, due to the manufacturing process, different batches of materials can have different properties. In that case parameters for a batch can be seen as a random variable and let us assume that these parameters have a mean $\boldsymbol{\theta}^0$ and covariance matrix $\boldsymbol{P}^0$. Then to estimate parameters using this information would be included in a Bayesian estimator to determine new parameters for this particular batch. In that case Eq. 5.3 could be applied using $\boldsymbol{V} = \boldsymbol{\Psi}^{-1}$ and $\boldsymbol{W} = \boldsymbol{P}^0$. In this way the prior probability distribution of the parameters can be regarded as a mathematical way to express the confidence in the initial parameter estimates. In a biological context one could imagine that ex vivo studies help to generate a priori knowledge about material parameters that can be used as initial parameters for in vivo studies.

There are many methods available to minimise J. In this chapter we focus on the Gauss–Newton algorithm. A necessary condition at a local minimum of $J(\boldsymbol{\theta})$ is given by

$$\left[\frac{\partial J(\boldsymbol{\theta})}{\partial \boldsymbol{\theta}}\right]^T = \mathbf{0} \tag{5.5}$$

For a point in the parameter space to be a true(local) minimum, the second derivative of J has to be positive definite. Equation 5.5 results in a set of P nonlinear equations for the P unknown parameters

$$\boldsymbol{H}^T(\boldsymbol{\theta})\ \boldsymbol{V}[\boldsymbol{m} - \boldsymbol{h}(\boldsymbol{\theta})] + \boldsymbol{W}[\boldsymbol{\theta}^0 - \boldsymbol{\theta}] = \mathbf{0} \tag{5.6}$$

with:

$$\boldsymbol{H}(\boldsymbol{\theta}) = \frac{\partial \boldsymbol{h}(\boldsymbol{\theta})}{\partial \boldsymbol{\theta}} \tag{5.7}$$

Since the model based response $\boldsymbol{h}(\boldsymbol{\theta})$ is a nonlinear function Eq. 5.6 has to be solved iteratively. For this we assume that an estimate of the optimal parameter set is available. This set is denoted by $\boldsymbol{\theta}^i$ with i the iteration counter. The (a priori unknown) optimal set is given by $\boldsymbol{\theta}_{LS}$. In that case

$$\boldsymbol{\theta}_{LS} = \boldsymbol{\theta}^i + \delta\boldsymbol{\theta}^i \tag{5.8}$$

Substitution of (5.8) in (5.6) leads to:

$$\boldsymbol{H}^T(\boldsymbol{\theta}^i + \delta\boldsymbol{\theta}^i)\boldsymbol{V}[\boldsymbol{m} - \boldsymbol{h}(\boldsymbol{\theta}^i + \delta\boldsymbol{\theta}^i)] + \boldsymbol{W}[\boldsymbol{\theta}^0 - \boldsymbol{\theta}^i - \delta\boldsymbol{\theta}^i] = \mathbf{0} \tag{5.9}$$

By assuming that the error $\boldsymbol{\theta}^i$ is small the following iterative scheme can be derived to update the estimate $\boldsymbol{\theta}^i$:

$$\begin{aligned} \boldsymbol{\theta}^{i+1} &= \boldsymbol{\theta}^i + \delta\boldsymbol{\theta}^i && (5.10)\\ \delta\boldsymbol{\theta}^i &= \boldsymbol{K}_i^{-1}\left[\boldsymbol{H}_i^T\boldsymbol{V}[\boldsymbol{m}-\boldsymbol{h}^i] + \boldsymbol{W}[\boldsymbol{\theta}^0-\boldsymbol{\theta}^i]\right] && (5.11)\\ \boldsymbol{K}_i &= \boldsymbol{H}_i^T\boldsymbol{V}\boldsymbol{H}_i + \boldsymbol{W} && (5.12) \end{aligned}$$

In the neighbourhood of the optimal solution this scheme has quadratic convergence. If the initial estimate of the parameters is further away from the optimal solution, convergence is lower or the scheme may diverge. To improve convergence properties further away from the optimal solution several modifications of this scheme are proposed [6].

The iterative procedure is continued until the change in the parameter updates is smaller than a critical value

$$\sqrt{\delta\overline{\boldsymbol{\theta}}^{i\,T}\delta\overline{\boldsymbol{\theta}}^{i}} < \delta_\theta \qquad (5.13)$$

where:

$$\begin{aligned} \delta\overline{\boldsymbol{\theta}}^{i\,T} &= [\delta\overline{\theta}_1^i, ..., \delta\overline{\theta}_P^i] && (5.14)\\ \delta\overline{\theta}_1^i &= \frac{|\theta_j^i|}{\left(|\theta_j^i| + \delta_j\right)} \qquad j = 1, ..., P && (5.15) \end{aligned}$$

Here, δ_θ is an arbitrary small number that is used as a critical value and δ_j is introduced to avoid numerical problems when θ_j^i is nearly zero.

In the iterative scheme the sensitivity matrix $\boldsymbol{H}^i$ must be determined for each new estimate $\boldsymbol{\theta}^i$. Usually an analytical differentiation of $\boldsymbol{h}(\boldsymbol{\theta}^i)$ is impossible, because there is no explicit expression available. Therefore often the matrix is determined numerically, e.g. using a forward difference scheme

$$H_{kj}^i \approx \frac{h_k(\boldsymbol{\theta}^i + \Delta\theta_j\boldsymbol{e}_j) - h_k(\boldsymbol{\theta}^i)}{\Delta\theta_j} \qquad (5.16)$$

where $\boldsymbol{e}_j$ is a P-dimensional column. The jth entry is one and all other entries are zero and $\Delta\theta_j$ is a small variation of parameter j. Two types of error play a role in this process: the truncation error and the round off error. The truncation error originates from neglecting higher order terms in a Taylor series expansion

$$\frac{h_k(\boldsymbol{\theta}^i + \Delta\theta_j\boldsymbol{e}_j) - h_k(\boldsymbol{\theta}^i)}{\Delta\theta_j} = \frac{\partial h_k}{\partial\theta_j} + \frac{1}{2}\frac{\partial^2 h_k}{\partial\theta_j^2}\Delta\theta_j + \ldots \qquad (5.17)$$

The truncation error is on the order of

$$\varepsilon_t \approx \Delta\theta_j \left| \frac{\partial^2 h_k}{\partial \theta_j^2} \right| \tag{5.18}$$

On the other hand, if $\Delta\theta_j$ is too small, the influence of round off errors becomes important

$$\varepsilon_r \approx \varepsilon_h \frac{|h_k(\boldsymbol{\theta}^i)|}{\delta\theta_j} \tag{5.19}$$

with ε_r the round off error and ε_h the relative error in $h_k(\boldsymbol{\theta}^i)$ which depends on the accuracy of the forward analysis. Minimising the sum of the truncation and round off error leads to the following optimal choice for the step size $\Delta\theta_j^{opt}$:

$$\Delta\theta_j^{opt} = \sqrt{\varepsilon_h \frac{|h_k|}{|\partial^2 h_k / \partial \theta_j^2|}} = \sqrt{\varepsilon_h}\theta_j^c \tag{5.20}$$

and:

$$\theta_J^c = \sqrt{\varepsilon_h \frac{|h_k|}{|\partial^2 h_k / \partial \theta_j^2|}} \tag{5.21}$$

In the absence of information to calculate θ_j^c often θ_j^i is used, [7].

A very practical book for engineers that may be used for implementation of minimisation schemes is “Numerical Recipes” by [7]. For further reading on parameter estimation the textbook of [8] can be recommended.

In the sequel two examples will be discussed which have been used for an in vivo characterisation of human skin. For an extensive treatment the reader is referred to the original papers [9–11].

Example 1

Meijer et al. [10] developed an in vivo method to determine the anisotropic and nonlinear properties of the skin. The method was based on placing an oval ring at the inside of the lower arm of volunteers. The ring was glued to the skin, thus defining the domain that was analysed and defining essential boundary conditions at the edge of the domain. Within the domain two pads were glued to the skin which could be used to stretch the skin. See Fig. 5.3.

On the skin between the pads small markers were attached used to measure the inhomogeneous displacement field of the skin when the pads were moved to stretch the skin. The marker displacements and the force applied to the pads were used as experimental output for the column $\boldsymbol{m}$. The constitutive model was based on [12] and accounted for large strains and an in-plane fibre distribution. The estimation procedure was a least squares procedure similar to the one discussed above.

The result of the estimation procedure was disappointing. In simulations in which an “experiment” was defined with known material properties and the procedure was

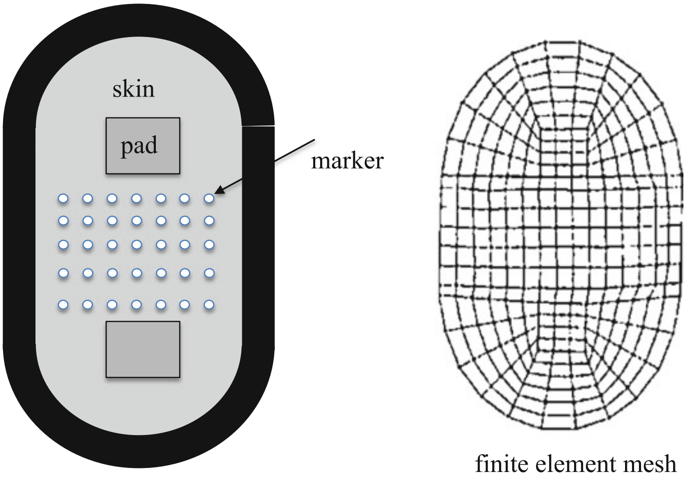

Fig. 5.3 Schematic drawing of experimental setup to determine anisotropic properties of skin and the FE mesh that was used (adapted from [10])

used to find those parameters everything worked fine. This means that in principle the setup and protocol should enable a proper parameter estimation. In practice it appeared that the stiffness of the fibres was not determined very accurately because the global level of strain was not high enough in the experiment for various reasons. A bigger problem was the constitutive model that was used to describe the skin. The authors came to the conclusion that the model errors for this application were too big, resulting in large residuals after the estimation process, which were not completely random.

Example 2

One of the tests that is used very often for in vivo characterization of skin is the suction test. In most applications the test is only used for comparative studies and not to determine parameters in a constitutive model. Diridollou et al. [13] already pointed out that without constitutive modelling the results are purely descriptive. The test works with a chamber that is placed on the skin usually fixed with adhesive tape. The contact area with the skin is a ring with an aperture in the middle, with varying diameters. By applying a partial vacuum (relative under pressure) in the chamber of the device, the skin is sucked into the chamber via the aperture and the displacement of the skin as a function of the pressure is used to derive material properties. By controlling the pressure history, time dependent aspects can also be taken into consideration. [9] extended the method by combining it with ultrasound. Later optical coherence tomography [11] was used to measure displacements of different skin layers. This allowed them to combine the method with subject specific FE modelling and to determine material parameters in a constitutive model. Figure 5.4a shows a schematic drawing of the suction device. The device was filled with water and combined with an ultrasound system to measure the local skin thickness and the

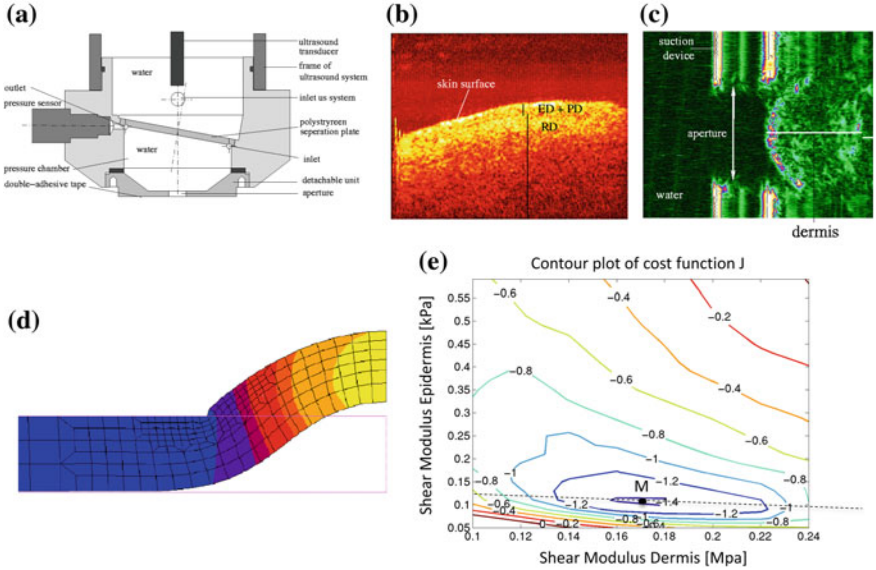

Fig. 5.4 Overview of the suction method **a** schematic drawing of the device **b** OCT image of deformed skin **c** ultrasound image of deformed skin **d** deformed FE mesh during suction **e** sensitivity analysis of two layer skin model (adapted from [9, 11])

bulging of the skin in the aperture during suction. Figure 5.4a. A stepwise decrease of the pressure in the chamber uplifted the skin to a maximum of 1.5 mm. Measurements were performed on the left forearm of 10 subjects (age 19 to 24 years old) in a climate controlled room at 22 °C and 50 % humidity. To analyse the experiment a patient specific axi-symmetric FE model was developed (thickness of the skin was based on the ultrasound measurement). A small part of the model is shown in Fig. 5.4d in deformed state.

In a first study, Hendriks et al. [9] used a one layer model for skin. Skin was assumed to behave like an isotropic hyper-elastic material described by a Mooney type of material model based on the following strain energy function:

$$W = C_{10}(I_1 - 3) + C_{11}(I_1 - 3)(I_2 - 3) \tag{5.22}$$

with C_{10} and C_{11} material parameters and I_1 and I_2 the first and second invariant of the left Cauchy–Green tensor $\boldsymbol{B} = \boldsymbol{F} \cdot \boldsymbol{F}^T$ and $\boldsymbol{F}$ the deformation gradient tensor. A large spread in data between the individual test persons was found, but in general the inverse method worked well and unique solutions were obtained for the material parameters. A part of the large spread in results was due to fact that these were very sensitive for the thickness of the skin that was used in the model and with the ultrasound system used the error was rather high. Furthermore, although the fat has a very low stiffness the subcutaneous layers do influence the results and this was not accounted for in the model, nor was the skin anisotropy and the multilayered structure.

In an attempt to include the layered structure of skin, Hendriks et al. [11] combined suction with Optical Coherence Tomography (OCT) a technique with a better resolution than ultrasound enabling to measure thickness changes of individual layers (Fig. 5.4b). In this case, it was possible to measure thickness changes of the epidermis/papillary layer and the dermis. Both layers were seen as individual layers in the FE model with different material properties. The constitutive model for both layers was neo-Hookean.

Although the authors managed to find mechanical properties for the individual layers, this was not easy. Why this was the case is illustrated with the contour plot of Fig. 5.4e. The plot shows the cost function for different combinations of the stiffness of the dermis and the stiffness of the epidermis. Although a minimum seems to be found near point M in the figure the small gradient along the dotted line makes it very difficult for an automatic minimization algorithm to find a converged solution. The good news is, that in the range of parameters that was studied only one minimum was found, which often is not the case.

These were only two examples of in vivo tests to characterise skin. Hopefully they illustrate how difficult it is to design proper in vivo tests for biological materials. In the next section we will reiterate on the pros and cons of both in vivo and in vitro testing and we will end with a procedure that may alleviate some of the problems.

5.4 In Vivo Versus Ex Vivo Testing

It is worthwhile at this stage to have a look again at the title of this chapter. Which method is the best suitable method to mechanically characterise biological tissues? Several arguments can be given for in vivo testing. It is the only way to obtain subject specific properties or properties at different locations of the body. To study effects of ageing, pathology or to individualise medical treatments or personal care devices in vivo studies are indispensable. A big advantage is that for in vivo studies preservation or isolation is not necessary and in case of skin, studies can be noninvasive, because skin is very accessible.

On the other hand there are also a number of obvious disadvantages. Because samples are not isolated and have no well-defined geometry the analysis of the experiment is much more complicate compared to standard testing and in most situations can only be done by means of FE simulations. This immediately implies that inverse analysis is necessary to find material parameters. Skin is readily accessible for in vivo studies, but for deeper tissues this is much more complicated. Although techniques are being developed that allow stiffness evaluations in deeper layers like Magnetic Resonance Elastography (MRE) and Ultrasound Elastography (UE), also requiring an inverse analysis of wave equations there is still a long way to go before a full characterisation with these techniques is possible. Until the present day they are limited to small deformations and a limited range of frequencies and usually very simple constitutive equations are being used. Moreover, the resolution of these methods is not high enough to for examples determine the mechanical properties of individual layers in the skin. To derive constitutive equations, fully appreciating the complexity of the material behaviour, in vivo testing is not the obvious solution. This requires a thorough study of the microstructure of tissues and much more focussed tests.

Clearly there are some advantages to ex vivo test. Although more difficult than for technical materials indeed also for biological materials it is easier to define very well-controlled tests, isolating some of the aspects of the constitutive behaviour. There is more freedom to define different loading histories (small strain versus large strain, creep and relaxation tests, large frequency range in harmonic testing, testing at different environmental conditions and tests up to failure). By isolating different aspects of loading (shear, indentation, uniaxial and biaxial stretch, torsion) and combining this with studies on the microstructure and how the microstructure changes during loading it is better possible to formulate the physics of the behaviour and derive the proper constitutive equations. It was already mentioned that preservation and storage is an issue, but in the last two decades knowledge on how to do this has benefitted enormously from the developments in tissue engineering. Despite this ex vivo testing requires that samples are taken out of their natural environment and the structural integrity may be disrupted and loss of pretension is a problem. Another problem is the availability of the tissues.

Combining ex vivo and in vivo testing is the best option possible. Ex vivo testing is indispensable to really understand the full constitutive behaviour of biological materials. These tests should be used to define the physics, translate that into a correct mathematical framework and this framework should be implemented in either commercial or freely available FE packages. Ex vivo experiments will also define the range in which the material parameters can be found. Then in vivo tests can be designed and modelled by means of the FE packages available and material parameters can be measured using inverse methods. The parameters from ex vivo studies can be used as initial estimates. This enables to define methods that can be used at different parts of the body or once fully established to follow behaviour over time.

One point should be mentioned at this stage which is quite important. The above suggests that a complete description of the constitutive equations has to be defined before a subject specific procedure can be done. Apart from the fact that it is impossible to obtain a full description of the constitutive behaviour it is also not necessary. Always the first thing to do is to define the purpose or objective of the model. Why do you need a model of the behaviour? Which question do you want to answer and which level of sophistication do you need to answer that question? In the end this defines the procedure that you need. Sometimes this means that a descriptive mechanical test is sufficient in other cases it means that a very sophisticated model is required.

References

1. Eilaghi, A., Flanagan, J. G., Brodland, G. W., & Ross Ethier, C. (2009). Strain uniformity in biaxial specimens is highly sensitive to attachment details. *Journal of Biomechanical Engineering*, *131*.
2. Ward, I. M., & Hadley, D. W. (1993) *Mechanical properties of solid polymers*. Wiley.
3. Hendriks, M. A. N. (1991). *Identification of the mechanical behaviour of solid materials*. Ph.D. thesis, Eindhoven University of Technology.
4. Meuwissen, M. H. H. (1998). *An inverse method for the mechanical characterization of metals*. Ph.D. thesis, Eindhoven University of Technology.
5. Beck, J. V. & Arnold, K. J. (1977). *Parameter estimation in engineering and science*. Wiley.
6. Bard, Y. (1974). *Nonlinear parameter estimation*. Academic Press Inc.
7. Press, W. H., Flannery, B. P., Teukoslky, S. A., & Vetterling, W. T. (1986). *Numerical recipes: The art of scientific computing*. Cambridge University Press.
8. Norton, J. P. (1986). *An introduction to identification*. Academic Press.
9. Hendriks, F. M., Brokken, D. V., Van Eemeren, J. T. W. M., Oomens, C. W. J., Baaijens, F. P. T., & Horsten, J. B. A. M. (2003). A numerical-experimental method to characterize the non-linear mechanical behaviour of human skin. *Skin Research and Technology*, *9*(3), 274–283.
10. Meijer, R., Douven, L. F. A., & Oomens, C. W. J. (1999). Characterisation of anisotropic and non-linear behaviour in human skin in-vivo. *CMBBE*, *1*, 13–27.
11. Hendriks, F. M., Brokken, D., Oomens, C. W. J., & Baaijens, F. P. T. (2004). Influence of hydration and experimental length scale on the mechanical response of human skin in vivo, using optical coherence tomography. *Skin Res Technol*, *4*, 231–241.
12. Lanir, Y. (1983). Constitutive equations for fibrous connective tissues. *Journal of Biomechanics*, *16*(1), 1–12.
13. Diridollou, S., Patat, F., Gens, F., Vaillant, L., Black, D., Lagarde, J., et al. (1998). An in vivo method for measuring the mechanical properties of the skin using ultrasound. *Ultrasound in Medicine and Biology*, *2*, 215–224.

Chapter 6
Soft Tissue Finite Element Modeling and Calibration of the Material Properties in the Context of Computer-Assisted Medical Interventions

Yohan Payan

Abstract This chapter aims at illustrating how patient-specific models of human organs and soft tissues can be implemented into FE packages. First is addressed the question of the generation of patient-specific FE models compatible with the clinical constraints. Then is discussed the calibration of the material properties, with choices that should be done between calibrations based on ex vivo or in vivo tissues loadings. The example of computer-assisted maxillofacial surgery is addressed and results based on patients' data are provided.

6.1 Introduction

Computer-Assisted Medical Interventions (CAMI) is now a mature domain, with pioneering works dating from the 1980s. Researchers, clinicians and industrial partners have developed CAMI applications by building links with classical domains such as Computer Science, Robotics, Image Processing and Mathematics. The connection to Biomechanics is more recent and began with the study of bony structures. This was motivated by the fact that the pioneering CAMI devices were dedicated to orthopedics, where bones are the main anatomical structures of interest and were assumed to be nondeformable with a 3D shape easily reconstructible from Computed Tomography (CT) imaging. The main idea for such biomechanical modeling was to define a theoretical and numerical framework that provided information about the mechanics of the bones after a clinical treatment or a surgical intervention. For example, a patient-specific FE model of the femur could be designed to estimate the internal stresses generated by a hip prosthesis and therefore to help limit fracture risks. In these continuous biomechanical models, bones were usually considered as linear elastic material that underwent small deformations, which permitted easy calculation of numerical solutions. More recently, CAMI has addressed a larger spectrum of clinical domains such as cardiology, neurosurgery, maxillofacial surgery, urology, or

Y. Payan (✉)
TIMC-IMAG Laboratory, Univ. Grenoble Alpes & CNRS, 38000 Grenoble, France
e-mail: Yohan.payan@imag.fr

S. Avril and S. Evans (eds.), *Material Parameter Identification and Inverse Problems in Soft Tissue Biomechanics*, CISM International Centre for Mechanical Sciences 573, DOI 10.1007/978-3-319-45071-1_6

abdominal surgery. For these applications, biomechanics faces a new challenge since the involved tissues are required to move and be deformed by stresses generated by clinical actions. Moreover, soft tissues are difficult to model accurately since they typically exhibit complex, patient-specific, time dependent, nonlinear, inhomogeneous, and anisotropic behavior. Most of the corresponding biomechanical models need to include large deformation effects and visco-hyperelastic constitutive laws. Such models are very computationally demanding which explains why most of them are limited to preoperative use, since the simulations often require many minutes or hours to compute. This chapter aims at illustrating soft tissues modeling in the context of maxillofacial surgery where FE models of the facial tissues have to be developed to predict the impact on facial aesthetics depending on the bone repositioning maxillofacial surgery plan. The following questions will be addressed:

1. "How to generate a patient-specific FE model in a framework compatible with the clinical constraints?"
2. "How to calibrate the material properties for the modeled soft tissues?"

6.2 Computed-Assisted Orthognatic Surgery

6.2.1 Clinical Context

Orthognathic surgery (the "surgery to create straight jaws", see [1]) involves a wide variety of surgical procedures performed to reposition maxilla, mandible and the dento-alveolar segments to achieve facial and occlusal balance. This may be necessary due to congenital abnormalities, growth disturbances, or trauma. Such corrections are largely achieved by osteotomies, surgical techniques by which parts of the jaw(s) are cut to create separate fragments, which can then be moved to new positions while preserving their blood supply (Fig. 6.1). Correction of these abnormalities generally normalizes patients' dental occlusion and temporo-mandibular joint function, and results in improvement in functions such as chewing, speaking, and breathing, while often enhancing facial aesthetics. A model of the patient face used to simulate the morphological modifications following bone repositioning could greatly improve the planning of the intervention, for both the surgeon and the patient.

6.2.2 Patient-Specific Biomechanical Model of the Human Face

Various models of the face soft tissue were proposed in the literature. Whereas the first works were based on discrete models such as mass-spring models [2–6], many continuous FE models were then proposed in the literature [7–11]. Building an FE model of an organ requires an accurate observation of the anatomy of that organ

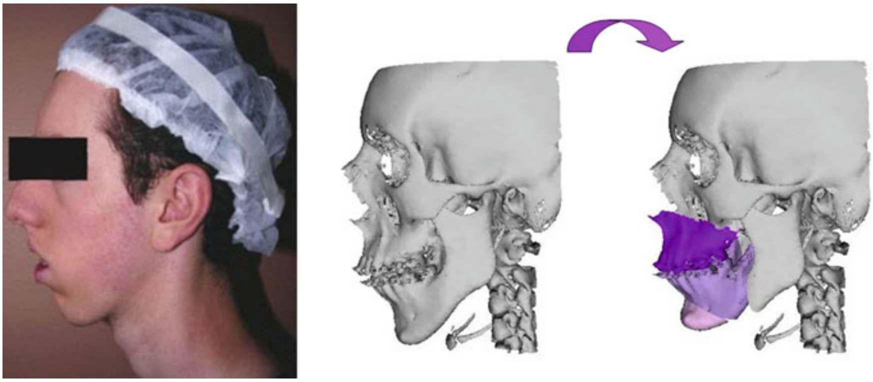

Fig. 6.1 A patient with a mandibular dysmorphosis (*left*) and the planned bone cuttings (*right*) [14]

with a description of the various structures that constitute the organ. In particular, a focus should be given to the mechanical differences that can be observed in terms of constitutive behavior, from one substructure to another one. Facial tissues are composed of a complex interweaving of muscular fibers, fat, glands, and mucosa [12]. The facial skin structure is basically made of three layers: the epidermis, the dermis, and the hypodermis. The epidermis is a superficial 0.1 mm thick layer, mainly composed of dead cells. The underlying dermis layer, which is much thicker (0.5 to 4 mm), is composed of elastin fibers mainly responsible for the global elastic behavior of the skin. Finally, the hypodermis layer, mainly fat tissues and mucosa, can slightly slide over the bones of the skull and jaw. The muscular structure (mostly flat muscles contained in the hypodermis layer) that connects these skin layers to the skull is extremely complex, with insertion points, orientations and interweaving fibers allowing great facial dexterity (mimics, expressions, lip gestures for speech production). A "generic" 3D FE model of the face was implemented in the ANSYS software [10, 13, 14]. The volume defined by the facial tissues located between the skull and the external skin surface of the face was manually meshed, as regularly as possible, with an eight-node hexahedra-dominant mesh representing the three layers of dermis and sub-dermis tissues with muscle courses identified inside the corresponding elements (Fig. 6.2). The mesh is symmetrical with respect to the mid-sagittal plane. Contacts are added to formulate inter-lip and lip/teeth collisions. In the framework of computer-assisted maxillofacial surgery, a model of each patient is required. A 3D mesh adapted to each patient's morphology must therefore be defined. Most of the existing FE face models are built from patient CT scans using automatic meshing methods. However, these methods usually lack robustness because of the complex geometry and topology of the face soft tissues, and the time needed to generate such meshes is generally several days, which is not compatible with clinical use. In addition, these models are limited in terms of biomechanical modeling. Indeed,

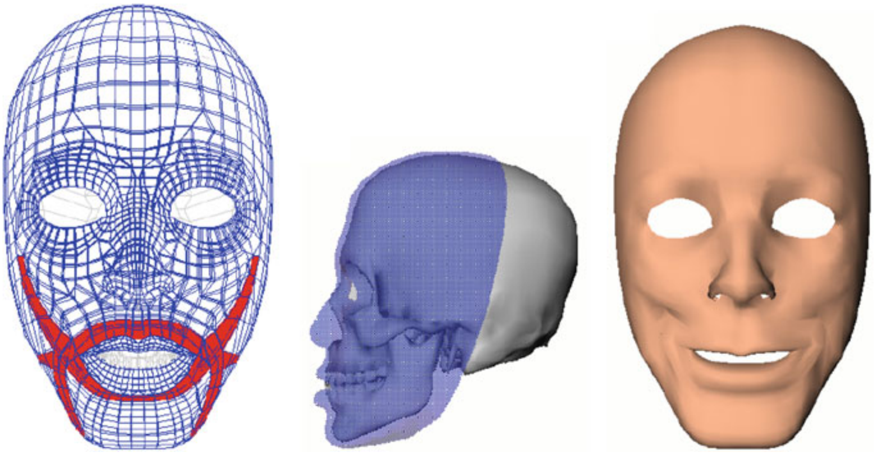

Fig. 6.2 Generic FE model: dermis and hypodermis fixed to the skull (*center*), course (*left*), and action (*right*) of the muscular fibers [10]

the unstructured organization of the elements does not allow one anatomical structure to be distinguished from another within the mesh. The face soft tissues are thus modeled as a single entity, without distinctions between dermis layers, fat, muscles, and mucosa. To overcome these limitations, our group has proposed a methodology called the Mesh-Match-and-Repair algorithm [15, 16] consisting first, in manually defining a structured 3D mesh, in order to build one "generic" model of the face. Emphasis is given to the design of the generic mesh, so that the elements inside the mesh can be associated to anatomical entities (dermis layers, fat, muscles, mucosa). Specific mechanical properties can therefore be explicitly given to such substructures. The next step of our methodology consists of matching the generic model to each patient's morphology, using an automatic elastic registration method: a structured FE model of each patient is then automatically generated (Fig. 6.3). Figures 6.1, 6.2, 6.3, 6.4 and 6.5 illustrate an example of the predictions provided by a FE model adapted to the geometry of a patient. The bone repositioning planned by the surgeon (Fig. 6.1) is put as an input to the model by imposing the corresponding displacements to the nodes that are supposed to be attached to the mandible, chin, and maxillary segments (Fig. 6.4). The results provided by the simulation can therefore be compared with the actual outcome of the surgery (Fig. 6.5).

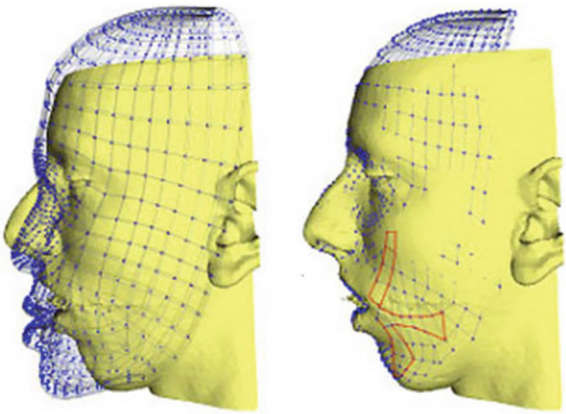

Fig. 6.3 Registration generic model to the morphology of the patient. *Left* generic model (*blue*) and 3D reconstruction of the patient's morphology (*yellow*). *Right* Result of the elastic registration [10]

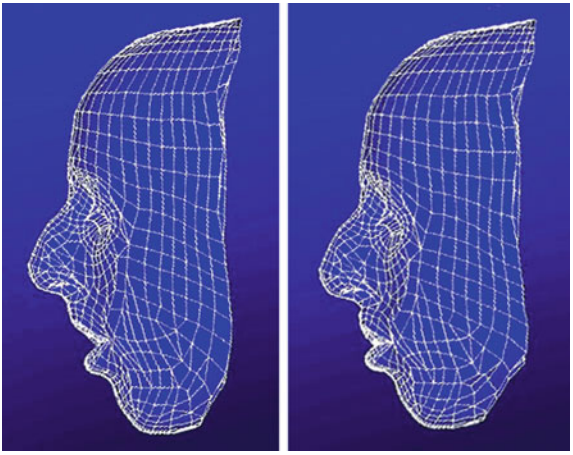

Fig. 6.4 Predictions of the skin deformations due to the planned bone repositioning [10]

Fig. 6.5 Postoperative data (*left*) and comparison with the predictions provided by the model (*right*)

6.3 Calibration of the Material Properties

The example provided in Figs. 6.1, 6.2, 6.3, 6.4 and 6.5 needs the facial soft tissues material properties to be calibrated to run the simulations. This can be done assuming mean generic values for such parameters (e.g., through ex vivo testing) or trying to fit the actual behavior of patient's soft tissues (in vivo measurements).

6.3.1 Generic Ex Vivo Calibration of the Material Properties

Some years ago, our group has proposed to characterize the mechanical behavior of the human cheek. For this, an indentation experiment was provided, by measuring the mechanical response of cheek tissues removed from the fresh cadaver of a 74-year-old female [17]. The experiment was run less than 24 h after death, in order to limit tissue deterioration. The method consists in exerting a calibrated pressure onto the material and simultaneously recording the corresponding deformations (Fig. 6.6). The indentation experiment itself does not provide the constitutive law of the material. Indeed, the measurements only give the nonlinear relationship between the local force applied to the external surface of the body and the resulting displacement. To get the constitutive law from this indentation experiment, i.e., the global relationship that

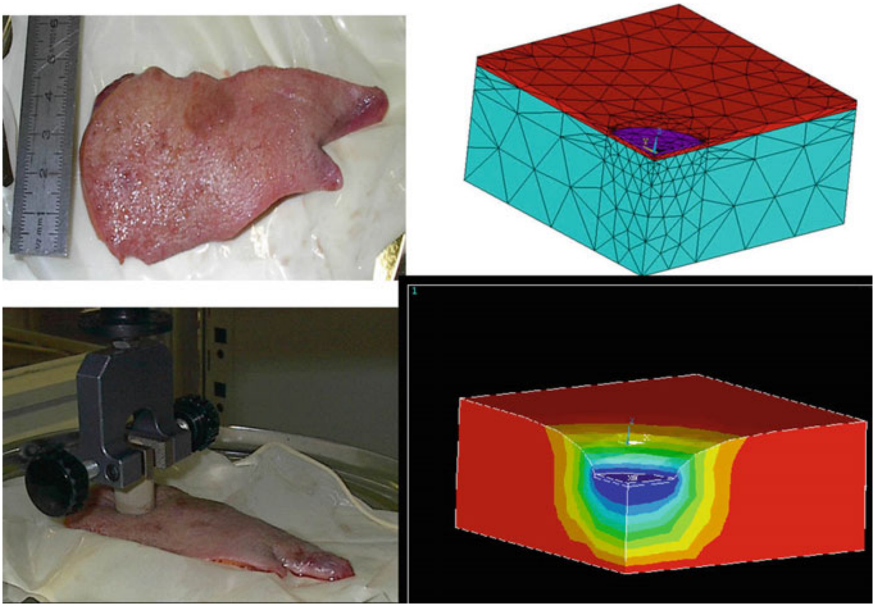

Fig. 6.6 Indentation on a cheek specimen and the corresponding axisymmetric FE analysis [17]

can be assumed between strain and stress inside the body, an optimization algorithm based on an "analysis by synthesis" strategy was elaborated. It consisted in

1. assuming a given constitutive law,
2. building a FE analysis (FEA) of the indentation experiment,
3. comparing the simulations provided by this FEA with the indentation measurements,
4. using this comparison to propose a change of the constitutive law that should make the FEA simulations and the measurements closer,
5. starting again until the comparison carried out in 3. gives satisfactory results.

Among the various strain-energy functions which can describe the nonlinear mechanical response measured during our indentation experiment (see Chap. 1 for the background on hyperelasticity), we have proposed to use the incompressible two parameter Yeoh strain-energy function [17]. Such a constitutive law was used to obtain results such as those shown in Fig. 6.4.

6.3.2 *In Vivo Calibration of the Material Properties*

Regarding the question of mechanical properties, it is now undoubtedly established that the constitutive behavior of human soft tissues are patient-specific and cannot be obtained by a generic value deduced from any standard ex vivo measurements. Indeed, it has clearly been shown [18–20] that the mechanical behavior of soft tissue can differ significantly between in vivo and ex vivo conditions, for a number of reasons, including the vascularization of the tissue. The various excitation methods range from suction to ultrasound with a variety of devices in each category. Aspiration is probably the most widely used technique. Starting from the pioneering work by Grahame and Holt [21], several authors proposed suction cups differing mostly in the way the aspirated height is measured (optically [22], using ultrasound [23]) or by their ability to accurately measure the dynamic response. Other excitation methods include indentation [19, 24] using a hand-held or robotic indenter, and torsion [25] or ballistometer [26] which consists of striking the tissue with a known mass and a known force. Ultrasound measurement [27, 28] is another method linked with the emerging field of elastography. Aspiration is probably the most widespread method because it is noninvasive and proved to be quite reliable. However, most of the papers rarely address the important issue of sterilization to any great depth of detail whereas such sterilization can be very important in case of the aspiration of human living tissues. In such a perspective, a sterilizable device has been developed (Fig. 6.7), called Light Aspiration device for in vivo Soft TIssue Characterization (LASTIC), based on the aspiration technique and originally introduced by Schiavone et al. [29] while quantifying the human brain behavior. LASTIC is a $33 \times 34\ \text{mm}^2$ metal cylinder composed of two compartments. The lower one is an airtight chamber, open at the bottom by a 10 mm diameter circular aperture and closed at the top by a glass window. The upper compartment holds the electronic part consisting of a miniature

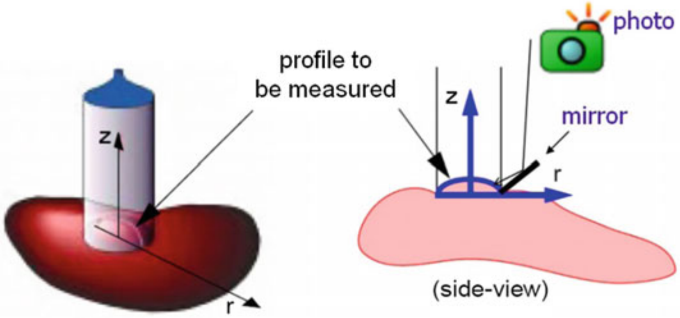

Fig. 6.7 Principle of the in vivo aspiration method [29]

2 megapixel digital camera and a LED used as a light source. The aspiration chamber is connected to a programmable syringe pump that can generate a negative pressure (measured by a manometer) which deforms the tissues on which LASTIC is laid on. This deformation is imaged by the camera via a 45° inclined mirror which provides a view of the tissue from the side. The height of the tissue deformation is segmented on the recorded image. Measuring the deformation height corresponding to several steps of increasing negative pressures can give an estimation of the behavior of the tissues. Like for the indentation experiment (Fig. 6.6), the deformation/pressure measurements are then processed through an inverse FE analysis to estimate the tissues constitutive laws.

To be able to improve the planning of the outcome of an aesthetic or maxillofacial surgery, it is necessary to estimate the stiffness of the facial soft tissues in several places. Four locations with presumably different tissue thicknesses and different amounts of fat and muscle were consequently chosen: the cheek, the cheekbone, the forehead, and the lower lip. To study the possible variations between subjects, the stiffness estimation was performed on a group of 16 healthy subjects, eight males

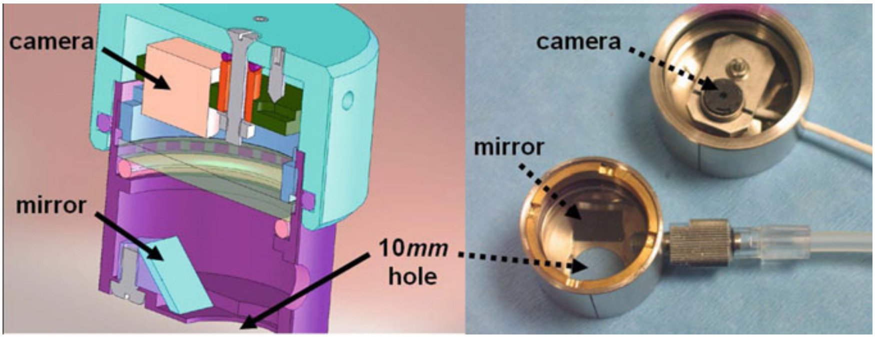

Fig. 6.8 LASTIC's two compartments. The *lower part* is the aspiration chamber with the mirror and the *upper part* contains the camera that images the deformation [29]

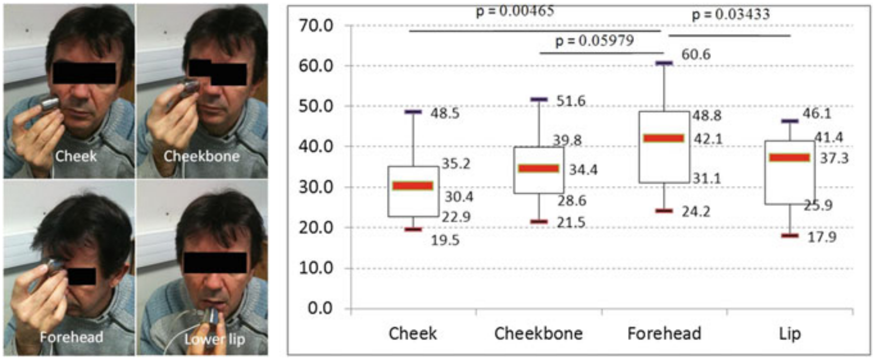
[redacted]
[redacted]
[redacted]
[redacted]

Fig. 6.9 Facial tissues equivalent Young moduli (kPa) measured at four locations [30]

and eight females, of different ages and body mass indexes. LASTIC was used to estimate the stiffness of the soft tissues at these four locations for these 16 subjects (Figs. 6.8 and 6.9).

Significant intra-subject differences in tissue stiffness are highlighted by these estimations. They also show important inter-subject variability for some locations

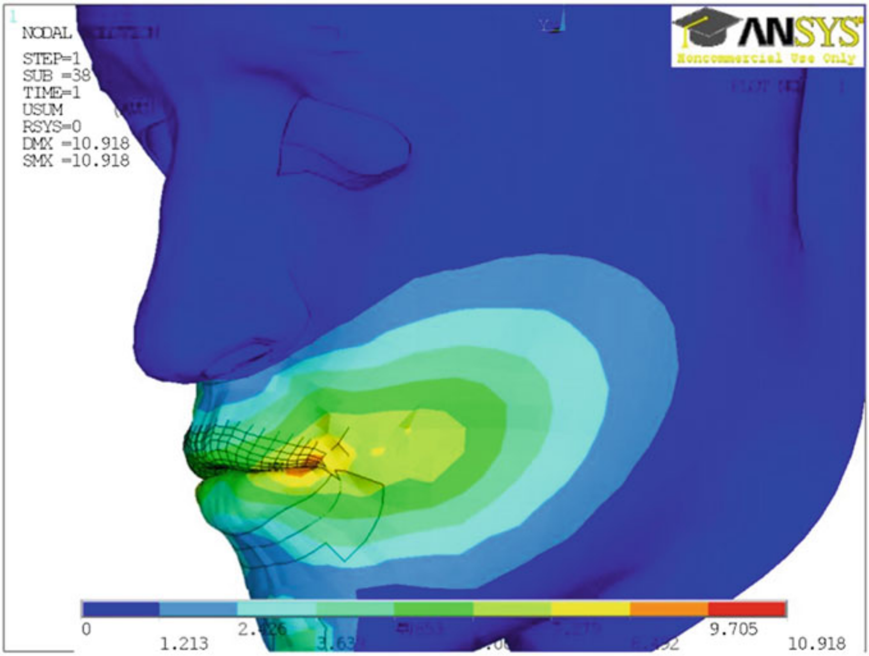

Fig. 6.10 Face deformations due to the activation of the orbicularis oris peripheral muscle [31]

even when mean stiffness values show no statistical difference. This study stresses the importance of using a measurement device capable of evaluating the patient-specific tissue stiffness during an intervention. The corresponding constitutive parameters can therefore be entered into our ANSYS environment to simulate face deformations due to bone repositioning. With a dedicated *Usermat* functionality of ANSYS, a transversely isotropic material was implemented to model muscle contraction [31]. The activation is accounted for by adding an active stress to the Cauchy stress in the direction of fibers. An additional isochoric term is included in the strain-energy function, to account for lateral normal stiffness. Figure 6.10 illustrates such muscle action with the deformations induced by the activation of the orbicularis oris peripheral muscle which is a sphincter muscle running around the lips and responsible for lip protrusion [32, 33].

6.4 Conclusion

This chapter aimed at illustrating the design of a patient-specific FE model of soft tissues in a clinical context. Assistance to orthognathic surgery was chosen as an example with the use of a biomechanical model of facial soft tissues including skin layers and muscular structures. The idea was to use such a model to predict the aesthetic and functional consequences of maxillary and mandible bone repositioning. The chapter has focused on the two main difficulties in elaborating such a model, namely

1. how to generate structured patient-specific FE models in a time scale that remains compatible with the clinical constraints
2. how to calibrate the mechanical parameters of these models.

Ex vivo and in vivo calibrations were both addressed. However, if the constitutive laws based on such calibration processes are important, it should be acknowledged that this importance is relative if boundary conditions are not sufficiently accurately taken into account. Indeed, as was shown in [34], changes in such boundary conditions (the displacements assigned to some nodes attached to the bony surfaces in our case) can have a much larger influence than any changes in the constitutive behavior of facial soft tissues. This point is consistent with the recent observations of [35] who mentioned, in the case of a brain FE model deformed by nodes' imposed displacements, the "unimportance of constitutive models in computing brain deformation for image-guided surgery".

Acknowledgments The author of this chapter is grateful to the important and valuable input of scientific colleagues and clinicians who participated to the studies cited in this chapter. He would like to thank: Georges Bettega, Franck Boutault, Marek Bucki, Matthieu Chabanas, Jean-Michel Gérard, Vincent Luboz, Christophe Marécaux, Mohammad Nazari, Jacques Ohayon, Pascal Perrier, Emmanuel Promayon and Patrick Schiavone.

References

1. Richter, M., Mossaz, C., De Tonnac, N., Jaquinet, A., Laurent, F., & Goudot, P. (2002). Chirurgie correctice des malformations ou “dysmorphies” maxillomandibulaires “avant d’agir”. *Encycl Méd Chir*.
2. Delingette, H., Subsol, G., Cotin, S., & Pignon, J. (1994). Craniofacial surgery simulation testbed. In *Visualization in Biomedical Computing 1994* (pp. 607–618). International Society for Optics and Photonics.
3. Waters, Keith. (1996). *Synthetic muscular contraction on facial tissue derived from computerized tomography data. Computer integrated surgery-technology and clinical applications*. Cambridge, London: MIT Press.
4. Keeve, E., Girod, S., & Girod, B. (1996). Computer-aided craniofacial surgery. In *Proceedings of Computer Assisted Radiology CAR 96* (pp. 757–762).
5. Teschner, M. (2001). *Direct computation of soft-tissue deformation in craniofacial surgery simulation*. Shaker Verlag.
6. Barre, S., Fernandez-Maloigne, C., Paume, P., & Subrenat, G. (2000). Simulating facial surgery. In *Electronic imaging* (pp. 334–345). International Society for Optics and Photonics.
7. Koch, R. M., Gross, M. H., Carls, F. R., von Büren, D. F., Fankhauser, G., & Parish, Y. I. H. (1996). Simulating facial surgery using finite element models. In *Proceedings of the 23rd annual conference on Computer graphics and interactive techniques* (pp. 421–428). ACM.
8. Keeve, E., Girod, S., Kikinis, R., & Girod, B. (1998). Deformable modeling of facial tissue for craniofacial surgery simulation. *Computer Aided Surgery*, *3*(5), 228–238.
9. Zachow, S., Gladiline, E., Hege, H. C., & Deuflhard, P. (2000). Finite-element simulation of soft tissue deformation. In *Proceedings of CARS* (pp. 23–28). Citeseer.
10. Chabanas, M., Luboz, V., & Payan, Y. (2003). Patient specific finite element model of the face soft tissues for computer-assisted maxillofacial surgery. *Medical Image Analysis*, *7*(2), 131–151.
11. Mollemans, W., Schutyser, F., Nadjmi, N., Maes, F., & Suetens, P. (2007). Predicting soft tissue deformations for a maxillofacial surgery planning system: From computational strategies to a complete clinical validation. *Medical Image Analysis*, *11*(3), 282–301.
12. Rouvière, H., & Delmas, A. (2002). *Anatomie humaine: Descriptive, topographique et fonctionnelle. Tête et cou*, vol. 1. Elsevier Masson.
13. Nazari, M. A., Perrier, P., Chabanas, M., & Payan, Y. (2010). Simulation of dynamic orofacial movements using a constitutive law varying with muscle activation. *Computer Methods in Biomechanics and Biomedical Engineering*, *13*(4), 469–482.
14. Chabanas, M. (2002). *Modélisation des tissus mous de la face pour la chirurgie orthognatique assistée par ordinateur*. Ph.D. thesis, Université Joseph-Fourier-Grenoble I.
15. Couteau, B., Payan, Y., & Lavallée, S. (2000). The mesh-matching algorithm: An automatic 3D mesh generator for finite element structures. *Journal of Biomechanics*, *33*(8), 1005–1009.
16. Bucki, M., Lobos, C., & Payan, Y. (2010). A fast and robust patient specific finite element mesh registration technique: Application to 60 clinical cases. *Medical Image Analysis*, *14*(3), 303–317.
17. Gérard, J.-M., Ohayon, J., Luboz, V., Perrier, P., & Payan, Y. (2005). Non-linear elastic properties of the lingual and facial tissues assessed by indentation technique: Application to the biomechanics of speech production. *Medical Engineering & Physics*, *27*(10), 884–892.
18. Kerdok, A. E., Ottensmeyer, M. P., & Howe, R. D. (2006). Effects of perfusion on the viscoelastic characteristics of liver. *Journal of Biomechanics*, *39*(12), 2221–2231.
19. Ottensmeyer, M. P. (2001). *Minimally invasive instrument for in vivo measurement of solid organ mechanical impedance*. Ph.D. thesis, Massachusetts Institute of Technology.
20. Gefen, A., & Margulies, S. S. (2004). Are in vivo and in situ brain tissues mechanically similar? *Journal of Biomechanics*, *37*(9), 1339–1352.
21. Grahame, R., & Holt, P. J. L. (1969). The influence of ageing on the in vivo elasticity of human skin. *Gerontology*, *15*(2–3), 121–139.

22. Kauer, M., Vuskovic, V., Dual, J., Székely, G., & Bajka, M. (2002). Inverse finite element characterization of soft tissues. *Medical Image Analysis*, *6*(3), 275–287.
23. Diridollou, S., Patat, F., Gens, F., Vaillant, L., Black, D., Lagarde, J. M., et al. (2000). In vivo model of the mechanical properties of the human skin under suction. *Skin Research and technology*, *6*(4), 214–221.
24. Carter, F. J., Frank, T. G., Davies, P. J., McLean, D., & Cuschieri, A. (2001). Measurements and modelling of the compliance of human and porcine organs. *Medical Image Analysis*, *5*(4), 231–236.
25. Agache, P. G., Monneur, C., Leveque, J. L., & De Rigal, J. (1980). Mechanical properties and young's modulus of human skin in vivo. *Archives of Dermatological Research*, *269*(3), 221–232.
26. Jemec, G. B. E., Selvaag, E., Ågren, M., & Wulf, H. C. (2001). Measurement of the mechanical properties of skin with ballistometer and suction cup. *Skin Research and Technology*, *7*(2), 122–126.
27. Chen, E. J., Novakofski, J., Jenkins, W. K., & O'Brien, W. (1996). Young's modulus measurements of soft tissues with application to elasticity imaging. *IEEE Transactions on Ultrasonics, Ferroelectrics, and Frequency Control*, *43*(1):191–194.
28. Gennisson, J.-L., Baldeweck, T., Tanter, M., Catheline, S., Fink, M., Sandrin, L., et al. (2004). Assessment of elastic parameters of human skin using dynamic elastography. *IEEE Transactions on Ultrasonics, Ferroelectrics, and Frequency Control*, *51*(8), 980–989.
29. Schiavone, P., Promayon, E., & Payan, Y. (2010). LASTIC: A light aspiration device for *in vivo* soft tissue characterization. In *Biomedical simulation* (pp. 1–10). Springer.
30. Luboz, V., Promayon, E., & Payan, Y. (2014). Linear elastic properties of the facial soft tissues using an aspiration device: Towards patient specific characterization. *Annals of Biomedical Engineering*, *42*(11), 2369–2378.
31. Nazari, M. A., Perrier, P., Chabanas, M., & Payan, Y. (2011). Shaping by stiffening: A modeling study for lips. *Motor Control*, *15*(1), 141–168.
32. Nazari, M. A., Perrier, P., Chabanas, M., & Payan, Y. (2011). A 3D finite element muscle model and its application in driving speech articulators. In *23rd Congress of the International Society of Biomechanics (ISB2011)*, Paper–ID.
33. Stavness, I., Nazari, M. A., Perrier, P., Demolin, D., & Payan, Y. (2013). A biomechanical modeling study of the effects of the orbicularis oris muscle and jaw posture on lip shape. *Journal of Speech, Language, and Hearing Research*, *56*(3), 878–890.
34. Chabanas, M., Payan, Y., Marécaux, C., Swider, P., & Boutault, F. (2004). Comparison of linear and non-linear soft tissue models with post-operative ct scan in maxillofacial surgery. In *Medical Simulation* (pp. 19–27). Springer.
35. Wittek, A., Hawkins, T., & Miller, K. (2009). On the unimportance of constitutive models in computing brain deformation for image-guided surgery. *Biomechanics and Modeling in Mechanobiology*, *8*(1), 77–84.